UNIVERSITY OF CALIFORNIA

Los Angeles

Quantitative methods to characterize viral infection dynamics inside hosts

A dissertation submitted in partial satisfaction of the

requirements for the degree

Doctor of Philosophy in Biology

by

Celine Elisa Snedden

2024

ABSTRACT OF THE DISSERTATION

Quantitative methods to characterize
viral infection dynamics inside hosts

by

Celine Elisa Snedden
Doctor of Philosophy in Biology
University of California, Los Angeles, 2024
Professor James O. Lloyd-Smith, Chair

The pathogenicity and transmissibility of a virus are strongly governed by spatial patterns of viral growth and spread across the internal tissue landscape of the host individual. These 'within-host dynamics' can differ widely among pathogens, and even among individuals infected with the same pathogen. Epidemiologists and microbiologists have long understood that many factors contribute to this observed heterogeneity, including the dose and route of exposure, host demographic and health factors, the cellular properties of different tissues (e.g., receptor expression), viral sensitivity to within-host abiotic conditions (e.g., temperature, pH), and physical connectivity between tissues (e.g., via blood). However, the relative effects of these governing processes on realized infection patterns inside hosts are difficult to disentangle and remain poorly understood, largely due to sampling constraints and data limitations. For humans, natural exposure

events are inherently unobservable, and available data can be biased towards individuals with more severe disease that seek treatment. Animal challenge experiments can control the relevant dimensions, but they either have limited clinical relevance due to crucial physiological differences from humans (e.g., for small animal models), or their small sample sizes cannot support robust statistical inferences under the standard approach of analyzing data only within the study that generated them (e.g., for non-human primate models).

Modern, data-driven computational models offer a powerful but underutilized toolkit to overcome these observational and analytical limitations. By using Bayesian statistical approaches to integrate quantitative modeling techniques with experimental data, it is possible to extract underlying patterns and putative mechanisms from limited empirical observations and to enhance these insights by jointly analyzing disparate datasets. In this dissertation, I develop and apply such methods to characterize the effects of exposure route, exposure dose, tissue connectivity, tissue traits, and host demographic factors on within-host SARS-CoV-2 dynamics. These analyses are supported by a large database of 107 studies that I have constructed, which includes 22,183 viral measurements from 721 non-human primates that were experimentally challenged with SARS-CoV-2 by various routes and with various doses.

In chapter 1, I address the fundamental question of when (if ever) RT-qPCR measurements of viral RNA load can reliably indicate the presence of infectious virus in a sampled tissue. This work constitutes the largest analysis of this question using *in vivo* infection data from individuals with known exposure conditions, and it lays crucial groundwork for the application of my customized statistical approach to public health contexts. I demonstrate that total RNA measurements can indeed predict culture positivity with a remarkable 85% accuracy on out-of-

sample data as long as predictions also account for other factors, including exposure conditions, host demographics, and assay protocols.

In chapter 2, I conduct the first large-scale quantitative analysis of respiratory virus challenge experiments in non-human primates to characterize the relative impacts of exposure route, exposure dose, age, sex, and species on within-host dynamics. I show that exposure route more strongly modulates the probability, onset, peak, and conclusion of SARS-CoV-2 infection across the respiratory and gastrointestinal tracts than exposure dose or demographic factors. I also show that infection patterns following aerosol inhalation are clearly distinct from any other exposure route, including intranasal or combined intranasal/intratracheal inoculation. This work provides the most comprehensive and quantitative evidence to date that exposure conditions shape infection patterns inside hosts, in ways that affect disease risk and shedding potential.

In chapter 3, I develop a novel modeling framework that formally investigates how tissue traits (e.g., receptor expression, protease availability) and connectivity structure interact to determine spatiotemporal infection patterns inside hosts, which I fit to the data from nine challenge studies. This model shows that SARS-CoV-2 infection patterns across the respiratory and gastrointestinal tracts are shaped by high rates of within-host viral dissemination. I also show that infections are overall more successful in the nose and throat than in the lung and lower GI, which is consistent with an estimated increase in the local infection rates at the lower ambient temperature of the upper respiratory tract.

Together, these chapters demonstrate that meta-analysis of the data from *in vivo* challenge experiments can overcome the difficulties arising from limited sample sizes in crucial but costly animal models and that they can yield robust insights beyond those attainable from individual studies, all while reducing overall animal use in infectious disease research. This dissertation

focuses on characterizing SARS-CoV-2 infections in non-human primates, but the methods developed here can be readily adapted to any other pathogen-host system, and they present generalizable, quantitative approaches to answer questions at the frontier of virology.

The dissertation of Celine Elisa Snedden is approved.

Nandita Garud

Van Maurice Savage

Thomas Friedrich

James O. Lloyd-Smith, Committee Chair

University of California, Los Angeles

2024

To my family

Table of Contents

List of Figures

List of Tables

List of Supplementary Figures

List of Supplementary Tables

Acknowledgements

To my advisor, Jamie Lloyd-Smith, I am so grateful for your mentorship throughout the past six years. Thank you for helping me explore as my projects took shape, and for your guidance and support in the niche that I ended up in. Thank you for celebrating with me when things went right, and for the encouragement, perspectives, and humor when they didn't. I am continually inspired by the example you set as a scientist, and I have learned so much from you about so many things, including ecology, virology, and statistics, just to name a few.

I am lucky to have had many other excellent mentors throughout my time as a student. To Daniel Becker, Richard Hall, and Sonia Altizer, thank you for introducing me to research and to disease ecology when I was just a young, mathematics undergraduate. That experience changed the course of my life in ways that I am immensely grateful for. To Ruian Ke and Alan Perelson, thank you for your guidance as I took my first steps into the challenging but rewarding world of within-host modeling. To Thomas Friedrich, thank you for helping ensure my research remains relevant and impactful for the virology community, and a huge thank you for generously serving on my committee even as a professor from a different university. To Van Savage and Nandita Garud, my other committee members, thank you both for your helpful comments on my research and for your advice during my time at UCLA.

To the past and present members of the Lloyd-Smith lab, it has been such a privilege to work with and learn from you all. To Dylan Morris and Amandine Gamble, the previous postdocs of the beloved Viro Group, thank you for your support and for the exemplary example you both set as quantitative virologists. Amandine, you were always willing to involve me in projects, and that meant so much to me. Thank you. Dylan, the Bayesian statistics wizard, you introduced me

to Stan, and you always advocated for the log scale, both of which had such a big impact on this dissertation. I learned a lot from you about a myriad of topics, and I'm a better scientist because of it. Thank you. To Lizzie Blackmore, Riley Mummah, Sarah Helman, Santiago Cardenas, Philip Lee, Oshiomah Oyageshio, Dave Daversa, Ana Gomez, Benny Borremans, and Katie Prager, thank you for being such kind, brilliant, and generally awesome colleagues and friends.

To Amanda Tokuyama, I am so grateful to have had you by my side since the start of this PhD adventure. Our friendship is one of the most meaningful outcomes of my UCLA experience. Thank you for every 1-2-3-send, for the pizza and the ice cream, for the trains and the birds, for Kirby (not) eating Zelda, for collecting feathers, and for always catching me when I fall, on the climbing wall or otherwise.

To Kaitlyn Allen, for always cheering me on and for keeping me grounded, since years and years before this experience even began. To Sara Makanani, for writing our first paper together, for listening and commiserating, and for being an all-around excellent friend in the past six years. To Samantha Wu, Samantha Inouye, Alexandra Ehrreich, Petko Fiziev, and the many other friends that have supported me leading up to or during this process, I owe you all a huge thank you.

To the Jaroszewiczowie and the Lewandowscy – thank you for welcoming me so warmly into your family and for making LA feel like home. I have treasured all of the Sunday brunches, the movie nights, and your many, many words of encouragement throughout this process. *Dziękuję. Ciasteczka.*

To my family, this PhD would not have been possible without you or the lessons you have taught me. To Mom, thank you for showing me how to maintain perspective, stay positive, and take everything one step at a time, even when times are tough. To Dadder, thank you for sharing your sense of curiosity and for modeling what it means to work hard but also play hard. To Beepa,

thank you for fostering my love of science, for teaching me biology on napkins, and for always believing (even when I was so young) that I would one day have a PhD. To Meema, thank you for showing me the value and the craft of a good story – I use those lessons all the time. To Opi, thank you for sharing your incredible resolve and determination, and for teaching me the valuable lesson that dessert is always an appropriate reward at the end (or middle) of a good day's work. To Omi, thank you for sharing your creative spirit, which has allowed me to see and treasure the art in science. To all of you and to my extended family, you have always believed in me whole-heartedly, and it taught me how to believe in myself. Thank you from the bottom of my heart for your unwavering support, endless fountain of love, and everything else you have done for me, which is so vast that it's unlistable. I love you all, and I am immeasurably grateful.

And, finally, to Artur Jaroszewicz. My husband, my best friend, my rock. You have been by my side for nearly every step of this journey. Thank you for so many things. For silly faces, stupid jokes, and terrible mispronunciations. For impromptu dance parties. For making up our own lyrics. For board game rivalry. For introducing me to many excellent video games that distracted me when I needed it. For bringing me coffee, tea, and snacks. For your excellent advice and for helping me let go. For believing in me, cheering me on, and building me up. For ten million other things that will have to go unsaid but that are so appreciated. Thank you. You brighten every single day, and words cannot express how grateful I am.

Chapter 1 is the accepted version of a manuscript that was published as: Snedden, C. E., & Lloyd-Smith, J.O. (2024). Predicting the presence of infectious virus from PCR data: A meta-analysis of SARS-CoV-2 in non-human primates. *PLOS Pathogens*, *20*(4), e1012171. https://doi.org/10.1371/journal.ppat.1012171. Author contributions were as follows: Conceptualization, J.O.L.-S and C.E.S; Methodology, J.O.L.-S and C.E.S; Formal Analysis,

C.E.S.; Writing – Original Draft, C.E.S.; Writing – Review & Editing, J.O.L.-S and C.E.S; Visualization, C.E.S; Funding Acquisition, J.O.L.-S and C.E.S.

Chapter 2 is a version of a manuscript currently in preparation for publication: Snedden, C.E., Morris, D.H., Friedrich, T.C., Lloyd-Smith, J.O. *Exposure route and dose shape SARS-CoV-2 infection patterns in non-human primates.* Author contributions were as follows: Conceptualization, J.O.L.-S and C.E.S; Methodology, J.O.L.-S, C.E.S, D.H.M; Formal Analysis, C.E.S.; Writing – Original Draft, C.E.S.; Writing – Review & Editing, J.O.L.-S, T.C.F, D.H.M, C.E.S; Visualization, C.E.S.

The work contained in this dissertation was supported by funding from multiple sources, including the National Institutes of Health (T32-GM008185), the Defense Advanced Research Projects Agency (DARPA PREEMPT #D18AC00031), and the UCLA Office of the Vice Chancellor for Research (3R Grant). I also gratefully acknowledge support from the UCLA Department of Ecology and Evolutionary Biology. The content of the article does not necessarily reflect the position or the policy of the US government, and no official endorsement should be inferred.

Vita

EDUCATION

B.A. in Mathematics (2014 – 2018)
Minor in Latin Studies
University of California, Berkeley

PUBLICATIONS

Snedden, C.E., & Lloyd-Smith, J.O. (2024). Predicting the presence of infectious virus from PCR data: A meta-analysis of SARS-CoV-2 in non-human primates. *PLOS Pathogens*, 20(4), e1012171. https://doi.org/10.1371/journal.ppat.1012171.

Helman, S.K., Tokuyama, A.F.N, Mummah, R.O., Stone, N.E., Gamble, M.W., **Snedden, C.E.**, Borremans, B., Gomez, A.C.R., Cox, C., Nussbaum, J., Tweedt, I., Haake, D.A., Galloway, R.L., Monzon, J., Riley, S.P.D., Sikich, J.A., Brown, J., Friscia, A., Lynch, J.W., Prager, K.C., Lloyd-Smith, J.O. (2023) Pathogenic Leptospira are widespread in the urban wildlife of southern California. *Scientific Reports*, 13(14368). https://doi.org/10.1038/s41598-023-40322-2

Snedden, C.E.*, Makanani, S.M.*, Schwartz, S.T., Gamble, A., Blakey, R.V., Borremans, B., Helman, S.K., Espericueta, L., Valencia, A., Endo, A., Alfaro, M.E., Lloyd-Smith, J.O. (2021) SARS-CoV-2: Cross-scale Insights from Ecology and Evolution. *Trends in Microbiology*, 29(7). https://doi.org/10.1016/j.tim.2021.03.013

Gamble, A., Yeo, Y.Y.*, Butler, A.*, Tang, H., **Snedden, C.E.,** Mason, C.T., Buchholz, D.W., Aguilar, H.C., Lloyd-Smith, J.O. (2021) Drivers and Distribution of Henipavirus-Induced Syncytia: What Do We Know? *Viruses*, 13(9). https://doi.org/10.3390/v13091755

Ruiz-Aravena, M.*, McKee, C.*, Gamble, A., Lunn, T., Morris, A., **Snedden, C.E.,** Yinda, C.K., Port, J.R., Buchholz, D.W., Yeo, Y.Y., Faust, C., Jax, E., Dee, L., Jones, D.N., Kessler, M.K., Falvo, C., Crowley, D., Bharti, N., Brook, C.E., Aguilar, H.C., Peel, A.J., Restif, O., Schountz, T., Parrish, C.R., Gurley, E.S., Lloyd-Smith, J.O., Hudson, P.J., Munster, V.J., Plowright, R.K. (2021) Ecology, evolution, and spillover of coronaviruses from bats. *Nature Reviews Microbiology*. https://doi.org/10.1038/s41579-021-00652-2

Becker, D.J., **Snedden, C.E.,** Altizer, S., & Hall, R.J. (2018). Host dispersal responses to resource supplementation determine pathogen spread in wildlife metapopulations. *The American Naturalist*, 192(4). https://doi.org/10.1086/699477

** Equal Contributors*

HONORS AND AWARDS

2022 UCLA Mautner Graduate Award

2022 Office of the Vice Chancellor for Research: 3Rs Grant Award Renewal, UCLA

2021 Office of the Vice Chancellor for Research: 3Rs Grant Award, UCLA
Title: *More insights from fewer experiments: Modernizing the use and re-use of animal data in virology*
* Co-written by Dr. James Lloyd-Smith, three postdoctoral researchers, and myself

2020 Systems and Integrative Biology Training Grant
NIH Ruth L. Kirschtein National Research Service Award Renewal

2019 Systems and Integrative Biology Training Grant
NIH Ruth L. Kirschtein National Research Service Award

2019 Graduate Student Summer Fellowship
Los Alamos National Laboratory, Center for Nonlinear Studies

2016 Population Biology of Infectious Diseases Research Experience for Undergraduates
University of Georgia, Athens, Odum School of Ecology

PRESENTATIONS

2024 Ecology and Evolution of Infectious Diseases Conference; Stanford University — Poster
Exposure dose and route modulate within-host infection patterns of SARS-CoV-2

2024 Ecology and Evolutionary Biology Research Day; UCLA — Talk
Exposure dose and route modulate within-host infection patterns of SARS-CoV-2

2023 Virology Seminar; UCLA — Talk
PCR data accurately predict infectious virus: a characterization of SARS-CoV-2 in non-human primates

2023 American Society for Virology Conference; University of Georgia, Athens — Poster
PCR data accurately predict infectious virus: a characterization of SARS-CoV-2 in non-human primates

2023 Quantitative and Computational Biosciences (QCBio) Retreat; UCLA — Poster
PCR data accurately predict infectious virus: a characterization of SARS-CoV-2 in non-human primates

2022 Guest Lecture for EEB 143: Viral Ecology and Evolution; UCLA — Lecture
Spatial ecology: applications to within-host viral infection

2019 Center for Nonlinear Studies; Los Alamos National Laboratory — Talk
Implications of highly variable viral production on within-host infection dynamics

2016 REU Symposium; University of Georgia, Athens — Poster
Diet, dispersal, and disease: How food supplemented habitat alters metapopulation disease spread

Chapter 1. Predicting the presence of infectious virus from PCR data: A meta-analysis of SARS-CoV-2 in non-human primates

Abstract

Researchers and clinicians often rely on molecular assays like PCR to identify and monitor viral infections, instead of the resource-prohibitive gold standard of viral culture. However, it remains unclear when (if ever) PCR measurements of viral load are reliable indicators of replicating or infectious virus. The recent popularity of PCR protocols targeting subgenomic RNA for SARS-CoV-2 has caused further confusion, as the relationships between subgenomic RNA and standard total RNA assays are incompletely characterized and opinions differ on which RNA type better predicts culture outcomes. Here, we explore these issues by comparing total RNA, subgenomic RNA, and viral culture results from 24 studies of SARS-CoV-2 in non-human primates (including 2167 samples from 174 individuals) using custom-developed Bayesian statistical models. On out-of-sample data, our best models predict subgenomic RNA positivity from total RNA data with 91% accuracy, and they predict culture positivity with 85% accuracy. Further analyses of individual time series indicate that many apparent prediction errors may arise from issues with assay sensitivity or sample processing, suggesting true accuracy may be higher than these estimates. Total RNA and subgenomic RNA showed equivalent performance as predictors of culture positivity. Multiple cofactors (including exposure conditions, host traits, and assay protocols) influence culture predictions, yielding insights into biological and methodological sources of variation in assay outcomes–and indicating that no single threshold value applies across

study designs. We also show that our model can accurately predict when an individual is no longer infectious, illustrating the potential for future models trained on human data to guide clinical decisions on case isolation. Our work shows that meta-analysis of *in vivo* data can overcome longstanding challenges arising from limited sample sizes and can yield robust insights beyond those attainable from individual studies. Our analytical pipeline offers a framework to develop similar predictive tools in other virus-host systems, including models trained on human data, which could support laboratory analyses, medical decisions, and public health guidelines.

Author Summary

Although viral culture is the gold-standard method to detect replicating and infectious virus, decisions in virology research, clinical diagnostics, and public health often must rely on faster, cheaper PCR assays that detect viral genetic material. Substantial scientific effort has focused on assessing whether PCR assays (and what kind of PCR assays) can accurately predict culture outcomes, often finding conflicting results. In our study, we address this long-standing question by developing a customized statistical approach to analyze a large database of non-human primates experimentally infected with SARS-CoV-2. We demonstrate that two common PCR protocols can predict viral culture results with similarly high accuracy, as long as interpretations account for other factors such as exposure conditions, demographics, and assay protocols. For example, we show that inoculated tissues are more likely to be culture-positive (for a given PCR result) on the first day post infection than all later days post infection or non-inoculated tissue on any day–a finding that will clarify interpretation of results in experimental studies. Beyond these biological findings, we also showed that our framework can accurately identify when an individual

is no longer infectious, showing the potential for future versions (trained on human data) to offer an individualized approach to ending isolation. Overall, our work presents a standardized framework to quantitatively predict viral culture outcomes based on faster and cheaper assays, which can be readily adapted to any other pathogen-host system with relevant data. Our work also demonstrates the power of (Bayesian) meta-analysis, which will be essential for the new era of data sharing in virology.

Introduction

Assays that detect and quantify the presence of viral genetic material are invaluable tools for clinicians, virologists, and epidemiologists, since they are used to identify infections, monitor individual infection trajectories, and track population-wide disease trends. The global reliance on quantitative reverse transcription-polymerase chain reaction (RT-qPCR) during the COVID-19 pandemic underscores its importance as a fast, sensitive, and relatively inexpensive mainstay of research and public health. Yet positive RT-qPCR results do not necessarily indicate active infection or viral shedding because these assays only target and quantify viral genomic material (Kralik & Ricchi, 2017; Yang & Rothman, 2004). Viral culture is the gold-standard method to detect infectious virus, but it is slow, labor-intensive, and requires niche resources like permissive cells and biosafety facilities. This precludes its use as a primary diagnostic in public health crises or even in standard clinical and research practices where speed and accessibility matter. The development of alternate methods to accurately characterize infectiousness is an active priority.

Seeking a culture-free method to identify replicating virus, many studies on SARS-CoV-2 developed alternative RT-qPCR assays based on coronavirus transcription mechanisms. Within host cells, coronaviruses transcribe not only full-length genomic RNA (gRNA) but also multiple subgenomic RNAs (sgRNA), which are a nested set of RNA segments that function as mRNA for translation of some structural and accessory proteins (Fehr & Perlman, 2015). Standard RT-qPCR protocols (X. Lu et al., 2020) typically amplify both gRNA and sgRNA simultaneously (henceforth termed a total RNA assay and abbreviated to ‘totRNA’). Since sgRNAs are only transcribed after cellular entry and are generally not packaged into mature virions (Escors et al., 2003), sgRNA-specific assays for SARS-CoV-2 were developed as a proxy for replicating virus (Wölfel et al.,

2020), and they have been used in various contexts, including to distinguish between replicating virus and residual inoculum in animal challenge experiments (Dagotto et al., 2021; Speranza et al., 2021). Many studies have also retrospectively analyzed clinical samples with sgRNA assays to gauge evidence of local replication (Bhatnagar et al., 2021; Bravo et al., 2022; Perera et al., 2020; Rodríguez-Grande et al., 2021; Wölfel et al., 2020), but reports of using sgRNA for point-of-care clinical decisions are exceptionally rare (Osborn et al., 2023).

Despite the popularity of sgRNA assays, their diagnostic utility relative to totRNA or gRNA assays is debated. Based on evidence that sgRNA may degrade faster than gRNA (Speranza et al., 2021), is not found in virions (Escors et al., 2003), and correlates better with viral culture results (Bonenfant et al., 2022; Bravo et al., 2022; Ford et al., 2021; Perera et al., 2020), some consider sgRNA a better indicator of recent replication and infectiousness (Rodríguez-Grande et al., 2021; Wölfel et al., 2020). Others dispute these claims based on contrary findings, including evidence of similar degradation rates between sgRNA and gRNA (Alexandersen et al., 2020; Dimcheff et al., 2021; Verma et al., 2021), the discovery of membrane-associated and nuclease-resistant sgRNA (Alexandersen et al., 2020), and analyses showing that sgRNA does not correlate better with culture outcomes (van Kampen et al., 2021). Studies finding that sgRNA quantities scale linearly with totRNA prompted further claims that sgRNA quantification offers no additional value relative to totRNA (Dimcheff et al., 2021; van Kampen et al., 2021; Verma et al., 2021), and skeptics have argued that any improved correlation between sgRNA and culture likely reflects the assay's lower sensitivity rather than true biological signal (Alexandersen et al., 2020; Dimcheff et al., 2021; Verma et al., 2021). Meanwhile, samples with large quantities of totRNA but undetectable sgRNA or unculturable virus are widely evident in the literature, especially in animal challenge experiments, but they go largely unexplained (Salguero et al., 2021; Speranza et al.,

2021). These patterns highlight the complexity of the relationships among PCR assays and viral culture, and they underscore that our understanding of their relative trajectories during infection remains incomplete. Given their foundational importance for research and potentially for healthcare, many studies have called for better methods to interpret these assays and their interrelationships (Bruce et al., 2022; Bullard et al., 2020; Gniazdowski et al., 2021; La Scola et al., 2020).

Data limitations are central to these unresolved debates on how well PCR predicts culture and whether that varies by RNA type since the generalizability of observed patterns remains unclear. Each study's sample size is typically quite small (e.g., often less than 100 RNA-positive samples), protocols differ between studies (e.g., PCR target genes, cell lines), patient demographics vary (e.g., hospitalized patients versus routine screening of university students), and analytical methods differ (e.g., descriptive statistics, logistic or linear regressions). Further unexplained variation may depend on patients' age, sex, and comorbidities, which can affect infection outcomes (Bajaj et al., 2021; Fajnzylber et al., 2020; Gadi et al., 2020; T. C. Jones et al., 2021) but are often unaccounted for in assay comparisons. Exposure route and dose are also unknown for clinical infections, and because the true infection time is unknown, analyses of clinical data must rely on metrics like time since symptom onset (Bullard et al., 2020; Dimcheff et al., 2021; M.-C. Kim et al., 2021; Salvatore et al., 2021; Wölfel et al., 2020), for which individual heterogeneity and recall bias can introduce substantial noise. Despite considerable effort to correlate RNA presence with culture outcomes, no study yet has jointly evaluated these various cofactors to identify and quantify their effects, and thus no method exists to integrate all of this information to quantitatively predict an individual's infectiousness on a per-sample basis. Instead, public health agencies have recommended isolating until obtaining two consecutive negative tests

or until ten days after an individual's first positive test, where the latter was later revised to only five days depending on symptom severity and other risk factors (CDC, 2020). However, some individuals experience prolonged shedding, and many individuals cease to be infectious well before testing PCR or antigen negative (Ford et al., 2021; Liu et al., 2020; van Kampen et al., 2021; Wölfel et al., 2020). An individualized, evidence-based method to ending isolation (i.e., a precision medicine approach) could improve these practices substantially, by alleviating personal and economic burdens imposed by unnecessarily long isolation while also reducing the number of days individuals may still be infectious after release under static guidelines.

In this study, we compiled and jointly analyzed a database of non-human primate (NHP) experiments, including 24 articles that reported per-sample measurements of at least two of the following assays: totRNA, sgRNA, and viral culture. This meta-analytic design enabled larger sample sizes and knowledge of variables that are unknowable with clinical data (i.e., exposure time, dose, and route), all for a gold-standard animal model of human disease (Estes et al., 2018). We developed a Bayesian hurdle model to predict the results from these disparate assays and to evaluate the effects of NHP species, demographic characteristics (age, sex), exposure conditions (dose and route), time since infection, and study protocols (sample type, target gene, cell line, culture assay) on the relationships among assay outcomes. We first applied this method to predict sgRNA results from totRNA results, which enabled us to reconstruct their relative trajectories for all included individuals. Then, we tested the ability of both PCR assays to predict viral culture results. We characterized model performance on withheld data to evaluate predictive accuracy and generalizability, and we analyzed apparent prediction errors in the context of individual time courses to diagnose possible sources of these errors. Finally, we assessed our model's ability to identify when an individual is no longer infectious, which we benchmarked against standard public

health guidelines implemented for humans. With this work, we aimed to: (i) uncover the fundamental relationships among SARS-CoV-2 PCR assays and the presence of infectious virus, in the most human-relevant experimental model, (ii) provide a quantitative tool that can directly support the analysis, interpretation, and comparison of SARS-CoV-2 studies conducted in NHPs, and (iii) offer a standardized framework that future models can adapt to analyze relationships among disparate assays in other pathogen-host systems.

Methods

Database compilation

Following many of the PRISMA guidelines for systematic literature searches (Moher et al., 2009), we constructed a comprehensive database of SARS-CoV-2 viral load and infectious virus data from non-human primate experiments (Figure S1.1). To be included, articles were required to: (i) experimentally infect rhesus macaques (*Macaca mulatta*), cynomolgus macaques (*Macaca fascicularis*), or African green monkeys (*Chlorocebus sabaeus*) with SARS-CoV-2 (restricted to basal strains, excluding those reported with the D614G mutation or other named variant), and (ii) report quantitative or qualitative measurements of viral load (measured by RT-qPCR) or infectious virus (measured by plaque assay or endpoint titration) from at least one biological specimen for at least one individual and at least one sample time post infection. Only individuals receiving no or placebo treatments were recorded.

Of 86 studies meeting these criteria, we used the 24 articles that reported at least two of the following assays: totRNA PCR, sgRNA PCR, or viral culture (Table S1.1, Figure S1.1) (Baum et al., 2020; Chandrashekar et al., 2020; Corbett et al., 2020; Cross et al., 2020; Dagotto et al., 2021; Deng et al., 2020; Gabitzsch et al., 2021; Ishigaki et al., 2021; Jiao et al., 2021; Johnston et al., 2021; B. E. Jones et al., 2021; Kobiyama et al., 2021; Li et al., 2021; Munster et al., 2020; Nagata et al., 2021; Patel et al., 2021; Salguero et al., 2021; Shan et al., 2020; Singh et al., 2021; Speranza et al., 2021; van Doremalen et al., 2020; Williamson et al., 2020; Woolsey et al., 2021; Yu et al., 2020). Raw data were used when available (published or obtained via email correspondence); otherwise, one author (CES) extracted data from published figures using the package ‘digitize’

(Poisot, 2011) in R (R Core Team, 2022). Additional details of data acquisition and standardization are described in the Supplementary Methods.

Bayesian hurdle model framework

To compare disparate assays, we developed a Bayesian hurdle model with two components: (i) a logistic regression that predicts whether assay Y will fall above the limit of detection ($Y_{>LOD}$) based on assay X, and (ii) a linear regression that describes the quantitative relationship between X and Y when both are measurable (Y_{value}) (Figure S1.2). Each component may include distinct sets of additional predictor variables (A_i and B_j, respectively). For the linear component, we incorporated hierarchical errors such that the model estimates article-specific error distributions (σ_a) based on distributions of population average errors ($\overline{\sigma}$) and error standard deviations (σ_{sd}). This captures potential differences in experimental noise among studies and protocols. The basic form of this model is as follows, where δ and β are regression coefficients associated with the predictors noted in the subscript:

Logistic

$$Y_{>LOD} \sim Bernoulli(p)$$

$$logit(p) = \gamma + \delta_X X + \sum_i \delta_{A_i} A_i$$

Linear

$$Y_{value} \sim N(y, \sigma_a)$$

$$y = \alpha + \beta_X X + \sum_j \beta_{B_j} B_j$$

$$\sigma_a \sim N(\overline{\sigma}, \sigma_{sd})$$

We evaluated the predictive performance of multiple models with different combinations of candidate predictors, and so the $\sum\delta_{Ai}A_i$ and $\sum\beta_{Bj}B_j$ terms varied for each considered model. Categorical predictors with more than two classifications were treated as unordered index variables, while binary predictors were treated as indicator variables. For instances of unknown age or sex, we marginalized over all possibilities. Unless otherwise stated, we used a threshold of 50% for the logistic components when classifying a sample as predicted positive or negative.

We first applied this framework to predict sgRNA from totRNA results (termed the 'sgRNA model'). All totRNA-negative samples are predicted to be sgRNA-negative, by definition. We then predicted viral culture results from PCR data using a parallel framework (termed the 'culture model'), with the following minor modifications: (i) we considered models depending on totRNA, sgRNA, or both as predictors, and (ii) we restricted analyses to the logistic component, given scarcity of quantitative culture results. The model predicts all RNA-negative samples are culture negative.

Candidate predictor selection and prior sensitivity analyses

All candidate predictors were included because of hypothesized effects on the relationships among assay results, as summarized below. We chose informative priors to rule out implausible parameter values and to reflect existing knowledge on the expected direction of individual effects (outlined in the Supplementary Methods), where appropriate. Notably, prior predictive simulations confirmed variable but reasonable *a priori* expectations for these informative priors, with substantial improvement over non-informative priors that do not reflect existing knowledge (Figure S1.13). Parameter estimates for the best models were qualitatively similar between informative and non-informative priors (Figure S1.13).

All considered models included totRNA, sgRNA, or both as the primary predictor(s). For all models, we considered multiple demographic factors including age class, sex, and non-human primate species, given hypothesized effects on SARS-CoV-2 infection (Bajaj et al., 2021; Blair et al., 2021; Fajnzylber et al., 2020; Gadi et al., 2020; Johnston et al., 2021; S. Lu et al., 2020). Because exposure conditions can affect initial virion and totRNA quantities, we included inoculation dose (in log10 pfu) and day post infection as candidate predictors. For day post infection, we distinguished between inoculated tissues sampled on the first day versus all other days post infection, and non-inoculated tissues on any day post infection (see Table S1.11 for tissue-specific categorization). Because sample content and processing may vary between non-invasive (e.g., swabs) and invasive samples (e.g., whole tissues obtained at necropsy), we considered sample type as a binary predictor.

We also included predictors to account for assay-specific variation. For sgRNA models, we derived a target gene predictor based on the expected number of transcripts available for amplification during each PCR protocol, given that sgRNA abundance varies by gene (D. Kim et al., 2020) and totRNA assays can amplify both genomic and subgenomic RNA. We distinguished between totRNA assays that amplify most ('totRNA-high'; targeting the N gene) or few sgRNA species ('totRNA-low'; E gene) and sgRNA assays that target highly expressed ('sgRNA-high'; sgN) or less expressed sgRNA species ('sgRNA-low'; sgE, sg7), resulting in four possible protocol combinations. For culture models, we used the totRNA target gene as the predictor, except for the models including only sgRNA as the primary predictor. Since viral infectivity varies among cell lines (Bruce et al., 2022; Hoffmann et al., 2020; Matsuyama et al., 2020) and culture sensitivity differs between endpoint dilution and plaque assays (Smither et al., 2013), we included cell line and culture assay as additional predictors for culture.

Evaluating and comparing model performance

To find the highest performing model for each investigation, we first used a forward search to identify the model with the best performance for each possible number of predictors. We used 10-fold cross-validation to evaluate each model's predictive performance on withheld data, and for each stage we selected the predictor that most increased the expected log pointwise predictive density (ELPD) (Sivula et al., 2022). Following convention, we considered an ELPD difference of less than 4 to be small when comparing two models (Sivula et al., 2022). Of those models identified by the forward search, we selected the 'best model' as the one with fewest predictors that achieved similar or better performance compared to the 'full model' (containing all predictors) on out-of-sample (test) data for three relevant statistics: (i) ELPD, (ii) prediction accuracy (i.e., the percent of correctly classified samples for the logistic component, or the percent of samples where the observed value fell within the 50% prediction interval for the linear component), and (iii) Matthew's correlation coefficient (Chicco & Jurman, 2020) (MCC; logistic components) or median absolute error on the posterior predictive medians (MAE; linear component). Comprehensive descriptions of model evaluation and selection are provided in the Supplementary Methods.

Accounting for lab effects

Since there are other possible sources of methodological variation among articles besides target genes, cell lines, and culture assays (e.g., RNA extraction methods, sample storage conditions), we also fit all of our best models with an additional categorical predictor to account for lab effects. To reduce the risk of overfitting, when possible, we grouped labs based on where they conducted their primate experiments to account for common elements in lab protocols (e.g.,

many studies that analyzed sgRNA housed their primates at BIOQUAL, Inc.). Out of all articles, we identified eight groups of labs for the sgRNA analyses and ten groups of labs for the culture analyses (Table S1.8). We incorporated the lab effect as another linear predictor to the logit probability term for the logistic components or to the mean of the normal distribution for the linear component. The error term for the linear component remained article- (not lab-) specific. We fit each of these models with the same informative priors used in the models without lab effects, and we added non-informative priors for the lab effects.

Analyzing isolation end times

To assess performance on clinically relevant metrics, we evaluated how well our simple and best culture models can identify when an individual is no longer infectious (i.e., no longer culture positive). We restricted these analyses to individuals with at least two samples from the respiratory tract after their first positive test from the same location and sample type. For each individual, we estimated the end of their infectious period as the midpoint between their last true observed culture positive and their next observed culture negative (Figure S1.18). When this resulted in the infectious period ending on a half day, we rounded up to the nearest day, such that all individuals are assumed to be infectious from the day of their first positive test up to (but not including) the day on which they reach their calculated midpoint.

We then determined their model-specific isolation end time as the earliest day on which the associated model predicted a second consecutive culture negative, to mirror the public health guideline about two consecutive negative test results. Unless otherwise stated, we used our standard threshold of 50% to classify samples as predicted negative or predicted positive. We excluded the individuals for which neither model predicted a second consecutive negative,

resulting in 77 total trajectories for this analysis. When only one of the two models was unable to identify such a time, we conservatively assumed that, under that model, the individual would isolate until day 10 after their first positive. We benchmarked our analyses against standard guidelines developed for COVID-19 patients, where individuals are released from isolation (i.e., assumed to no longer be infectious) on days five or ten after their first positive test (CDC, 2020). To compare the performance of these isolation methods, we calculated: (i) the number of days each individual spent unnecessarily isolated when they were no longer infectious ('unnecessary isolation days'), and (ii) the number of days they were still infectious while no longer isolating ('non-isolated infectious days').

Computational methods and software

All data preparation, analysis, and plotting were completed with R version 4.2.0 (R Core Team, 2022). Posterior sampling of the Bayesian model was performed with No-U-Turn Sampling (NUTS) via the probabilistic programming language Stan (Stan Development Team, 2022) using the interface CmdStanR version 0.5.2. All model fits were generated by running six replicate chains with 4000 iterations each, of which the first 2000 iterations were treated as the warmup period and the final 2000 iterations were used to generate parameter estimates. Model convergence was assessed by the sampling software using $\hat{R}$, effective sample sizes, and other diagnostic measures employed by CmdStan by default. No issues were detected.

Results

The compiled dataset includes 2167 samples from 174 individual non-human primates

A comprehensive literature search for studies that challenged non-human primates with SARS-CoV-2 identified 24 articles that reported per-sample measurements of at least two of the following assays: totRNA RT-qPCR, sgRNA RT-qPCR, and viral culture (Figure S1.1, Table 1.1, Table S1.1). Of those, 14 articles reported totRNA and sgRNA for 116 individuals and 1194 samples, and 15 articles reported viral culture and either RNA type for 90 individuals and 1315 samples. Five articles reported results for all three assays, totaling 342 such samples.

The dataset includes various demographic groups, including both sexes, ages ranging from 1 to 22 years old, and three non-human primate species (rhesus macaque, cynomolgus macaque, African green monkey) (Tables 1.1 and S1.1). The included articles span multiple study protocols, including different target genes, cell lines, exposure conditions, sample types, and sampling times. Only studies using early SARS-CoV-2 strains (i.e., excluding those reporting the D614G mutation or named variants) were included, to minimize underlying strain-specific variation. Sampling locations include the upper and lower respiratory tracts, gastrointestinal tract, and other regions.

Total RNA quantity does not solely explain sgRNA and culture results

Across individuals and samples in the database, totRNA, sgRNA, and culture trajectories exhibit patterns and challenges consistent with previous reports, including unexpected instances of sgRNA negativity and culture positivity (Figure 1.1A, Figures S1.3-S1.10). Comparing PCR results, totRNA copy numbers are larger than sgRNA copy numbers when both are detectable (median difference: 1.45 log10 units) (Figure S1.11A), and totRNA becomes undetectable simultaneously or later in infection than sgRNA (Figure S1.11D), with rare exceptions for both

patterns likely due to assay noise or processing errors. When both totRNA and sgRNA are detectable for a given individual, their trajectories are typically highly correlated (median Pearson correlation coefficient: 0.92; Figure S1.11C). However, as is particularly common in animal challenge experiments but also reported in clinical data, totRNA-positive samples in this database are often sgRNA-negative (30.0%), and totRNA quantities for these samples can be curiously large, ranging from 0.15 up to 6.38 log10 copy numbers (Figure S1.11B).

TotRNA and culture positivity results are also often discordant, disagreeing for 39.3% of all available samples and 61.3% of all totRNA-positive samples. Up to 11.02 log10 totRNA copy numbers were quantified in a culture-negative sample, which is only 1 log10 smaller than the maximum copy numbers observed in a culture-positive sample (12.09 log10) (Figures S1.11E, S1.11F). As few as 2.06 log10 totRNA copy numbers (when detectable) were noted in a culture-positive sample. As expected, totRNA typically becomes detectable earlier and remains detectable later than infectious virus, although for six individuals culture positivity preceded RNA positivity and one culture-positive individual was never totRNA-positive (Figures S1.11G, S1.11H). Considerably fewer samples with culture data also had sgRNA results (Figure 1.1B), so comparisons are limited, but patterns broadly parallel those for totRNA. Together, these patterns highlight that totRNA quantity cannot entirely explain sgRNA and culture outcomes. Statistical models may uncover cofactors underlying the discrepancies among these essential assays.

		sgRNA & total RNA	Culture & either RNA	All data
Demographics	***Species***			
	Rhesus macaque	640 / 78 / 11	476 / 46 / 9	1071 / 112 / 17
	Cynomolgus macaque	371 / 28 / 3	412 / 21 / 5	601 / 37 / 6
	African green monkey	183 / 10 / 1	427 / 23 / 4	495 / 25 / 4
	Age class			
	Juvenile	430 / 48 / 7	290 / 33 / 7	678 / 67 / 11
	Adult	667 / 56 / 10	993 / 50 / 9	1362 / 89 / 16
	Geriatric	54 / 8 / 1	2 / 1 / 1	54 / 8 / 1
	Unknown	154 / 23 / 3	72 / 6 / 1	226 / 29 / 4
	Sex			
	Female	673 / 57 / 11	803 / 47 / 12	1213 / 84 / 18
	Male	367 / 36 / 9	440 / 37 / 10	728 / 61 / 16
	Unknown	43 / 4 / 1	30 / 6 / 1	73 / 10 / 2
Sampling & exposure conditions	***Exposure dose***			
	10^4 - $<10^6$	521 / 61 / 9	311 / 19 / 3	832 / 80 / 12
	$\geq 10^6$	673 / 55 / 7	1004 / 71 / 12	1335 / 94 / 14
	Exposure route			
	Single	0 / 0 / 0	441 / 31 / 5	441 / 31 / 5
	Multi	1194 / 116 / 14	874 / 59 / 10	1726 / 143 / 19
	Sample type			
	Invasive	311 / 45 / 6	229 / 36 / 8	432 / 65 / 10
	Non-invasive	883 / 96 / 12	1086 / 76 / 12	1735 / 146 / 21
	Sample time			
	Inoc, 1 dpi	136 / 72 / 11	89 / 36 / 8	187 / 94 / 17
	Inoc, 2+ dpi	724 / 99 / 13	595 / 72 / 12	1160 / 145 / 21
	Non-Inoc, 1+ dpi	334 / 54 / 7	631 / 72 / 13	820 / 106 / 16
Assay protocols	***PCR target genes***			
	N	814 / 86 / 11	824 / 54 / 9	1435 / 120 / 17
	E	380 / 34 / 4	383 / 30 / 5	624 / 52 / 7
	S	0 / 0 / 0	108 / 6 / 1	108 / 6 / 1
	Culture assay			
	TCID50	---	856 / 53 / 10	856 / 53 / 10
	Plaque	---	459 / 37 / 5	459 / 37 / 5
	Cell line			
	Vero E6	---	959 / 71 / 12	959 / 71 / 12
	Vero E6/TMPRSS2	---	191 / 8 / 2	191 / 8 / 2
	Vero 76	---	165 / 11 / 1	165 / 11 / 1
	Total	1194 / 116 / 14	1315 / 90 / 15	**2167 / 174 / 24**

Table 1.1 | Dataset summary.
Columns stratify by assay availability, including samples with results for sgRNA and totRNA, culture and either RNA type, and any combination of two or more included assays. Entries indicate sample sizes for the corresponding cofactor, formatted as: the number of samples / individuals / articles. Doses are grouped by total plaque forming units (though they are analyzed as a continuous variable). Target gene corresponds with the totRNA assay when available, otherwise the sgRNA assay. The full article-specific data distribution is shown in Table S1.1.

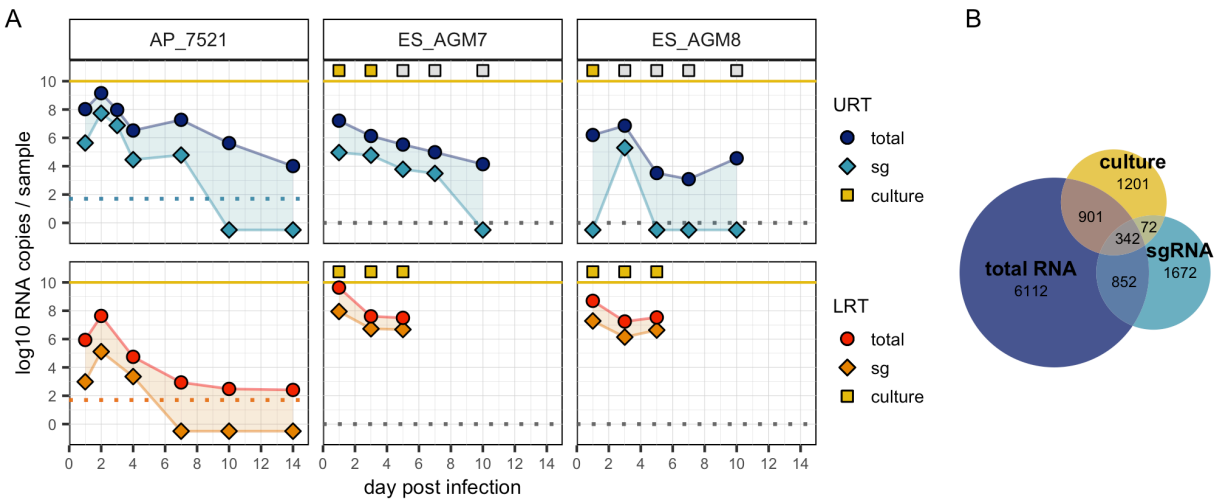

Figure 1.1 | Example trajectories and distribution of samples across assay types.
(**A**) Each column presents the totRNA (circle) and sgRNA (diamond) trajectories for the labelled individual. When available, culture results (square) are plotted above the yellow line, with yellow and grey fill indicating positive or negative culture, respectively. Samples from the upper respiratory tract (URT) are plotted above the lower respiratory tract (LRT). Dashed lines indicate reported limits of detection (plotted at 0 when unavailable). Samples with undetectable RNA are plotted below 0. Representative individuals were chosen from the full dataset. All individual trajectories are shown in Figures S1.3-1.10. (**B**) Number of samples available in our database for the corresponding assay(s).

Predictive performance on withheld data clearly identifies the best statistical models

To compare disparate assays, we developed a Bayesian hurdle model that predicts whether an assay of interest will fall above the limit of detection (the 'logistic component') and, if so, predicts a quantitative value for that assay (the 'linear component') (Figure S1.2). We used stepwise forward regression with 10-fold cross-validation to evaluate predictive performance on withheld data for variable numbers of predictors. This allowed us to identify the most parsimonious model with similar or better performance on three key metrics compared to the model containing all predictors (the 'best' and 'full' models, respectively). To benchmark our analysis against prior work, we also evaluated the 'simple model,' for which the logistic and linear components contain

PCR results as the sole predictor (i.e., it is a hurdle model comprised of a simple logistic regression and a simple linear regression).

We first applied this method to predict sgRNA from totRNA assays (the 'sgRNA model'), for which we considered species, age class, sex, exposure dose, day post infection, PCR target gene, and sample type (invasive vs. non-invasive) as candidate predictors. We then applied the logistic model framework to relate PCR results to culture positivity (the 'culture model'), including cell line and culture assay as additional candidate predictors (see Methods for justifications).

For both model types, the selection procedure clearly identified the best models (Figure 1.2), where each component included a unique set of predictors. These results were robust to alternate cross-validation procedures and prior distributions. Each selected model is generalizable, as shown by comparable prediction accuracy between training and test sets. See the Supplementary Methods for further details on model evaluation and selection.

Exposure dose, species, and PCR target gene improve predictions of sgRNA positivity

totRNA levels clearly correlate with sgRNA positivity, but the substantial overlap in totRNA quantities measured for both sgRNA-positive and sgRNA-negative samples emphasize that other factors must influence sgRNA outcomes (Figure 1.3A). The best sgRNA logistic model identified exposure dose, species, and PCR target gene as key additional predictors of sgRNA positivity (Figure 1.2, Table S1.2). This model is highly accurate, correctly classifying 91.1% of withheld samples. It outperforms the simple model both by increasing prediction accuracy and by assigning higher probabilities to correct classifications for more samples (Figure 1.3B). For intermediate quantities of totRNA (2-6 log10 copies), sgRNA positivity predictions differ between

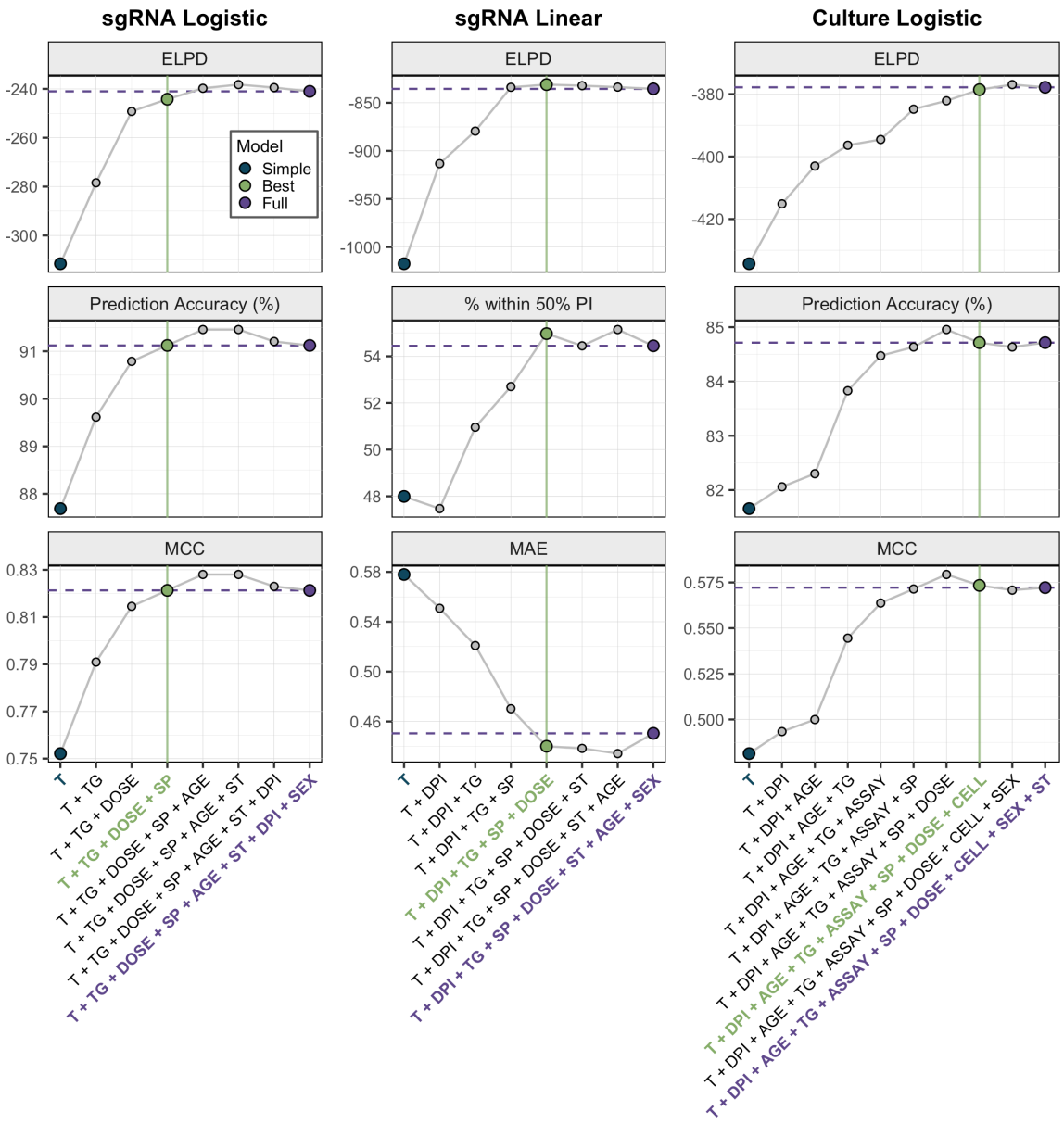

Figure 1.2 | Model selection criteria identify the best models.
The highest performing models for each predictor number and modeling component are shown, ordered by increasing predictor numbers. Purple horizontal lines depict performance of the full model. Green vertical lines indicate the best model, chosen according to the displayed metrics. These include estimated log pointwise predictive density (ELPD), prediction accuracy, percent of samples within the 50% prediction interval, Matthews correlation coefficient (MCC), and median absolute error around the median (MAE). These were generated using test data during 10-fold cross validation. For the culture logistic component, the model with seven predictors was not chosen because, although it outperformed the full model on MCC and prediction accuracy, it

underperformed on ELPD. This is because the ELPD for the full model was larger than the ELPD for this model by more than our threshold of 4 units. Please see the Methods for more details about our selection criteria and the Supplementary Methods for a full description of the selection procedure. Acronyms are: T, totRNA; DPI, day post infection; SP, species; TG, target gene; ST, sample type; CELL, cell line; ASSAY, culture assay. All tested models are shown in Tables S1.2-S1.5.

the simple and best models (Figure 1.3C), emphasizing the particular importance of accounting for cofactors in this range. The best and full models perform similarly (Figure 1.2).

Our best model reveals insights into the three additional predictors of sgRNA outcomes: exposure dose, species, and PCR target gene. The following trends hold for model predictions across any cofactor combination when holding totRNA quantity constant: (i) individuals inoculated with larger doses have smaller chances of detecting sgRNA, (ii) African green monkeys have the smallest chance of sgRNA detection, while rhesus and cynomolgus macaques have similar predictions, and (iii) assays targeting highly-expressed sgRNA species ('sgRNA-high' assays) have higher chances of sgRNA detection than those targeting less-expressed sgRNA species ('sgRNA-low'). We refer the reader to Figure 1.3C for quantitative median predicted chances of sgRNA detection for a select cofactor combination, Figure 1.3D for qualitative variability in those predictions, and Table S1.6 for the associated 90% prediction intervals. In Table S1.7, we also provide the 90% credible intervals for all parameters to facilitate predictions of other cofactor combinations. Columns within row groups in Figures 1.3C with a strong color gradient indicate substantial impacts of the associated cofactor on sgRNA predictions, and grey boxes highlight totRNA ranges where final classifications of sgRNA positivity differ within that cofactor group (for the standardized cofactor set).

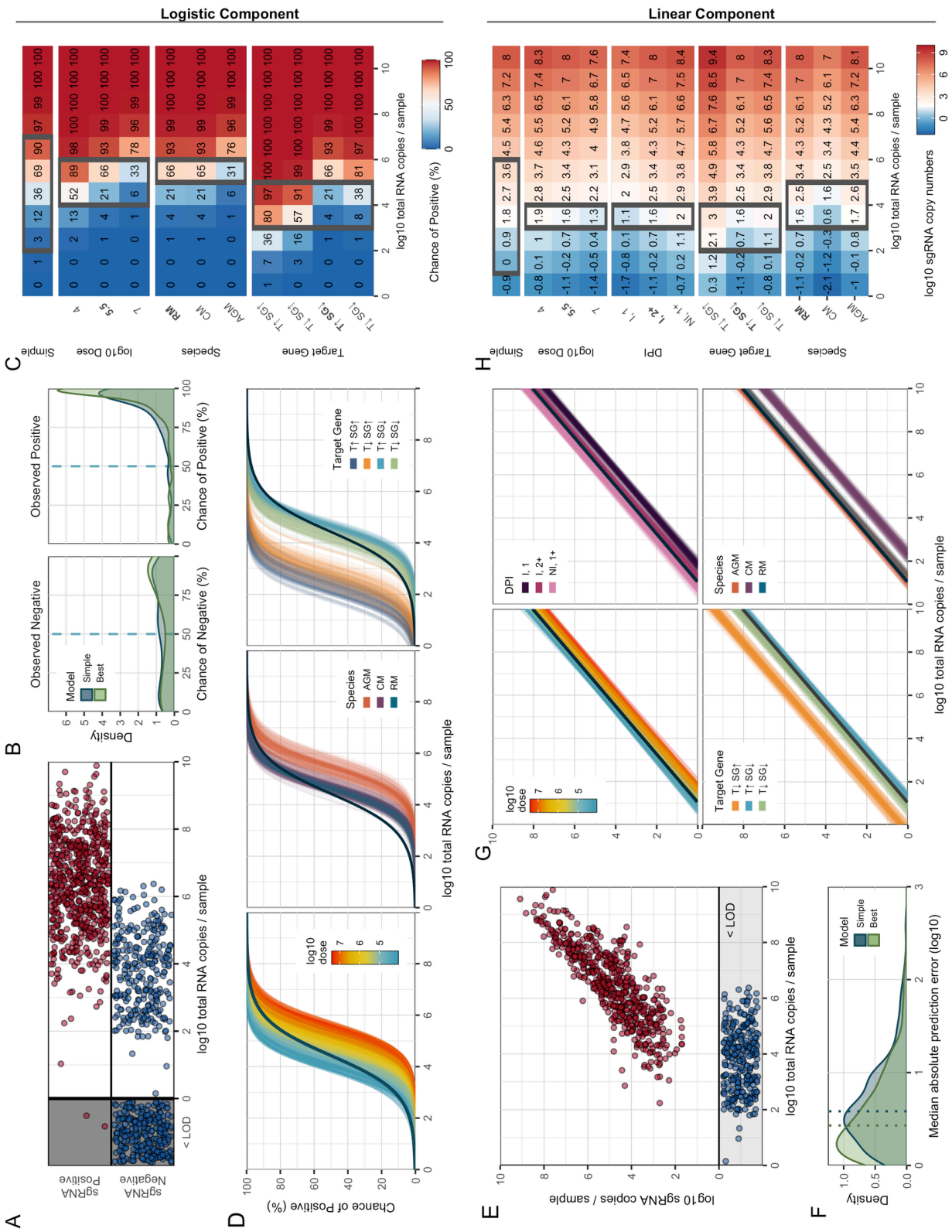
Logistic Component
Linear Component
A
B
C
D
E
F
G
H
sgRNA Negative
sgRNA Positive
< LOD
log10 total RNA copies / sample
Observed Negative
Observed Positive
Density
Chance of Negative (%)
Chance of Positive (%)
Model
Simple
Best
Chance of Positive (%)
Target Gene
Species
log10 Dose
Simple
log10 total RNA copies / sample
Chance of Positive (%)
log10 dose
Species
AGM
CM
RM
Target Gene
T↑ SG↑
T↓ SG↑
T↑ SG↓
T↓ SG↓
log10 sgRNA copies / sample
Median absolute prediction error (log10)
DPI
I, 1
I, 2+
NI, 1+
log10 sgRNA copy numbers

Figure 1.3 | The best sgRNA model captures key sources of underlying variation in PCR outcomes.
(**A**), All available sgRNA data plotted against totRNA results (with vertical jitter), with all totRNA-negative samples plotted in the grey region (with horizontal and vertical jitter). One totRNA- and sgRNA-positive sample with -1.18 log10 totRNA copies is not visible. (**B**), Distribution of median model-predicted chances of sgRNA detection for all available totRNA-positive samples, stratified by model type and observed outcomes. Samples right of the dashed line are correct predictions. (**C**)**,** Median predicted chances of sgRNA detection for the simple model (top row) and all cofactor groups for the best model (other rows), evaluated for specific totRNA levels. Predictions were generated using the following 'standardized cofactor set' (which are highlighted in bold text): rhesus macaques inoculated with 5.5 log10 pfu and sampled at least two days post infection from inoculated tissues, which were processed with a totRNA-high/sgRNA-low assay. For the simple model, the grey box encloses totRNA copies where classifications differ among the simple model and any possible combination of cofactors in the best model, based on our standard prediction threshold of 50%. For all other rows, grey boxes enclose regions where classifications differ within the displayed cofactor group for the standardized cofactor set. For example, 5 log10 totRNA copies / sample is enclosed for 'Species' because African green monkeys are predicted to be negative while both other species are predicted to be positive. The rows for the other cofactor groups (e.g., target gene) do not influence the grey boxes for 'Species'. (**D**), 300 posterior draws from the best logistic model for the standardized cofactor set, with colored lines as indicated in panel-specific legends. The dark blue line presents the simple model's mean fit. (**E**), All available sgRNA data for totRNA-positive samples, where sgRNA-negative samples are plotted below 0 (with vertical jitter). (**F**), Distribution of median absolute errors for all sgRNA-positive samples, stratified by model type. (**G**), As in (D) but for the best linear component. (**H**), As in (C) but reporting median sgRNA copy number predictions. Grey boxes enclose regions where predicted sample quantities within the displayed cofactor group fall both above and below a common limit of detection (1.69 log10), and otherwise follow the same rules as in panel (C). Acronyms are as follows: 'RM', rhesus macaque; 'CM': cynomolgus macaque; 'AGM': African green monkey; 'Non-Inv': non-invasive; 'Inv.': invasive; 'DPI': day post infection; 'I, 1': inoculated tissues sampled on day 1 post infection; 'I, 2+': inoculated tissues sampled any other day post infection; 'NI, 1+'; non-inoculated tissues on any day post infection; "T↑SG↑": totRNA-high/sgRNA-high; "T↓SG↑": totRNA-low/sgRNA-high; "T↑SG↓": totRNA-high/sgRNA-low; "T↓SG↓": totRNA-high/sgRNA-low.

To determine whether any of the observed patterns could stem from lab-level methodological variation, we tested whether the findings of our best model were altered by including an additional predictor for lab effects. Some lab groups were predicted to have higher chances of sgRNA detection per totRNA quantity (Figure S1.12A), but performance was similar to the model without an explicit lab effect (Figure S1.12B). Crucially, the predicted differences

among doses, species, and target genes were qualitatively unchanged between these models (Figures S1.12C, S1.12D), offering confidence in the robustness of our results.

Exposure conditions, species, and PCR target gene impact expected RNA ratios

sgRNA quantities scale positively with totRNA quantities, but with considerable unexplained variation (Figure 1.3E). Our best sgRNA linear model identified exposure dose, species, PCR target gene, and day post infection as key predictors of sgRNA quantity (note these are the same predictors as for the sgRNA logistic model, but with day post infection also included). This model performs well on withheld data, with 55.0% of observed sample values falling within the model-generated 50% prediction interval (Figure 1.2, Table S1.3). The best model clearly outperforms the simple model, decreasing the median absolute prediction error from 0.58 to 0.43 log10 copies (Figures 1.3F) and increasing the correlation between observed and median predicted values (from an adjusted R^2 of 0.68 to 0.77). The best model performs marginally better than the full model, with small improvements in prediction accuracy (Figure 1.2).

Below, we explore the effects of each selected cofactor on predicted sgRNA copy numbers. We report qualitative trends that hold across all cofactor combinations, and we refer the reader to Figures 1.3H for median (quantitative) predicted sgRNA copy numbers for a select cofactor combination (our 'standardized cofactor set', see figure legend). Variability in these predictions are presented qualitatively in Figure 1.3G and quantitatively (as 90% prediction intervals) in Table S1.6. Credible intervals for all parameters are included in Table S1.7. Similar to the logistic component, we also fit the best model with an additional predictor for lab group, which identified some modest differences in the expected sgRNA quantities among articles (Figure S1.12E**)** and had similar prediction accuracy to the model without lab effects (Figure S1.12F). We describe any

other qualitative differences in our results between these models below, which are also visualized in Figure S1.12.

The best model predicts that exposure conditions and sampling time impact RNA ratios. Samples obtained from individuals inoculated with larger doses must have higher total RNA copy numbers to expect the same sgRNA quantity. Results for day post infection parallel these exposure-dependent patterns. To expect a given sgRNA quantity, totRNA copies must be highest for inoculated tissues on the first day post infection, intermediate for inoculated tissues on all later days post infection, and lowest for non-inoculated tissues on any day post infection. When we added a predictor for lab group, the effects of day post infection were qualitatively unchanged while the dose effect weakened and reversed (Figure S1.12G, Figure S1.12H), although a substantial portion of the parameter density allowed for the original dose effect.

PCR target genes also affect predictions. Conditional on totRNA quantity, totRNA-low/sgRNA-high assays have the largest predicted median sgRNA quantities, followed by totRNA-low/sgRNA-low and totRNA-high/sgRNA-low assays. Quantitative sgRNA outcomes were unavailable for totRNA-high/sgRNA-high assays, so estimates were not possible for those protocols. These effects were qualitatively similar in our model with lab effects (Figure S1.12G, S1.12H).

The best model also predicted that sgRNA quantities vary by species. Regardless of whether a lab effect was included, rhesus macaques and African green monkeys had highly similar predictions. Cynomolgus macaques were predicted to have lower median sgRNA quantities for any given totRNA quantity, though this effect was substantially reduced when lab effects were

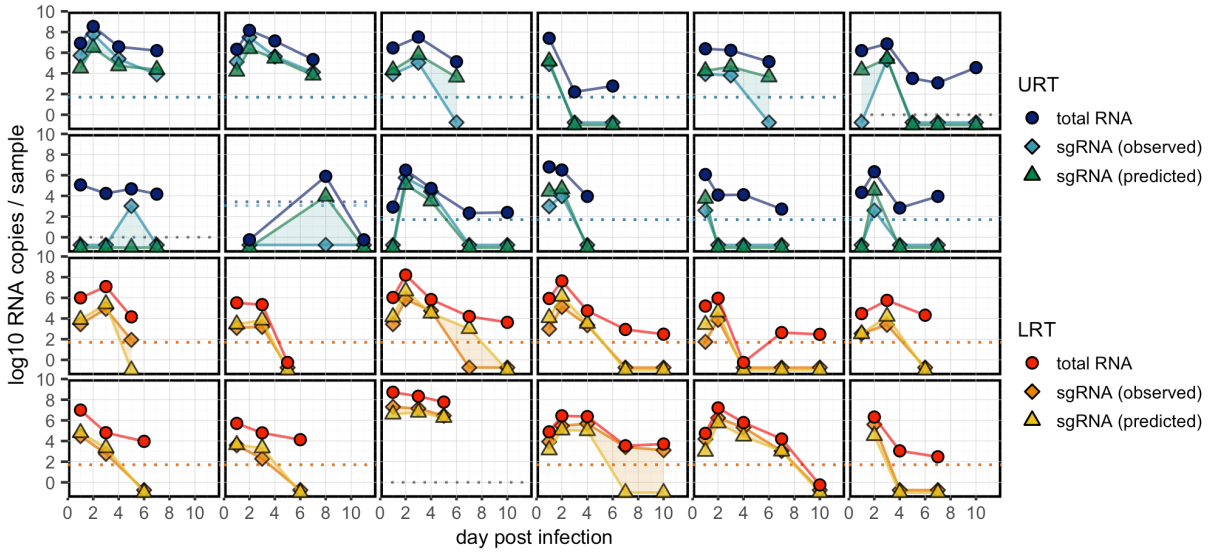

Figure 1.4 | The best sgRNA model reconstructs individual trajectories with high accuracy. Each panel includes the data for one randomly selected individual sampled from either the upper respiratory (URT) or lower respiratory tract (LRT), including observed totRNA (circle), observed sgRNA (diamond), and median predicted sgRNA (triangle) quantities. Detection limits are plotted as dashed lines in the corresponding color when available, otherwise grey lines are plotted at zero. All undetectable samples are plotted below zero. See Figures S1.3-S1.5 for all individuals.

included. Given that only one lab group had data from both cynomolgus macaques and another species (rhesus macaques), we view this species effect as an intriguing but tentative finding that warrants further investigation.

The sgRNA model accurately reconstructs individual viral load trajectories

To further analyze performance, we reconstructed individual viral load trajectories using the best sgRNA model (Figures 1.4, S1.3-S1.5). The model correctly predicted the timing of the first and last observed sgRNA positive for 90.1% (n=219/243) and 72.8% (n=177/243) of all individual- and (non-invasive) sample-specific trajectories with at least two sampling times, respectively (Figure S1.14). Notably, 70.0% (n=170/243) of those trajectories were predicted without a single misclassification. The distribution of predicted sgRNA quantities was highly

similar to the distribution of observed sgRNA quantities (median differences of estimated means: -0.04 log10 units; 90% Credible Interval [CI]: -0.18, 0.08; Supplementary Methods) but highly dissimilar to observed totRNA values (-0.79; 90%CrI: -0.92, -0.66), offering further confidence in the model's excellent performance.

Total RNA and sgRNA are both suitable predictors of viral culture

To determine which PCR assay best predicts viral culture, we compared models including totRNA, sgRNA, or both as predictors of culture positivity. We first evaluated performance only on samples with quantitative results for both assays and for models with no additional cofactors, for which totRNA, sgRNA, and both had similar prediction accuracy (Table S1.9). Because few samples had both sgRNA and culture outcomes (Figures 1.1B), we imputed median sgRNA predictions where needed, using the best performing sgRNA model. On this full dataset, all three models also performed similarly well, though totRNA showed some evidence of better predicting culture positive samples. We then ran our model selection procedure on totRNA and sgRNA separately for all available data, which resulted in highly similar prediction accuracy for both best models, though the model using totRNA was more parsimonious, with two fewer predictors (Tables S1.4, S1.5). Given this parsimony and the lack of reliance on imputed sgRNA values, plus the lack of evidence that sgRNA is a superior predictor, we based further analyses solely on totRNA.

Demography, exposure conditions, and assay protocols resolve disparities in culture results

We next sought to predict culture positivity from totRNA results using the logistic model framework. The best model contained day post infection, inoculation dose, age class, species, culture assay, cell line, and PCR target gene as predictors, and it correctly classifies 84.7% of

withheld data (Figure 1.2; Tables S1.4, S1.9). It outperforms the simple model by correctly predicting an additional 7.0% of culture positive samples and by assigning higher probabilities for true classifications (Figure 1.5B; Figure S15A). The difference in performance is especially pronounced at intermediate totRNA quantities (6-8 log10), which often occur during the critical transition between culture positive and negative states (i.e., in clinical terms, at the end of the infectious period). For these samples, the best model correctly predicts an additional 23.3% of culture positives (Figure S1.15B) and often with much higher confidence (Figure S1.15C). Strikingly, culture predictions can differ between the simple and best models for all considered quantities of totRNA (0-12 log10 copies) (Figure 1.5C), highlighting the benefit of accounting for cofactors when predicting culture outcomes across all totRNA quantities. The best model performs similarly to the full model (Figure 1.2; Table S1.4).

In the text below, we explore the effects of each selected cofactor on culture outcomes. Given the high dimensionality of these predictions, we report qualitative trends that hold across cofactor combinations, and we refer the reader to Figures 1.5C for median predicted chances of positive culture for a select combination of cofactors (i.e., our 'standardized cofactor set', see figure legend). Columns in Figure 1.5C with a strong color gradient indicate dramatic impacts of the associated cofactor on culture predictions, and grey boxes highlight totRNA ranges where final classifications differ within that cofactor group (for the standardized cofactor set). These ranges differ for other cofactor combinations. We present the variability of our results (for the standardized cofactor set) qualitatively in Figure 1.5D and quantitatively (as 90% prediction intervals) in Table S1.10. In Table S1.7, we provide the medians and 90% credible intervals for all parameters to facilitate predictions of other cofactor combinations.

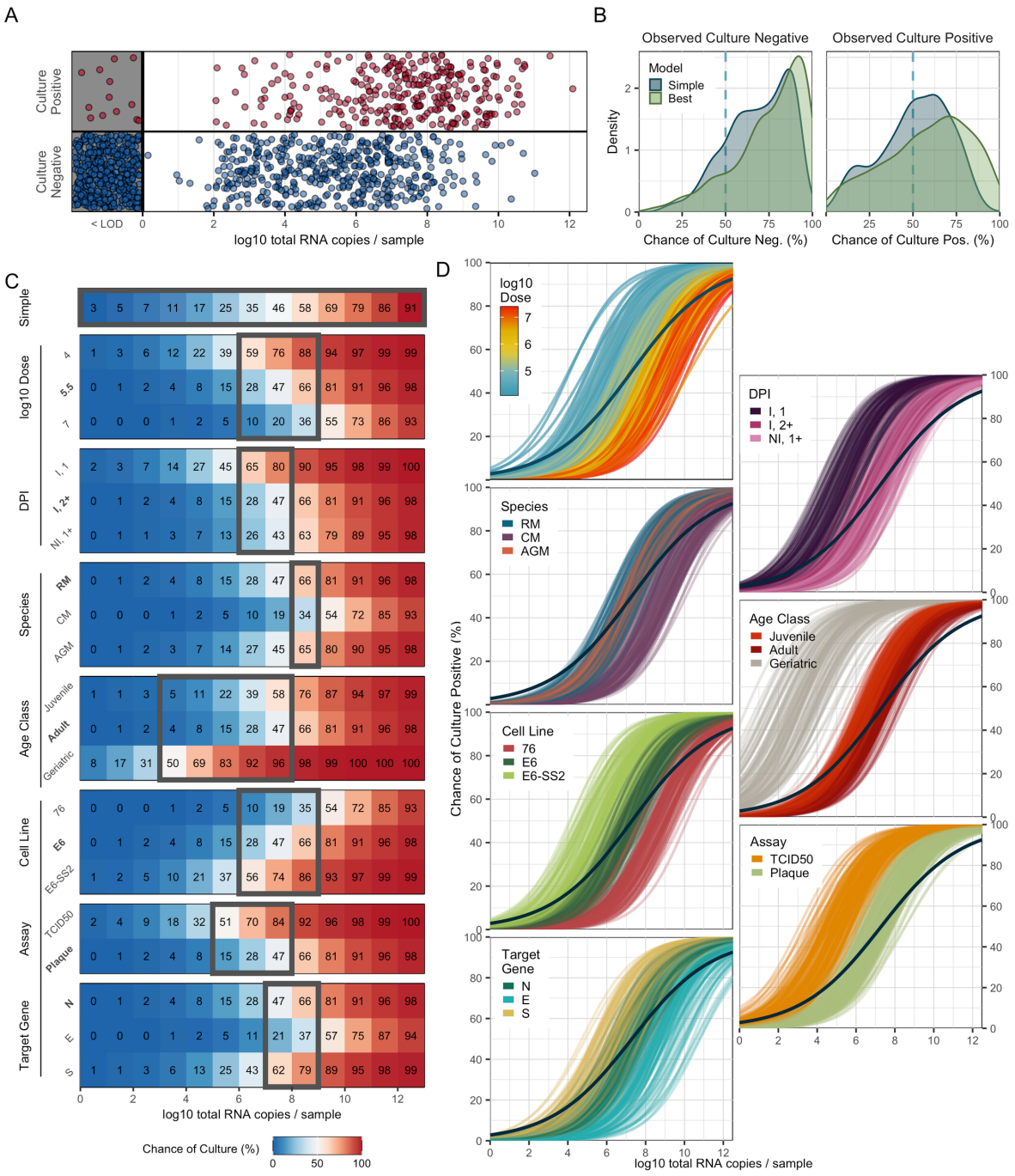

Figure 1.5 | The best culture model captures key sources of underlying variation in culture outcomes.

(A) All available culture data plotted against totRNA results (with vertical jitter), with all totRNA-negative samples plotted in the grey region (with horizontal and vertical jitter). (B) Distribution of median model-predicted chances of positive culture for all totRNA-positive samples, stratified by model type and observed outcomes. Samples right of the dashed vertical line are correct predictions. (C) Median predicted chance of positive culture for the simple model (top row) and

all cofactor groups included in the best model (other rows) for totRNA copies (evaluated at integer values, starting at 0). Predictions were generated using the following 'standardized cofactor set' (which are highlighted in bold text): adult rhesus macaques inoculated with 5.5 log10 pfu and sampled at least two days post infection from inoculated tissues, where PCR targets the Nucleocapsid gene and culture uses plaque assays with VeroE6 cells. Grey boxes enclose regions where classifications differ within the cofactor group for the standardized cofactor set, as described for Figure 1.3C. For the simple model, it encloses regions where classifications differ between the simple model and any possible combination of cofactors. (D) 300 posterior draws from the best model for the standardized cofactor set, with colored lines as indicated in panel-specific legends. The dark blue line presents the simple model's mean fit. Acronyms are as described in Figure 1.3, plus the following: E6, VeroE6; E6-SS2, VeroE6-TMPRSS2; and 76, Vero76 cells.

To determine whether unmodelled differences among labs could explain any of the observed patterns, we fit our best culture model with an additional term for lab effects. Some groups of labs were predicted to have higher overall chances of culture positivity per totRNA quantity (Figure S1.16A), but overall prediction accuracy was similar to the model without a lab effect (Figure S1.16B). There was some additional variation in the parameter estimates for the model with a lab effect, but the qualitative findings for all cofactors were consistent across both models (Figure S1.16C, S1.16D).

Exposure conditions had substantial impacts on culture predictions. Individuals inoculated with larger doses have smaller probabilities of obtaining successful culture for any given totRNA quantity. Interestingly, in contrast with results predicting lower sgRNA (per totRNA quantity) in inoculated tissues (Figure 1.3G, 1.3H), the culture model predicts that inoculated tissues sampled on the first day post infection have the highest probabilities of being culture positive per totRNA quantity. Inoculated tissues on later days post infection and all non-inoculated tissues are much less likely to be culture positive, with substantial overlap in the predicted probabilities of those two groups.

Multiple demographic factors also affect culture outcomes. Predictions for juvenile and adult age classes largely overlap, but geriatric individuals have substantially higher predicted chances of successful culture for the same viral load. This difference was reduced, though still clearly apparent, when including a lab effect. However, few samples from geriatric individuals were available (Table 1.1), and so these results should be interpreted cautiously. Predictions also vary based on species: the chances of successful culture for some viral load are smallest for cynomolgus macaques compared to rhesus macaques and African green monkeys, where the latter two species have highly similar predictions.

Assay conditions also influence culture outcomes, as expected. The model predicts that VeroE6-TMPRSS2 cells have the highest chance of positive culture, followed by VeroE6 and Vero76 cells. TCID50 assays are predicted to have higher sensitivity than plaque assays, and the chances of culture positivity (for a given viral load) are higher for PCR protocols targeting Spike (S) than for those targeting the Nucleocapsid (N) or Envelope (E) genes.

Individual trajectories uncover sources of culture prediction errors

Although our best culture model exhibits remarkable 84.7% accuracy on withheld data, we analyzed our predictions further to identify potential causes and implications of existing errors. 64.1% (n=116/181) of all incorrect predictions were false negatives, of which a curious 11.2% (n=13/116) were PCR negative. Even excluding these totRNA-negative samples, totRNA copies for false negative samples were substantially smaller than for true positives (median difference of estimated population means: -2.83 log10 units; 90%CrI: -3.13, -2.53) but more similar to true negatives (median difference: 0.57; 90%CrI: 0.27, 0.87). These RNA-low but culture-positive samples could be explained by PCR or sample processing issues resulting in the amplification of

less RNA (e.g., sample degradation), or by culture contamination. Similarly, totRNA copy numbers for false positive predictions were substantially larger than for true negatives (median difference: 3.05; 90%CrI: 2.74, 3.36) but were similar to true positives (median difference: -0.35, 90%CrI: -0.66, -0.04). Culture insensitivity could explain these RNA-high but culture-negative samples.

We further characterized errors by analyzing performance in the context of individual trajectories for (non-invasive) samples with at least two sampling times (Figures 1.6, S1.7-S1.9, S1.17). Overall, the best model correctly predicted 58.3% (n=120/206) of these trajectories without a single culture misclassification, compared to only 47.6% (n=98/206) by the simple model. Within all trajectories, the best model made a total of 131 errors in predicting culture status of individual samples, while the simple model made 171 errors. We categorized these errors into four types: (i) samples obtained on the first or last sampling day (termed an 'edge'), (ii) samples obtained as culture results transition between positive and negative states ('transition'), (iii) samples where observed culture results change for one sampling time despite surrounding instances of the opposite classification ('data blip'), and (iv) samples where culture predictions change for one sampling time despite surrounding instances of the opposite classification ('prediction blip'). Notably, while edge errors are difficult to analyze, given limited information from surrounding time points, transitions may reflect sample quality and assay sensitivity interacting to drive noisy outcomes for samples with intermediate RNA or virion quantities.

When considering all prediction errors, we find that edge errors are the most common for both the best (n=51/131; 38.9%) and simple (n=78/171; 45.6%) models. Transition errors, however, are of particular interest, given that the shift from positive to negative states determines the end of infectivity. The best model made 44 transition errors (n=44/131; 33.6%), while the

simple model made 49 transition errors (n=49/171; 28.7%). We then calculated how many edge errors could also be considered transition errors, and once again we found that the best model made fewer such errors (23 vs. 34). Thus, model accuracy at this critical point during infection is improved by accounting for key covariates.

For the best model, data blips are less common (n=19/131; 14.5%) than edge and transition errors, and all except one data blip are observed culture positives surrounded by culture negatives (leading to false-negative prediction errors) (Figures 1.6B, S1.17A). Eight of these samples co-occur with increases in totRNA quantities from the previous sampling time, suggesting they may reflect true local replication (e.g., as in rebound cases). The remaining instances accompany decreases in totRNA quantities, where sample contamination could drive spurious culture positivity or PCR processing issues could result in RNA underestimates. Prediction blips are the least common (n=17/131; 13.0%), of which 70.6% (n=12/17) are false negatives that often have lower totRNA quantities than the previous sampling time (Figures 1.6B, S1.17B). These could be explained by sample quality or PCR processing issues resulting in RNA underestimates, which is particularly plausible for instances where totRNA levels increase in the next sampling time. In contrast, false positive prediction blips primarily occur after sharp increases and high quantities of totRNA, and all occur for plaque assays. Given our model predicts lower sensitivity for plaque assays, these errors could reflect failed culture, though RNA overestimates could also explain this pattern.

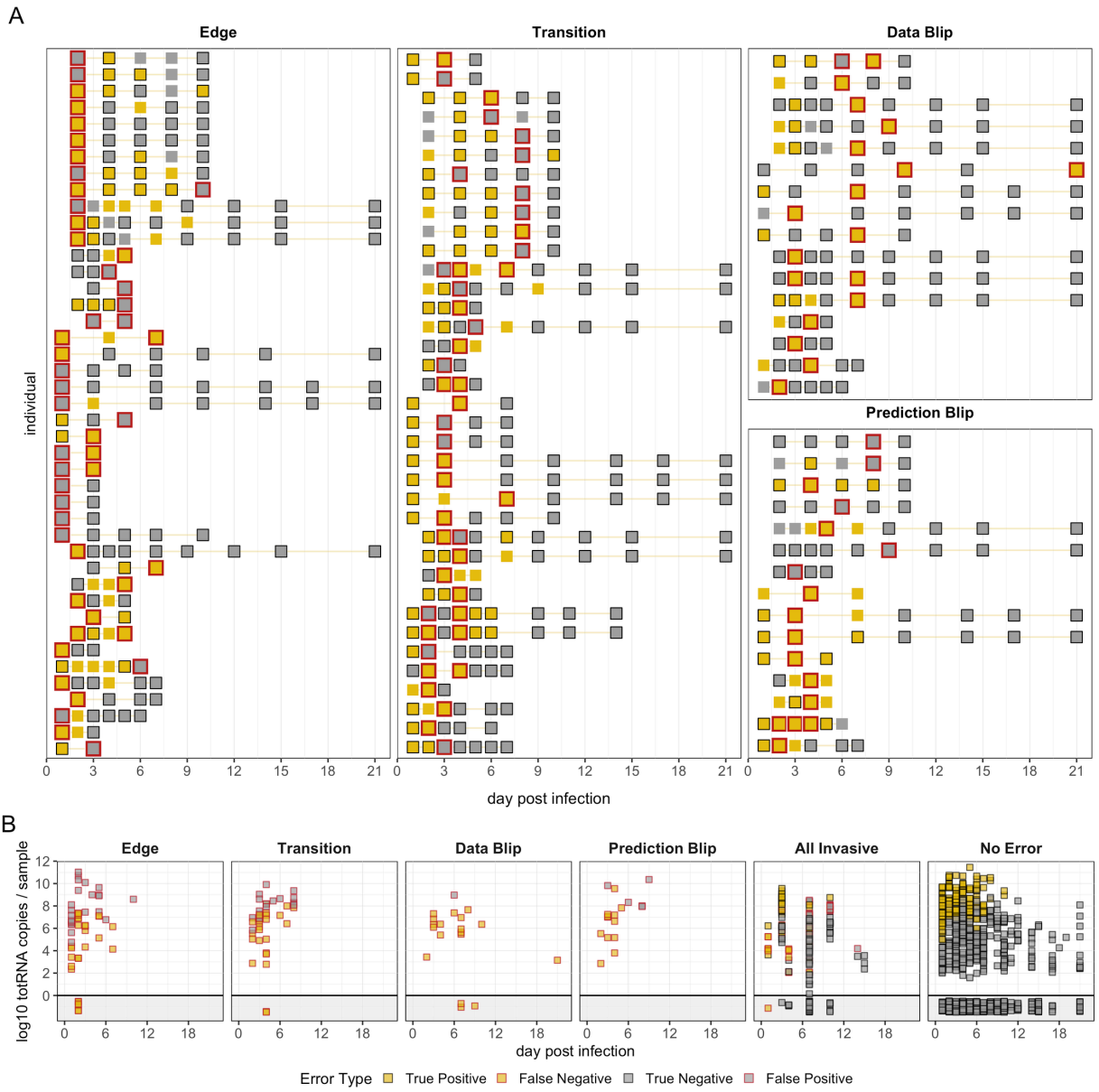

Figure 1.6 | Error analysis reveals potential causes of culture prediction errors.
(A) Each row shows culture results for one individual-sample trajectory that contains at least one instance of the panel-specific error type. Trajectories may appear in multiple panels if they contain multiple error types, though trajectory ordering is inconsistent. Red outlines highlight samples with the denoted error type. (B) TotRNA values over time for each error type, all invasive samples, and all correctly classified non-invasive samples ('no error'). In (A) and (B), yellow squares indicate culture positives and grey indicates culture negatives. Squares with black outline are correctly classified, while those with no or red outline are incorrectly classified. The data blip individual on day 21 post infection has another sample available at a later timepoint, so it is not considered an 'edge.'

The best culture model shows potential for accurate, individualized isolation practices

Although our model is trained on NHP data and cannot be applied directly to humans, we sought to illustrate the potential clinical utility of such a framework. To do so, we assessed the simple and best models' ability to identify when an individual is no longer infectious (i.e., no longer culture positive). For all available individuals (n=77), we determined their (model-specific) isolation end times as the earliest day on which the associated model predicted a second consecutive culture negative (Figure S1.18). Because the time between consecutive tests increases over the course of infection (Figure S1.19), there is an implicit bias towards longer isolation times for individuals that test positive longer and hence are observed less frequently during the period that they lose infectiousness. To account for this bias, we also ran analyses for a hypothetical 'perfect' model that identifies culture status correctly for every sample, and so it always releases individuals from isolation on the day of their true second consecutive culture negative. For further comparison, we included two standard public health guidelines for SARS-CoV-2, which release all individuals from isolation on days five or ten after their first positive (CDC 2020).

We found that, across all procedures, the best model resulted in the smallest number of days that individuals were unnecessarily isolating while no longer infectious (Figure 1.7A), with an especially large reduction compared to the ten-day protocol (126 vs. 510 days). We then considered the number of days on which individuals were not isolating but still infectious. If no isolation practices were used, there would be 260 such days. No individual was infectious up to day ten after the first positive test, and so the ten-day protocol was the only one with zero non-isolated infectious days (Figure 1.7B). The simple model had the largest number of non-isolated infectious days (65 days), followed by the best model (60 days), the five-day procedure (37 days), and the perfect model (34 days). Upon further investigation, many of these non-isolated infectious

days arose from 16 individuals that showed evidence of rebound infection, which we defined as at least one known culture negative occurring between two known culture positives (Figure S1.18**)**. Of these 16 individuals, many of them (n=6/16; 37.5%) had their final culture positive before day 5 ("early rebound"), which thus did not affect the performance of the five-day protocol but did penalize the best and simple models despite them accurately identifying many intermittent culture negatives. All protocols (except for the ten day procedure) were also affected by the 10 individuals that had their final culture positive on or after day 5 ("late rebound"; n=10/16; 62.5%). When we excluded any rebound individuals, the best model and the five-day procedure differed by only three non-isolated infectious day (20 vs. 17 days).

To further compare the protocols, we also evaluated their ability to identify the first time that individuals experienced a true (observed) second consecutive culture negative. For these analyses, we excluded the 12 individuals where this never occurred. We classified the protocols based on whether they accurately identified this time ('Correct') or whether the predicted time occurred before ('Early') or after ('Late') the known time. The best model was correct for the most individuals (n=30/65; 46.2%; Figure 1.7E; Figure S1.18), with the exception of the perfect model that by definition classifies all individuals correctly. The simple model only classified 30.8% (n=20/65) of individuals correctly, which is 15.4% (n=10/65) fewer individuals than the best model. The best model also generated 10.8% (n=7/65) fewer early predictions, which is a particularly important improvement given the public health cost of premature release from isolation. We also analyzed the confidence with which the two models identified the first two consecutive true negatives. The best model misclassified fewer of these samples as culture positive

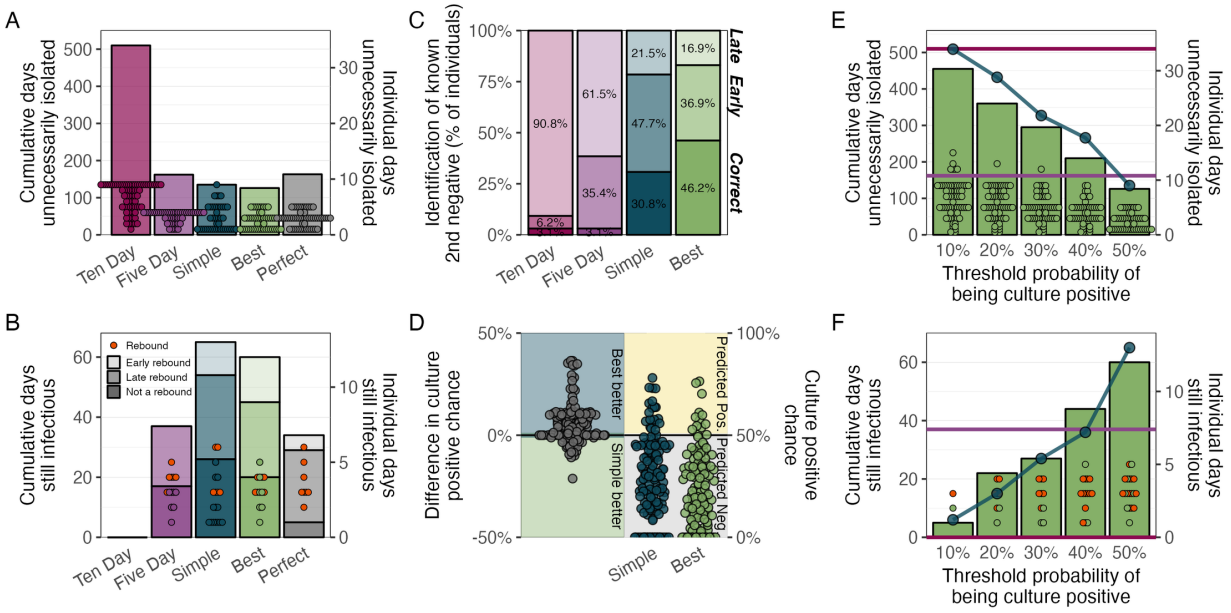

Figure 1.7 | The best culture model captures the end of infectiousness better than existing approaches.

(A) The cumulative days unnecessarily isolated by all individuals (histogram, left axis) and the distribution of individual days unnecessarily isolated (points, right axis) for the ten-day, five-day, simple, best, and perfect protocols. Individuals that were isolated for too few or the exact number of days are not shown. (B) The cumulative days that individuals were still infectious after the end of isolation (histogram, left axis) and the distribution of days that individuals were still infectious (points, right axis) for all the protocols in panel A. Transparency shows the classification of individual trajectories as either showing no indication of a rebound (darkest), indication of a late rebound (medium, day 5 after the first positive test or later), or indication of an early rebound (lightest, before day 5 after the first positive test). Rebound individuals are indicated by red points. Individuals that were not still infectious are not displayed. (C) Performance of each protocol on identifying the true (observed) time of the second consecutive culture negative for all individuals where this occurred. 'Correct' (darkest, bottom) includes all individuals for which the protocol exactly identified the second consecutive negative. 'Early' (medium, middle) includes all individuals where the prediction occurred before the true time, while 'Late' (lightest, top) includes all individuals where the prediction occurred after the true time. The perfect model is not shown, as by definition it is 100% correct. (D) Comparison of the culture positive probabilities predicted for the simple and best models on both samples from the first true instance of consecutive negatives. The right panel shows the raw predicted probabilities for each model. The left panel shows the per-sample difference between those probabilities for the simple and the best model, where the best model is more confident in the upper region (i.e., it has smaller predicted probabilities of being culture positive) and the simple model is more confident in the lower region. (E) The cumulative days unnecessarily isolated by all individuals (green histogram, left axis) and the distribution of individual days unnecessarily isolated (green points, right axis) for five different threshold probabilities at which a sample is considered culture positive. The best model results are displayed in the green bars (cumulative) and by the green points (individuals). The horizontal lines

show the results for the five- and ten-day procedures, with the same colors as in (A). The blue points and connecting lines show the cumulative days for the simple model. (F) As in panel E, except displaying the number of days individuals were still infectious after the end of isolation. Red points are rebound individuals.

(difference: n=7/130; 5.4%), and it was equally or more confident (by up to 36.4%) in the correct prediction for 80.0% of the samples (n=104/130; Figure 1.7D).

Finally, we investigated the sensitivity of our results to the threshold probability at which samples are predicted to be culture positive. We sequentially decreased this probability from 50% (our standard threshold) to a more conservative 10%, which increased the number of samples predicted to be culture positive. Because the five- and ten-day protocols are discrete rules, varying thresholds do not affect their metrics. For the best and simple models (Figure 1.7E; green bars and blue dots, respectively), lower thresholds increased the number of unnecessary isolation days, though notably the best model always had fewer days than the simple model. Lower thresholds also resulted in substantially fewer non-isolated infectious days, and both the simple and best models can outperform the five-day protocol (Figure 1.7F). Notably, lowering this threshold reduced the number of rebound individuals that are prematurely released from isolation. Although the simple model appeared to outperform the best model on the number of infectious days, this reduction actually resulted from the simple model failing to identify a second consecutive negative more often than the best model for all threshold values (e.g., 64.6% vs. 51.9% of individuals for a 10% threshold). This causes more individuals to default (by our assumption) to the ten-day procedure, thus also decreasing the number of non-isolated infectious days. Overall, the best model provides the most accurate and customizable approach – offering the potential to tune predictions to minimize non-isolated infectious days or to minimize unnecessary isolation days, depending on context and local priorities.

Discussion

In this study, we developed a generalizable model to infer the results of one virological assay from another. By applying this framework to our compiled database of non-human primate experiments on SARS-CoV-2, we generated highly accurate predictions of sgRNA and culture results from standard PCR protocols. These analyses allowed us to answer foundational questions about whether totRNA and sgRNA assays are fundamentally interchangeable and what factors drive the complicated relationships between PCR and culture outcomes. Our best models identify key sources of biological and methodological variation (including exposure conditions, demographics, and assay protocols), across which predictions varied widely. We showed that because standard, single regression models (like our 'simple models') ignore this variation, they could incorrectly infer culture outcomes for samples with totRNA copy numbers spanning twelve orders of magnitude; our biologically-informed multiple regression models showed substantial gains in accuracy and precision. Our findings highlight the importance of accounting for the influence of cofactors on viral load and culture positivity – no single threshold value applies across study designs.

We addressed the unresolved debate about the relative merit of sgRNA to predict culture outcomes by conducting the first comprehensive analysis of a large dataset of controlled exposures. We found no clear evidence that sgRNA outperforms totRNA, and instead we found that both infer culture outcomes with high accuracy when accounting for key biological covariates. Given these results and that we can reconstruct sgRNA trajectories from totRNA outcomes with high accuracy, underlying cofactors may explain previously observed differences in the relative predictive capacity of totRNA and sgRNA (Ford et al., 2021; Perera et al., 2020). Future studies

could prospectively measure all three assays (ideally with quantitative culture) to confirm and extend our findings, though notably our model achieved a remarkable 85% accuracy in predicting culture outcomes and our error analysis showed that many prediction errors may have arisen from upstream data issues (see below).

Our models characterize many biological patterns hypothesized (or known) based on previous experimental work on SARS-CoV-2, including the effects of exposure conditions on sgRNA and culture outcomes. In particular, we find that larger exposure doses increase the totRNA copy numbers associated with predicting culture positivity and detectable sgRNA. This suggests that the amplification of residual (inoculum-derived) genomic RNA may explain curious instances of sgRNA- or culture-negative samples with large totRNA copies, substantiating concerns in the animal challenge literature that inoculation procedures can directly influence viral detection and quantification (Dagotto et al., 2021). Interestingly, when we included a lab effect, our best sgRNA model predicted that (for any given totRNA quantity) larger doses would increase or have no effect on sgRNA quantities. This pattern could arise from two dueling effects of the inoculation procedure, whereby larger doses may increase (at least initial) sgRNA production, but inoculum-derived and newly produced gRNA could mask this effect. Future experimental work could test this hypothesis by directly comparing a range of doses.

The amplification of residual inoculum may also explain differences predicted between inoculated and non-inoculated tissues, where exposed tissues tend to have larger totRNA quantities than non-exposed tissues for any given sgRNA value, particularly on the first day post infection. Inoculum effects on totRNA quantity appear to linger throughout infection, given that sgRNA predictions for exposed tissues on later days post infection fall between predictions for exposed tissues on the first day and non-exposed tissues on all days. Interestingly, the chance of positive

culture (for a given totRNA value) is highest for exposed tissues sampled on the first day post infection, which is consistent with detection of lingering inoculum-derived virions. In contrast to sgRNA, culture predictions for exposed tissues on all later days post infection are highly similar to non-exposed tissues. These patterns are consistent with most inoculated virions having infected cells, dispersed to other tissues, or been cleared by the immune system within the first two days of infection, whereas the high stability of RNA (at least in human respiratory fluids monitored *ex vivo*; Matson et al., 2020) could enable its prolonged detection.

Our work showed that the relationships between virological assays were also shaped by host demographic factors. Primate species affected all relationships we considered, where cynomolgus macaques were predicted to have the lowest sgRNA:totRNA ratio and the smallest chance of positive culture per totRNA quantity. African green monkeys and rhesus macaques have highly similar predictions for sgRNA:totRNA ratios and chances of positive culture. Curiously, African green monkeys also have the smallest chance of sgRNA detection per totRNA quantity, but only one study (Speranza et al., 2021) reported totRNA and sgRNA outcomes for this species. Our models did not identify age-mediated effects on sgRNA outcomes but did predict that geriatric animals have the highest chances of positive culture per totRNA quantity. Sex did not influence either sgRNA or culture outcomes. While these results may reflect differing susceptibility, disease severity, or infection kinetics among non-human primate species and age classes, as has been previously suggested (Bajaj et al., 2021; Blair et al., 2021; Johnston et al., 2021; T. C. Jones et al., 2021; S. Lu et al., 2020; Yuan et al., 2021), sample sizes were limited for African green monkeys and geriatrics, so these patterns should be interpreted cautiously. Also, given the complexity of viral fitness, cellular processes, and immune responses, inference on the cause of demographic-specific differences is difficult without mechanistic theory. Mathematical models of the cellular

life cycle (Grebennikov et al., 2021) may uncover processes that explain the stoichiometric differences we observed among RNA types and virions.

Assay protocols had clear impacts on model predictions. PCR target gene was a consistent factor in our best models, with effects aligned with known differences in RNA quantities. We find that totRNA protocols targeting the Spike (S) gene must amplify less totRNA than those targeting the Envelope (E) or Nucleocapsid (N) genes to predict the same chance of positive culture. This likely reflects that totRNA assays targeting S will amplify only sgS and no other sgRNA species (because it is the most upstream sgRNA), whereas the others amplify multiple sgRNA species and thus will have inherently higher per-sample totRNA copy numbers. Notably, this result does not imply that spike assays better predict infectivity. Different genes simply require different RNA quantities to expect the same chance of culture positivity, and so other considerations should motivate choice of target gene (e.g., selecting target sequences that are conserved across variants). Similar reasoning can explain observed differences in sgRNA outcomes, where sgRNA protocols amplifying the highly-expressed sgN have higher chances of detecting sgRNA (per totRNA quantity) and also larger sgRNA:totRNA ratios than protocols amplifying the less-expressed sgE and sg7 species. For viral culture, our model predicts VeroE6-TMPRSS2 cells have the highest chance of detecting infectious virus (per totRNA quantity), which is concordant with the importance of TMPRSS2 for SARS-CoV-2 cellular entry (Hoffmann et al., 2020) and agrees with experiments showing VeroE6-TMPRSS2 cells are more permissive to infection than VeroE6 cells (Bruce et al., 2022; Matsuyama et al., 2020). In accordance with our results, prior work has also shown that VeroE6 cells are more sensitive than Vero76 cells, which is likely related to increased TMPRSS2 expression in VeroE6 cells (Amarilla et al., 2021). Our model also predicts that TCID50 assays are more likely to detect infectious SARS-CoV-2 than plaque assays, agreeing

with standard assay conversions (Carter & Saunders, 2007) and prior experimental work (Smither et al., 2013).

Although we developed this model to analyze SARS-CoV-2 in non-human primates, our results showed many similarities with patterns previously noted in humans. Multiple studies have found that, depending on the dataset, human-derived samples with around 5-9 log10 RNA copies had a 50% chance of being culture positive (T. C. Jones et al., 2021; Ke et al., 2021; van Kampen et al., 2021; Wölfel et al., 2020). The prediction from our analogous model without cofactors falls within this range (7 log10 totRNA copies). Other work has found evidence of age-dependent increases in infectious virus shedding (Ke et al., 2022) or in culture probability on any day rescaled to the time since peak viral load (T. C. Jones et al., 2021). Both of these findings are consistent with, although not directly comparable to, our result that geriatric NHPs have higher probabilities of culture positivity per totRNA quantity. Another study also discovered that the ratios of RNA to culturable virus differed substantially throughout infection (Porter et al., 2023). We unfortunately did not have sufficient quantitative culture information to obtain a similar ratio, but their findings agree with our observation that (for any given totRNA quantity) sgRNA copy numbers and culture probability vary by day post infection. Finally, we observed no culture positive (non-invasive) samples from the respiratory tract more than seven days after an individual's first positive test, and so the public health guidelines of isolating for five or ten days (CDC, 2020) performed remarkably well on our dataset, despite being designed for an entirely different host species. Collectively, these concordances further underscore that non-human primates are an excellent model system for human SARS-CoV-2 infection.

By analyzing our culture predictions for individual trajectories, we identified potential causes of prediction errors. Many occurred during transition periods when viral replication slows

or begins (i.e., when infectivity changes). During this crucial phase, our best culture model clearly outperformed the simple model by making fewer mistakes. In any case, during these periods, assay readouts will depend strongly on sample quality and assay sensitivity, so additional caution in interpreting culture outcomes is warranted. Beyond this, while we expect some errors due to complex and non-stationary biological effects, many errors are also consistent with PCR or culture processing issues. Sample quality, preservation methods, and storage conditions can substantially impact the quantification of RNA copy numbers and the detection of infectious virus (Ørpetveit et al., 2010; Puhach et al., 2023). PCR issues resulting in the amplification of less RNA may explain curious culture-positive samples with low or no detectable RNA (generating false negative predictions), while culture insensitivity may explain some culture-negative samples with especially large RNA quantities (i.e., false positives). Alternatively, sample contamination or sample swapping could cause elevated RNA levels or spurious culture positivity, where the latter is particularly plausible for 'data blips' of a single culture positive surrounded by a series of culture negatives, although these could reflect brief, intermittent replication. In any case, if we assume our model predictions were correct for at least some of these suspect samples (or else if we exclude them from accuracy calculations entirely), our culture model's true accuracy would be higher than 85%.

With this study, we demonstrated the utility and feasibility of meta-analyses and Bayesian statistical techniques for virological studies, which will become increasingly important tools under new data sharing mandates (Kozlov, 2022). Multiple factors enabled us to rigorously analyze our aggregate database: (i) PCR results were reported as RNA copy numbers, which are internally standardized (as opposed to unstandardized Ct values) (Puhach et al., 2023), (ii) processing techniques and viral concentrations per reported sample volume are consistent within each study,

(iii) many articles reported results for multiple cofactors, and (iv) we accounted for any additional between-study variation by including article-level hierarchical error rates when possible. To evaluate whether any of the observed patterns could be explained by unmodelled methodological differences among articles, we also ran our best models with an additional predictor for lab effects. Reassuringly, we found that all of our results were qualitatively unchanged between the models with and without lab effects (with one minor exception, discussed above), offering confidence in the robustness of our results. Under typical analytical approaches, our investigations would have required one study to generate the data for all protocols, samples, and demographics of interest, which would be time and resource prohibitive. Crucially, our approach did not require the generation of new data, which is especially important for non-human primate models where ethical principles (Prescott, 2010; Russell & Burch, 1959) and constrained supply (National Primate Research Center, 2020; Subbaraman, 2021) demand principled data reuse whenever possible.

Although the concordances noted between prior work and our results offer confidence in our models' performance, our study has limitations. Multiple source articles did not report age class or sex, requiring our model fits to marginalize over all possibilities. Consequently, parameter estimates for age and sex may underestimate their effects. This underscores the importance of comprehensive reporting, especially for animal challenge experiments where using previously collected data would increase adherence to the 3R principles (Russell & Burch, 1959). Also, few articles reported results for both sgRNA and culture, so some of our investigations relied on imputed sgRNA values. Prospective data on all three assays and more comprehensive data panels across cofactors would enable deeper exploration of the predictive capacity of totRNA and sgRNA for viral culture. Finally, while some cofactors were not selected for inclusion in our best models, we cannot exclude the possibility that their effects exist but were not evident or were masked by

other predictors. Because covariate coverage relied on different studies in different labs, it remains possible that lab or study effects impacted our results even though we found no evidence of this when including lab-specific predictor variables. Some covariate effects may have also been absorbed into our article-level error or lab effect terms. Despite these limitations, our analysis (and similar analyses) can help prioritize resource allocation, so future experiments can more easily adopt the gold-standard approach of testing model-based findings in head-to-head comparisons under fixed conditions.

While the quantitative results of our models should not be used directly to predict culture results for any host-pathogen system besides non-human primates and SARS-CoV-2, the general framework could be adapted easily to generate similar predictions for other host species, other viruses, or other assays. For example, our model could be modified to robustly compare the relationships among antigen tests, PCR, and viral culture, which has recently garnered interest (Bonenfant et al., 2022; Ford et al., 2021; Kirby et al., 2023; Zhang et al., 2022) and would benefit from the increased sample size and cofactor coverage possible with meta-analytical treatment. Notably, when applying the framework to other scenarios, careful model development is still necessary, especially given that different viruses and assays may have other defining characteristics that could affect their relationships, which should influence the choice of candidate cofactors.

We believe our framework also shows particular promise for future development to support clinical diagnostics. Beyond the fact that our model trained on NHP data recapitulated many patterns previously observed in humans, we also demonstrated its excellent performance on clinically relevant metrics. Relative to the five- or ten-day isolation protocols outlined by public health agencies (CDC, 2020), our best model substantially reduced unnecessary isolation time

(relative to the ten-day rule), and it reduced the risk of releasing individuals while still infectious (relative to the 5-day rule). Our best model also clearly outperformed the simple model on both of these metrics, in addition to correctly classifying more sequential culture negative samples and with markedly higher confidence, all of which could be crucial improvements in public health settings. In fact, because sampling frequency decreased over the course of infection in our data, our results likely underestimate the potential improvements achievable in humans where sampling can be more frequent. To realize the clinical potential of this approach, however, the model framework must be trained on human data. This would involve some model modifications, including the consideration of other cofactors such as viral variant, prior infection, vaccination history, disease severity, and co-morbidities. Outside the very rare context of human challenge trials, the model will also need to function without knowledge of exposure dose, route, or exact timing (requiring the use of a proxy such as time since symptom onset or first positive test). If such a model performs well, then it would offer a straightforward, standardized pipeline to predict whether an individual is infectious based on SARS-CoV-2 PCR results, which is a clear need (Bravo et al., 2022; Bruce et al., 2022; Bullard et al., 2020; Dimcheff et al., 2021; Gniazdowski et al., 2021; La Scola et al., 2020; van Kampen et al., 2021). To further increase prediction accuracy, future work could also modify the framework to capitalize on individual-specific trajectories for patients undergoing regular screening (e.g., by incorporating a mechanistic modeling component (Ke et al., 2022)). Once the modeling pipeline is established, it could be readily tailored to any other pathogen with sufficient clinical data, either to improve management strategies of existing viruses or even to help characterize and contain an emerging one. With these tools, public health officials and clinicians would be better-equipped to weigh transmission risk with medical resource

availability and economic burden to designate evidence-based (and pathogen-specific) hospital discharge criteria and public health guidelines.

By assembling and analyzing a large database that captures infection patterns described in the clinical and animal challenge literature, we demonstrated that highly accurate RNA-based culture predictions are possible with our statistical framework. By using non-human primate data, we were able to identify underlying effects of exposure conditions, which would be impossible for humans without experimental challenge trials (of which only one exists for SARS-CoV-2, to date; Killingley et al., 2022). Consequently, our model offers the first set of explicit quantitative guidelines on interpreting SARS-CoV-2 assay outcomes in light of exposure conditions, which has direct implications for analyzing non-human primate experiments and thus could affect human health by improving interpretations of crucial preclinical trials for human vaccines and therapeutics. We propose our method as a standardized framework to conduct assay comparisons, whether for individual virology experiments, clinical diagnostic settings, qualitative literature syntheses, or quantitative meta-analyses. Such approaches for data aggregation and (meta-) analysis are vital and powerful tools for an era of increasing data-sharing, with untapped potential to develop translational applications and to guide further research into fundamental mechanisms.

Data and code availability

All data and code used to produce the results and figures in this manuscript are available at: https://doi.org/10.5281/zenodo.10947025.

Acknowledgements

We thank the authors of all articles included in this study, many of whom kindly corresponded with us to provide clarifications and raw data. We also thank the members of the Lloyd-Smith lab for valuable discussions of this work. J.O.L.-S. and C.E.S were both supported by the Defense Advanced Research Projects Agency DARPA PREEMPT #D18AC00031. C.E.S was also supported by the National Institutes of Health (grant 5T32 GM008185-33) and the UCLA Office of the Vice Chancellor for Research 3R Grant. J.O.L.-S. was also supported by the National Science Foundation (DEB-1557022 and DEB-2245631) and the UCLA AIDS Institute and Charity Treks. The content of the article does not necessarily reflect the position or the policy of the US government, and no official endorsement should be inferred.

Supplementary Methods

Comprehensive literature search

To construct our database, we conducted comprehensive literature searches on 11 March 2021, which was the chosen cutoff date for inclusion in the database. One author (CS) screened the Web of Science (Core Collection) and PubMed for articles published in English with the following search string: (SARS-CoV-2 OR COVID-19) AND (primate* OR macaque* OR monkey* OR "macaca" OR "chlorocebus"). On the same day, CS also jointly screened bioRxiv and medRxiv, with two separate search strings: (i) (SARS-CoV-2 OR COVID-19) AND (primate* OR macaque* OR monkey*), and (ii) (SARS-CoV-2 OR COVID-19) AND ("macaca" OR "chlorocebus"). These searches returned 163 records from Web of Science, 761 from PubMed, and 259 from bioRxiv and medRxiv. An additional 60 records were obtained from Google Scholar searches and citation trackers (before 11 March 2021) using the following search terms: SARS-CoV-2, COVID-19, macaque, monkey, non-human primate (Figure S1.1). In total, this returned 1,243 results, with 866 unique records after removing duplicates. Of those, the following were immediately excluded: (i) articles published before 2020, (ii) article types that do not generate primary data (e.g., opinions, reviews), and (iii) articles with clearly irrelevant titles based on our predefined eligibility/inclusion criteria (described in the Methods). CS inspected the abstracts of the remaining 275 studies and the full texts of 122 records, according to the same eligibility criteria.

Data collection process

For each included article and every infected individual, the following study design details were obtained from the text, figures, supplementary files, or the corresponding authors, when available: primate species, rhesus macaque origin (Chinese or Indian), ID, sex, age (years or

months), age class, treatment group, viral inoculum strain, inoculation route(s), and route specific inoculation dose(s). For every sample, the following information was recorded when available: sample value (converted to log10, when quantitative and reported otherwise), sample time (day post infection, starting at 0), sample type (e.g., swab, tissue), sample location (e.g., liver), sample units (e.g., viral RNA copies/mL), method of quantification (e.g., RT-qPCR, plaque assay), target gene (for PCR), cell line (e.g., VeroE6, for viral culture), and limit of detection and/or quantification. We standardized all ID names as follows: [the first and last initial of the study's first author] _ [the ID name as assigned in the original study, if available].

When raw data was not published or methodological/biological details were missing or inconsistently reported, we contacted the corresponding author(s) using a standardized email template (paired with study-specific questions) to resolve discrepancies and/or request raw data. When clarification and/or raw data were obtained, the details were updated accordingly. In instances where clarification was not obtained but conflicting information existed in the article, we recorded the information most consistent with the methods section. Unclarified information that was missing entirely from the article materials is considered unknown.

Standardizing age class and inoculation doses

We developed a consistent method to assign age classes for all studies, following methods used in prior studies (Cramer et al., 2018; Darusman et al., 2014; Koo et al., 2019; Lee et al., 2020; Simmons, 2016). When age was reported in months and years, juvenile rhesus and cynomolgus macaques include individuals with ages <5 years, adults include 5-19 years, and geriatrics include ≥20 years. Juvenile African green monkeys include ages <5 years, adults include 5-14 years, and

geriatrics include ≥15 years. When reported age ranges spanned multiple assignments, we used the reported age class if available, otherwise we considered it unknown.

Since inoculation doses are frequently reported as either plaque forming units (pfu) or tissue culture infectious dose 50 (TCID50), we converted all inoculation doses reported in TCID50 to pfu using a standard conversion factor (1 TCID50=0.69 pfu) (Carter & Saunders, 2007).

Confirming RNA types

To confirm whether articles quantified full-length genomic RNA, subgenomic RNA, or total RNA (since reporting practices varied across studies), all relevant primer and probe sequences were extracted from each study or from referenced articles. We used SnapGene software (from Insightful Science; available at snapgene.com) to map all sequences to the SARS-CoV-2/human/CHN/Wu-1 reference genome. Any assays with both forward and reverse primers located within the ORF1ab gene were considered to amplify full-length genomic RNA, as this gene is not located on any canonical subgenomic RNAs. Assays with both forward and reverse primers located within any individual gene downstream of ORF1ab were considered to amplify total RNA, as these sequences can be found on both subgenomic and full-length genomic RNA. Assays where the forward primer was located in the 5' UTR but the reverse primer was located within a gene downstream of ORF1ab were classified as amplifying subgenomic RNA.

Justification and prior description for candidate predictors

Below, we provide further justification for the selection of all candidate predictors, including descriptions of all assigned priors. For the sgRNA models (that predict sgRNA results from totRNA), we use γ/δ to signify parameters for the logistic component and α/β for the linear

component. For the culture model (that predicts culture positivity from totRNA quantities), we use γ/ψ to signify the relevant parameters.

Primary predictors: We required all sgRNA models to include total RNA copy number (T) as a predictor, given this is the primary effect of interest. We expect the probability of detecting sgRNA to increase as total RNA copy numbers increase, which is supported by studies that find more sgRNA positive samples for those with large quantities of total RNA (Dimcheff et al., 2021; Perera et al., 2020). Given that we expect this relationship to be positive, we assign the following prior: $\delta_T \sim N(2,1)$. We also expect sgRNA copy numbers to increase with total RNA copy numbers, as observed in other studies that find positive linear relationships between them (Dimcheff et al., 2021; van Kampen et al., 2021; Verma et al., 2021). We assign the following prior: $\beta_T \sim Gamma(2,0.5)$. We evaluated culture models including total RNA, sgRNA (SG), or both as primary predictors. We expect the likelihood of detecting infectious virus to increase with increasing quantities of either RNA type, so we set the priors to be: $\Psi_T, \Psi_{SG} \sim N(2, 1)$.

Age, sex, and non-human primate species: As with other viruses, age (AGE) and sex (SEX) are hypothesized to affect individual responses to SARS-CoV-2 infection, including within-host infection kinetics and disease severity. Inter-species variability in infection dynamics has also been noted among non-human primate species (SP) and other animal models (Chu et al., 2022). These differences may affect observed relationships between assays. However, given the complexity of these biological interactions, we do not assign *a priori* expectations about the direction of these effects, and we set all associated priors to be $N(0,1)$.

Inoculation dose: Since sgRNA is not typically packaged into virions (Escors et al., 2003) and thus should not meaningfully exist in viral stocks, we expect to find detectable levels of total RNA earlier than sgRNA after inoculation (i.e., lower probabilities of sgRNA detection per total

RNA quantity for higher doses; $\delta_{DOSE} \sim N(-1,0.5)$). Larger inoculum doses could also result in (at least initially) higher levels of total RNA relative to sgRNA ($\beta_{DOSE} \sim N(-0.25,1)$). Exposure dose affects virion quantity and hence also total RNA quantity, which in turn may affect the probability of culture positivity through the presence of residual inoculum or other effects on infection kinetics. We make no *a priori* predictions on the direction of this effect ($\Psi_{DOSE} \sim N(0,1)$).

Day post infection: sgRNA levels likely remain low for some time in recently infected tissues. They may rise as virions infect local cells and replicate, and the ratio between total RNA and sgRNA may stabilize (Dimcheff et al., 2021). These dynamic changes may be especially pronounced when large quantities of virions (and thus also genomic RNA) are introduced simultaneously, as in animal infection experiments. Consequently, we expect newly infected tissues to contain small, likely undetectable quantities of sgRNA, whereas tissues infected one or more days prior, which have experienced sufficient replication, likely contain more sgRNA copies. For infectious virus, residual inoculum-derived virus may actually increase the probability of culture positivity in infected tissues relative to non-inoculated tissues (where virions must be produced). We derived a categorical predictor with three levels: DPI[1], DPI[2], and DPI[3]. For inoculated tissues, we distinguish between the first day (DPI[1]) and all other days post infection (DPI[2]). Since infection timing is unknown for non-inoculated tissues, we group all days into one level (DPI[3]). Table S1.3 lists which tissues were considered inoculated for each exposure procedure. We used the following priors: $\delta_{DPI[1]} \sim N(-1,1)$, $\delta_{DPI[2]} \sim N(1,1)$, $\delta_{DPI[3]} \sim N(0,1)$, $\beta_{DPI[1]} \sim N(-0.5,1)$ $\beta_{DPI[2]} \sim N(0.5,1)$, $\beta_{DPI[3]} \sim N(0,1)$, $\Psi_{DPI[1]} \sim N(1,1)$, $\Psi_{DPI[2]} \sim N(0.5,1)$, $\Psi_{DPI[3]} \sim N(0,1)$.

Sample type: Differences in the processing and content of non-invasive (e.g., swabs, biofluids) and invasive (e.g., whole tissues obtained at necropsy) samples may affect assay

readouts, and so we include sample type as a candidate predictor. We make no *a priori* predictions on their differences, and instead we assign non-informative priors (δ_{ST},β_{ST},Ψ_{ST}~$N(0,1)$).

Target gene: The RT-qPCR target gene affects quantification of SARS-CoV-2 copy numbers (Dimcheff et al., 2021; Lieberman et al., 2020; Moreira et al., 2021; Verma et al., 2021), which stems from the nature of PCR in addition to the organizational structure and transcription mechanisms of the coronavirus genome. The production and abundance of sgRNA species varies by gene (e.g., sgRNA N > sgRNA E; Kim et al., 2020), and sgRNA assays only amplify gene-specific sgRNA transcripts. In contrast, total RNA assays can amplify not only full-length genomic RNA and gene-specific sgRNA, but also other, larger sgRNAs that contain the target sequence. Given the many possible combinations of target gene pairs for total RNA and sgRNA assays, in our pooled dataset, we derived a generalizable predictor based on the number of transcripts available for amplification for each protocol. We distinguished between totRNA assays that amplify most (i.e., targets the Nucleocapsid gene; termed 'totRNA-high') or few sgRNA species (i.e., targets the Envelope gene; 'totRNA-low'). We also distinguish between sgRNA assays that target highly expressed (i.e., sgN; 'sgRNA-high') or less expressed sgRNA species (i.e., sgE, sg7; 'sgRNA-low'). This predictor thus has the following four levels: (1) totRNA-high/sgRNA-high, (2) totRNA-low/sgRNA-high, (3) totRNA-high/sgRNA-low, and (4) totRNA-low/sgRNA-low. We expect sgRNA-high assays to have higher probabilities of sgRNA detection and higher quantities of sgRNA per totRNA quantity ($\delta_{TG[1]}$, $\delta_{TG[2]}$~$N(1,1)$; $\beta_{TG[1]}$, $\beta_{TG[2]}$~$N(0.5,1)$) than sgRNA-low assays ($\delta_{TG[3]}$, $\delta_{TG[4]}$~$N(-1,1)$; $\beta_{TG[3]}$, $\beta_{TG[4]}$~$N(-0.5,1)$). For all culture models containing total RNA, we simply used the total RNA target gene as the predictor. When predicting culture from sgRNA, we used the sgRNA target gene as the predictor. Given SARS-CoV-2's genomic structure, we expect decreasing per-sample viral loads for totRNA protocols targeting the

Nucleocapsid ($\Psi_{TG[1]} \sim N(-1,1)$), Envelope ($\Psi_{TG[2]} \sim N(0,1)$), and Spike ($\Psi_{TG[3]} \sim N(1,1)$) genes, respectively. Since these stoichiometric ratios apply in any infected cell, we expect the relative probability of culture positivity to be higher for target genes with lower expression, such that the probability is highest for Spike ($\Psi_{TG[3]} \sim N(1,1)$), intermediate for Envelope ($\Psi_{TG[2]} \sim N(0,1)$), and lowest for Nucleocapsid ($\Psi_{TG[1]} \sim N(-1,1)$).

Cell line: Viral infectivity can vary by cell line, which can influence the likelihood of detecting infectious virus in a sample. Our data includes three distinct cell lines (VeroE6, Vero76, VeroE6-TMPRSS2) which we group into a three-level categorical predictor (CELL) for the culture model only. Given evidence of increased SARS-CoV-2 entry in cells expressing TMPRSS2 (Hoffmann et al., 2020; Matsuyama et al., 2020), we expect the probability of detection to be highest for VeroE6-TMPRSS2 cells ($\Psi_{CELL[3]} \sim N(1,1)$). We use the same non-informative prior for the other two ($\Psi_{CELL[1]} \sim N(0,1)$, $\Psi_{CELL[2]} \sim N(0,1)$).

Culture assay: The sensitivity of endpoint dilution (TCID50) and plaque assays can also vary, with plaque assays typically having lower sensitivity (Smither et al., 2013). We distinguish between these protocols in a binary predictor (ASSAY), with endpoint dilution treated as the reference. We assign the following prior ($\Psi_{ASSAY} \sim N(-0.5,1)$).

Article and lab effects: We assigned the same non-informative priors for the mean and standard deviation of each article's error term in the linear component ($\overline{\sigma} \sim N(0, 1)$; $\sigma_{sd} \sim Exp(1)$). We also assigned the same non-informative priors for all lab effect terms ($N(0, 0.5)$).

Approximate leave-one-out cross-validation

Beyond standard 10-fold cross-validation used in our main analyses, we also evaluated model performance and conducted model selection using Pareto-Smoothed Importance Sampling

Approximate Leave-One-Out cross-validation (PSIS-LOO) via the 'loo' R package (Vehtari et al., 2017). We ran this method for the linear component of the sgRNA model using RStan version 2.21.0 to use additional functionality of the LOO software (Vehtari et al., 2022). All other models were run using CmdStan, as described in the main Methods.

Pareto-k values indicate the accuracy of PSIS-LOO approximations, where values below 0.7 indicate sufficiently reliable estimates. We use the moment-matching functionality offered by the 'loo' package to correct Pareto-k values exceeding 0.7, after which all PSIS-LOO estimates generated in this study were reliable (adjusted Pareto-k < 0.7).

Cross-validation methods and model evaluation metrics

For 10-fold cross-validation, we assigned folds randomly, although we required each fold to contain similar quantities of data from each article. This allowed us to distribute protocols, demographics, and sampling types more evenly across folds. All statistics for this method were calculated separately for training and test sets to evaluate performance on out-of-sample data and assess potential bias or overfitting, with the exception of ELPD and MCC which were only calculated for test sets.

As outlined in the model description of the main Methods, the linear component of the sgRNA models contained article-specific hierarchical error rates. We used the estimates of each article's specific error distribution to generate ELPD values. However, when we calculated median absolute error and the percent of samples falling within given prediction intervals, we did not incorporate article-specific errors. Instead, for each iteration, we sampled the full range of estimated errors by sampling the error distribution of a random included article (uniformly

distributed), so these statistics better correspond to performance on new data (e.g., new studies) where prior information on error distributions is unavailable.

Selection procedure and results for the best sgRNA model

In the paragraphs below, we describe our model selection procedure for the sgRNA model, which relied on various performance metrics for each component. Overall, this procedure clearly identified the best model for both the logistic and linear components of the sgRNA model (Figure 1.2). Parallel analyses conducted with Pareto-Smoothed Importance Sampling approximate leave-one-out cross-validation resulted in qualitatively similar outcomes and selection of the same model (Tables S1.2, S1.3). Sensitivity analyses confirmed qualitatively similar results between informative and non-informative priors for the model selection procedure and for the parameter estimates of the best model (Figure S1.12). Prediction accuracy and median absolute error (MAE) showed minimal differences between training and test datasets, for all PCR models considered, offering confidence in the models' generalizability (Table S1.2, S1.3).

For the logistic component, the best model performed substantially better than the simple model for all three statistics considered. The best model had considerably higher ELPD (difference: 67.3; Figure 1.2, Table S1.2). Prediction accuracy on test data increased overall by 3.4 percent, and MCC increased from 0.75 to 0.82 (Figures 1.2, 1.3C; Table S1.2). The best model also correctly predicted sgRNA detectability with higher probability for more samples and had a substantially higher ELPD, both of which reflect higher certainty for true classifications (Figures 1.2, 1.3C). Prediction accuracy and Matthews correlation coefficient (MCC) indicate nearly identical performance of the best and full models (Figure 1.2, Table S1.2). The difference between the estimated log pointwise predictive density (ELPD) for the best and full models falls within two

standard errors of the difference (difference: 1.60; standard error: 3.50), again indicating similar model performance (Sivula et al., 2022).

When predicting copy numbers for all sgRNA positive samples with the linear component, the best model showed better performance than the full and simple models on all three statistics considered. Predictive performance of the best model is substantially better than the simple model, with 55.0 versus 48.0 percent of samples falling within the 50 percent prediction interval (Figure 1.2, Table S1.3) and a decrease in median prediction error from 0.58 to 0.44 (Figure 1.3F). The ELPD difference is also substantial (-186.2). Posterior predictive checks show a strong correlation between observed and median predicted sgRNA values for the best model (adjusted R^2=0.77), which further supports superior performance of the multiple regression model compared to the simple single regression model (adjusted R^2=0.68). Relative to the full model, the best model has higher ELPD (difference: -4.44) and similar prediction error on test data (0.44 vs. 0.45) (Figure 1.2, Table S1.3). A higher percent of (test) samples fall within the model-generated 50 percent prediction interval for the best model (55.0 vs. 54.5).

Selection procedure and results for the best culture model

In the paragraphs below, we describe our model selection procedure for the culture model, which relied on three primary performance metrics. This procedure clearly identified the best culture model. Model selection did not vary between cross-validation methods. Prior choice also did not alter model selection nor did it qualitatively affect parameter estimates (Figure S1.12). Prediction accuracy between training and test sets was comparable (Table S1.4), again supporting model generalizability.

The evaluation procedure identified the best model as the one containing all but two candidate predictors (Figure 1.2). For all three statistics considered, the best model performed better than the simple model. The best model had considerably higher ELPD, for which the difference was larger than two standard errors (difference: 55.70; standard error: 13.96; Figure 1.2, Table S1.4). For totRNA-positive samples, prediction accuracy on test data increased overall by 3.1 percent, but notably the best model correctly classified an additional 7.0 percent of culture positive samples (Figure 1.4C), both of which are reflected in the improvement of MCC from 0.48 to 0.57 (Table S1.4). The difference between the ELPD for the best and full models is small (difference: 0.76; standard error: 3.42), and their overall prediction accuracy and MCC are nearly identical (Figure 1.2, Table S1.4).

Mathematical form of the best sgRNA model

The mathematical form of the best sgRNA model is outlined below, where we use γ/δ to signify parameters for the logistic component and α/β for the linear component. Acronyms are as follows: SG: sgRNA, T: total RNA, DOSE: inoculation dose (log10 pfu), SP: species, TG: target gene (standardized to four levels), and DPI: day post infection.

$$SG_{>LOD,i} \sim Bernoulli(p_i)$$

$$logit(p_i) = \gamma + \delta_T T_i + \delta_{DOSE} DOSE_i + \delta_{TG_i} + \delta_{SP_i}$$

$$SG_{value,i} \sim N(y_i, \sigma_{article_i})$$

$$y_i = \alpha + \beta_T T_i + \beta_{DOSE} DOSE_i + \beta_{TG_i} + \beta_{DPI_i} + \beta_{SP_i}$$

$$\sigma_{article_i} \sim N(\bar{\sigma}, \sigma_{sd})$$

Mathematical form of the best culture model

The mathematical form of the best culture model is outlined below, where we use γ/ψ to signify the relevant parameters. Acronyms are as follows: C: culture, T: total RNA, DOSE: inoculation dose (log10 pfu), DPI: day post infection, AGE: age class, SP: species, CELL: culture cell line, ASSAY: culture assay, and TG: target gene (standardized to three levels).

$$C_{>LOD,i} \sim Bernoulli(p_i)$$

$$logit(p_i) = \gamma + \psi_T T_i + \psi_{DOSE} DOSE_i + \psi_{DPI_i} + \psi_{AGE_i} + \psi_{SP_i} + \psi_{CELL_i} + \psi_{ASSAY} ASSAY_i + \psi_{TG_i}$$

Prediction intervals and parameter estimates

To generate prediction intervals for various statistics, including median probabilities of sgRNA or culture positivity and median predicted sgRNA copy numbers, we used all available post-warmup parameter samples from the best model. We used the same procedure to generate the fit lines shown in Figures 1.3 and 1.5. Each prediction is generated using grouped parameter samples (e.g., samples from the same chain and iteration) to preserve correlation structure.

Estimating differences between predicted and known outcomes

To compare median predicted sgRNA copies to observed sgRNA or totRNA copies, we modeled the distribution of each of these quantities as normally distributed random variables with unique means and variances. We also compared totRNA quantities for culture samples with false negative, true positive, and true negative predictions by estimating the population means for each

group (captured as a normally distributed variable). For both of these investigations, we calculated the median and quantiles of the distribution of differences between these populations means, where we subtracted estimates only from the same chain and iteration. We fit these Bayesian models using the same procedures as described in the Methods.

Supplementary Figures

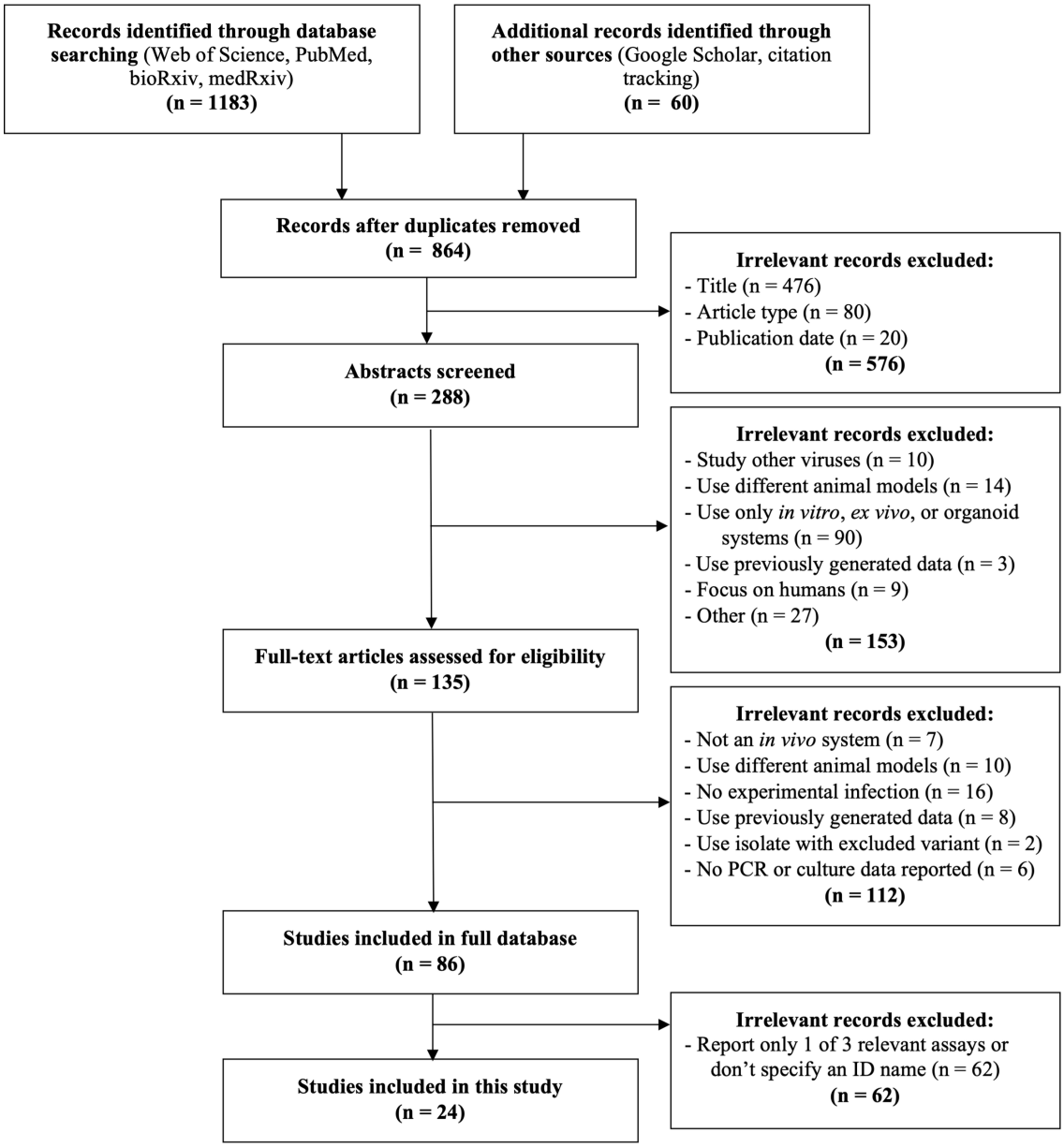

Figure S 1.1 | Screening and selection procedure for database compilation.
We created this figure by adapting the template flowchart provided in Moher et al., 2009, which offers guidelines and resources for systematic reviews and meta-analyses. We incorporated all of their suggested steps for reporting the results of systematic literature searches, but all of the substantive content (e.g., numbers, exclusion reasons) is based entirely on our literature search. Additional detail on the screening procedure is provided in the Supplementary Methods.

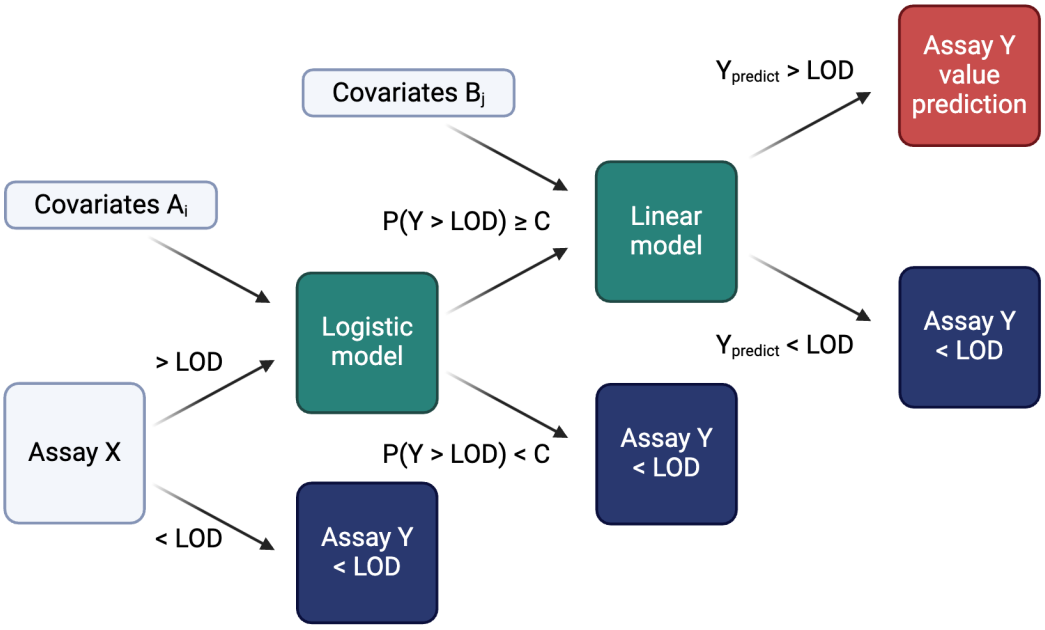

Figure S 1.2 | Schematic diagram of generalizable hurdle model predicting assay Y from a more sensitive assay X.
Predictors are grey, model components are green, and predictions are red (positive) or blue (negative). If assay X falls below the limit of detection (< LOD), assay Y is also predicted to fall below the limit of detection. (Note that this particular assumption may not hold for all assay relationships, and modeling adjustments may need to be made in these scenarios.) If assay X falls above the limit of detection (> LOD), then the value of assay X is passed as a predictor to the logistic component of the hurdle model, which uses a set of additional covariates A_i to predict whether assay Y falls above or below the LOD. If the posterior probability of assay Y falling above the limit of detection is less than some assigned threshold C ($P(Y > LOD) < C$), then the model predicts assay Y falls below the LOD. Otherwise, the model predicts assay Y falls above the LOD. Note that the probability cut-off value C should be selected to balance false positive and false negative rates as appropriate to investigator aims. In this study, we used a standard value of C=0.5. For samples predicted to fall above the LOD, the linear model component will generate a predicted value of assay Y ($Y_{predict}$) based on another set of covariates (B_j). If $Y_{predict}$ is larger than the reported LOD for assay Y, the model will return the predicted value. Created with BioRender.com.

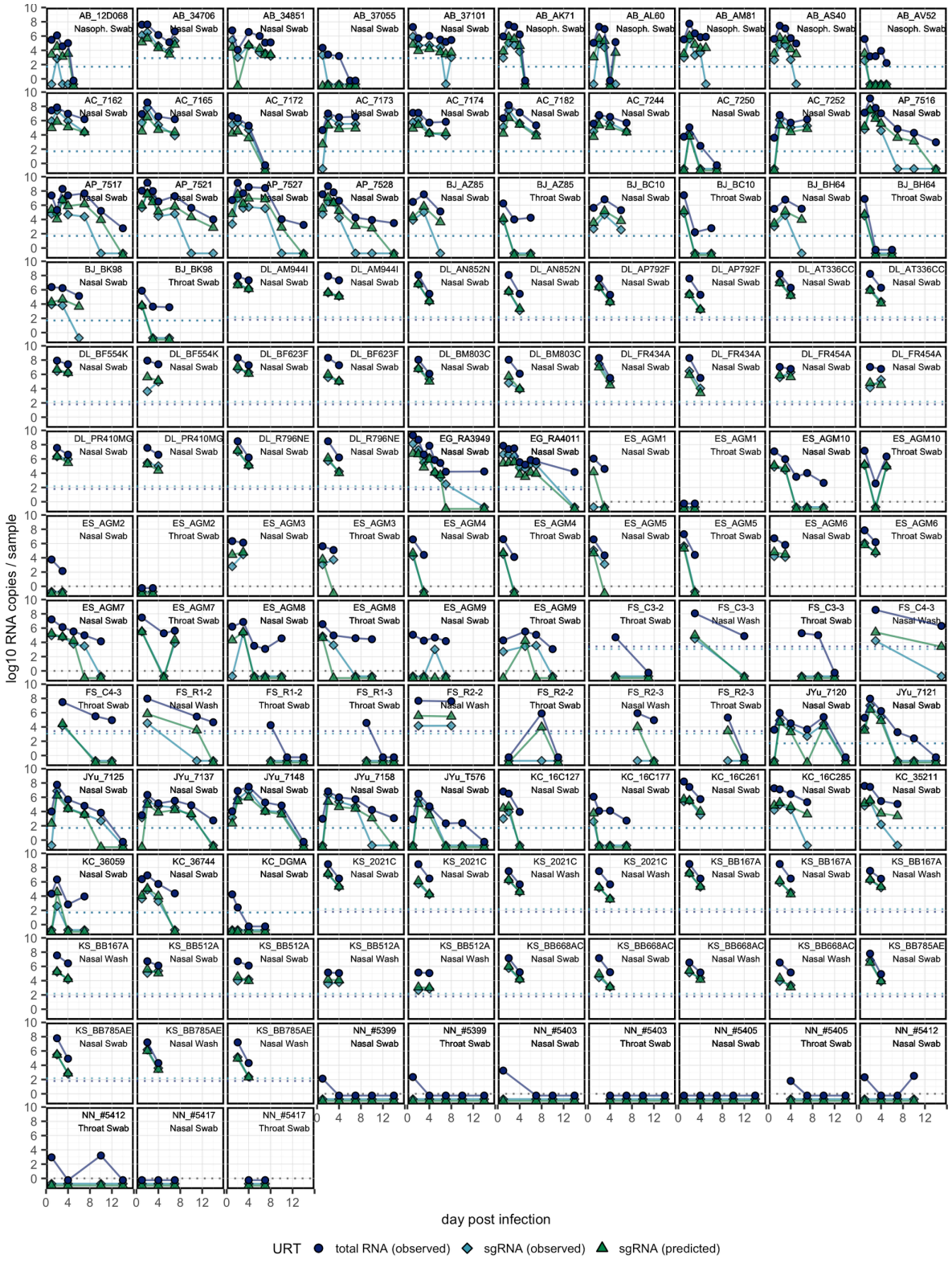
AB_12D068 Nasoph. Swab
AB_34706 Nasal Swab
AB_34851 Nasal Swab
AB_37055 Nasal Swab
AB_37101 Nasal Swab
AB_AK71 Nasoph. Swab
AB_AL60 Nasoph. Swab
AB_AM81 Nasoph. Swab
AB_AS40 Nasoph. Swab
AB_AV52 Nasoph. Swab
AC_7162 Nasal Swab
AC_7165 Nasal Swab
AC_7172 Nasal Swab
AC_7173 Nasal Swab
AC_7174 Nasal Swab
AC_7182 Nasal Swab
AC_7244 Nasal Swab
AC_7250 Nasal Swab
AC_7252 Nasal Swab
AP_7516 Nasal Swab
AP_7517 Nasal Swab
AP_7521 Nasal Swab
AP_7527 Nasal Swab
AP_7528 Nasal Swab
BJ_AZ85 Nasal Swab
BJ_AZ85 Throat Swab
BJ_BC10 Nasal Swab
BJ_BC10 Throat Swab
BJ_BH64 Nasal Swab
BJ_BH64 Throat Swab
BJ_BK98 Nasal Swab
BJ_BK98 Throat Swab
DL_AM944I Nasal Swab
DL_AM944I Nasal Swab
DL_AN852N Nasal Swab
DL_AN852N Nasal Swab
DL_AP792F Nasal Swab
DL_AP792F Nasal Swab
DL_AT336CC Nasal Swab
DL_AT336CC Nasal Swab
DL_BF554K Nasal Swab
DL_BF554K Nasal Swab
DL_BF623F Nasal Swab
DL_BF623F Nasal Swab
DL_BM803C Nasal Swab
DL_BM803C Nasal Swab
DL_FR434A Nasal Swab
DL_FR434A Nasal Swab
DL_FR454A Nasal Swab
DL_FR454A Nasal Swab
DL_PR410MG Nasal Swab
DL_PR410MG Nasal Swab
DL_R796NE Nasal Swab
DL_R796NE Nasal Swab
EG_RA3949 Nasal Swab
EG_RA4011 Nasal Swab
ES_AGM1 Nasal Swab
ES_AGM1 Throat Swab
ES_AGM10 Nasal Swab
ES_AGM10 Throat Swab
ES_AGM2 Nasal Swab
ES_AGM2 Throat Swab
ES_AGM3 Nasal Swab
ES_AGM3 Throat Swab
ES_AGM4 Nasal Swab
ES_AGM4 Throat Swab
ES_AGM5 Nasal Swab
ES_AGM5 Throat Swab
ES_AGM6 Nasal Swab
ES_AGM6 Throat Swab
ES_AGM7 Nasal Swab
ES_AGM7 Throat Swab
ES_AGM8 Nasal Swab
ES_AGM8 Throat Swab
ES_AGM9 Nasal Swab
ES_AGM9 Throat Swab
FS_C3-2 Throat Swab
FS_C3-3 Nasal Wash
FS_C3-3 Throat Swab
FS_C4-3 Nasal Wash
FS_C4-3 Throat Swab
FS_R1-2 Nasal Wash
FS_R1-2 Throat Swab
FS_R1-3 Throat Swab
FS_R2-2 Nasal Wash
FS_R2-2 Throat Swab
FS_R2-3 Nasal Wash
FS_R2-3 Throat Swab
JYu_7120 Nasal Swab
JYu_7121 Nasal Swab
JYu_7125 Nasal Swab
JYu_7137 Nasal Swab
JYu_7148 Nasal Swab
JYu_7158 Nasal Swab
JYu_T576 Nasal Swab
KC_16C127 Nasal Swab
KC_16C177 Nasal Swab
KC_16C261 Nasal Swab
KC_16C285 Nasal Swab
KC_35211 Nasal Swab
KC_36059 Nasal Swab
KC_36744 Nasal Swab
KC_DGMA Nasal Swab
KS_2021C Nasal Swab
KS_2021C Nasal Swab
KS_2021C Nasal Wash
KS_2021C Nasal Wash
KS_BB167A Nasal Swab
KS_BB167A Nasal Swab
KS_BB167A Nasal Wash
KS_BB167A Nasal Wash
KS_BB512A Nasal Swab
KS_BB512A Nasal Swab
KS_BB512A Nasal Wash
KS_BB512A Nasal Wash
KS_BB668AC Nasal Swab
KS_BB668AC Nasal Swab
KS_BB668AC Nasal Wash
KS_BB668AC Nasal Wash
KS_BB785AE Nasal Swab
KS_BB785AE Nasal Swab
KS_BB785AE Nasal Wash
KS_BB785AE Nasal Wash
NN_#5399 Nasal Swab
NN_#5399 Throat Swab
NN_#5403 Nasal Swab
NN_#5403 Throat Swab
NN_#5405 Nasal Swab
NN_#5405 Throat Swab
NN_#5412 Nasal Swab
NN_#5412 Throat Swab
NN_#5417 Nasal Swab
NN_#5417 Throat Swab
log10 RNA copies / sample
day post infection
URT
total RNA (observed)
sgRNA (observed)
sgRNA (predicted)

Figure S 1.3 | Individual viral load trajectories in the upper respiratory tract, including sgRNA predictions generated by the best sgRNA model.
Each panel corresponds with one individual and one non-invasive sample type, indicated in the top right of each panel. Only individuals with both total RNA and sgRNA results for at least two days post infection are plotted. Some individuals were sampled from multiple locations in the upper respiratory tract, in which case they are plotted as neighboring panels. Each line and the accompanying points track the individual's total RNA (dark blue, circle), observed sgRNA (light blue, diamond), and median predicted sgRNA (green, triangle) trajectories. For some individuals (e.g., KS_2021C), multiple RT-qPCR assays targeting different genes were run on the same sample, which are plotted as distinct panels. All samples observed or predicted to fall below the limit of detection are plotted below 0 at set values for visual clarity (totRNA: -0.5, observed sgRNA: -0.75, predicted sgRNA: -1). When available, the limits of detection (LOD) or quantification (LOQ) for PCR assays are plotted as dotted lines in the assay-specific color. When both the LOD and LOQ were available, only the LOD is plotted. In instances where the total RNA and sgRNA assay LOD are equal, only the sgRNA line is visible. No instances exist in this dataset where the LOD or LOQ is only available for one RNA type.

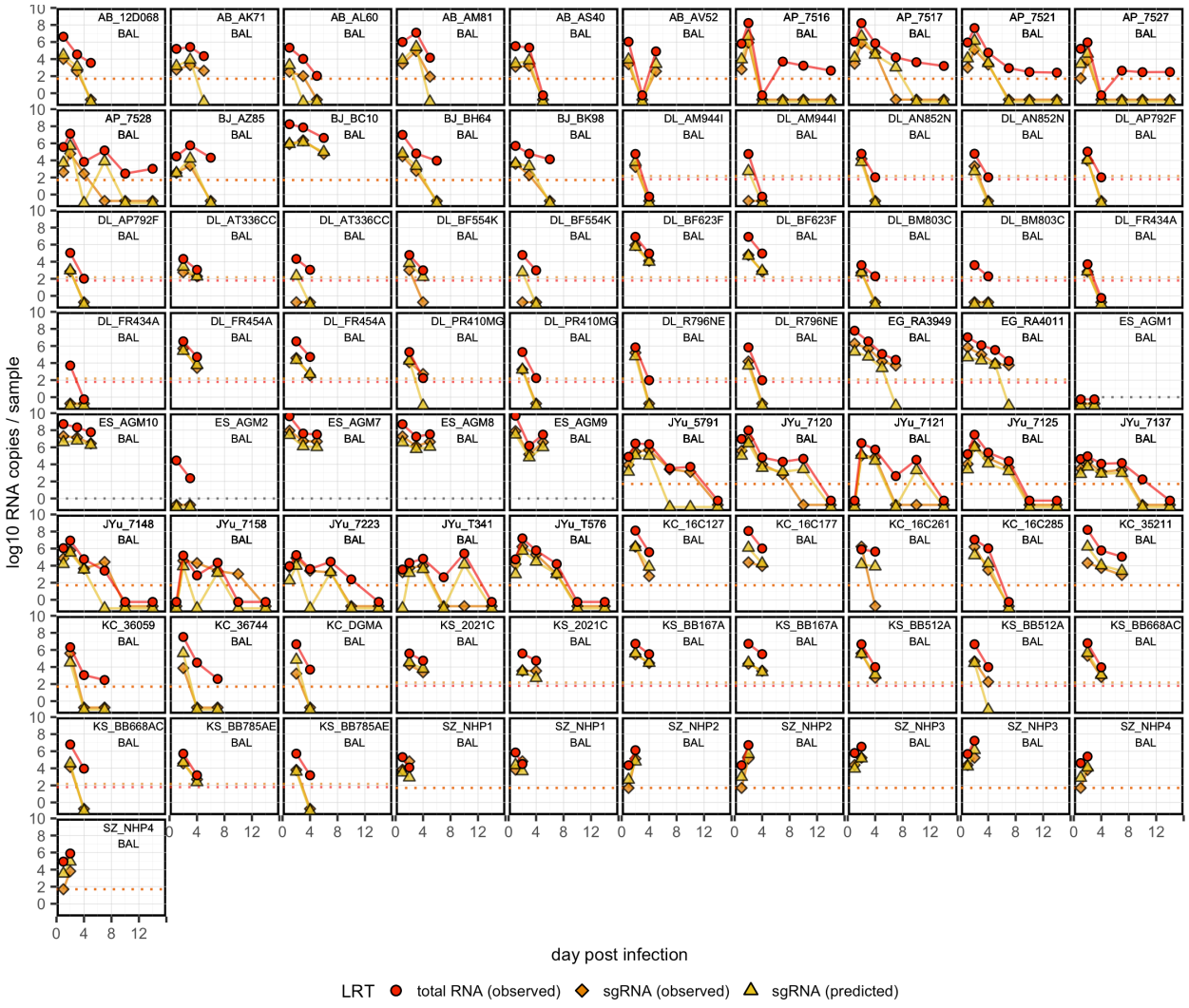

Figure S 1.4 | Individual viral load trajectories in the lower respiratory tract, including sgRNA predictions generated by the best sgRNA model.
Each panel corresponds with one individual and one non-invasive sample type, indicated in the top right of each panel ('BAL': bronchoalveolar lavage). Only individuals with both total RNA and sgRNA results for at least two days post infection are plotted. Each line and the accompanying points track the individual's total RNA (dark red, circle), observed sgRNA (orange, diamond), and median predicted sgRNA (yellow, triangle) trajectories. For some individuals (e.g., KS_2021C), multiple RT-qPCR assays targeting different genes were run on the same sample, which are plotted as distinct panels. All samples observed or predicted to fall below the limit of detection are plotted below 0 at set values for visual clarity (totRNA: -0.5, observed sgRNA: -0.75, predicted sgRNA: -1). When available, the limits of detection (LOD) or quantification (LOQ) for PCR assays are plotted as dotted lines in the assay-specific color. When both the LOD and LOQ were available, only the LOD is plotted. In instances where the total RNA and sgRNA assay LOD are equal, only the sgRNA line is visible. No instances exist in this dataset where the LOD or LOQ is only available for one RNA type.

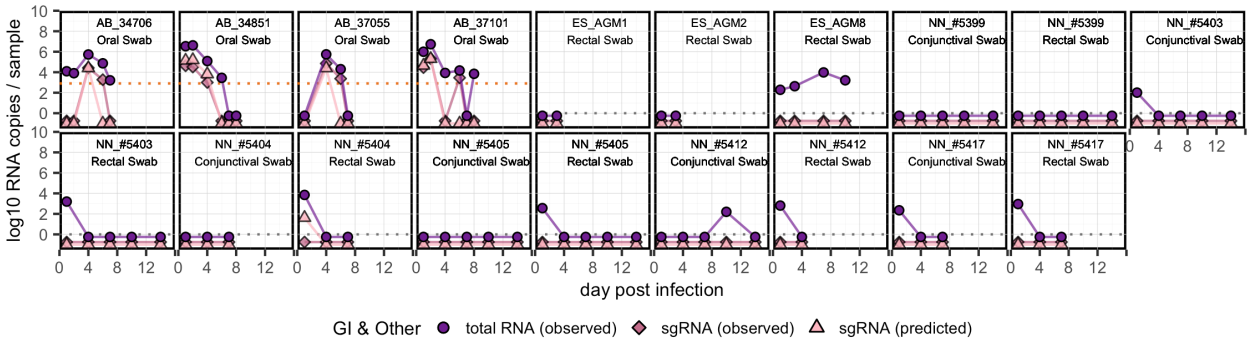

Figure S 1.5 | Individual viral load trajectories in the gastrointestinal and other systems, including sgRNA predictions generated by the best sgRNA model.
Each panel corresponds with one individual and one non-invasive sample type, indicated in the top right of each panel. Only individuals with both total RNA and sgRNA results for at least two days post infection are plotted. Each line and the accompanying points track the individual's total RNA (dark purple, circle), observed sgRNA (dark pink, diamond), and median predicted sgRNA (light pink, triangle) trajectories. All samples observed or predicted to fall below the limit of detection are plotted below 0 at set values for visual clarity (totRNA: -0.5, observed sgRNA: -0.75, predicted sgRNA: -1). When available, the limits of detection (LOD) or quantification (LOQ) for PCR assays are plotted as dotted lines in the assay-specific color. When both the LOD and LOQ were available, only the LOD is plotted. In instances where the total RNA and sgRNA assay LOD are equal, only the sgRNA line is visible. No instances exist in this dataset where the LOD or LOQ is only available for one RNA type.

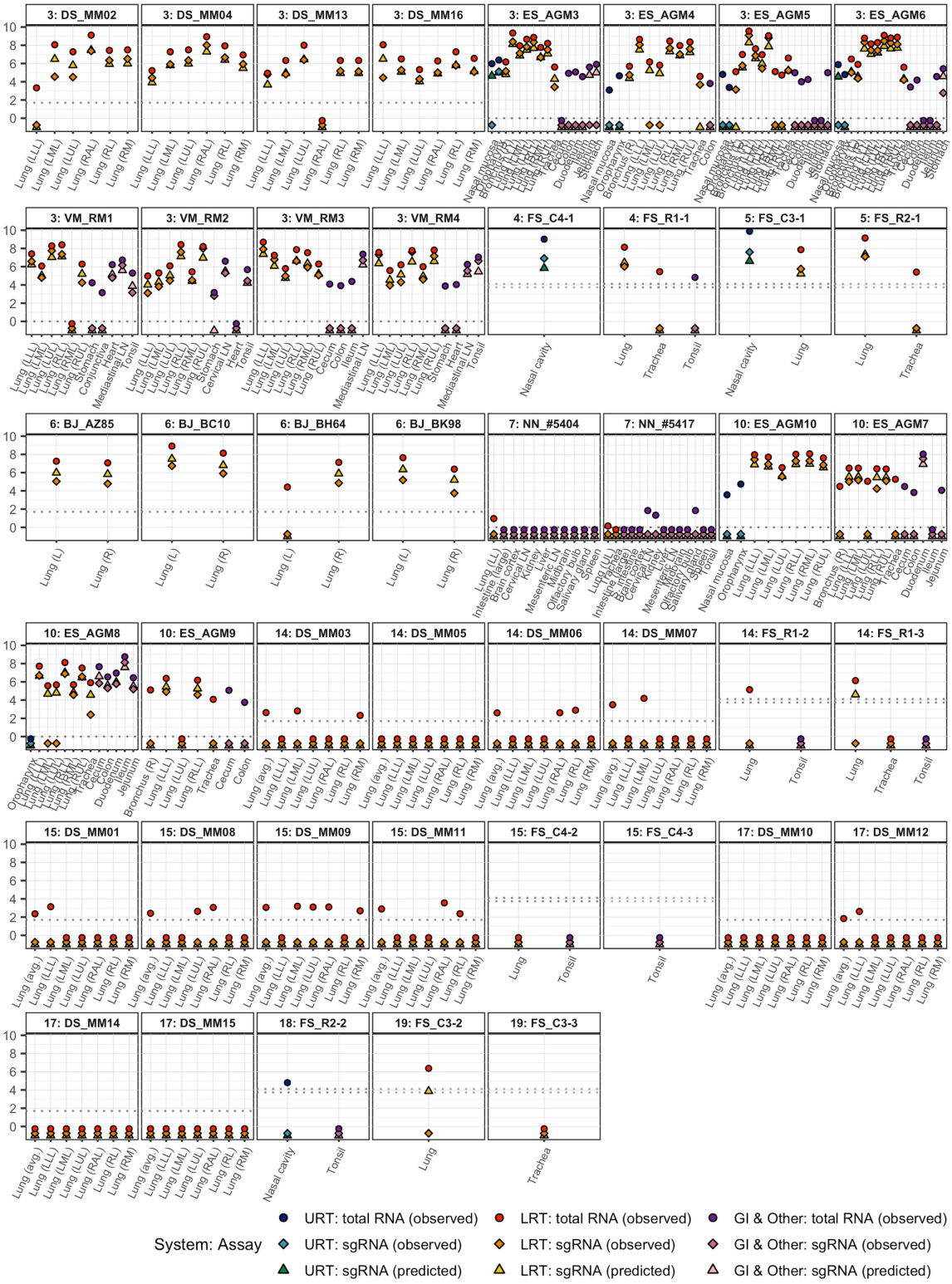
3: DS_MM02
3: DS_MM04
3: DS_MM13
3: DS_MM16
3: ES_AGM3
3: ES_AGM4
3: ES_AGM5
3: ES_AGM6
3: VM_RM1
3: VM_RM2
3: VM_RM3
3: VM_RM4
4: FS_C4-1
4: FS_R1-1
5: FS_C3-1
5: FS_R2-1
6: BJ_AZ85
6: BJ_BC10
6: BJ_BH64
6: BJ_BK98
7: NN_#5404
7: NN_#5417
10: ES_AGM10
10: ES_AGM7
10: ES_AGM8
10: ES_AGM9
14: DS_MM03
14: DS_MM05
14: DS_MM06
14: DS_MM07
14: FS_R1-2
14: FS_R1-3
15: DS_MM01
15: DS_MM08
15: DS_MM09
15: DS_MM11
15: FS_C4-2
15: FS_C4-3
17: DS_MM10
17: DS_MM12
17: DS_MM14
17: DS_MM15
18: FS_R2-2
19: FS_C3-2
19: FS_C3-3
System: Assay
URT: total RNA (observed)
URT: sgRNA (observed)
URT: sgRNA (predicted)
LRT: total RNA (observed)
LRT: sgRNA (observed)
LRT: sgRNA (predicted)
GI & Other: total RNA (observed)
GI & Other: sgRNA (observed)
GI & Other: sgRNA (predicted)

Figure S 1.6 | Individual viral loads for invasive samples, including sgRNA predictions generated by the best sgRNA model.
Each panel corresponds with one individual, indicated with text in the panel (day post infection: individual). Each point presents the total RNA (circle), observed sgRNA (diamond), and predicted sgRNA (triangle) values. All samples observed or predicted to fall below the limit of detection are plotted below 0 at set values for visual clarity (totRNA: -0.5, observed sgRNA: -0.75, predicted sgRNA: -1). When available, the limits of detection (LOD) or quantification (LOQ) for PCR assays are plotted as dotted lines in the assay-specific color. When both the LOD and LOQ were available, only the LOD is plotted. In instances where the total RNA and sgRNA assay LOD are equal, only the sgRNA line is visible. No instances exist in this dataset where the LOD or LOQ is only available for one RNA type.

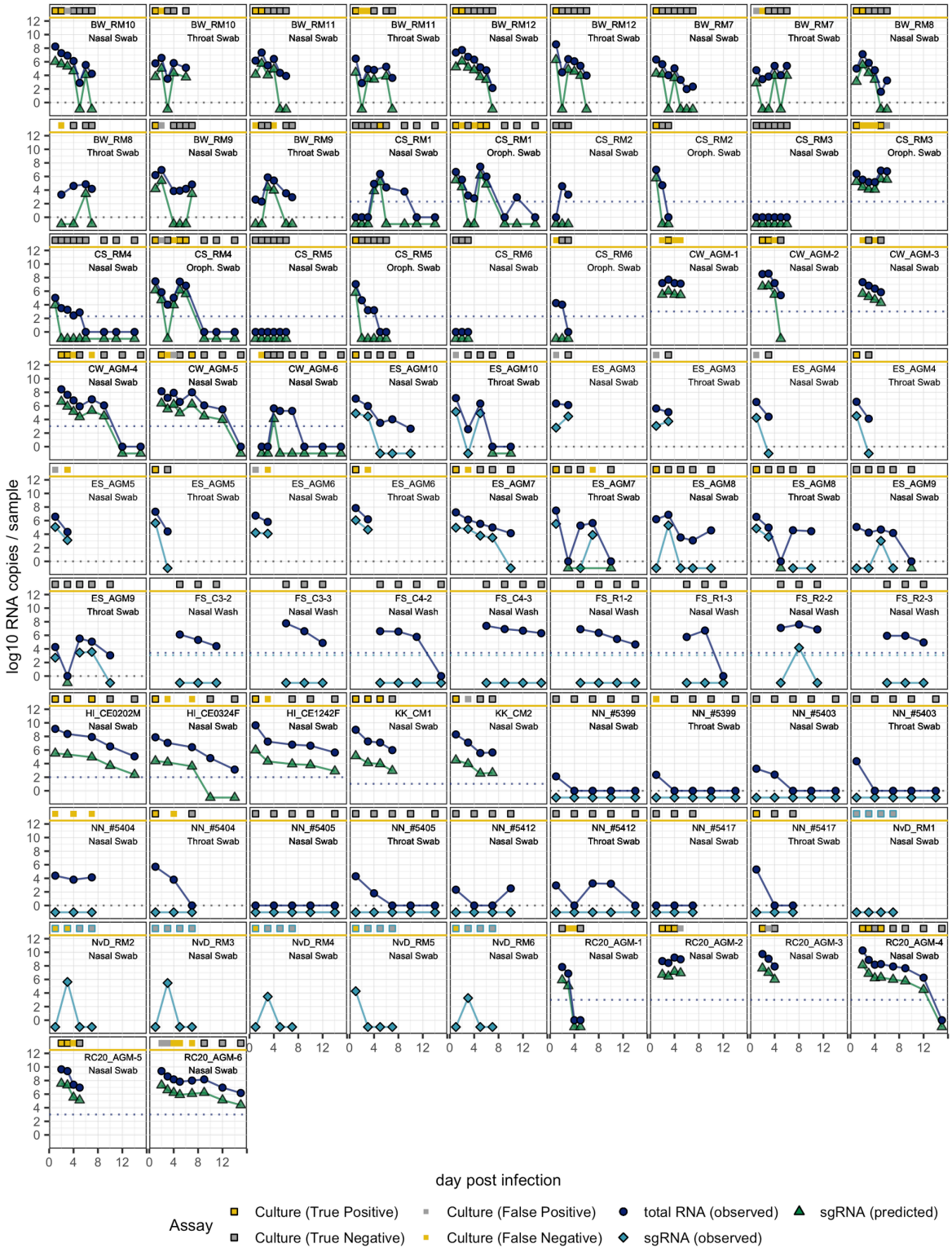
BW_RM10 Nasal Swab
BW_RM10 Throat Swab
BW_RM11 Nasal Swab
BW_RM11 Throat Swab
BW_RM12 Nasal Swab
BW_RM12 Throat Swab
BW_RM7 Nasal Swab
BW_RM7 Throat Swab
BW_RM8 Nasal Swab
BW_RM8 Throat Swab
BW_RM9 Nasal Swab
BW_RM9 Throat Swab
CS_RM1 Nasal Swab
CS_RM1 Oroph. Swab
CS_RM2 Nasal Swab
CS_RM2 Oroph. Swab
CS_RM3 Nasal Swab
CS_RM3 Oroph. Swab
CS_RM4 Nasal Swab
CS_RM4 Oroph. Swab
CS_RM5 Nasal Swab
CS_RM5 Oroph. Swab
CS_RM6 Nasal Swab
CS_RM6 Oroph. Swab
CW_AGM-1 Nasal Swab
CW_AGM-2 Nasal Swab
CW_AGM-3 Nasal Swab
CW_AGM-4 Nasal Swab
CW_AGM-5 Nasal Swab
CW_AGM-6 Nasal Swab
ES_AGM10 Nasal Swab
ES_AGM10 Throat Swab
ES_AGM3 Nasal Swab
ES_AGM3 Throat Swab
ES_AGM4 Nasal Swab
ES_AGM4 Throat Swab
ES_AGM5 Nasal Swab
ES_AGM5 Throat Swab
ES_AGM6 Nasal Swab
ES_AGM6 Throat Swab
ES_AGM7 Nasal Swab
ES_AGM7 Throat Swab
ES_AGM8 Nasal Swab
ES_AGM8 Throat Swab
ES_AGM9 Nasal Swab
ES_AGM9 Throat Swab
FS_C3-2 Nasal Wash
FS_C3-3 Nasal Wash
FS_C4-2 Nasal Wash
FS_C4-3 Nasal Wash
FS_R1-2 Nasal Wash
FS_R1-3 Nasal Wash
FS_R2-2 Nasal Wash
FS_R2-3 Nasal Wash
HI_CE0202M Nasal Swab
HI_CE0324F Nasal Swab
HI_CE1242F Nasal Swab
KK_CM1 Nasal Swab
KK_CM2 Nasal Swab
NN_#5399 Nasal Swab
NN_#5399 Throat Swab
NN_#5403 Nasal Swab
NN_#5403 Throat Swab
NN_#5404 Nasal Swab
NN_#5404 Throat Swab
NN_#5405 Nasal Swab
NN_#5405 Throat Swab
NN_#5412 Nasal Swab
NN_#5412 Throat Swab
NN_#5417 Nasal Swab
NN_#5417 Throat Swab
NvD_RM1 Nasal Swab
NvD_RM2 Nasal Swab
NvD_RM3 Nasal Swab
NvD_RM4 Nasal Swab
NvD_RM5 Nasal Swab
NvD_RM6 Nasal Swab
RC20_AGM-1 Nasal Swab
RC20_AGM-2 Nasal Swab
RC20_AGM-3 Nasal Swab
RC20_AGM-4 Nasal Swab
RC20_AGM-5 Nasal Swab
RC20_AGM-6 Nasal Swab
log10 RNA copies / sample
day post infection
Assay
Culture (True Positive)
Culture (True Negative)
Culture (False Positive)
Culture (False Negative)
total RNA (observed)
sgRNA (observed)
sgRNA (predicted)

Figure S 1.7 | Individual culture trajectories in the upper respiratory tract.
Each panel corresponds with one individual and one non-invasive sample type, indicated in the top right of each panel. Only individuals with culture results for at least two days post infection are plotted. Culture data are plotted as squares above the yellow line at 10 log10 copies. Yellow squares are culture positive samples, while grey squares are culture negative. Squares outlined in black are correct predictions, squares with no outline are incorrect predictions. We did not generate predictions for the culture samples outlined in blue, as they do not have available totRNA results. We also plot observed total RNA values (circle) and observed sgRNA values (diamond), otherwise we plot predicted median sgRNA values generated by our best sgRNA model (triangle). Some individuals were sampled from multiple locations in the upper respiratory tract, in which case they are plotted as neighboring panels. All samples observed or predicted to fall below the limit of detection are plotted below 0 at set values for visual clarity (totRNA: 0, sgRNA: -1). When available, the limits of detection (LOD) or quantification (LOQ) for PCR assays are plotted as dotted lines in the assay-specific color. When both the LOD and LOQ were available, only the LOD is plotted. In instances where the total RNA and sgRNA assay LOD are equal, only the sgRNA line is visible. No instances exist in this dataset where the LOD or LOQ is only available for one RNA type. Individuals from one study cannot be included in this figure due to a data sharing agreement.

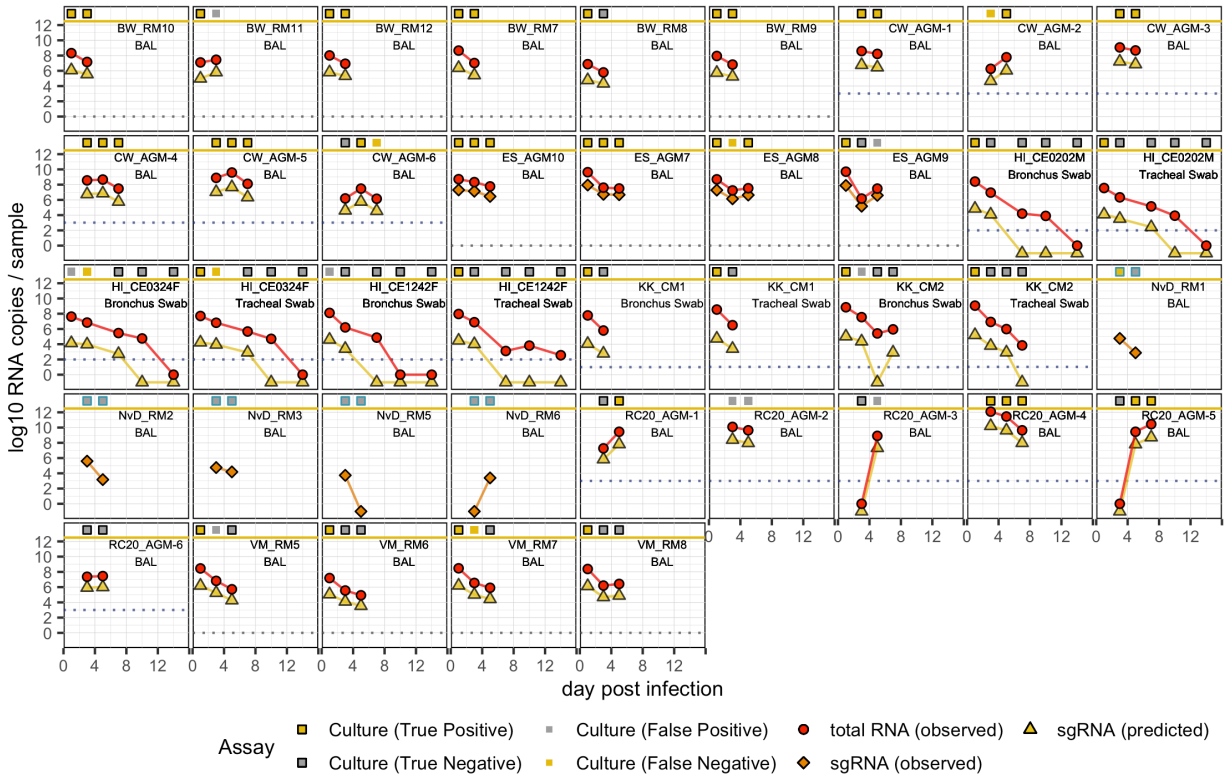

Figure S 1.8 | Individual culture trajectories in the lower respiratory tract.
Each panel corresponds with one individual and one non-invasive sample type, indicated in the top right of each panel. Only individuals with culture results for at least two days post infection are plotted. Culture data are plotted as squares above the yellow line at 10 log10 copies. Yellow squares are culture positive samples, while grey squares are culture negative. Squares outlined in black are correct predictions, squares with no outline are incorrect predictions. We did not generate predictions for the culture samples outlined in blue, as they do not have available totRNA results. We also plot observed total RNA values (circle) and observed sgRNA values (diamond) when available, otherwise we plot predicted median sgRNA values generated by our best sgRNA model (triangle). Some individuals were sampled from multiple locations in the lower respiratory tract, in which case they are plotted as neighboring panels. All samples observed or predicted to fall below the limit of detection are plotted below 0 at set values for visual clarity (totRNA: 0, sgRNA: -1). When available, the limits of detection (LOD) or quantification (LOQ) for PCR assays are plotted as dotted lines in the assay-specific color. When both the LOD and LOQ were available, only the LOD is plotted. In instances where the total RNA and sgRNA assay LOD are equal, only the sgRNA line is visible. No instances exist in this dataset where the LOD or LOQ is only available for one RNA type.

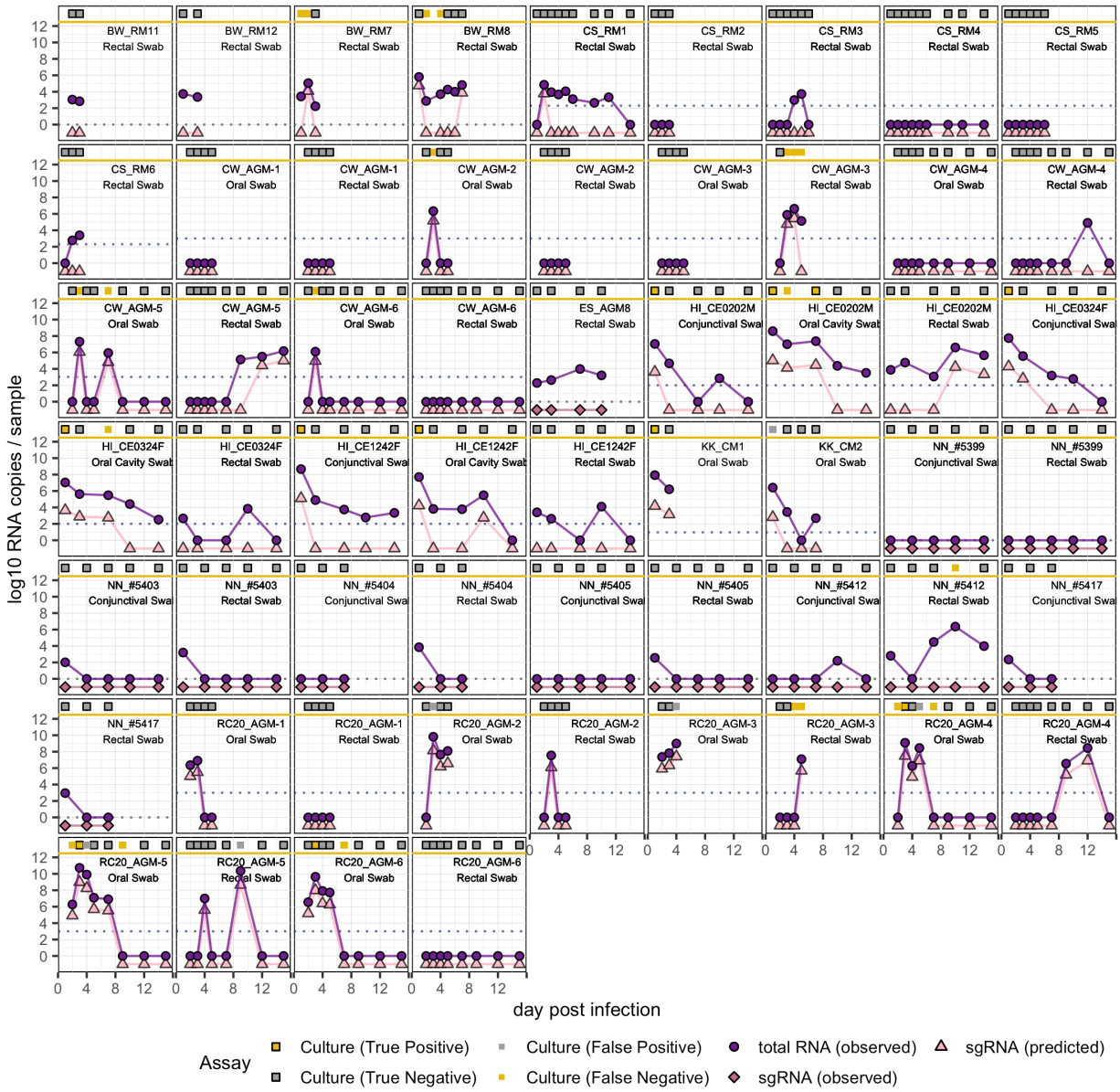

Figure S 1.9 | Individual culture trajectories in the gastrointestinal and other systems.
Each panel corresponds with one individual and one non-invasive sample type, indicated in the top right of each panel. Only individuals with culture results for at least two days post infection are plotted. Culture data are plotted as squares above the yellow line at 10 log10 copies. Yellow squares are culture positive samples, while grey squares are culture negative. Squares outlined in black are correct predictions, squares with no outline are incorrect predictions. We also plot observed total RNA values (circle) and observed sgRNA values (diamond) when available, otherwise we plot predicted median sgRNA values generated by our best sgRNA model (triangle). Some individuals were sampled from multiple locations, in which case they are plotted as

neighboring panels. All samples observed or predicted to fall below the limit of detection are plotted below 0 at set values for visual clarity (totRNA: 0, sgRNA: -1). When available, the limits of detection (LOD) or quantification (LOQ) for PCR assays are plotted as dotted lines in the assay-specific color. When both the LOD and LOQ were available, only the LOD is plotted. In instances where the total RNA and sgRNA assay LOD are equal, only the sgRNA line is visible. No instances exist in this dataset where the LOD or LOQ is only available for one RNA type. Individuals from one study cannot be included in this figure due to a data sharing agreement.

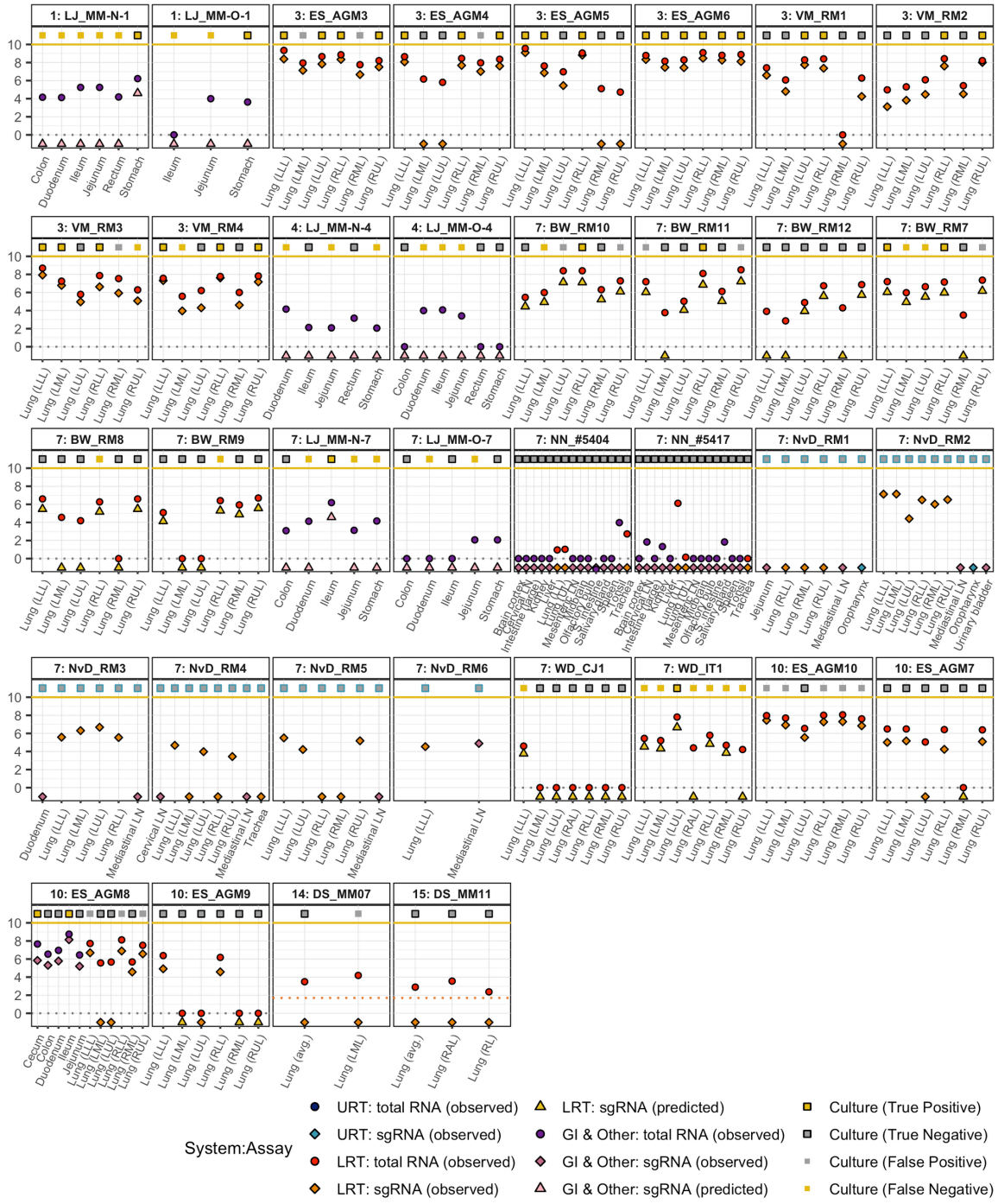

Figure S 1.10 | Individual culture data for invasive samples.
Each panel corresponds with one individual, indicated with text in the panel (day post infection: individual). Culture data are plotted as squares above the yellow line at 10 log10 copies. Yellow squares are culture positive samples, while grey squares are culture negative. Squares outlined in black are correct predictions, squares with no outline are incorrect predictions. We did not generate

predictions for the culture samples outlined in blue, as they do not have available totRNA results. We also plot the observed total RNA (circle) and observed sgRNA (diamond) values when available, otherwise we plot predicted median sgRNA values generated by our best sgRNA model (triangle). Color corresponds to the organ system from which the tissue was obtained (URT, upper respiratory tract; LRT, lower respiratory tract; GI & Other, gastrointestinal and other systems). All samples observed or predicted to fall below the limit of detection are plotted below 0 at set values for visual clarity (totRNA: 0, sgRNA: -1). When available, the limits of detection (LOD) or quantification (LOQ) for PCR assays are plotted as dotted lines in the assay-specific color. When both the LOD and LOQ were available, only the LOD is plotted. In instances where the total RNA and sgRNA assay LOD are equal, only the sgRNA line is visible. No instances exist in this dataset where the LOD or LOQ is only available for one RNA type.

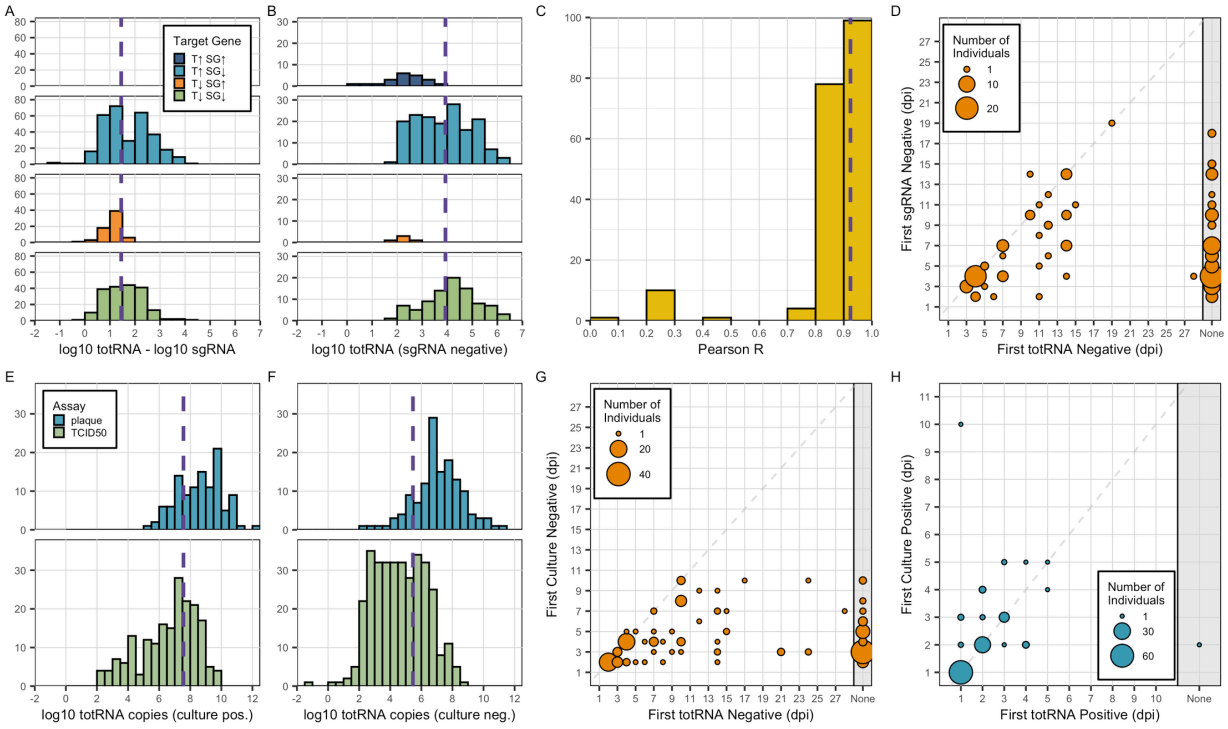

Figure S 1.11 | Statistics relating PCR and culture results.
(A) Difference between total RNA and sgRNA copy numbers when both are detectable, stratified by target gene predictor with the following acronyms: "T↑SG↑": totRNA-high/sgRNA-high; "T↓SG↑": totRNA-low/sgRNA-high; "T↑SG↓": totRNA-high/sgRNA-low; "T↓SG↓": totRNA-high/sgRNA-low. No totRNA-high/sgRNA-high data was available for this investigation. (B) Total RNA copy numbers for all sgRNA negative samples, stratified by target gene as in (A). (C) Pearson correlation coefficients between total RNA and sgRNA copy numbers when both are detectable, for all individual-sample trajectories with at least three sampling days where both were positive. (D) Comparison of the timing of the first negative results from total RNA and sgRNA assays for each available individual-sample trajectory (dpi: day post infection). (E) Total RNA copy numbers (when detectable) for all culture positive samples, stratified by culture assay type. (F) Total RNA copy numbers (when detectable) for all culture negative samples, stratified by culture assay type as in (E). (G) Comparison of the timing of the first negative results from total RNA and culture assays for each available individual-sample trajectory. (H) Comparison of the timing of the first positive results from total RNA and culture assays for each individual-sample trajectory. For panels (A), (B), (C), (E), and (F), the purple dashed line indicates the median for the full distribution (i.e., not stratified by assay or target gene). For panels (D), (G), and (H), the size of each circle indicates the number of individuals with the indicated observation. Individuals in the 'None' column were never negative (D, G) or positive (H) for total RNA. Individuals that were never sgRNA negative (D), culture negative (G), or culture positive (H) are not plotted.

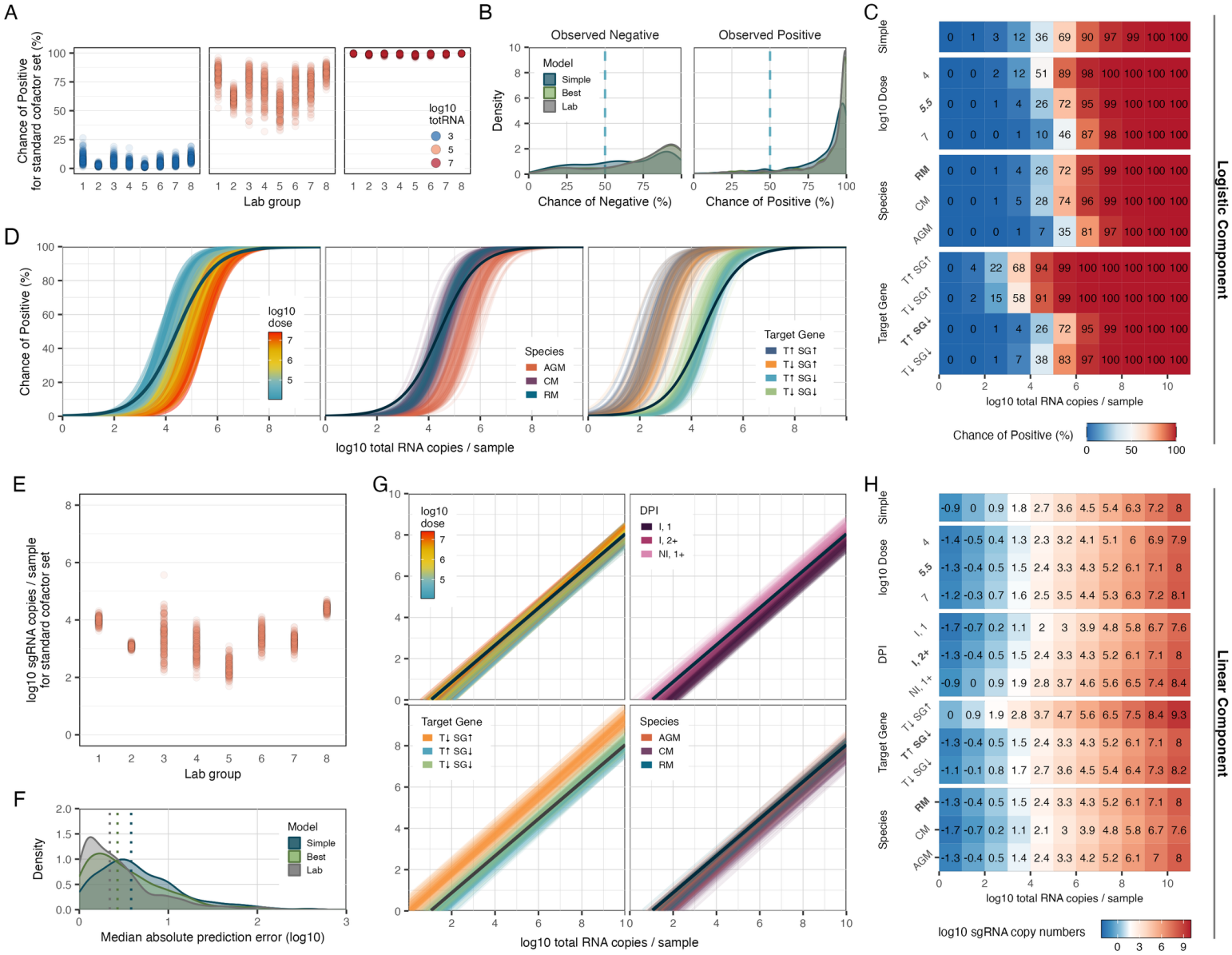
A
Chance of Positive for standard cofactor set (%)
Lab group
log10 totRNA
3
5
7
B
Observed Negative
Observed Positive
Model
Simple
Best
Lab
Density
Chance of Negative (%)
Chance of Positive (%)
C
Simple
log10 Dose
Species
Target Gene
log10 total RNA copies / sample
Chance of Positive (%)
Logistic Component
D
Chance of Positive (%)
log10 dose
Species
AGM
CM
RM
Target Gene
T↑ SG↑
T↓ SG↑
T↑ SG↓
T↓ SG↓
log10 total RNA copies / sample
E
log10 sgRNA copies / sample for standard cofactor set
Lab group
F
Density
Model
Simple
Best
Lab
Median absolute prediction error (log10)
G
log10 dose
DPI
I, 1
I, 2+
NI, 1+
Target Gene
Species
AGM
CM
RM
log10 total RNA copies / sample
H
Simple
log10 Dose
DPI
Target Gene
Species
log10 total RNA copies / sample
log10 sgRNA copy numbers
Linear Component

Figure S 1.12 | Results from the best sgRNA model with an additional predictor for lab group. (A) The predicted chances of sgRNA detection for three key totRNA quantities (3 log10, blue; 5 log10, salmon; 7 log10, red), across the eight available lab groups and for the standard cofactor set. The article(s) included in each group are provided in S8 Table. Each point is one out of 200 samples generated for each lab group, with transparency to show the density of points. (B) As in Fig 3B, with additional predictions from the model including a lab effect ('Lab', grey). (C and D) As in Figure 1.3C and 1.3D, except showing the results from the model including a lab effect. (E) The predicted quantities of sgRNA for a sample with 5 log10 totRNA copies, across the eight available lab groups and for the standard cofactor set. (F) As in Figure 1.3F, with additional predictions from the model including a lab effect ('Lab', grey). (G and H) As in Figure 1.3G and 1.3H, except showing the results from the model including a lab effect. In panels C, D, G and H, the predictions are not specific to a particular lab group (i.e., we set the lab effect term to zero to extract general patterns across all labs).

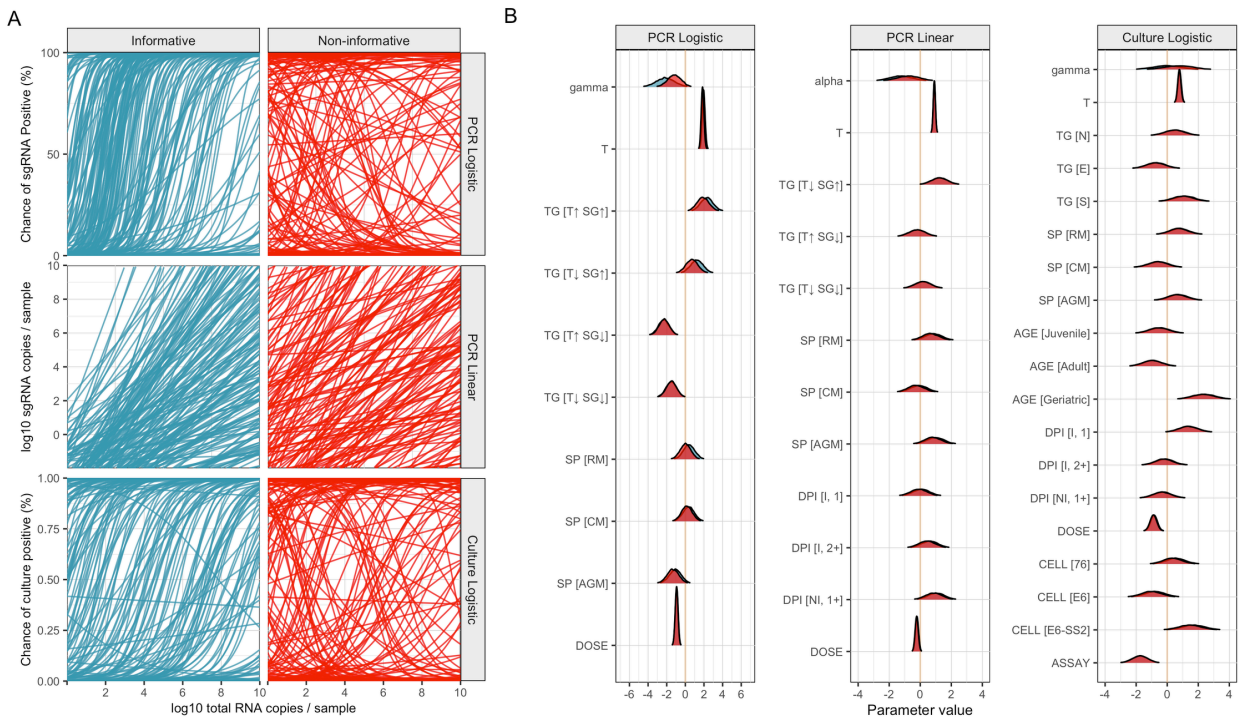

Figure S 1.13 | Sensitivity analyses comparing informative (blue) and non-informative (red) priors.

(A) Each line presents an expected model fit generated by sampling the indicated prior distributions. Informative priors are outlined in the Methods and Supplementary Methods. All parameters were given a $N(0,1)$ prior for all non-informative investigations. Informative priors much better represent *a priori* understanding of the relationships between total RNA copy numbers and both sgRNA and culture outcomes. (B) Each panel compares the final parameter estimates obtained for the corresponding best model using the different prior types (red: non-informative; blue: informative), where each row is a distinct parameter. Acronyms are as described in Figures 1.3, 1.4, and 1.5. Note that in many instances parameter estimates are almost perfectly overlapping, so only the non-informative (red) priors are visible.

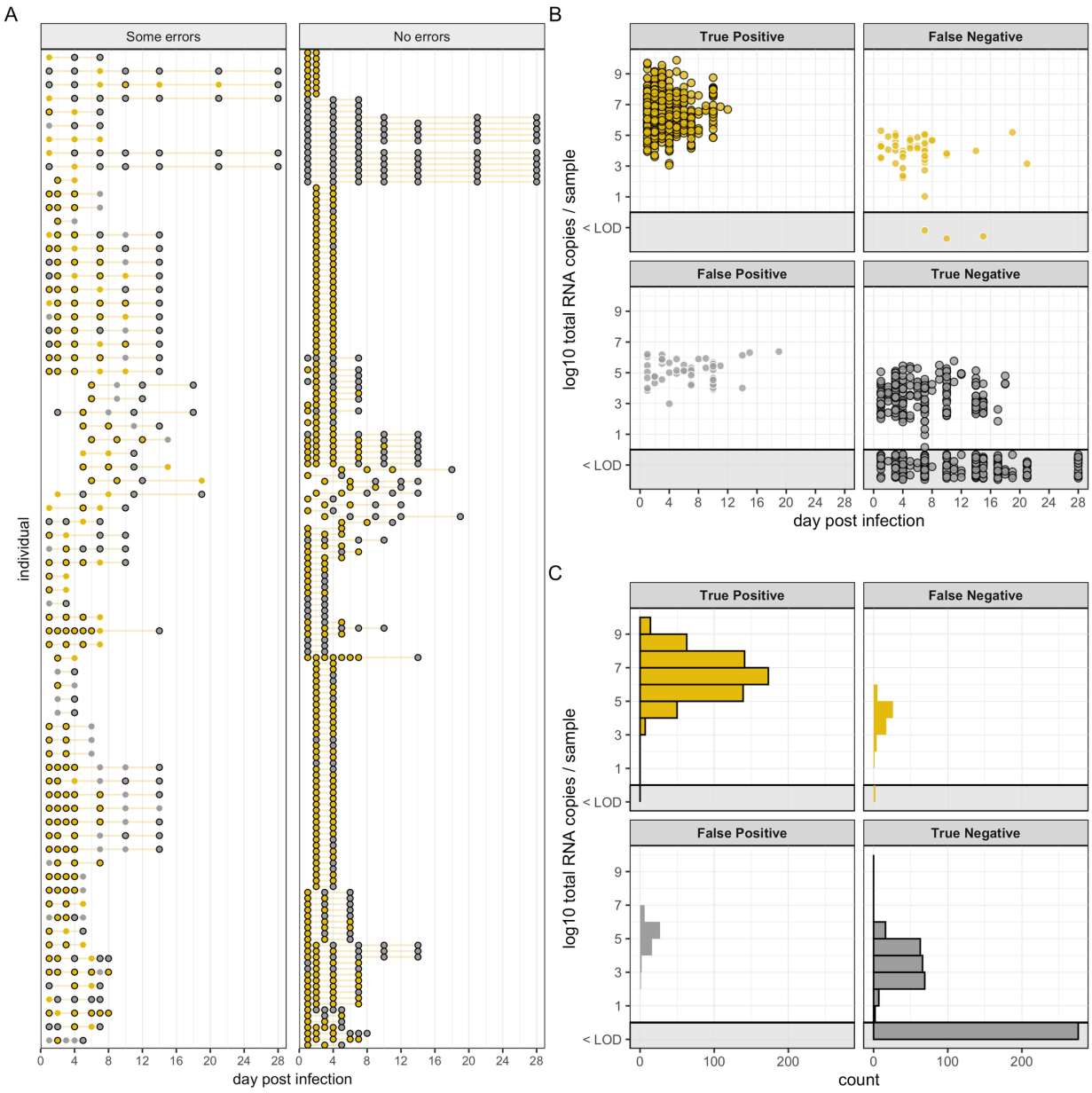

Figure S 1.14 | Error analysis for the best sgRNA model.
(A) Individual-specific sgRNA trajectories, where each row presents one individual. These are stratified by whether the model misclassifies any samples for that individual ("Some errors") or whether the model makes no misclassifications ("No errors"). In both (A) and (B), yellow circles indicate positive samples and grey indicates negative samples. Circles with a black outline correspond with correctly classified samples, while no outline indicates incorrectly classified samples. (B) Scatterplot of all samples with sgRNA results, stratified by the elements of a confusion matrix and colored as in (A). The x-axis tracks the day post infection and the y-axis plots log10 total RNA copy numbers. Samples in the grey shaded region along the bottom present all samples where total RNA was undetectable. (C) Histograms of all samples grouped by the elements of a confusion matrix, where log10 total RNA copy numbers per sample is plotted on the

y-axis. Bins located in the grey shaded region along the bottom (labelled "<LOD") include all totRNA-negative samples.

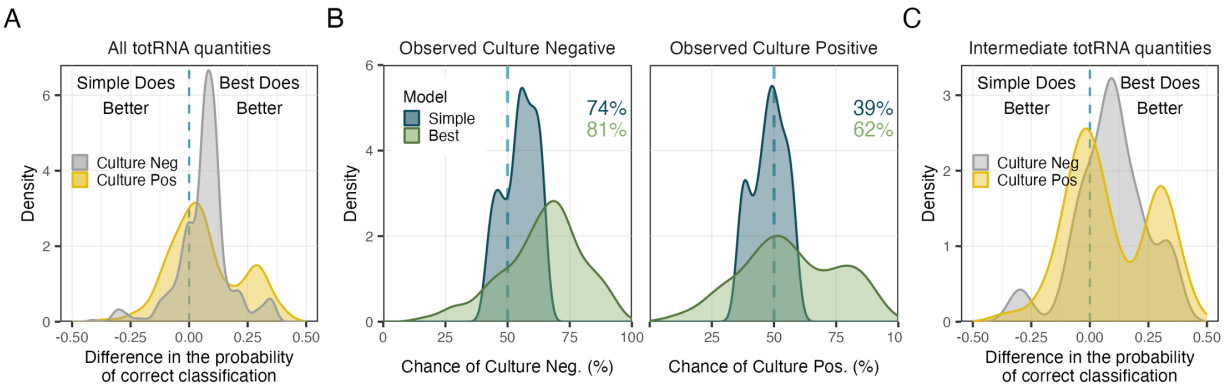

Figure S 1.15 | Additional performance comparisons between the simple and best culture models.
(A) Distribution of the differences between the predicted probabilities of both models for all totRNA-positive samples, stratified by whether the sample was culture positive (yellow) or negative (grey). Samples on the right side of the dashed blue line were predicted with higher confidence by the best model, while those on the left side were predicted with higher confidence by the simple model. (B) Distribution of median model-predicted chances of positive culture for intermediate totRNA-positive samples (6-8 log10 copies), stratified by model type and observed outcomes. Samples right of the dashed vertical line are correct predictions. The colored text gives the percent of samples that are correctly classified by each model. (C) As in panel A, except only for intermediate totRNA-positive samples (6-8 log10 copies).

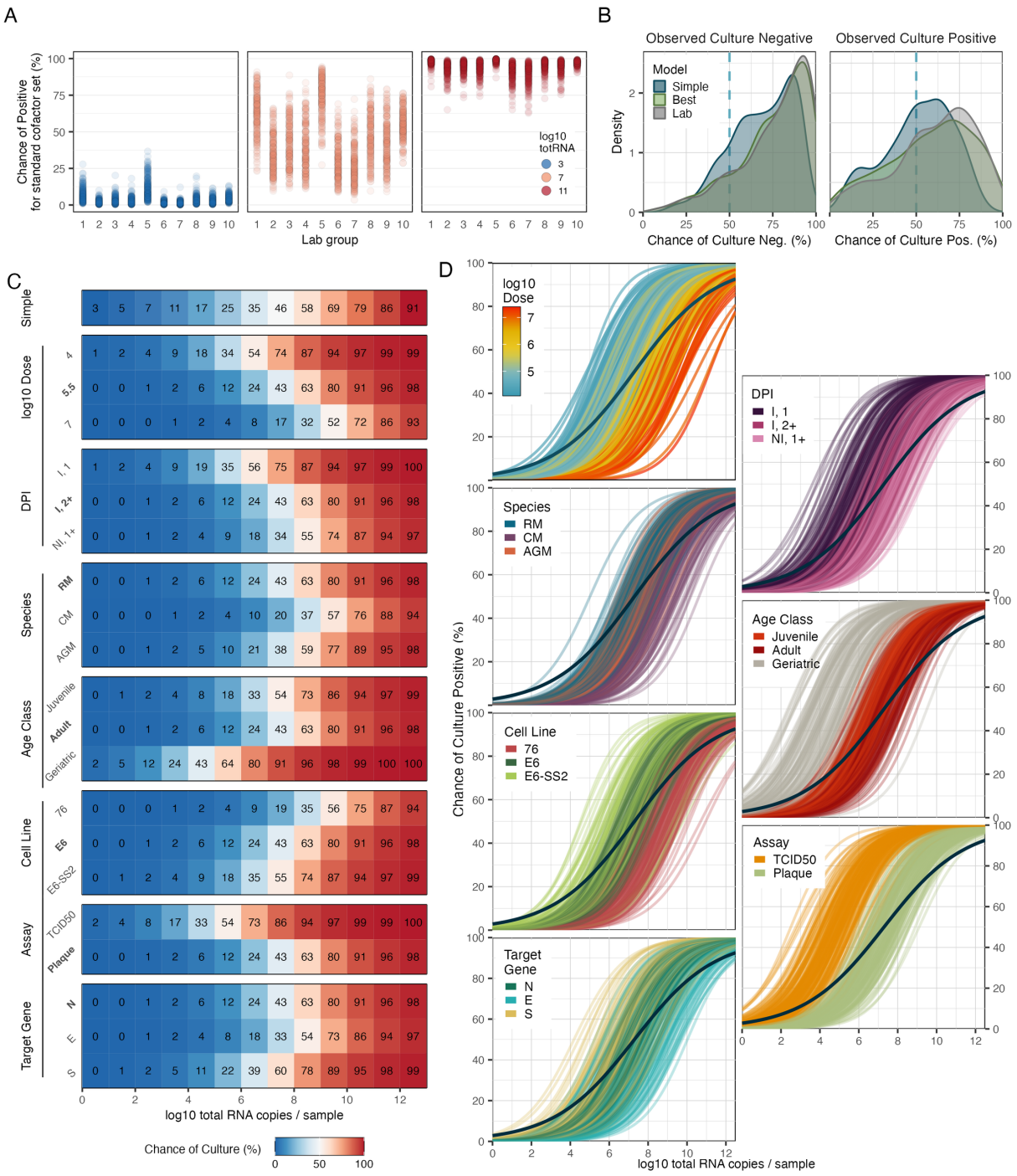

Figure S 1.16 | Results from the best culture model with an additional predictor for lab group. (A) The predicted chances of culture positivity for three key totRNA quantities (3 log10, blue; 7 log10, salmon; 11 log10, red), across the ten available lab groups and for the standard cofactor set. The article(s) included in each group are listed in Table S1.8. Each point is one out of 200 samples generated for each lab group, with transparency to show the density of points. (B) As in Figure

1.5B, with additional predictions from the model including a lab effect ('Lab', grey). (C and D) As in Figure 1.5C and 1.5D, except showing the results from the model including a lab effect. In panels C and D, the predictions are not specific to a particular lab group (i.e., we set the lab effect term to zero to extract general patterns across all labs).

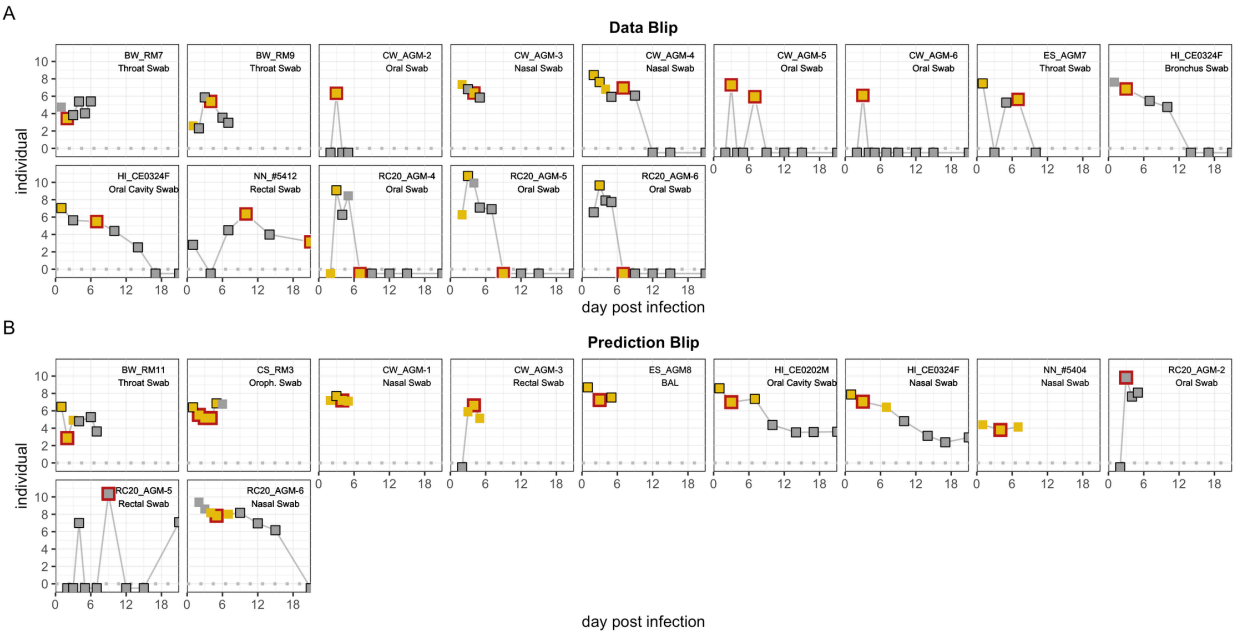

Figure S 1.17 | Viral load and culture trajectories for individuals with data blip (A) or prediction blip (B) error types.
Panel-specific errors are indicated with red outlines. All other samples with prediction errors have no outline. Correct predictions are outlined in black. Yellow squares indicate known culture positive samples, while grey squares indicate known culture negative samples. Text in the upper right corner of each panel indicates the ID name and sample type of the individual from whom the data was derived. All totRNA-negative samples are plotted below the grey dashed line at zero. Note that individual NN_#5412 has an additional (true negative) sample available on a later day post infection, which is not shown for visual clarity. Six trajectories from one study cannot be included in this figure due to a data sharing agreement.

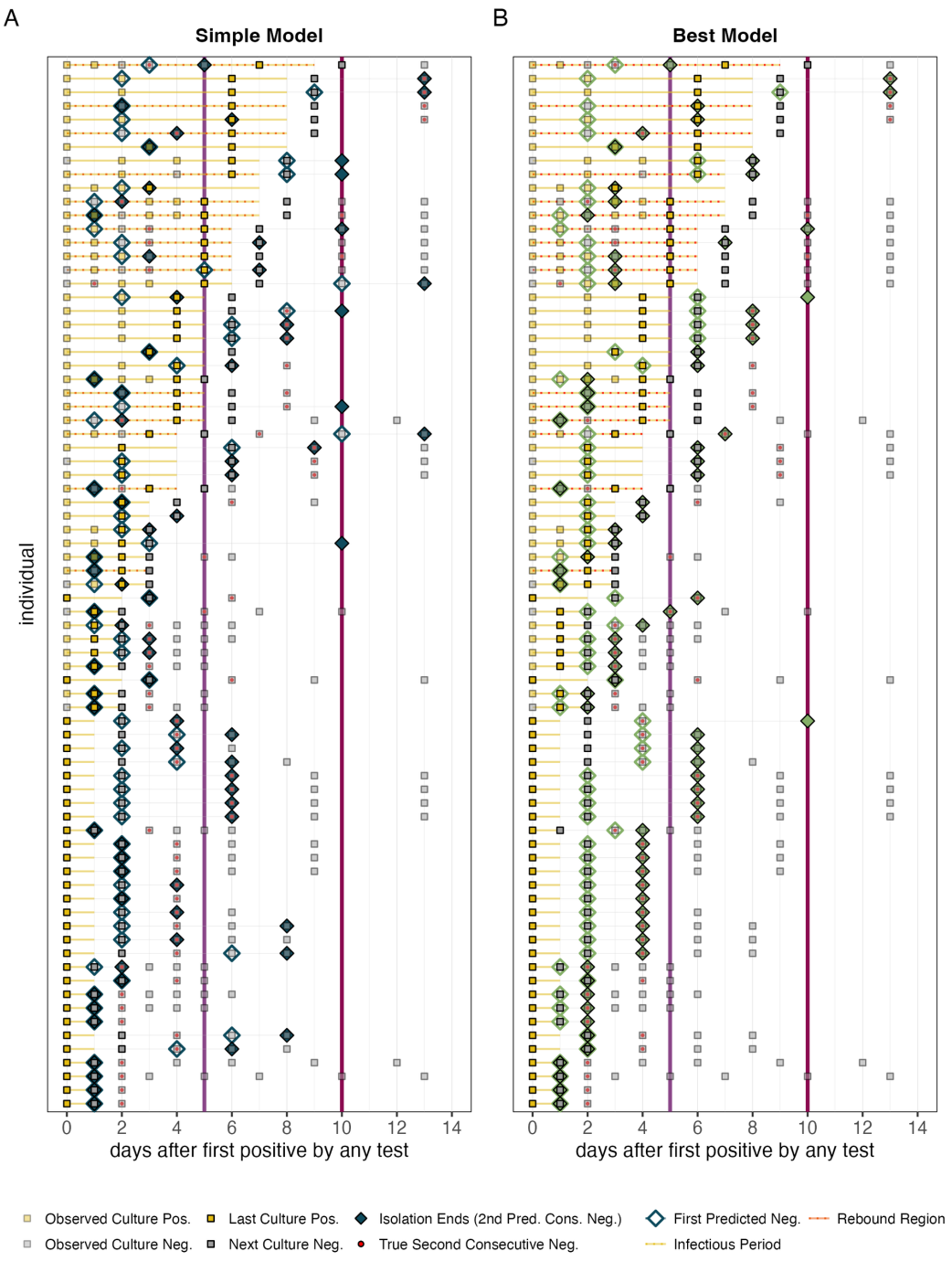

Figure S 1.18 | Isolation end times predicted by the simple (A) and best (B) culture models. Each row is a unique individual, and each panel displays all individuals included in the isolation analyses. The results of all samples after every individual's first positive test (PCR or culture) are displayed, where culture positive samples are yellow and negative samples are grey. Each individual's last culture positive and their subsequent culture negative times are plotted with more

intensity for better visualization. For each individual, their isolation end time is shown with colored, filled diamonds (i.e., the time of their second consecutive predicted culture negative test). When isolation end time could not be determined by the model (i.e., the model did not predict a second consecutive negative), we conservatively set that individual's end time to day 10. Each individual's first predicted negative is shown by an empty diamond, and the true (observed) time of their second consecutive negative is shown with a small red point. With yellow lines, we show the time range that we consider each individual to be infectious, based on the data, which ranges from their first total RNA positive day up to the midpoint between their first culture negative test after their last observed culture positive test. For individuals with no observed negative after their last positive, we conservatively assumed their next observed negative to be day 10. With dashed red lines, we also indicate which individuals show evidence of a rebound infection (i.e., the individuals with at least one culture negative occurring between two culture positives). Finally, we use colored vertical lines to display the days on which the five- and ten-day protocols would release individuals from isolation.

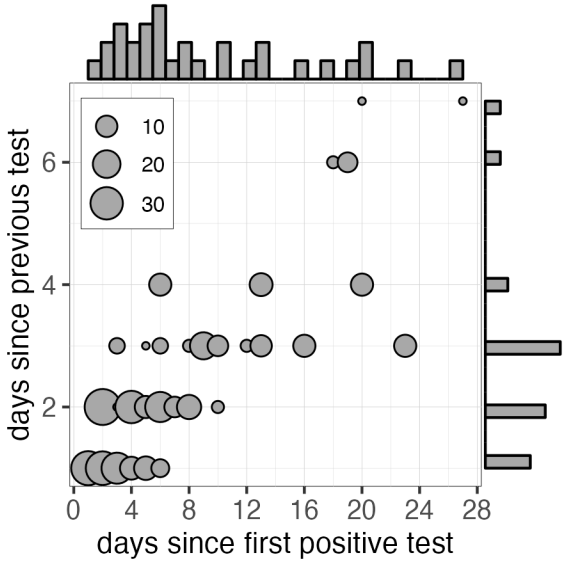

Figure S 1.19 | Days between consecutive tests relative to the number of days since the first positive test.
The size of the point shows the number of samples at the given coordinate. The marginal histograms show the distribution of points along each individual axis.

Supplementary Tables

Article (ref.)	N	Species	Sex	Age class	Exposure route	Exposure dose	Viral isolate	Sample type	Sample time	Sample location	PCR target gene		Culture cell line
											totRNA	*sgRNA*	
Baum et al. 2020	43 (4)	RM	F, M	U	IT, IN	6.02	USA/WA1/2020	NI	1, 2, 3	URT, Other	N	E (3)	--
	48 (6)	RM	F, M	A	IT, IN	5.04	USA/WA1/2020	NI	1, 2	URT, LRT	N	E (3)	--
Chandrashekar et al. 2020	12 (3)	RM	U	A	IT, IN	6.04	USA/WA1/2020	NI	1, 2	URT	N	E (3)	--
	12 (3)	RM	U	A	IT, IN	5.04	USA/WA1/2020	NI	1, 2	URT	N	E (3)	--
	12 (3)	RM	U	A	IT, IN	4.04	USA/WA1/2020	NI	1, 2	URT	N	E (3)	--
Corbett et al. 2020	50 (8)	RM	F, M	J, A	IT, IN	5.88	USA/WA1/2020	NI	1, 2	URT, LRT	N	E (3)	--
Cross et al. 2020	124 (6)	AGM	F	A	IN	6.45	ITA/INMI1/2020	NI	2, 3	URT, LRT, GI, Other	N	--	Vero E6
Dagotto et al. 2021	16 (4)	RM	U	A	IT, IN	4.04	USA/WA1/2020	NI	1, 2	LRT	N, E	E (3, 4)	--
Deng et al. 2020	7 (1)	RM	M	J	IT	5.85*	CHN/WH-09/2020	I	3	LRT	E	--	Vero E6†
	7 (1)	RM	M	J	OC	5.85*	CHN/WH-09/2020	I	3	LRT	E	--	Vero E6†
Gabitzsch et al. 2021	24 (2)	RM	F, M	J	IT, IN	5.85*	USA/WA1/2020	NI	1, 2	URT, LRT	N	E (3)	--
Ishigaki et al. 2021	144 (3)	CM	F, M	A	IT, IN, OR, OC	6.19*	JPN/WK-521/2020	NI	1, 2, 3	URT, LRT, GI, Other	N	--	Vero E6†
Jiao et al. 2021	16 (3)	RM	M	U	IN	7	CHN/U	I	3	GI	N	--	Vero E6†
	14 (3)	RM	M	U	IG	7	CHN/U	I	1, 2, 3	GI	N	--	Vero E6†
Johnston et al. 2020	60 (4)	RM	F, M	A	AE	4.46	USA/WA1/2020	NI	2, 3	URT, GI	N	--	Vero 76
	45 (3)	AGM	F, M	A	AE	4.58	USA/WA1/2020	NI	2, 3	URT, GI	N	--	Vero 76
	60 (4)	CM	F, M	J, A	AE	4.69	USA/WA1/2020	NI	2, 3	URT, GI	N	--	Vero 76
Jones et al. 2021	44 (4)	RM	F	A	IT, IN	5.04	USA/WA1/2020	I, NI	1, 2, 3	URT, LRT	N	E (3)	--
Kobiyama et al. 2021	26 (2)	CM	F	A	IT, IN, OR, OC	7.3	U/U	NI	1, 2	URT, LRT, Other	N	--	Vero E6-
Li et al. 2021	148 (16)	CM	F, M	J, A	IT, IN	5	USA/WA1/2020	NI	2	URT, LRT	E	E, N (4, 2)	--
Munster et al. 2020	53 (8)	RM	F, M	J, A	IT, IN, OR, OC	6.26*	USA/WA1/2020	I, NI	1, 2, 3	LRT, GI, Other	E	ORF7 (4)	Vero E6
Nagata et al. 2021	165 (6)	CM	F	A	IT, IN, OC	7.42*	JPN/WK-521/2020	I, NI	1, 2, 3	URT, LRT, GI, Other	N	N (1)	Vero E6-
Patel et al. 2021	65 (5)	RM	F, M	J	IT, IN	4.04	USA/WA1/2020	NI	1, 2	URT, LRT	N	E (3)	--
Salguero et al. 2021	63 (6)	RM	F, M	J	IT, IN	6.7	AUS/VIC01/2020	I, NI	1, 2, 3	URT, LRT, Other	N	E (3)	Vero E6
	58 (6)	CM	F, M	J	IT, IN	6.7	AUS/VIC01/2020	I, NI	1, 2, 3	URT, LRT, Other	N	E (3)	Vero E6
Shan et al. 2020	108 (6)	RM	F, M	A	IT	6.69*	CHN/WIV04/2019	NI	3	URT, GI	S	--	Vero E6†
Singh et al. 2020	108 (16)	RM	F, M	G, J	IT, IN, OC	6.02	USA/WA1/2020	I	3	LRT	N	E (3)	Vero E6
Speranza et al. 2020	194 (10)	AGM	F, M	A	IT, IN, OR, OC	6.26*	USA/WA1/2020	I, NI	1, 2, 3	URT, LRT, GI	E	E (4)	Vero E6
van Doremalen et al. 2020	72 (6)	RM	U	J	IT, IN, OR, OC	6.26*	USA/WA1/2020	I, NI	1, 2, 3	URT, LRT, GI, Other	--	E	Vero E6†
Williamson et al. 2020	135 (6)	RM	F, M	J	IT, IN, OR, OC	6.26*	USA/WA1/2020	I, NI	1, 2, 3	URT, LRT, GI	E	--	Vero E6†
Woolsey et al. 2020	132 (6)	AGM	F, M	A	IT, IN	5.66	ITA/INMI1/2020	NI	2, 3	URT, LRT, GI, Other	N	--	Vero E6
Yu et al. 2020	102 (10)	RM	U	A	IT, IN	4.04	U/U	NI	1, 2	URT, LRT	N	E (3)	--

Table S 1.1 | Summary of articles included in the dataset.
Multiple rows for an individual article are included when the study involved multiple species and/or multiple exposure doses. In all columns, U indicates the detail is unknown. Sample sizes (N) are presented in the following format: number of available datapoints (number of individuals). Species abbreviations are as follows: RM, rhesus macaque; CM, cynomolgus macaque; AGM, African green

monkey. Age class presents the standardized assignments according to our protocol (Supplementary Methods), and the abbreviations are: J, juvenile; A, adult; G, geriatric. Individuals inoculated via multiple routes are indicated by exposure routes joined by commas, where the abbreviations are: AE, aerosol; IT, intratracheal; IN, intranasal; IG, intragastric; OC, ocular; OR, oral. Exposure dose is presented as log10 plaque forming units, and an adjoining * indicates the dose was originally reported as TCID50, so those values were converted using the standard method described in the Supplementary Methods. NI indicates non-invasive sample types (i.e., swabs, biofluids, BAL), while I indicates invasive tissue samples obtained at necropsy. Sample location distinguishes between the following systems: URT, upper respiratory tract; LRT, lower respiratory tract; GI, gastrointestinal tract; and Other, all other locations. Sample time presents the days post infection with available samples according to our DPI predictor, where 1: 1 dpi, inoculated tissues, 2: 2+ dpi, inoculated tissues, 3: any dpi, non-inoculated tissue (further categorization information is in Table S1.9). PCR target genes are stratified by total RNA (totRNA) and sgRNA. The level of the target gene predictor for the sgRNA model follows the sgRNA gene in parentheses: (1) totRNA-high/sgRNA-high, (2) totRNA-low/sgRNA-high, (3) totRNA-high/sgRNA-low, and (4) totRNA-low/sgRNA-low. The cell lines used for culture are indicated when available, with SS2 as an abbreviation for TMPRSS2. An adjoining † indicates the use of a TCID50 assay, while no symbol indicates a plaque assay.

Model	Predictors	*Cross-validation*		*PSIS-LOO Approximation*		*Prediction*		
		ELPD Difference (SE)	**ELPD (SE)**	**ELPD Difference (SE)**	**ELPD (SE)**	**MCC**	**% correctly predicted**	
							train	**test**
l1		**-73.31 (10.63)**	**-311.56 (17.36)**	**-71.13 (10.76)**	**-311.33 (17.29)**	**0.75**	**87.75**	**87.69**
l2.1	DOSE	-60.78 (10.02)	-299.03 (19.7)	-58.16 (10.15)	-298.36 (19.46)	0.78	89.35	89.28
l2.2	ST	-58.37 (9.44)	-296.62 (18.51)	-56.4 (9.65)	-296.6 (18.45)	0.79	89.31	89.45
l2.3	SP	-45.45 (9.79)	-283.71 (17.24)	-43.66 (9.94)	-283.86 (17.26)	0.79	89.93	89.78
l2.4	AGE	-71.06 (10.53)	-309.31 (17.43)	-69.38 (10.65)	-309.58 (17.39)	0.76	88.63	88.27
l2.5	SEX	-72.66 (10.58)	-310.91 (17.57)	-73.37 (10.75)	-313.57 (17.64)	0.75	87.89	87.52
l2.6	DPI	-67.27 (10.05)	-305.52 (18.06)	-64.8 (10.2)	-305 (17.98)	0.76	88.28	88.19
l2.7	TG	-40.19 (9.13)	-278.44 (16.42)	-37.97 (9.2)	-278.17 (16.39)	0.79	89.61	89.61
l3.1	TG + DOSE	-10.98 (4.22)	-249.23 (17.36)	-8.53 (4.25)	-248.73 (17.25)	0.81	91.02	90.79
l3.2	TG + ST	-32.17 (7.81)	-270.42 (17.23)	-30.17 (7.96)	-270.37 (17.15)	0.8	90.27	89.95
l3.3	TG + SP	-24.62 (7.97)	-262.87 (16.06)	-22.69 (8.03)	-262.89 (16.07)	0.79	89.86	89.7
l3.4	TG + AGE	-33.67 (8.07)	-271.92 (16.34)	-32.3 (8.09)	-272.5 (16.33)	0.78	89.61	89.2
l3.5	TG + SEX	-43.33 (9.22)	-281.58 (16.7)	-43.32 (9.48)	-283.52 (16.88)	0.78	89.87	88.86
l3.6	TG + DPI	-37.05 (8.46)	-275.3 (16.91)	-34.24 (8.52)	-274.44 (16.84)	0.79	89.86	89.7
l4.1	TG + DOSE + ST	-9.37 (3.78)	-247.62 (17.99)	-7.31 (3.84)	-247.51 (17.84)	0.82	91.4	90.95
l4.2	**TG + DOSE + SP**	**-5.98 (3.58)**	**-244.23 (17.2)**	**-4.19 (3.61)**	**-244.39 (17.16)**	**0.82**	**91.41**	**91.12**
l4.3	TG + DOSE + AGE	-10.94 (3.87)	-249.19 (17.45)	-9.11 (3.9)	-249.31 (17.38)	0.81	91.1	90.79
l4.4	TG + DOSE + SEX	-12.48 (4.26)	-250.73 (17.42)	-10.3 (4.24)	-250.5 (17.35)	0.81	90.91	90.7
l4.5	TG + DOSE + DPI	-12.29 (4.2)	-250.54 (17.7)	-9.73 (4.21)	-249.93 (17.58)	0.82	91.09	91.04
l5.1	TG + DOSE + SP + ST	-4.58 (3)	-242.83 (17.74)	-3.05 (3.08)	-243.25 (17.64)	0.82	91.3	91.12
l5.2	TG + DOSE + SP + AGE	-1.52 (2.02)	-239.77 (17.25)	-1.15 (1.95)	-241.35 (17.28)	0.83	91.62	91.46
l5.3	TG + DOSE + SP + SEX	-7.43 (3.62)	-245.68 (17.28)	-5.92 (3.62)	-246.12 (17.24)	0.82	91.36	91.21
l5.4	TG + DOSE + SP + DPI	-6.66 (3.42)	-244.91 (17.51)	-4.74 (3.42)	-244.94 (17.41)	0.82	91.14	91.12
l6.1	TG + DOSE + SP + AGE + ST	0 (0)	-238.25 (17.79)	0 (0)	-240.2 (17.78)	0.83	91.69	91.46
l6.2	TG + DOSE + SP + AGE + SEX	-2.89 (2.02)	-241.14 (17.31)	-2.32 (1.94)	-242.52 (17.36)	0.83	91.69	91.46
l6.3	TG + DOSE + SP + AGE + DPI	-1.51 (1.88)	-239.76 (17.61)	-1.86 (1.83)	-242.05 (17.71)	0.82	91.35	91.04
l7.1	TG + DOSE + SP + AGE + ST + SEX	-1.41 (0.56)	-239.66 (17.87)	-1.28 (0.41)	-241.48 (17.85)	0.83	91.71	91.46
l7.2	TG + DOSE + SP + AGE + ST + DPI	-1.23 (0.99)	-239.48 (17.96)	-1.7 (1)	-241.9 (17.98)	0.82	91.62	91.21
l8.1	**TG + DOSE + SP + AGE + ST + DPI + SEX**	**-2.77 (1.25)**	**-241.02 (18.06)**	**-2.87 (1.13)**	**-243.07 (18.07)**	**0.82**	**91.68**	**91.12**

Table S 1.2 | Extended sgRNA logistic model performance comparisons.
Models are ordered by increasing number of predictors, with the simplest (l1), best (l4.2), and full (l8.1) models noted in bold. We report expected log pointwise predictive density (ELPD) generated by 10-fold cross validation (cross-validation columns), where larger ELPD indicates better performance. ELPD difference indicates the difference between ELPDs of the given model and the model with the largest ELPD (in this case model l6.1, though this is not our 'best model'). The PSIS-LOO approximation columns present statistics generated by running Pareto-Smoothed Importance Sampling approximate leave-one-out cross validation, including ELPD and ELPD difference as above. The prediction columns indicate the percent of samples (stratified by training and test sets) for which posterior predictions generated by 10-fold cross validation correctly classified them as below or above the limit of detection (i.e., where the per-sample posterior predictive distributions exhibited at least a probability of 0.5 for the true, observed classification). MCC is the Matthews correlation coefficient. Note that all models included total RNA as a predictor, even though it is not specified in the predictor column. Standard error (SE) is shown in parentheses following all relevant statistics.

Model	Predictors	*Cross-validation*		*PSIS-LOO Approximation*		*Prediction*					
		ELPD Difference (SE)	**ELPD (SE)**	**ELPD Difference (SE)**	**ELPD (SE)**	**MAE (scaled)**		**% within 50% PI**		**%within 95% PI**	
						train	**test**	**train**	**test**	**train**	**test**
f1		**-186.24 (17.05)**	**-1017.32 (29.41)**	**-196.49 (21.07)**	**-1017.12 (29.35)**	**0.58 (0.7)**	**0.58 (0.7)**	**47.5**	**48**	**94.9**	**94.8**
f2.1	DOSE	-114.04 (11.7)	-945.12 (32.24)	-111.91 (15.27)	-932.54 (30.49)	0.6 (0.65)	0.6 (0.65)	46.9	46.6	95.9	95.6
f2.2	ST	-98.38 (10.49)	-929.46 (32.38)	-95.87 (13.7)	-916.5 (30.74)	0.56 (0.63)	0.56 (0.63)	49.9	50.3	96.5	96
f2.3	SP	-109.47 (11.8)	-940.55 (32.74)	-106.94 (15.43)	-927.56 (31.08)	0.56 (0.61)	0.57 (0.62)	50.7	49.4	96.2	95.8
f2.4	AGE	-107.02 (12.6)	-938.1 (32.65)	-104.67 (16.34)	-925.29 (30.91)	0.57 (0.62)	0.57 (0.64)	50.7	49.6	96.9	96.5
f2.5	SEX	-120.9 (12.58)	-951.98 (32.98)	-129.78 (17.11)	-950.41 (32.6)	0.56 (0.62)	0.58 (0.64)	50.6	48.5	96.2	95.8
f2.6	DPI	-82.23 (9.7)	-913.31 (31.99)	-79.37 (12.66)	-900 (30.31)	0.56 (0.65)	0.55 (0.64)	47.9	47.5	96.1	96
f2.7	TG	-94.6 (11.02)	-925.68 (33.96)	-93.29 (14.53)	-913.91 (32.33)	0.55 (0.61)	0.57 (0.63)	50.7	50.4	97.8	97.7
f3.1	DPI + DOSE	-83.66 (9.65)	-914.74 (32.05)	-81.44 (12.63)	-902.06 (30.39)	0.56 (0.65)	0.56 (0.65)	48	48.5	96.4	96
f3.2	DPI + ST	-82.78 (9.59)	-913.86 (32.07)	-80.27 (12.56)	-900.9 (30.46)	0.55 (0.65)	0.55 (0.65)	47.6	47.8	96.1	96
f3.3	DPI + SP	-78.12 (9.53)	-909.2 (32.18)	-76.32 (12.54)	-896.95 (30.58)	0.55 (0.65)	0.55 (0.65)	48.1	48.5	96	95.8
f3.4	DPI + AGE	-74.78 (10.35)	-905.86 (32.11)	-72.99 (13.5)	-893.62 (30.54)	0.54 (0.64)	0.54 (0.65)	49.6	48.9	96.3	96.2
f3.5	DPI + SEX	-87.71 (10.23)	-918.79 (32.22)	-91.38 (13.37)	-912 (30.95)	0.54 (0.64)	0.57 (0.67)	48.9	46.6	95.9	95.5
f3.6	DPI + TG	-48.36 (8.3)	-879.44 (34.01)	-46.14 (10.88)	-866.77 (32.38)	0.51 (0.61)	0.52 (0.6)	50.8	51	97.7	97.7
f4.1	DPI + TG + DOSE	-40.6 (8.79)	-871.68 (35.31)	-38.35 (11.32)	-858.98 (33.91)	0.49 (0.54)	0.49 (0.53)	52.1	52.2	96.6	96.7
f4.2	DPI + TG + ST	-44.28 (7.39)	-875.36 (34.38)	-42.03 (9.66)	-862.65 (32.86)	0.51 (0.6)	0.51 (0.59)	51.3	51.7	97.7	97.6
f4.3	DPI + TG + SP	-2.82 (3.66)	-833.9 (34.41)	-1.33 (4.81)	-821.95 (33.02)	0.46 (0.57)	0.47 (0.57)	53.1	52.7	96.5	97
f4.4	DPI + TG + AGE	-36.03 (7.45)	-867.11 (33.05)	-34.98 (9.47)	-855.6 (31.27)	0.48 (0.56)	0.49 (0.59)	53.8	52.9	97	96.7
f4.5	DPI + TG + SEX	-52.59 (8.54)	-883.67 (34.03)	-53.68 (11.25)	-874.3 (32.66)	0.5 (0.6)	0.52 (0.61)	51.6	50.8	97.6	97.4
f5.1	**DPI + TG + SP + DOSE**	**0 (0)**	**-831.08 (34.5)**	**0 (0)**	**-820.63 (33.24)**	**0.43 (0.53)**	**0.44 (0.54)**	**56**	**55**	**97**	**96.9**
f5.2	DPI + TG + SP + ST	-3.41 (3.65)	-834.49 (34.35)	-1.83 (4.82)	-822.45 (32.99)	0.46 (0.57)	0.48 (0.58)	52.8	52.7	96.4	96.7
f5.3	DPI + TG + SP + AGE	-4.88 (3.34)	-835.96 (34.24)	-4.13 (4.51)	-824.76 (32.79)	0.46 (0.57)	0.48 (0.58)	53.5	53.1	96.6	96.7
f5.4	DPI + TG + SP + SEX	-4.64 (3.6)	-835.72 (34.36)	-7.22 (4.65)	-827.85 (33.13)	0.45 (0.57)	0.48 (0.59)	53.4	52.4	96.5	96
f6.1	DPI + TG + SP + DOSE + ST	-1.11 (0.32)	-832.19 (34.53)	-0.68 (0.31)	-821.3 (33.14)	0.43 (0.53)	0.44 (0.54)	56	54.5	97	96.7
f6.2	DPI + TG + SP + DOSE + AGE	-1.51 (1.17)	-832.59 (34.4)	-1.01 (1.9)	-821.64 (32.86)	0.43 (0.53)	0.43 (0.53)	56.5	55.3	97	96.7
f6.3	DPI + TG + SP + DOSE + SEX	-1.5 (0.69)	-832.58 (34.48)	-5.76 (0.85)	-826.39 (33.37)	0.43 (0.53)	0.44 (0.54)	56.6	54.5	96.9	96.7
f7.1	DPI + TG + SP + DOSE + ST + AGE	-2.64 (1.22)	-833.72 (34.4)	-2.56 (1.85)	-823.19 (33.01)	0.43 (0.52)	0.43 (0.53)	56.4	55.1	97	96.7
f7.2	DPI + TG + SP + DOSE + ST + SEX	-2.72 (0.76)	-833.8 (34.54)	-6.76 (0.88)	-827.39 (33.4)	0.43 (0.53)	0.44 (0.54)	56.4	54.1	96.9	96.9
f8.1	**DPI + TG + SP + DOSE + ST + AGE + SEX**	**-4.44 (2.39)**	**-835.52 (34.2)**	**-9.76 (4.12)**	**-830.38 (33.19)**	**0.43 (0.53)**	**0.45 (0.56)**	**57.2**	**54.5**	**96.9**	**96.7**

Table S 1.3 | Extended sgRNA linear model performance comparisons.

Models are ordered by increasing number of predictors, with the simplest (f1), best (f5.1), and full (f8.1) models noted in bold. We report expected log pointwise predictive density (ELPD) generated by 10-fold cross validation (cross-validation columns), where larger ELPD indicates better performance. The top logistic model was run in tandem with all tested linear components, so the ELPD reported here reflects the sum of the ELPD for the top logistic and the considered linear components. ELPD difference indicates the difference between ELPDs of the given model and the model with the largest ELPD (in this case model l5.1, the 'best model'). The PSIS-LOO approximation columns present statistics generated by running Pareto-Smoothed Importance Sampling approximate leave-one-out cross validation, including ELPD and ELPD difference. Standard error (SE) is shown in parentheses following all relevant statistics. We also used multiple metrics to assess model predictions, which are all stratified by performance on training versus test data sets and were generated by 10-fold cross validation. MAE is the median difference between the observed value and the posterior predictive median (i.e., median absolute error around the median) for all samples with sgRNA above the LOD, and this metric was also scaled by one standard deviation (Scaled). '% within 50% PI' and '% within 95% PI' columns indicate the percent of sgRNA positive samples where the true, observed value fell within the sample-specific 50% and 95% prediction intervals, respectively. Note that all models included total RNA as a predictor, even though it is not specified in the predictor column.

Model	Predictors	*Cross-validation*		*PSIS-LOO Approximation*		*Prediction*		
		ELPD Difference (SE)	**ELPD (SE)**	**ELPD Difference (SE)**	**ELPD (SE)**	**MCC**	**% correctly predicted**	
							train	**test**
c1	**T**	**-57.32 (14.47)**	**-434.28 (12.5)**	**-44.26 (8.66)**	**-434.2 (12.56)**	**0.48**	**81.9**	**81.7**
c2.1	T + CELL	-56.61 (14.45)	-433.58 (12.83)	-42.96 (8.91)	-432.9 (12.88)	0.51	82.6	82.5
c2.2	T + ASSAY	-45 (12.78)	-421.96 (12.88)	-32.05 (7.62)	-421.99 (12.95)	0.53	83.3	83.1
c2.3	T + DOSE	-58.54 (14.58)	-435.5 (12.63)	-45.22 (8.68)	-435.16 (12.65)	0.48	81.8	81.7
c2.4	T + ST	-56.44 (13.99)	-433.41 (12.34)	-42.62 (8.53)	-432.56 (12.38)	0.45	81	80.5
c2.5	T + SP	-50.39 (13.4)	-427.35 (12.63)	-37.65 (8.02)	-427.59 (12.69)	0.47	81.2	81
c2.6	T + AGE	-43.81 (12.94)	-420.77 (13.36)	-44.83 (8.31)	-434.77 (14.43)	0.48	81.5	81.6
c2.7	T + SEX	-53.21 (13.65)	-430.17 (12.63)	-39.79 (8.2)	-429.73 (12.69)	0.48	81.6	81.7
c2.8	T + DPI	-38.17 (12.08)	-415.14 (13.29)	-25.16 (6.99)	-415.1 (13.32)	0.49	82.3	82.1
c2.9	T + TG	-54.07 (14.1)	-431.03 (13.27)	-41.53 (8.26)	-431.47 (13.32)	0.52	83	82.9
c3.1	T + DPI + CELL	-39.93 (11.97)	-416.89 (13.43)	-26.62 (6.94)	-416.56 (13.48)	0.49	82.3	81.9
c3.2	T + DPI + ASSAY	-34.81 (11.29)	-411.77 (13.46)	-21.83 (6.45)	-411.77 (13.5)	0.53	83.2	83.3
c3.3	T + DPI + DOSE	-39.4 (12.33)	-416.36 (13.58)	-26.1 (6.98)	-416.04 (13.58)	0.49	82.1	82
c3.4	T + DPI + ST	-36.89 (11.47)	-413.85 (13.25)	-23.7 (6.75)	-413.65 (13.3)	0.48	82	81.7
c3.5	T + DPI + SP	-30.04 (10.37)	-407 (13.34)	-17.39 (5.84)	-407.33 (13.41)	0.52	82.9	82.7
c3.6	T + DPI + AGE	-26.08 (9.99)	-403.04 (13.99)	-26.6 (6.39)	-416.54 (15.01)	0.5	82.2	82.3
c3.7	T + DPI + SEX	-33.16 (10.83)	-410.12 (13.38)	-19.74 (6.24)	-409.68 (13.4)	0.5	82.3	82.1
c3.8	T + DPI + TG	-37.17 (11.6)	-414.13 (13.88)	-24.37 (6.52)	-414.32 (13.93)	0.51	82.9	82.8
c4.1	T + DPI + AGE + CELL	-27.26 (9.94)	-404.22 (14.09)	-28.6 (6.74)	-418.54 (15.27)	0.5	82.4	82.2
c4.2	T + DPI + AGE + ASSAY	-20.97 (8.63)	-397.93 (14.24)	-23.2 (5.8)	-413.14 (15.44)	0.54	84.1	83.7
c4.3	T + DPI + AGE + DOSE	-27.09 (10.2)	-404.05 (14.18)	-27.87 (6.44)	-417.81 (15.24)	0.5	82.4	82.4
c4.4	T + DPI + AGE + ST	-27.07 (10.02)	-404.03 (14.04)	-27.71 (6.41)	-417.65 (15.07)	0.5	82.2	82.3
c4.5	T + DPI + AGE + SP	-20.32 (8.28)	-397.28 (14.21)	-19.06 (5.05)	-409 (15.05)	0.5	82.9	82.3
c4.6	T + DPI + AGE + SEX	-23.74 (9.1)	-400.7 (14.11)	-21.94 (5.56)	-411.88 (14.92)	0.5	82.9	82.3
c4.7	T + DPI + AGE + TG	-19.42 (7.68)	-396.38 (14.66)	-29.38 (6.66)	-419.32 (16.85)	0.54	83.9	83.8
c5.1	T + DPI + AGE + TG + CELL	-20.13 (7.58)	-397.09 (14.63)	-32.11 (7.53)	-422.05 (17.21)	0.54	84.3	83.6
c5.2	T + DPI + AGE + TG + ASSAY	-17.58 (7.13)	-394.54 (14.82)	-24.06 (5.78)	-414 (16.55)	0.56	84.5	84.5
c5.3	T + DPI + AGE + TG + DOSE	-20.39 (7.9)	-397.35 (14.85)	-30.78 (6.8)	-420.73 (17.13)	0.55	83.9	84
c5.4	T + DPI + AGE + TG + ST	-20.11 (7.52)	-397.07 (14.77)	-28.8 (6.36)	-418.74 (16.79)	0.54	83.9	83.7
c5.5	T + DPI + AGE + TG + SP	-18.93 (7.2)	-395.89 (14.71)	-25.99 (5.7)	-415.93 (16.5)	0.56	84	84.2
c5.6	T + DPI + AGE + TG + SEX	-18.29 (6.87)	-395.25 (14.79)	-25.23 (5.62)	-415.17 (16.56)	0.55	84.1	84.1
c6.1	T + DPI + AGE + TG + ASSAY + CELL	-19.07 (7.23)	-396.03 (14.83)	-27.82 (6.48)	-417.76 (16.89)	0.55	84.8	84.1
c6.2	T + DPI + AGE + TG + ASSAY + DOSE	-16.79 (7.13)	-393.75 (15.15)	-23.08 (5.5)	-413.02 (16.85)	0.54	84.3	83.8
c6.3	T + DPI + AGE + TG + ASSAY + ST	-18.54 (7.11)	-395.5 (14.9)	-24.69 (5.76)	-414.63 (16.6)	0.56	84.6	84.2
c6.4	T + DPI + AGE + TG + ASSAY + SP	-7.88 (5.11)	-384.84 (14.74)	-5.17 (2.87)	-395.11 (15.4)	0.57	84.9	84.6

c6.5	T + DPI + AGE + TG + ASSAY + SEX	-16.07 (6.08)	-393.03 (14.93)	-19.51 (4.6)	-409.45 (16.28)	0.55	84.4	84.1
c7.1	T + DPI + AGE + TG + ASSAY + SP + CELL	-9.5 (5.15)	-386.46 (14.69)	-8.23 (3.39)	-398.18 (15.49)	0.56	85	84.3
c7.2	T + DPI + AGE + TG + ASSAY + SP + DOSE	-5.18 (4.83)	-382.14 (15.06)	-2.2 (1.65)	-392.14 (15.68)	0.58	85.1	85
c7.3	T + DPI + AGE + TG + ASSAY + SP + ST	-8.26 (5.12)	-385.22 (14.85)	-4.88 (2.83)	-394.82 (15.43)	0.56	84.9	84.3
c7.4	T + DPI + AGE + TG + ASSAY + SP + SEX	-5.72 (3.81)	-382.68 (14.86)	-0.93 (1.58)	-390.87 (15.35)	0.57	85.3	84.7
c8.1	**T + DPI + AGE + TG + ASSAY + SP + DOSE + CELL**	**-1.62 (3.25)**	**-378.59 (15.12)**	**-4.38 (4.11)**	**-394.32 (16.45)**	**0.57**	**85.4**	**84.7**
c8.2	T + DPI + AGE + TG + ASSAY + SP + DOSE + ST	-5.77 (4.88)	-382.73 (15.14)	-1.98 (1.62)	-391.93 (15.74)	0.58	85.2	85
c8.3	T + DPI + AGE + TG + ASSAY + SP + DOSE + SEX	-4.57 (4.14)	-381.54 (15.14)	0 (0)	-389.94 (15.63)	0.57	85.1	84.8
c9.1	T + DPI + AGE + TG + ASSAY + SP + DOSE + CELL + ST	-2.33 (3.3)	-379.29 (15.2)	-4.74 (4.05)	-394.69 (16.51)	0.58	85.5	84.9
c9.2	T + DPI + AGE + TG + ASSAY + SP + DOSE + CELL + SEX	0 (0)	-376.96 (15.2)	-0.76 (3.27)	-390.7 (16.31)	0.57	85.8	84.6
c10.1	**T + DPI + AGE + TG + ASSAY + SP + DOSE + CELL + SEX + ST**	**-0.87 (0.81)**	**-377.83 (15.28)**	**-1.67 (3.29)**	**-391.61 (16.39)**	**0.57**	**85.8**	**84.7**

Table S 1.4 | Extended culture model performance comparisons with totRNA as the primary predictor.
Models are ordered by increasing number of predictors, with the simplest (c1), best (c8.1), and full (c10.1) models noted in bold. We report expected log pointwise predictive density (ELPD) generated by 10-fold cross validation (cross-validation columns), where larger ELPD indicates better performance. ELPD difference indicates the difference between ELPDs of the given model and the model with the largest ELPD (in this case model l9.2, though this is not our 'best model'). The PSIS-LOO approximation columns present statistics generated by running Pareto-Smoothed Importance Sampling approximate leave-one-out cross validation, including ELPD and ELPD difference. The prediction column indicates the percent of samples (stratified by training and test sets) for which posterior predictions generated by 10-fold cross validation correctly classified them as below or above the limit of detection (i.e., where the per-sample posterior predictive distributions exhibited at least a probability of 0.5 for the true, observed classification). MCC is the Matthews correlation coefficient. Standard error (SE) is shown in parentheses following all relevant statistics.

Model	Predictors	*Cross-validation*		*PSIS-LOO Approximation*		*Prediction*		
		ELPD Difference (SE)	**ELPD (SE)**	**ELPD Difference (SE)**	**ELPD (SE)**	**MCC**	**% correctly predicted**	
							train	**test**
c1	**SG**	**-48.77 (17.87)**	**-350.19 (7.87)**	**-47.12 (9.22)**	**-350.38 (7.97)**	**0.43**	**80.8**	**80.8**
c2.1	SG + CELL	-46.15 (17.66)	-347.58 (8.24)	-45.15 (9.11)	-348.41 (8.36)	0.46	81.5	81.6
c2.2	SG + ASSAY	-43.94 (17.39)	-345.37 (8.14)	-42.73 (8.97)	-345.98 (8.26)	0.44	81.1	80.9
c2.3	SG + DOSE	-49.75 (18.01)	-351.18 (8.13)	-48.24 (9.27)	-351.5 (8.2)	0.42	80.6	80.5
c2.4	SG + ST	-44.12 (16.49)	-345.55 (8.51)	-42.39 (8.48)	-345.64 (8.65)	0.47	82.1	81.9
c2.5	SG + SP	-47.13 (16.95)	-348.56 (8.21)	-45.76 (8.76)	-349.02 (8.31)	0.43	81.1	80.9
c2.6	SG + AGE	-47.52 (17.64)	-348.94 (8.27)	-46.21 (9.12)	-349.47 (8.34)	0.44	80.9	80.9
c2.7	SG + SEX	-48.93 (17.77)	-350.35 (8.13)	-47.77 (9.19)	-351.03 (8.24)	0.44	81.3	81.1
c2.8	SG + DPI	-16.3 (10.84)	-317.73 (10.23)	-14.63 (5.69)	-317.89 (10.32)	0.52	83.5	83.4
c2.9	SG + TG	-49.06 (17.9)	-350.49 (8.11)	-47.51 (9.23)	-350.77 (8.19)	0.43	80.7	80.8
c3.1	SG + DPI + CELL	-15.02 (10.4)	-316.44 (10.4)	-13.52 (5.47)	-316.78 (10.51)	0.54	84	84
c3.2	SG + DPI + ASSAY	-13.09 (9.9)	-314.52 (10.36)	-11.79 (5.18)	-315.05 (10.47)	0.52	83.8	83.6
c3.3	SG + DPI + DOSE	-17.31 (11.11)	-318.74 (10.42)	-15.68 (5.81)	-318.93 (10.47)	0.51	83.6	83.3
c3.4	SG + DPI + ST	-16.67 (10.63)	-318.1 (10.31)	-15.35 (5.58)	-318.61 (10.4)	0.52	83.5	83.5
c3.5	SG + DPI + SP	-17.26 (10.42)	-318.68 (10.34)	-15.78 (5.46)	-319.04 (10.46)	0.51	83.6	83
c3.6	SG + DPI + AGE	-16.06 (10.62)	-317.49 (10.56)	-14.41 (5.57)	-317.67 (10.6)	0.52	83.4	83.6
c3.7	SG + DPI + SEX	-16.15 (10.48)	-317.57 (10.45)	-14.71 (5.53)	-317.97 (10.51)	0.53	83.9	83.7
c3.8	SG + DPI + TG	-15.41 (10.6)	-316.83 (10.55)	-14 (5.57)	-317.26 (10.63)	0.52	83.8	83.5
c4.1	SG + DPI + ASSAY + CELL	-13.64 (9.66)	-315.06 (10.51)	-12.25 (5.08)	-315.5 (10.63)	0.52	84	83.6
c4.2	SG + DPI + ASSAY + DOSE	-14.07 (10.26)	-315.49 (10.75)	-12.81 (5.33)	-316.07 (10.82)	0.53	83.8	83.7
c4.3	SG + DPI + ASSAY + ST	-10.94 (8.41)	-312.36 (10.56)	-9.72 (4.42)	-312.98 (10.7)	0.53	84.4	83.8
c4.4	SG + DPI + ASSAY + SP	-14.16 (9.73)	-315.59 (10.53)	-13.13 (5.08)	-316.39 (10.68)	0.52	83.9	83.5
c4.5	SG + DPI + ASSAY + AGE	-10.83 (8.96)	-312.26 (10.81)	-9.42 (4.68)	-312.67 (10.9)	0.52	84.3	83.7
c4.6	SG + DPI + ASSAY + SEX	-13.32 (9.61)	-314.74 (10.58)	-12.4 (5.06)	-315.66 (10.68)	0.52	83.9	83.4
c4.7	SG + DPI + ASSAY + TG	-12.51 (9.7)	-313.93 (10.66)	-11.52 (5.09)	-314.78 (10.77)	0.53	83.9	83.8
c5.1	SG + DPI + ASSAY + AGE + CELL	-11.65 (8.76)	-313.07 (10.92)	-10.11 (4.62)	-313.36 (11)	0.52	84.2	83.7
c5.2	SG + DPI + ASSAY + AGE + DOSE	-11.86 (9.18)	-313.28 (11.06)	-10.32 (4.78)	-313.58 (11.1)	0.52	84.1	83.5
c5.3	SG + DPI + ASSAY + AGE + ST	-9.45 (7.96)	-310.87 (11.01)	-8.18 (4.19)	-311.43 (11.13)	0.54	84.3	84.2
c5.4	SG + DPI + ASSAY + AGE + SP	-10.83 (8.15)	-312.25 (10.94)	-9.82 (4.29)	-313.08 (11.07)	0.53	84.2	83.8
c5.5	SG + DPI + ASSAY + AGE + SEX	-10.02 (8.18)	-311.44 (10.99)	-9.01 (4.29)	-312.27 (11.07)	0.52	84.5	83.7
c5.6	SG + DPI + ASSAY + AGE + TG	-10.65 (8.79)	-312.07 (11.01)	-9.56 (4.62)	-312.82 (11.13)	0.54	84.3	84.1
c6.1	SG + DPI + ASSAY + AGE + ST + CELL	-10.58 (7.89)	-312.01 (11.14)	-9.22 (4.17)	-312.48 (11.25)	0.53	84.2	83.8
c6.2	SG + DPI + ASSAY + AGE + ST + DOSE	-10.03 (7.98)	-311.46 (11.3)	-8.65 (4.17)	-311.91 (11.39)	0.54	84.6	84.2
c6.3	SG + DPI + ASSAY + AGE + ST + SP	-9.89 (7.24)	-311.31 (11.13)	-8.99 (3.84)	-312.25 (11.31)	0.53	84.5	84
c6.4	SG + DPI + ASSAY + AGE + ST + SEX	-8.37 (6.83)	-309.8 (11.19)	-7.57 (3.62)	-310.83 (11.28)	0.53	84.4	83.9

c6.5	SG + DPI + ASSAY + AGE + ST + TG	-8.33 (7.55)	-309.76 (11.33)	-7.31 (4.01)	-310.57 (11.48)	0.54	84.5	84.1
c7.1	SG + DPI + ASSAY + AGE + ST + TG + CELL	-9.56 (7.57)	-310.99 (11.47)	-8.36 (4.02)	-311.62 (11.61)	0.53	84.5	83.8
c7.2	SG + DPI + ASSAY + AGE + ST + TG + DOSE	-8.94 (7.49)	-310.37 (11.51)	-7.84 (3.95)	-311.1 (11.61)	0.54	84.7	84.2
c7.3	SG + DPI + ASSAY + AGE + ST + TG + SP	-9.35 (7.08)	-310.77 (11.39)	-8.76 (3.78)	-312.02 (11.61)	0.54	84.7	84.3
c7.4	SG + DPI + ASSAY + AGE + ST + TG + SEX	-7.14 (6.32)	-308.56 (11.46)	-6.8 (3.39)	-310.06 (11.63)	0.54	84.7	84.3
c8.1	SG + DPI + ASSAY + AGE + ST + TG + SEX + CELL	-7.25 (5.87)	-308.67 (11.57)	-6.67 (3.13)	-309.93 (11.69)	0.56	85	84.6
c8.2	SG + DPI + ASSAY + AGE + ST + TG + SEX + DOSE	-7.92 (6.52)	-309.35 (11.57)	-7.34 (3.45)	-310.6 (11.7)	0.55	84.8	84.5
c8.3	SG + DPI + ASSAY + AGE + ST + TG + SEX + SP	-8.19 (5.88)	-309.62 (11.54)	-8.03 (3.19)	-311.29 (11.76)	0.55	84.9	84.4
c9.1	SG + DPI + ASSAY + AGE + ST + TG + SEX + CELL + DOSE	-2.88 (4.95)	-304.3 (11.8)	-2.43 (2.57)	-305.69 (11.95)	0.55	85.2	84.6
c9.2	SG + DPI + ASSAY + AGE + ST + TG + SEX + CELL + SP	-5.56 (3.71)	-306.99 (11.64)	-5.3 (2.01)	-308.56 (11.85)	0.56	85.2	84.8
c10.1	**SG + DPI + ASSAY + AGE + ST + TG + SEX + CELL + DOSE + SP**	**0 (0)**	**-301.42 (11.91)**	**0 (0)**	**-303.26 (12.15)**	**0.56**	**85.7**	**84.9**

Table S 1.5 | Extended culture model performance comparisons with sgRNA as the primary predictor.
Models are ordered by increasing number of predictors, with the simplest (c1) and best/full (c10.1) models noted in bold. We report expected log pointwise predictive density (ELPD) generated by 10-fold cross validation (cross-validation columns), where larger ELPD indicates better performance. ELPD difference indicates the difference between ELPDs of the given model and the model with the largest ELPD (in this case model c10.1, our 'best model'). The PSIS-LOO approximation columns present statistics generated by running Pareto-Smoothed Importance Sampling approximate leave-one-out cross validation, including ELPD and ELPD difference. The prediction column indicates the percent of samples (stratified by training and test sets) for which posterior predictions generated by 10-fold cross validation correctly classified them as below or above the limit of detection (i.e., where the per-sample posterior predictive distributions exhibited at least a probability of 0.5 for the true, observed classification). MCC is the Matthews correlation coefficient. Standard error (SE) is shown in parentheses following all relevant statistics.

TotRNA			0	1	2	3	4	5	6	7	8	9	10
sgRNA Logistic	Dose	4	0, 0	0, 1	1, 4	9, 19	43, 61	84, 92	97, 99	100, 100	100, 100	100, 100	100, 100
		5.5	0, 0	0, 0	0, 1	2, 6	16, 27	6, 72	91, 95	98, 99	100, 100	100, 100	100, 100
		7	0, 0	0, 0	0, 0	0, 2	4, 10	23, 43	69, 84	94, 98	99, 100	100, 100	100, 100
	Spe-cies	RM	0, 0	0, 0	0, 1	2, 6	16, 27	6, 72	91, 95	98, 99	100, 100	100, 100	100, 100
		CM	0, 0	0, 0	0, 1	2, 7	12, 33	5, 77	87, 96	98, 100	100, 100	100, 100	100, 100
		AGM	0, 0	0, 0	0, 0	0, 2	3, 12	17, 49	59, 88	91, 98	98, 100	100, 100	100, 100
	Target Gene	T↑SG↑	0, 3	3, 17	18, 58	61, 91	91, 99	99, 100	100, 100	100, 100	100, 100	100, 100	100, 100
		T↓SG↑	0, 1	1, 8	6, 38	3, 81	75, 97	95, 100	99, 100	100, 100	100, 100	100, 100	100, 100
		T↑SG↓	0, 0	0, 0	0, 1	2, 6	16, 27	60, 72	91, 95	98, 99	100, 100	100, 100	100, 100
		T↓SG↓	0, 0	0, 0	0, 3	4, 15	24, 55	69, 90	94, 98	99, 100	100, 100	100, 100	100, 100
sgRNA Linear	Dose	4	-1.16, -0.5	-0.23, 0.39	0.7, 1.28	1.63, 2.17	2.55, 3.07	3.47, 3.97	4.38, 4.87	5.29, 5.79	6.2, 6.7	7.1, 7.62	8, 8.55
		5.5	-1.4, -0.88	-0.46, 0	0.48, 0.89	1.41, 1.77	2.34, 2.66	3.27, 3.56	4.18, 4.46	5.09, 5.37	5.99, 6.29	6.88, 7.22	7.77, 8.15
		7	-1.76, -1.14	-0.83, -0.25	0.1, 0.64	1.02, 1.53	1.94, 2.43	2.86, 3.33	3.77, 4.24	4.68, 5.15	5.58, 6.06	6.48, 6.98	7.38, 7.91
	DPI	I, 1	-1.96, -1.39	-1.02, -0.5	-0.09, 0.38	0.84, 1.28	1.77, 2.17	2.69, 3.06	3.61, 3.97	4.52, 4.88	5.42, 5.79	6.32, 6.71	7.2, 7.64
		I, 2+	-1.4, -0.88	-0.46, 0	0.48, 0.89	1.41, 1.77	2.34, 2.66	3.27, 3.56	4.18, 4.46	5.09, 5.37	5.99, 6.29	6.88, 7.22	7.77, 8.15
		NI, 1+	-1.01, -0.41	-0.08, 0.47	0.86, 1.35	1.79, 2.24	2.72, 3.13	3.65, 4.03	4.57, 4.92	5.48, 5.83	6.38, 6.74	7.28, 7.66	8.18, 8.58
	Target Gene	T↓SG↑	0.01, 0.6	0.94, 1.49	1.87, 2.38	2.79, 3.28	3.71, 4.18	4.62, 5.09	5.53, 6	6.43, 6.91	7.33, 7.83	8.22, 8.76	9.11, 9.69
		T↑SG↓	-1.4, -0.88	-0.46, 0	0.48, 0.89	1.41, 1.77	2.34, 2.66	3.27, 3.56	4.18, 4.46	5.09, 5.37	5.99, 6.29	6.88, 7.22	7.77, 8.15
		T↓SG↓	-1.05, -0.48	-0.11, 0.4	0.81, 1.29	1.74, 2.19	2.66, 3.08	3.57, 3.99	4.48, 4.9	5.39, 5.82	6.28, 6.73	7.18, 7.66	8.07, 8.59
	Spe-cies	RM	-1.4, -0.88	-0.46, 0	0.48, 0.89	1.41, 1.77	2.34, 2.66	3.27, 3.56	4.18, 4.46	5.09, 5.37	5.99, 6.29	6.88, 7.22	7.77, 8.15
		CM	-2.42, -1.74	-1.49, -0.86	-0.55, 0.03	0.38, 0.92	1.3, 1.81	2.23, 2.71	3.14, 3.61	4.05, 4.52	4.96, 5.43	5.86, 6.34	6.76, 7.26
		AGM	-1.36, -0.65	-0.43, 0.23	0.5, 1.12	1.43, 2.01	2.35, 2.9	3.28, 3.8	4.2, 4.7	5.11, 5.61	6.02, 6.51	6.92, 7.43	7.82, 8.35

Table S 1.6 | 90% prediction intervals for the best sgRNA model.
These intervals correspond with the predictions in Figure 1.3C and 1.3H.

Model	Parameter	5% CI	Median	95% CI	Standard Dev.
PCR Logistic	intercept	-3.8	-2.15	-0.49	1
	T	1.75	1.96	2.19	0.13
	DOSE	-1.16	-0.93	-0.71	0.14
	SP [RM]	-0.59	0.4	1.41	0.61
	SP [CM]	-0.65	0.36	1.36	0.61
	SP [AGM]	-2.14	-1.06	-0.04	0.64
	TG [T↑ SG↑]	1.23	2.32	3.41	0.66
	TG [T↓ SG↑]	0.13	1.24	2.35	0.68
	TG [T↑ SG↓]	-3.29	-2.32	-1.38	0.58
	TG [T↓ SG↓]	-2.46	-1.51	-0.57	0.58
PCR Linear	intercept	-2.48	-1.25	-0.03	0.75
	T	0.88	0.91	0.94	0.02
	DOSE	-0.34	-0.21	-0.08	0.08
	DPI [I, 1]	-0.81	0.08	0.95	0.54
	DPI [I, 2+]	-0.26	0.61	1.5	0.54
	DPI [NI, 1+]	0.14	1.03	1.93	0.54
	SP [RM]	-0.05	0.85	1.75	0.55
	SP [CM]	-0.99	-0.09	0.8	0.54
	SP [AGM]	0.07	0.98	1.88	0.55
	TG [T↓ SG↑]	0.36	1.25	2.14	0.53
	TG [T↑ SG↓]	-1.09	-0.19	0.71	0.54
	TG [T↓ SG↓]	-0.71	0.18	1.06	0.54
Culture	intercept	-1.56	-0.04	1.47	0.92
	T	0.69	0.8	0.91	0.07
	DOSE	-1.19	-0.85	-0.52	0.2
	DPI [I, 1]	0.41	1.39	2.4	0.61
	DPI [I, 2+]	-1.09	-0.14	0.83	0.58
	DPI [NI, 1+]	-1.26	-0.28	0.69	0.59
	SP [RM]	-0.18	0.79	1.77	0.59
	SP [CM]	-1.58	-0.55	0.46	0.62
	SP [AGM]	-0.28	0.72	1.74	0.61
	AGE [Juvenile]	-1.53	-0.48	0.57	0.64
	AGE [Adult]	-1.93	-0.94	0.07	0.61
	AGE [Geriatric]	1.2	2.39	3.57	0.72
	TG [N]	-0.56	0.51	1.55	0.65
	TG [E]	-1.73	-0.69	0.31	0.62
	TG [S]	0.06	1.13	2.23	0.66
	ASSAY	-2.56	-1.75	-0.96	0.49
	CELL [76]	-0.48	0.54	1.56	0.61
	CELL [E6]	-1.81	-0.78	0.27	0.63
	CELL [E6-SS2]	0.49	1.71	2.92	0.73

Table S 1.7 | Parameter estimates for the best models.
These were generated for the models without a lab effect.

Lab number (C / SG)	Articles (ref.)	Location of primate studies (if multiple articles)
1 / --	Deng et al. 2020	
2 / --	Ishigaki et al. 2021	
3 / --	Johnston et al. 2020	
4 / --	Kobiyama et al. 2021	
5 / 3	Jiao et al. 2021; Nagata et al. 2021	Kunming Primate Center
6 / 5	Salguero et al. 2021	
7 / 6	Munster et al. 2020; Speranza et al. 2020; van Doremalen et al. 2020; Williamson et al. 2020	Rocky Mountain Laboratories
8 / --	Shan et al. 2020	
9 / 7	Singh et al. 2020	
10 / --	Cross et al. 2020; Woolsey et al. 2020	University of Texas Medical Branch, Galveston
-- / 1	Gabitzsch et al. 2021	
-- / 2	Baum et al. 2020; Chandrashekar et al. 2020; Corbett et al. 2020; Dagotto et al. 2020; Jones et al. 2021; Patel et al. 2021	Bioqual
-- / 4	Li et al. 2021	
-- / 8	Yu et al. 2020	

Table S 1.8 | Articles grouped into labs based on where the primate study was conducted. The group number used to display lab effects in Figures S1.12A, S1.12E, and S1.16A are provided in the first column. The number for culture analyses (C) precedes the one for the sgRNA analyses (SG).

	Predictors	Prediction Accuracy (%)			MCC
		Overall	Positive	Negative	
Data subset	T	90.4	72.2	94.3	0.67
	SG	90.0	70.4	94.3	0.66
	T + SG	90.0	68.5	94.7	0.65
All data	T	81.9	53.7	91.4	0.49
	SG*†	80.8	46.7	91.7	0.43
	T + SG*	81.7	51.8	91.7	0.48
	Best T	84.7	60.7	92.8	0.57
	Best SG*†	84.9	57.7	93.6	0.56

Table S 1.9 | Performance comparison of culture models using totRNA, sgRNA, or both as the primary predictor(s).
Statistics are stratified by predictor(s) and the dataset used for fitting, including the full dataset (based on sgRNA predictions; 'all data') and the subset containing only samples with known sgRNA and totRNA results ('data subset'). Prediction accuracy reflects aggregate performance on test data across the full 10 train-test folds, stratified by all available samples (Overall), only known positive samples, and only known negative samples. MCC corresponds to the Matthews correlation coefficient. Note that we do not report ELPD because these models were fit with different quantities of data and so ELPD is not comparable. * includes imputed data. † includes data with observed sgRNA outcomes but no observed totRNA outcomes.

TotRNA		0	1	2	3	4	5	6	7	8	9	10	11	12
Dose	4	0, 4	1, 7	2, 14	4, 26	10, 44	19, 63	35, 79	55, 90	72, 95	85, 98	92, 99	96, 100	98, 100
	5.5	0, 1	0, 2	1, 4	2, 7	4, 15	8, 27	17, 44	31, 64	50, 80	68, 90	82, 96	90, 98	95, 99
	7	0, 0	0, 1	0, 1	0, 2	1, 5	2, 10	5, 19	11, 33	21, 52	37, 71	56, 85	73, 93	85, 97
DPI	I, 1	0, 5	1, 9	3, 18	6, 31	13, 49	25, 67	43, 82	63, 91	79, 96	89, 98	95, 99	97, 100	99, 100
	I, 2+	0, 1	0, 2	1, 4	2, 7	4, 15	8, 27	17, 44	31, 64	50, 80	68, 90	82, 96	90, 98	95, 99
	NI, 1+	0, 1	0, 2	1, 3	1, 7	3, 13	7, 24	15, 41	28, 61	46, 78	65, 89	80, 95	89, 98	95, 99
Spe-cies	RM	0, 1	0, 2	1, 4	2, 7	4, 15	8, 27	17, 44	31, 64	50, 80	68, 90	82, 96	90, 98	95, 99
	CM	0, 0	0, 1	0, 1	0, 2	1, 5	2, 9	4, 19	9, 33	19, 53	34, 72	52, 85	70, 93	83, 97
	AGM	0, 1	0, 2	1, 3	2, 6	4, 12	9, 21	20, 36	36, 55	55, 73	73, 87	85, 94	92, 97	96, 99
Age Class	Juvenile	0, 1	1, 3	1, 5	3, 10	6, 19	14, 33	27, 52	45, 71	64, 85	79, 93	89, 97	94, 99	97, 99
	Adult	0, 1	0, 2	1, 4	2, 7	4, 15	8, 27	17, 44	31, 64	50, 80	68, 90	82, 96	90, 98	95, 99
	Geriatric	3, 24	6, 40	13, 59	25, 76	42, 87	62, 94	78, 97	89, 99	94, 99	97, 100	99, 100	99, 100	100, 100
Cell Line	76	0, 1	0, 2	1, 4	2, 7	4, 15	8, 27	17, 44	31, 64	50, 80	68, 90	82, 96	90, 98	95, 99
	E6	0, 0	0, 1	0, 1	0, 2	1, 4	2, 9	5, 17	11, 31	23, 49	39, 68	59, 83	75, 92	87, 96
	E6-SS2	0, 4	1, 7	2, 14	4, 26	8, 43	16, 62	31, 78	49, 89	68, 95	82, 98	91, 99	95, 100	98, 100
Assay	TCID50	1, 5	2, 10	4, 18	8, 33	17, 51	32, 70	51, 84	69, 92	83, 96	91, 98	96, 99	98, 100	99, 100
	Plaque	0, 1	0, 2	1, 4	2, 7	4, 15	8, 27	17, 44	31, 64	50, 80	68, 90	82, 96	90, 98	95, 99
Target Gene	N	0, 1	0, 2	1, 4	2, 7	4, 15	8, 27	17, 44	31, 64	50, 80	68, 90	82, 96	90, 98	95, 99
	E	0, 0	0, 1	0, 2	0, 4	1, 7	2, 15	3, 28	8, 46	15, 65	28, 81	47, 91	65, 96	80, 98
	S	0, 2	0, 4	1, 9	2, 17	5, 31	10, 49	20, 68	36, 83	55, 92	72, 96	85, 98	92, 99	96, 100

Table S 1.10 | 90% prediction intervals for the best culture model.
These intervals correspond with the predictions in Figure 1.5C.

Inoculation Route(s)	Inoculated Locations	Non-inoculated Locations
AE	Nose/Nasopharynx, Oropharynx	Anus/Rectum
IT		Anus/Rectum, Lung, Nose/Nasopharynx, Oropharynx
IN	Nose/Nasopharynx	Anus/Rectum, BAL, Colon, Mouth, Small intestine, Stomach
IG	Stomach	Anus/Rectum, Colon, Small intestine
OC		Lung
IT, IN	BAL, Nose/Nasopharynx, Oropharynx, Trachea	Anus/Rectum, Lung, Mouth, Tonsil
IT, IN, OC	Eye, Nose/Nasopharynx, Oropharynx, Trachea	Anus/Rectum, Brain, Cervical LN, Colon, Kidney, Liver, Lung, Mesenteric LN, Salivary gland, Small intestine, Spleen, Tonsil
IT, IN, OR, OC	BAL, Bronchus, Eye, Mouth, Nose/Nasopharynx, Oropharynx, Tonsil, Trachea	Anus/Rectum, Cervical LN, Colon, Heart, Lung, Mediastinal LN, Small intestine, Stomach

Table S 1.11 | Categorization of inoculated versus non-inoculated sample locations per exposure route.

For every inoculation route, only the tissues with data available for that route are displayed. Because fluid is administered in the trachea for intratracheal (IT) inoculations, which is connected directly to the bronchioles, we include bronchus as an exposure tissue for IT inoculations. We also consider BAL an inoculated tissue for IT exposures since this procedure collects fluid from similar areas where the inoculum is administered. Exposure route abbreviations are: AE, aerosol; IT, intratracheal; IN, intranasal; IG, intragastric; OC, ocular; OR, oral.

References

Alexandersen, S., Chamings, A., & Bhatta, T. R. (2020). SARS-CoV-2 genomic and subgenomic RNAs in diagnostic samples are not an indicator of active replication. *Nature Communications*, *11*(1), 6059. https://doi.org/10.1038/s41467-020-19883-7

Amarilla, A. A., Modhiran, N., Setoh, Y. X., Peng, N. Y. G., Sng, J. D. J., Liang, B., McMillan, C. L. D., Freney, M. E., Cheung, S. T. M., Chappell, K. J., Khromykh, A. A., Young, P. R., & Watterson, D. (2021). An Optimized High-Throughput Immuno-Plaque Assay for SARS-CoV-2. *Frontiers in Microbiology*, *12*. DOI: https://www.frontiersin.org/articles/10.3389/fmicb.2021.625136

Bajaj, V., Gadi, N., Spihlman, A. P., Wu, S. C., Choi, C. H., & Moulton, V. R. (2021). Aging, Immunity, and COVID-19: How Age Influences the Host Immune Response to Coronavirus Infections? *Frontiers in Physiology*, *11*. https://www.frontiersin.org/articles/10.3389/fphys.2020.571416

Baum, A., Ajithdoss, D., Copin, R., Zhou, A., Lanza, K., Negron, N., Ni, M., Wei, Y., Mohammadi, K., Musser, B., Atwal, G. S., Oyejide, A., Goez-Gazi, Y., Dutton, J., Clemmons, E., Staples, H. M., Bartley, C., Klaffke, B., Alfson, K., … Kyratsous, C. A. (2020). REGN-COV2 antibodies prevent and treat SARS-CoV-2 infection in rhesus macaques and hamsters. *Science*, *370*(6520), 1110–1115. https://doi.org/10.1126/science.abe2402

Bhatnagar, J., Gary, J., Reagan-Steiner, S., Estetter, L. B., Tong, S., Tao, Y., Denison, A. M., Lee, E., DeLeon-Carnes, M., Li, Y., Uehara, A., Paden, C. R., Leitgeb, B., Uyeki, T. M., Martines, R. B., Ritter, J. M., Paddock, C. D., Shieh, W.-J., & Zaki, S. R. (2021). Evidence of Severe Acute Respiratory Syndrome Coronavirus 2 Replication and Tropism in the Lungs, Airways, and Vascular Endothelium of Patients With Fatal Coronavirus Disease 2019: An Autopsy Case Series. *The Journal of Infectious Diseases*, *223*(5), 752–764. https://doi.org/10.1093/infdis/jiab039

Blair, R. V., Vaccari, M., Doyle-Meyers, L. A., Roy, C. J., Russell-Lodrigue, K., Fahlberg, M., Monjure, C. J., Beddingfield, B., Plante, K. S., Plante, J. A., Weaver, S. C., Qin, X., Midkiff, C. C., Lehmicke, G., Golden, N., Threeton, B., Penney, T., Allers, C., Barnes, M. B., … Rappaport, J. (2021). Acute Respiratory Distress in Aged, SARS-CoV-2–Infected African Green Monkeys but Not Rhesus Macaques. *The American Journal of Pathology*, *191*(2), 274–282. https://doi.org/10.1016/j.ajpath.2020.10.016

Bonenfant, G., Deyoe, J. E., Wong, T., Grijalva, C. G., Cui, D., Talbot, H. K., Hassell, N., Halasa, N., Chappell, J., Thornburg, N. J., Rolfes, M. A., Wentworth, D. E., & Zhou, B. (2022). Surveillance and Correlation of Severe Acute Respiratory Syndrome Coronavirus 2 Viral RNA, Antigen, Virus Isolation, and Self-Reported Symptoms in a Longitudinal Study With Daily Sampling. *Clinical Infectious Diseases*, *75*(10), 1698–1705. https://doi.org/10.1093/cid/ciac282

Bravo, M. S., Berengua, C., Marín, P., Esteban, M., Rodriguez, C., del Cuerpo, M., Miró, E., Cuesta, G., Mosquera, M., Sánchez-Palomino, S., Vila, J., Rabella, N., & Marcos, M. Á. (2022). Viral Culture Confirmed SARS-CoV-2 Subgenomic RNA Value as a Good Surrogate Marker of Infectivity. *Journal of Clinical Microbiology*, *60*(1), e01609-21. https://doi.org/10.1128/JCM.01609-21

Bruce, E. A., Mills, M. G., Sampoleo, R., Perchetti, G. A., Huang, M.-L., Despres, H. W., Schmidt, M. M., Roychoudhury, P., Shirley, D. J., Jerome, K. R., Greninger, A. L., & Botten, J. W. (2022). Predicting infectivity: Comparing four PCR-based assays to detect culturable SARS-CoV-2 in clinical samples. *EMBO Molecular Medicine*, *14*(2), e15290. https://doi.org/10.15252/emmm.202115290

Bullard, J., Dust, K., Funk, D., Strong, J. E., Alexander, D., Garnett, L., Boodman, C., Bello, A., Hedley, A., Schiffman, Z., Doan, K., Bastien, N., Li, Y., Van Caeseele, P. G., & Poliquin, G. (2020). Predicting Infectious Severe Acute Respiratory Syndrome Coronavirus 2 From Diagnostic Samples. *Clinical Infectious Diseases*, *71*(10), 2663–2666. https://doi.org/10.1093/cid/ciaa638

Carter, J., & Saunders, V. A. (2007). *Virology: Principles and Applications*. John Wiley & Sons.

CDC. (2020, February 11). *Healthcare Workers*. Centers for Disease Control and Prevention. https://archive.cdc.gov/www_cdc_gov/coronavirus/2019-ncov/hcp/duration-isolation.html

Chandrashekar, A., Liu, J., Martinot, A. J., McMahan, K., Mercado, N. B., Peter, L., Tostanoski, L. H., Yu, J., Maliga, Z., Nekorchuk, M., Busman-Sahay, K., Terry, M., Wrijil, L. M., Ducat, S., Martinez, D. R., Atyeo, C., Fischinger, S., Burke, J. S., Slein, M. D., … Barouch, D. H. (2020). SARS-CoV-2 infection protects against rechallenge in rhesus macaques. *Science*, eabc4776–eabc4776. https://doi.org/10.1126/science.abc4776

Chicco, D., & Jurman, G. (2020). The advantages of the Matthews correlation coefficient (MCC) over F1 score and accuracy in binary classification evaluation. *BMC Genomics*, *21*(1), 6. https://doi.org/10.1186/s12864-019-6413-7

Chu, H., Chan, J. F.-W., & Yuen, K.-Y. (2022). Animal models in SARS-CoV-2 research. Nature Methods, 19(4), Article 4. https://doi.org/10.1038/s41592-022-01447-w

Corbett, K. S., Flynn, B., Foulds, K. E., Francica, J. R., Boyoglu-Barnum, S., Werner, A. P., Flach, B., O'Connell, S., Bock, K. W., Minai, M., Nagata, B. M., Andersen, H., Martinez, D. R., Noe, A. T., Douek, N., Donaldson, M. M., Nji, N. N., Alvarado, G. S., Edwards, D. K., … Graham, B. S. (2020). Evaluation of the mRNA-1273 Vaccine against SARS-CoV-2 in Nonhuman Primates. *The New England Journal of Medicine*, NEJMoa2024671–NEJMoa2024671. https://doi.org/10.1056/NEJMoa2024671

Cramer, P. E., Gentzel, R. C., Tanis, K. Q., Vardigan, J., Wang, Y., Connolly, B., Manfre, P., Lodge, K., Renger, J. J., Zerbinatti, C., & Uslaner, J. M. (2018). Aging African green monkeys manifest transcriptional, pathological, and cognitive hallmarks of human Alzheimer's disease. Neurobiology of Aging, 64, 92–106. https://doi.org/10.1016/j.neurobiolaging.2017.12.011

Cross, R. W., Agans, K. N., Prasad, A. N., Borisevich, V., Woolsey, C., Deer, D. J., Dobias, N. S., Geisbert, J. B., Fenton, K. A., & Geisbert, T. W. (2020). Intranasal exposure of African green monkeys to SARS-CoV-2 results in acute phase pneumonia with shedding and lung injury still present in the early convalescence phase. *Virology Journal*, *17*(1), 125–125. https://doi.org/10.1186/s12985-020-01396-w

Dagotto, G., Mercado, N. B., Martinez, D. R., Hou, Y. J., Nkolola, J. P., Carnahan, R. H., Crowe, J. E., Baric, R. S., & Barouch, D. H. (2021). Comparison of Subgenomic and Total RNA in SARS-CoV-2-Challenged Rhesus Macaques. *Journal of Virology*, *95*(8). https://doi.org/10.1128/JVI.02370-20

Darusman, H. S., Call, J., Sajuthi, D., Schapiro, S. J., Gjedde, A., Kalliokoski, O., & Hau, J. (2014). Delayed response task performance as a function of age in cynomolgus monkeys (Macaca fascicularis). Primates, 55(2), 259–267. https://doi.org/10.1007/s10329-013-0397-8

Deng, W., Bao, L., Gao, H., Xiang, Z., Qu, Y., Song, Z., Gong, S., Liu, J., Liu, J., Yu, P., Qi, F., Xu, Y., Li, F., Xiao, C., Lv, Q., Xue, J., Wei, Q., Liu, M., Wang, G., … Qin, C. (2020). Ocular conjunctival inoculation of SARS-CoV-2 can cause mild COVID-19 in rhesus macaques. *Nature Communications*, *11*(1), 4400–4400. https://doi.org/10.1038/s41467-020-18149-6

Dimcheff, D. E., Valesano, A. L., Rumfelt, K. E., Fitzsimmons, W. J., Blair, C., Mirabelli, C., Petrie, J. G., Martin, E. T., Bhambhani, C., Tewari, M., & Lauring, A. S. (2021). Severe Acute Respiratory Syndrome Coronavirus 2 Total and Subgenomic RNA Viral Load in Hospitalized Patients. *The Journal of Infectious Diseases*, *224*(8), 1287–1293. https://doi.org/10.1093/infdis/jiab215

Escors, D., Izeta, A., Capiscol, C., & Enjuanes, L. (2003). Transmissible Gastroenteritis Coronavirus Packaging Signal Is Located at the 5′ End of the Virus Genome. *Journal of Virology*, *77*(14), 7890–7902. https://doi.org/10.1128/JVI.77.14.7890-7902.2003

Estes, J. D., Wong, S. W., & Brenchley, J. M. (2018). Nonhuman primate models of human viral infections. *Nature Reviews Immunology*, *18*(6), Article 6. https://doi.org/10.1038/s41577-018-0005-7

Fajnzylber, J., Regan, J., Coxen, K., Corry, H., Wong, C., Rosenthal, A., Worrall, D., Giguel, F., Piechocka-Trocha, A., Atyeo, C., Fischinger, S., Chan, A., Flaherty, K. T., Hall, K., Dougan, M., Ryan, E. T., Gillespie, E., Chishti, R., Li, Y., … Li, J. Z. (2020). SARS-CoV-2 viral load is associated with increased disease severity and mortality. *Nature Communications*, *11*(1), Article 1. https://doi.org/10.1038/s41467-020-19057-5

Fehr, A. R., & Perlman, S. (2015). Coronaviruses: An Overview of Their Replication and Pathogenesis. In H. J. Maier, E. Bickerton, & P. Britton (Eds.), *Coronaviruses: Methods and Protocols* (pp. 1–23). Springer. https://doi.org/10.1007/978-1-4939-2438-7_1

Ford, L., Lee, C., Pray, I. W., Cole, D., Bigouette, J. P., Abedi, G. R., Bushman, D., Delahoy, M. J., Currie, D. W., Cherney, B., Kirby, M. K., Fajardo, G. C., Caudill, M., Langolf, K., Kahrs, J., Zochert, T., Kelly, P., Pitts, C., Lim, A., … CDC COVID-19 Surge Laboratory Group. (2021). Epidemiologic Characteristics Associated With Severe Acute Respiratory Syndrome Coronavirus 2 (SARS-CoV-2) Antigen-Based Test Results, Real-Time Reverse Transcription Polymerase Chain Reaction (rRT-PCR) Cycle Threshold Values, Subgenomic RNA, and Viral Culture Results From University Testing. *Clinical Infectious Diseases*, *73*(6), e1348–e1355. https://doi.org/10.1093/cid/ciab303

Gabitzsch, E., Safrit, J. T., Verma, M., Rice, A., Sieling, P., Zakin, L., Shin, A., Morimoto, B., Adisetiyo, H., Wong, R., Bezawada, A., Dinkins, K., Balint, J., Peykov, V., Garban, H., Liu, P., Bacon, A., Bone, P., Drew, J., … Soon-Shiong, P. (2021). Dual-Antigen COVID-19 Vaccine Subcutaneous Prime Delivery With Oral Boosts Protects NHP Against SARS-CoV-2 Challenge. *Frontiers in Immunology*, *12*. https://www.frontiersin.org/articles/10.3389/fimmu.2021.729837

Gadi, N., Wu, S. C., Spihlman, A. P., & Moulton, V. R. (2020). What's Sex Got to Do With COVID-19? Gender-Based Differences in the Host Immune Response to Coronaviruses. *Frontiers in Immunology*, *11*. https://www.frontiersin.org/articles/10.3389/fimmu.2020.02147

Gniazdowski, V., Paul Morris, C., Wohl, S., Mehoke, T., Ramakrishnan, S., Thielen, P., Powell, H., Smith, B., Armstrong, D. T., Herrera, M., Reifsnyder, C., Sevdali, M., Carroll, K. C., Pekosz, A., & Mostafa, H. H. (2021). Repeated Coronavirus Disease 2019 Molecular Testing: Correlation of Severe Acute Respiratory Syndrome Coronavirus 2 Culture With Molecular Assays and Cycle Thresholds. *Clinical Infectious Diseases*, *73*(4), e860–e869. https://doi.org/10.1093/cid/ciaa1616

Grebennikov, D., Kholodareva, E., Sazonov, I., Karsonova, A., Meyerhans, A., & Bocharov, G. (2021). Intracellular Life Cycle Kinetics of SARS-CoV-2 Predicted Using Mathematical Modelling. *Viruses*, *13*(9), Article 9. https://doi.org/10.3390/v13091735

Hoffmann, M., Kleine-Weber, H., Schroeder, S., Krüger, N., Herrler, T., Erichsen, S., Schiergens, T. S., Herrler, G., Wu, N. H., Nitsche, A., Müller, M. A., Drosten, C., & Pöhlmann, S. (2020). SARS-CoV-2 Cell Entry Depends on ACE2 and TMPRSS2 and Is Blocked by a Clinically Proven Protease Inhibitor. *Cell*, *181*(2), 271–280. https://doi.org/10.1016/j.cell.2020.02.052

Ishigaki, H., Nakayama, M., Kitagawa, Y., Nguyen, C. T., Hayashi, K., Shiohara, M., Gotoh, B., & Itoh, Y. (2021). Neutralizing antibody-dependent and -independent immune responses against SARS-CoV-2 in cynomolgus macaques. *Virology*, *554*, 97–105. https://doi.org/10.1016/j.virol.2020.12.013

Jiao, L., Li, H., Xu, J., Yang, M., Ma, C., Li, J., Zhao, S., Wang, H., Yang, Y., Yu, W., Wang, J., Yang, J., Long, H., Gao, J., Ding, K., Wu, D., Kuang, D., Zhao, Y., Liu, J., … Peng, X. (2021). The Gastrointestinal Tract Is an Alternative Route for SARS-CoV-2 Infection in a Nonhuman Primate Model. *Gastroenterology*, *160*(5), 1647–1661. https://doi.org/10.1053/j.gastro.2020.12.001

Johnston, S. C., Ricks, K. M., Jay, A., Raymond, J. L., Rossi, F., Zeng, X., Scruggs, J., Dyer, D., Frick, O., Koehler, J. W., Kuehnert, P. A., Clements, T. L., Shoemaker, C. J., Coyne, S. R., Delp, K. L., Moore, J., Berrier, K., Esham, H., Shamblin, J., … Nalca, A. (2021). Development of a coronavirus disease 2019 nonhuman primate model using airborne exposure. *PLOS ONE*, *16*(2), e0246366. https://doi.org/10.1371/journal.pone.0246366

Jones, B. E., Brown-Augsburger, P. L., Corbett, K. S., Westendorf, K., Davies, J., Cujec, T. P., Wiethoff, C. M., Blackbourne, J. L., Heinz, B. A., Foster, D., Higgs, R. E., Balasubramaniam, D., Wang, L., Zhang, Y., Yang, E. S., Bidshahri, R., Kraft, L., Hwang, Y., Žentelis, S., … Falconer, E. (2021). The neutralizing antibody, LY-CoV555, protects against SARS-CoV-2 infection in nonhuman primates. *Science Translational Medicine*, *13*(593), eabf1906. https://doi.org/10.1126/scitranslmed.abf1906

Jones, T. C., Biele, G., Mühlemann, B., Veith, T., Schneider, J., Beheim-Schwarzbach, J., Bleicker, T., Tesch, J., Schmidt, M. L., Sander, L. E., Kurth, F., Menzel, P., Schwarzer, R., Zuchowski, M., Hofmann, J., Krumbholz, A., Stein, A., Edelmann, A., Corman, V. M., & Drosten, C. (2021). Estimating infectiousness throughout SARS-CoV-2 infection course. *Science*, *373*(6551), eabi5273. https://doi.org/10.1126/science.abi5273

Ke, R., Martinez, P. P., Smith, R. L., Gibson, L. L., Mirza, A., Conte, M., Gallagher, N., Luo, C. H., Jarrett, J., Zhou, R., Conte, A., Liu, T., Farjo, M., Walden, K. K. O., Rendon, G., Fields, C. J., Wang, L., Fredrickson, R., Edmonson, D. C., … Brooke, C. B. (2022). Daily longitudinal sampling of SARS-CoV-2 infection reveals substantial heterogeneity in infectiousness. *Nature Microbiology*, *7*(5), Article 5. https://doi.org/10.1038/s41564-022-01105-z

Ke, R., Zitzmann, C., Ho, D. D., Ribeiro, R. M., & Perelson, A. S. (2021). In vivo kinetics of SARS-CoV-2 infection and its relationship with a person's infectiousness. *Proceedings of the National Academy of Sciences*, *118*(49), e2111477118. https://doi.org/10.1073/pnas.2111477118

Killingley, B., Mann, A. J., Kalinova, M., Boyers, A., Goonawardane, N., Zhou, J., Lindsell, K., Hare, S. S., Brown, J., Frise, R., Smith, E., Hopkins, C., Noulin, N., Löndt, B., Wilkinson, T., Harden, S., McShane, H., Baillet, M., Gilbert, A., … Chiu, C. (2022). Safety, tolerability and viral kinetics during SARS-CoV-2 human challenge in young adults. *Nature Medicine*, 1–11. https://doi.org/10.1038/s41591-022-01780-9

Kim, D., Lee, J.-Y., Yang, J.-S., Kim, J. W., Kim, V. N., & Chang, H. (2020). The Architecture of SARS-CoV-2 Transcriptome. *Cell*, *181*(4), 914-921.e10. https://doi.org/10.1016/j.cell.2020.04.011

Kim, M.-C., Cui, C., Shin, K.-R., Bae, J.-Y., Kweon, O.-J., Lee, M.-K., Choi, S.-H., Jung, S.-Y., Park, M.-S., & Chung, J.-W. (2021). Duration of Culturable SARS-CoV-2 in Hospitalized Patients with Covid-19. *New England Journal of Medicine*, *384*(7), 671–673. https://doi.org/10.1056/NEJMc2027040

Kirby, J. E., Riedel, S., Dutta, S., Arnaout, R., Cheng, A., Ditelberg, S., Hamel, D. J., Chang, C. A., & Kanki, P. J. (2023). Sars-Cov-2 antigen tests predict infectivity based on viral culture: Comparison of antigen, PCR viral load, and viral culture testing on a large sample cohort. *Clinical Microbiology and Infection*, *29*(1), 94–100. https://doi.org/10.1016/j.cmi.2022.07.010

Kobiyama, K., Imai, M., Jounai, N., Nakayama, M., Hioki, K., Iwatsuki-Horimoto, K., Yamayoshi, S., Tsuchida, J., Niwa, T., Suzuki, T., Ito, M., Yamada, S., Watanabe, T., Kiso, M., Negishi, H., Temizoz, B., Ishigaki, H., Kitagawa, Y., Nguyen, C. T., … Ishii, K. J. (2021). *Optimization of an LNP-mRNA vaccine candidate targeting SARS-CoV-2 receptor-binding domain* (p. 2021.03.04.433852). bioRxiv. https://doi.org/10.1101/2021.03.04.433852

Koo, B.-S., Lee, D.-H., Kang, P., Jeong, K.-J., Lee, S., Kim, K., Lee, Y., Huh, J.-W., Kim, Y.-H., Park, S.-J., Jin, Y. B., Kim, S.-U., Kim, J.-S., Son, Y., & Lee, S.-R. (2019). Reference values of hematological and biochemical parameters in young-adult cynomolgus monkey (Macaca fascicularis) and rhesus monkey (Macaca mulatta) anesthetized with ketamine hydrochloride. Laboratory Animal Research, 35(1). https://doi.org/10.1186/s42826-019-0006-0

Kozlov, M. (2022). NIH issues a seismic mandate: Share data publicly. *Nature*, *602*(7898), 558–559. https://doi.org/10.1038/d41586-022-00402-1

Kralik, P., & Ricchi, M. (2017). A Basic Guide to Real Time PCR in Microbial Diagnostics: Definitions, Parameters, and Everything. *Frontiers in Microbiology*, *8*, 108. https://doi.org/10.3389/fmicb.2017.00108

La Scola, B., Le Bideau, M., Andreani, J., Hoang, V. T., Grimaldier, C., Colson, P., Gautret, P., & Raoult, D. (2020). Viral RNA load as determined by cell culture as a management tool for discharge of SARS-CoV-2 patients from infectious disease wards. *European Journal of Clinical Microbiology & Infectious Diseases*, *39*(6), 1059–1061. https://doi.org/10.1007/s10096-020-03913-9

Lee, J.-R., Choe, S.-H., Kim, Y.-H., Cho, H.-M., Park, H.-R., Lee, H.-E., Jin, Y. B., Kim, J.-S., Jeong, K. J., Park, S.-J., & Huh, J.-W. (2020). Longitudinal profiling of the blood transcriptome in an African green monkey aging model. Aging, 13(1), 846–864. https://doi.org/10.18632/aging.202190

Li, D., Edwards, R. J., Manne, K., Martinez, D. R., Schäfer, A., Alam, S. M., Wiehe, K., Lu, X., Parks, R., Sutherland, L. L., Oguin, T. H., McDanal, C., Perez, L. G., Mansouri, K., Gobeil, S. M. C., Janowska, K., Stalls, V., Kopp, M., Cai, F., … Saunders, K. O. (2021). In vitro and in vivo functions of SARS-CoV-2 infection-enhancing and neutralizing antibodies. *Cell*, *184*(16), 4203-4219.e32. https://doi.org/10.1016/j.cell.2021.06.021

Lieberman, J. A., Pepper, G., Naccache, S. N., Huang, M.-L., Jerome, K. R., & Greninger, A. L. (2020). Comparison of Commercially Available and Laboratory-Developed Assays for In Vitro Detection of SARS-CoV-2 in Clinical Laboratories. Journal of Clinical Microbiology, 58(8), e00821-20. https://doi.org/10.1128/JCM.00821-20

Liu, W.-D., Chang, S.-Y., Wang, J.-T., Tsai, M.-J., Hung, C.-C., Hsu, C.-L., & Chang, S.-C. (2020). Prolonged virus shedding even after seroconversion in a patient with COVID-19. *Journal of Infection*, *81*(2), 318–356. https://doi.org/10.1016/j.jinf.2020.03.063

Lu, S., Zhao, Y., Yu, W., Yang, Y., Gao, J., Wang, J., Kuang, D., Yang, M., Yang, J., Ma, C., Xu, J., Qian, X., Li, H., Zhao, S., Li, J., Wang, H., Long, H., Zhou, J., Luo, F., … Peng, X. (2020). Comparison of nonhuman primates identified the suitable model for COVID-19. *Signal Transduction and Targeted Therapy*, *5*(1), 157–157. https://doi.org/10.1038/s41392-020-00269-6

Lu, X., Wang, L., Sakthivel, S. K., Whitaker, B., Murray, J., Kamili, S., Lynch, B., Malapati, L., Burke, S. A., Harcourt, J., Tamin, A., Thornburg, N. J., Villanueva, J. M., & Lindstrom, S. (2020). *US CDC Real-Time Reverse Transcription PCR Panel for Detection of Severe Acute Respiratory Syndrome Coronavirus 2*. *26*(8), 1654–1665. https://doi.org/10.3201/eid2608.201246

Matson, M. J., Yinda, C. K., Seifert, S. N., Bushmaker, T., Fischer, R. J., Doremalen, N. van, Lloyd-Smith, J. O., & Munster, V. J. (2020). Effect of Environmental Conditions on SARS-CoV-2 Stability in Human Nasal Mucus and Sputum. *Emerging Infectious Diseases*, *26*(9), 2276–2278. https://doi.org/10.3201/eid2609.202267

Matsuyama, S., Nao, N., Shirato, K., Kawase, M., Saito, S., Takayama, I., Nagata, N., Sekizuka, T., Katoh, H., Kato, F., Sakata, M., Tahara, M., Kutsuna, S., Ohmagari, N., Kuroda, M., Suzuki, T., Kageyama, T., & Takeda, M. (2020). Enhanced isolation of SARS-CoV-2 by TMPRSS2-expressing cells. *Proceedings of the National Academy of Sciences*, *117*(13), 7001–7003. https://doi.org/10.1073/pnas.2002589117

Moher, D., Liberati, A., Tetzlaff, J., & Altman, D. G. (2009). Preferred Reporting Items for Systematic Reviews and Meta-Analyses: The PRISMA Statement. *Annals of Internal Medicine*, *151*(4), 264–269. https://doi.org/10.7326/0003-4819-151-4-200908180-00135

Moreira, L. V. L., Luna, L. K. de S., Barbosa, G. R., Perosa, A. H., Chaves, A. P. C., Conte, D. D., Carvalho, J. M. A., & Bellei, N. (2021). Test on stool samples improves the diagnosis of hospitalized patients: Detection of SARS-CoV-2 genomic and subgenomic RNA. Journal of Infection, 82(5), 186–230. https://doi.org/10.1016/j.jinf.2020.11.034

Munster, V. J., Feldmann, F., Williamson, B. N., van Doremalen, N., Pérez-Pérez, L., Schulz, J., Meade-White, K., Okumura, A., Callison, J., Brumbaugh, B., Avanzato, V. A., Rosenke, R., Hanley, P. W., Saturday, G., Scott, D., Fischer, E. R., & de Wit, E. (2020). Respiratory disease in rhesus macaques inoculated with SARS-CoV-2. *Nature*, *585*(7824), Article 7824. https://doi.org/10.1038/s41586-020-2324-7

Nagata, N., Iwata-Yoshikawa, N., Sano, K., Ainai, A., Shiwa, N., Shirakura, M., Kishida, N., Arita, T., Suzuki, Y., Harada, T., Kawai, Y., Ami, Y., Iida, S., Katano, H., Fujisaki, S., Sekizuka, T., Shimizu, H., Suzuki, T., & Hasegawa, H. (2021). *The peripheral T cell population is associated with pneumonia severity in cynomolgus monkeys experimentally infected with severe acute respiratory syndrome coronavirus 2* (p. 2021.01.07.425698). bioRxiv. https://doi.org/10.1101/2021.01.07.425698

National Primate Research Center. (2020, December 15). *NPRCs Further Collaborations to Overcome Nonhuman Primate Shortage*. https://nprc.org/research/nprcs-further-collaborations-to-overcome-nonhuman-primate-shortage/

Ørpetveit, I., Mikalsen, A. B., Sindre, H., Evensen, Ø., Dannevig, B. H., & Midtlyng, P. J. (2010). Detection of Infectious Pancreatic Necrosis Virus in Subclinically Infected Atlantic Salmon by Virus Isolation in Cell Culture or Real-Time Reverse Transcription Polymerase Chain Reaction: Influence of Sample Preservation and Storage. *Journal of Veterinary Diagnostic Investigation*, *22*(6), 886–895. https://doi.org/10.1177/104063871002200606

Osborn, L. J., Chen, P. Y., Flores-Vazquez, J., Mestas, J., Salas, E., Glucoft, M., Smit, M. A., Costales, C., & Dien Bard, J. (2023). Clinical utility of SARS-CoV-2 subgenomic RT-PCR in a pediatric quaternary care setting. *Journal of Clinical Virology*, *164*, 105494. https://doi.org/10.1016/j.jcv.2023.105494

Patel, A., Walters, J. N., Reuschel, E. L., Schultheis, K., Parzych, E., Gary, E. N., Maricic, I., Purwar, M., Eblimit, Z., Walker, S. N., Guimet, D., Bhojnagarwala, P., Adeniji, O. S., Doan, A., Xu, Z., Elwood, D., Reeder, S. M., Pessaint, L., Kim, K. Y., … Broderick, K. E. (2021). Intradermal-delivered DNA vaccine induces durable immunity mediating a reduction in viral load in a rhesus macaque SARS-CoV-2 challenge model. *Cell Reports Medicine*, *2*(10), 100420. https://doi.org/10.1016/j.xcrm.2021.100420

Perera, R. A. P. M., Tso, E., Tsang, O. T. Y., Tsang, D. N. C., Fung, K., Leung, Y. W. Y., Chin, A. W. H., Chu, D. K. W., Cheng, S. M. S., Poon, L. L. M., Chuang, V. W. M., & Peiris, M. (2020). SARS-CoV-2 Virus Culture and Subgenomic RNA for Respiratory Specimens from Patients with Mild Coronavirus Disease. *Emerging Infectious Diseases*, *26*(11), 2701–2704. https://doi.org/10.3201/eid2611.203219

Poisot, T. (2011). *The digitize package: Extracting numerical data from scatterplots* [Computer software]. http://rjournal.github.io/archive/2011-1/RJournal_2011-1.pdf#page=25

Porter, M. K., Winnett, A. V., Hao, L., Shelby, N., Reyes, J. A., Schlenker, N. W., Romano, A. E., Tognazzini, C., Feaster, M., Goh, Y.-Y., Gale, M., & Ismagilov, R. F. (2023). *The ratio between SARS-CoV-2 RNA viral load and culturable viral titer differs depending on stage of infection* (p. 2023.07.06.23292300). medRxiv. https://doi.org/10.1101/2023.07.06.23292300

Prescott, M. J. (2010). Ethics of primate use. *Advances in Science and Research*, *5*(1), 11–22. https://doi.org/10.5194/asr-5-11-2010

Puhach, O., Meyer, B., & Eckerle, I. (2023). SARS-CoV-2 viral load and shedding kinetics. *Nature Reviews Microbiology*, *21*(3), Article 3. https://doi.org/10.1038/s41579-022-00822-w

R Core Team. (2022). *R: A Language and Environment for Statistical Computing* [Computer software]. R Foundation for Statistical Computing. https://www.R-project.org/

Rodríguez-Grande, C., Adán-Jiménez, J., Catalán, P., Alcalá, L., Estévez, A., Muñoz, P., Pérez-Lago, L., García de Viedma, D., & on behalf of the Gregorio Marañón Microbiology-ID COVID-19 Study Group. (2021). Inference of Active Viral Replication in Cases with Sustained Positive Reverse Transcription-PCR Results for SARS-CoV-2. *Journal of Clinical Microbiology*, *59*(2), e02277-20. https://doi.org/10.1128/JCM.02277-20

Russell, W. M. S., & Burch, R. L. (1959). *The principles of humane experimental technique*. Methuen.

Salguero, F. J., White, A. D., Slack, G. S., Fotheringham, S. A., Bewley, K. R., Gooch, K. E., Longet, S., Humphries, H. E., Watson, R. J., Hunter, L., Ryan, K. A., Hall, Y., Sibley, L., Sarfas, C., Allen, L., Aram, M., Brunt, E., Brown, P., Buttigieg, K. R., … Carroll, M. W. (2021). Comparison of rhesus and cynomolgus macaques as an infection model for COVID-19. *Nature Communications*, *12*(1), Article 1. https://doi.org/10.1038/s41467-021-21389-9

Salvatore, P. P., Dawson, P., Wadhwa, A., Rabold, E. M., Buono, S., Dietrich, E. A., Reses, H. E., Vuong, J., Pawloski, L., Dasu, T., Bhattacharyya, S., Pevzner, E., Hall, A. J., Tate, J. E., & Kirking, H. L. (2021). Epidemiological Correlates of Polymerase Chain Reaction Cycle Threshold Values in the Detection of Severe Acute Respiratory Syndrome Coronavirus 2 (SARS-CoV-2). *Clinical Infectious Diseases*, *72*(11), e761–e767. https://doi.org/10.1093/cid/ciaa1469

Shan, C., Yao, Y.-F., Yang, X.-L., Zhou, Y.-W., Gao, G., Peng, Y., Yang, L., Hu, X., Xiong, J., Jiang, R.-D., Zhang, H.-J., Gao, X.-X., Peng, C., Min, J., Chen, Y., Si, H.-R., Wu, J., Zhou, P., Wang, Y.-Y., … Yuan, Z.-M. (2020). Infection with novel coronavirus (SARS-CoV-2) causes pneumonia in Rhesus macaques. *Cell Research*, 1–8. https://doi.org/10.1038/s41422-020-0364-z

Simmons, H. A. (2016). Age-Associated Pathology in Rhesus Macaques (Macaca mulatta). Veterinary Pathology, 53(2), 399–416. https://doi.org/10.1177/0300985815620628

Singh, D. K., Singh, B., Ganatra, S. R., Gazi, M., Cole, J., Thippeshappa, R., Alfson, K. J., Clemmons, E., Gonzalez, O., Escobedo, R., Lee, T.-H., Chatterjee, A., Goez-Gazi, Y., Sharan, R., Gough, M., Alvarez, C., Blakley, A., Ferdin, J., Bartley, C., … Kaushal, D. (2021). Responses to acute infection with SARS-CoV-2 in the lungs of rhesus macaques, baboons and marmosets. *Nature Microbiology*, *6*(1), Article 1. https://doi.org/10.1038/s41564-020-00841-4

Sivula, T., Magnusson, M., Matamoros, A. A., & Vehtari, A. (2022). *Uncertainty in Bayesian Leave-One-Out Cross-Validation Based Model Comparison* (arXiv:2008.10296). arXiv. https://doi.org/10.48550/arXiv.2008.10296

Smither, S. J., Lear-Rooney, C., Biggins, J., Pettitt, J., Lever, M. S., & Olinger, G. G. (2013). Comparison of the plaque assay and 50% tissue culture infectious dose assay as methods for measuring filovirus infectivity. *Journal of Virological Methods*, *193*(2), 565–571. https://doi.org/10.1016/j.jviromet.2013.05.015

Speranza, E., Williamson, B. N., Feldmann, F., Sturdevant, G. L., Pérez, L. P.-, Meade-White, K., Smith, B. J., Lovaglio, J., Martens, C., Munster, V. J., Okumura, A., Shaia, C., Feldmann, H., Best, S. M., & Wit, E. de. (2021). Single-cell RNA sequencing reveals SARS-CoV-2 infection dynamics in lungs of African green monkeys. *Science Translational Medicine*, *13*(578). https://doi.org/10.1126/scitranslmed.abe8146

Stan Development Team. (2022). *Stan Modeling Language Users Guide and Reference Manual* (Version 2.30) [Computer software]. https://mc-stan.org

Subbaraman, N. (2021). The US is boosting funding for research monkeys in the wake of COVID. *Nature*, *595*(7869), 633–634. https://doi.org/10.1038/d41586-021-01894-z

van Doremalen, N., Lambe, T., Spencer, A., Belij-Rammerstorfer, S., Purushotham, J. N., Port, J. R., Avanzato, V. A., Bushmaker, T., Flaxman, A., Ulaszewska, M., Feldmann, F., Allen, E. R., Sharpe, H., Schulz, J., Holbrook, M., Okumura, A., Meade-White, K., Pérez-Pérez, L., Edwards, N. J., … Munster, V. J. (2020). ChAdOx1 nCoV-19 vaccine prevents SARS-CoV-2 pneumonia in rhesus macaques. *Nature*, 1–8. https://doi.org/10.1038/s41586-020-2608-y

van Kampen, J. J. A., van de Vijver, D. A. M. C., Fraaij, P. L. A., Haagmans, B. L., Lamers, M. M., Okba, N., van den Akker, J. P. C., Endeman, H., Gommers, D. A. M. P. J., Cornelissen, J. J., Hoek, R. A. S., van der Eerden, M. M., Hesselink, D. A., Metselaar, H. J., Verbon, A., de Steenwinkel, J. E. M., Aron, G. I., van Gorp, E. C. M., van Boheemen, S., … van der Eijk, A. A. (2021). Duration and key determinants of infectious virus shedding in hospitalized patients with coronavirus disease-2019 (COVID-19). *Nature Communications*, *12*(1), Article 1. https://doi.org/10.1038/s41467-020-20568-4

Vehtari, A., Gabry, J., Magnusson, M., Yuling, Y., Bürkner, P.-C., Paananen, T., & Gelman, A. (2022). loo: Efficient leave-one-out cross-validation and WAIC for Bayesian models (Version 2.5.1) [Computer software]. https://mc-stan.org/loo/

Vehtari, A., Gelman, A., & Gabry, J. (2017). Practical Bayesian model evaluation using leave-one-out cross-validation and WAIC. Statistics and Computing, 27(5), 1413–1432. https://doi.org/10.1007/s11222-016-9696-4

Verma, R., Kim, E., Martínez-Colón, G. J., Jagannathan, P., Rustagi, A., Parsonnet, J., Bonilla, H., Khosla, C., Holubar, M., Subramanian, A., Singh, U., Maldonado, Y., Blish, C. A., & Andrews, J. R. (2021). SARS-CoV-2 Subgenomic RNA Kinetics in Longitudinal Clinical Samples. *Open Forum Infectious Diseases*, *8*(7), ofab310. https://doi.org/10.1093/ofid/ofab310

Williamson, B. N., Feldmann, F., Schwarz, B., Meade-White, K., Porter, D. P., Schulz, J., van Doremalen, N., Leighton, I., Yinda, C. K., Pérez-Pérez, L., Okumura, A., Lovaglio, J., Hanley, P. W., Saturday, G., Bosio, C. M., Anzick, S., Barbian, K., Cihlar, T., Martens, C., … de Wit, E. (2020). Clinical benefit of remdesivir in rhesus macaques infected with SARS-CoV-2. *Nature*, 1–7. https://doi.org/10.1038/s41586-020-2423-5

Wölfel, R., Corman, V. M., Guggemos, W., Seilmaier, M., Zange, S., Müller, M. A., Niemeyer, D., Jones, T. C., Vollmar, P., Rothe, C., Hoelscher, M., Bleicker, T., Brünink, S., Schneider, J., Ehmann, R., Zwirglmaier, K., Drosten, C., & Wendtner, C. (2020). Virological assessment of hospitalized patients with COVID-2019. *Nature*, *581*(7809), Article 7809. https://doi.org/10.1038/s41586-020-2196-x

Woolsey, C., Borisevich, V., Prasad, A. N., Agans, K. N., Deer, D. J., Dobias, N. S., Heymann, J. C., Foster, S. L., Levine, C. B., Medina, L., Melody, K., Geisbert, J. B., Fenton, K. A., Geisbert, T. W., & Cross, R. W. (2021). Establishment of an African green monkey model for COVID-19 and protection against re-infection. *Nature Immunology*, *22*(1), Article 1. https://doi.org/10.1038/s41590-020-00835-8

Yang, S., & Rothman, R. E. (2004). PCR-based diagnostics for infectious diseases: Uses, limitations, and future applications in acute-care settings. *The Lancet Infectious Diseases*, *4*(6), 337–348. https://doi.org/10.1016/S1473-3099(04)01044-8

Yu, J., Tostanoski, L. H., Peter, L., Mercado, N. B., McMahan, K., Mahrokhian, S. H., Nkolola, J. P., Liu, J., Li, Z., Chandrashekar, A., Martinez, D. R., Loos, C., Atyeo, C., Fischinger, S., Burke, J. S., Slein, M. D., Chen, Y., Zuiani, A., N. Lelis, F. J., … Barouch, D. H. (2020). DNA vaccine protection against SARS-CoV-2 in rhesus macaques. *Science*, eabc6284–eabc6284. https://doi.org/10.1126/science.abc6284

Yuan, L., Tang, Q., Zhu, H., Guan, Y., Cheng, T., & Xia, N. (2021). SARS-CoV-2 infection and disease outcomes in non-human primate models: Advances and implications. *Emerging Microbes & Infections*, *10*(1), 1881–1889. https://doi.org/10.1080/22221751.2021.1976598

Zhang, C., Cui, H., Guo, Z., Chen, Z., Yan, F., Li, Y., Liu, J., Gao, Y., & Zhang, C. (2022). SARS-CoV-2 Virus Culture, Genomic and Subgenomic RNA Load, and Rapid Antigen Test in Experimentally Infected Syrian Hamsters. *Journal of Virology*, *96*(18), e01034-22. https://doi.org/10.1128/jvi.01034-22

Chapter 2. Exposure route and dose shape SARS-CoV-2 infection patterns in non-human primates

Abstract

Disease severity and shedding kinetics can differ widely among individuals infected with the same pathogen, but the biological drivers of this variation remain largely unknown. In this study, using an unprecedented database of non-human primate challenge experiments (107 studies; 721 animals; 22,183 observations), we demonstrate that the route and dose of exposure shape within-host SARS-CoV-2 infection patterns in the respiratory and gastrointestinal tracts. Exposed tissues exhibited distinct spatiotemporal dynamics from non-exposed tissues, with aerosol inoculation resulting in the highest nasal and gastrointestinal shedding but the lowest lung severity compared to other routes. Median infectious doses (ID50) ranged from $<10^1$ up to $>10^{7.4}$ pfu depending on the exposure route, tissue sampled, and detection assay. Dose effects on temporal infection patterns were also highly route- and location-specific, with larger doses increasing shedding primarily for nasally-challenged animals. Our results provide a foundation and direction to uncover the unifying principles that govern the dynamics of respiratory pathogens inside hosts.

Introduction

A pathogen's transmissibility and pathogenicity are both strongly governed by spatiotemporal patterns of infection within a host. These 'within-host dynamics' can differ widely among pathogens (McCall 2021), and even among individuals infected with the same pathogen. Epidemiologists and microbiologists have long understood that the dose and route of exposure contribute to this individual-level variability, alongside other demographic and health factors. Larger doses are generally believed to have higher infection probabilities and lead to enhanced disease severity (Bradburne et al., 1967; de Wit et al., 2011; Marois et al., 2012; Memoli et al., 2015; Tao et al., 2015). This theory is tied to many public health and research practices, including the estimation of 50% infectious and lethal doses (ID50, LD50; Mitchell et al., 2020; Watanabe et al., 2010), historical variolation procedures (Riedel, 2005), and modern discussions about whether masking reduces COVID-19 severity (Gandhi & Rutherford, 2020). The effects of route are studied less frequently, but ID50 estimates have varied by route (e.g., influenza A; Couch et al., 1966; Tellier, 2006) and severity is known to be route-specific for some pathogens (e.g., bubonic vs. pneumonic plague; Pechous et al., 2016; skin-scratch vs. inhalational smallpox, which is also related to variolation; Riedel, 2005). Animal challenge experiments have found evidence that within-host tissue dissemination, temporal patterns of infection, and shedding profiles can be both dose- and route-dependent (Althouse et al., 2014; de Wit et al., 2011; Dudley et al., 2017; Port et al., 2021; Tao et al., 2015) – all of which is consistent with ecological theory for population invasions (Lockwood et al., 2005; Schreiber & Lloyd-Smith, 2009; Snedden et al., 2021). Yet many fundamental questions remain unanswered. How do dose and route of exposure determine the extent and timing of within-host dissemination patterns? Do shedding and severity vary with

exposure dose, and is this pattern route-specific? Does individual-level variation in infections arise chiefly from exposure conditions or host characteristics?

These knowledge gaps about such important questions arise, at least partially, from sampling constraints and data limitations. For humans, natural exposure events are inherently unobservable, and available data can be biased towards individuals with more severe disease that seek treatment, though rare exceptions exist (e.g., human challenge trials; Killingley et al., 2022; prospective testing of focal communities; Mack et al., 2021). Animal challenge experiments can control the relevant dimensions, but they either have limited clinical relevance due to crucial physiological differences with humans (e.g., for small animal models) or their small sample sizes cannot support robust statistical comparisons under the standard approach of analyzing data only within the study that generated them (e.g., for non-human primate models). In order to extract more insights from costly animal experiments and help improve human health, novel analytical methods are needed to overcome these translational and statistical limitations.

When viewing the literature holistically, animal infection experiments have generated an immense amount of data and contributed irreplaceable insights into pathogen-host biology, despite small sample sizes per individual study. Although there are many potential benefits of jointly analyzing these data (Kieran et al., 2024), such meta-analyses are exceptionally rare due to concerns about variable protocols across laboratory groups. However, meta-analytic and Bayesian methods that account for study-specific differences have enabled robust advances across scientific disciplines, including in ecology (Anton et al., 2019), virological diagnostics (Snedden & Lloyd-Smith, 2024), and other fields that rely on animal research (e.g., neurobiology; Bonapersona et al., 2021). These modern statistical tools could resolve standing questions in microbiology that are

infeasible to address within individual experiments, including uncovering the determinants of within-host kinetics, without requiring any additional use of animal models.

In this study, to our knowledge, we completed the largest-ever quantitative meta-analysis of within-host infection patterns for a respiratory pathogen in non-human primates (NHPs). We built a database of SARS-CoV-2 challenge experiments, including 107 published studies, 721 individual NHPs, and 22,183 observations. We characterized and compared the effects of exposure dose, exposure route, and demographic factors (age, sex, species) on the probability, onset, peak, and conclusion of detectable infection across the upper respiratory, lower respiratory, and gastrointestinal tracts. With these analyses, we identified exposure conditions as the primary drivers of variation in within-host SARS-CoV-2 infection patterns in an important animal model with similar respiratory physiology and immune responses as humans (Estes et al., 2018). We demonstrated that the effects of dose (including ID50 values) are route- and location-specific and that aerosol inoculation results in significantly different spatiotemporal kinetics as well as disparate shedding profiles than all other tested exposure routes.

Methods

Database compilation

We have previously described the construction of our core database (Snedden & Lloyd-Smith, 2024, which is also Chapter 1), which contains SARS-CoV-2 viral load and infectious virus data from non-human primate experiments. We expanded the database for this study by conducting another systematic literature search with the same keywords. The first search included articles from January 1, 2020 through March 11, 2021, and the second search spanned March 12, 2021 through April 9, 2024 (Figure S2.1). For both searches, we identified articles that met the following criteria: (i) they experimentally infected rhesus macaques (*Macaca mulatta*), cynomolgus macaques (*Macaca fascicularis*), or African green monkeys (*Chlorocebus sabaeus*) with SARS-CoV-2 (restricted to basal strains, excluding any studies that reported a named variant), and (ii) they published quantitative or qualitative measurements of viral load (measured by RT-qPCR) or infectious virus (measured by plaque assay or endpoint titration) from at least one biological specimen for at least one individual and at least one sample time post infection.

Of the studies that met our criteria during the first search, single-route exposures (e.g., intranasal only, aerosol) were the least common and had more limited dose ranges. To increase sample sizes for these crucial exposures, we only considered studies with single-route exposures during our second search. Altogether, our database includes 107 articles (Figure S2.1; Table S2.1). For both searches, raw data were used when available (published or obtained via email correspondence); otherwise, one author (CES) extracted data from published figures using the package ‘digitize’(Poisot, 2011) in R (R Core Team, 2022).

The 107 articles included in the database are: An et al., 2022; Arunachalam et al., 2021; Baum et al., 2020; Berry et al., 2022; Bewley et al., 2021; Bixler et al., 2022; Blair et al., 2021; Böszörményi et al., 2021; Brouwer et al., 2021; Chandrashekar et al., 2020; Chen et al., 2021; Corbett et al., 2020; Cross et al., 2020, 2021; Dabisch et al., 2021; Dagotto et al., 2021; Deng, Bao, Gao, et al., 2020; Deng, Bao, Liu, et al., 2020; Fahlberg et al., 2020; Fears et al., 2022; Feng et al., 2020; Finch et al., 2020; Fischer et al., 2024; Francica et al., 2021; Furuyama et al., 2022; Gabitzsch et al., 2021; Gao et al., 2020; Gorman et al., 2021; C. Gu et al., 2021; S. H. Gu et al., 2020; Guebre-Xabier et al., 2020; Q. Guo et al., 2021; Y. Guo et al., 2021; Hassan et al., 2021; He et al., 2021; Hoang et al., 2021; Huang et al., 2021; Ishigaki et al., 2021; Ishii et al., 2022; Jiao, Li, et al., 2021; Jiao, Yang, et al., 2021; Johnston et al., 2021; B. E. Jones et al., 2021; Kim et al., 2021; Kobiyama et al., 2021; Koo et al., 2020; Lakshmanappa et al., 2021; Lambe et al., 2021; D. Li, Edwards, et al., 2021; D. Li, Luan, et al., 2021; M. Li, Guo, et al., 2021; Y. Li, Bi, et al., 2021; Liang et al., 2021; J.-F. Liu et al., 2022; X. Liu et al., 2022; Z. Liu et al., 2022; Lu et al., 2020, 2021; Ma et al., 2022; Maisonnasse et al., 2020, 2021; McMahan et al., 2021; Mercado et al., 2020; Munster et al., 2020; Nagata et al., 2021; Nawaz et al., 2020; Nomura et al., 2021; Pan et al., 2021; Patel et al., 2021; Philippens et al., 2022; Qin et al., 2020; Rauch et al., 2020; Rockx et al., 2020; Roozendaal et al., 2021; Rosenke et al., 2020; Rosenke et al., 2021; Routhu et al., 2021; Salguero et al., 2021; Sanchez-Felipe et al., 2021; Saunders et al., 2021; Seo et al., 2021; Shan et al., 2020; Shi et al., 2020; Singh et al., 2021; Sokol et al., 2021; Song et al., 2020, 2021; Speranza et al., 2021; C. Sun et al., 2023; S. Sun, Cai, et al., 2021; S. Sun, He, et al., 2021; J. Y. J. Tan et al., 2023; S. Tan et al., 2023; van Doremalen et al., 2020; Vogel et al., 2021; G. Wang et al., 2021; H. Wang et al., 2020; S. Wang et al., 2020; Z. Wang et al., 2022; Williamson et al., 2020; Woolsey et al.,

2021; Yadav, Ella, et al., 2021; Yadav, Kumar, et al., 2021; Yao et al., 2021; Yang et al., 2020; J. Yu et al., 2020; J. Yu et al., 2022; P. Yu et al., 2020; Zheng et al., 2020; Zost et al., 2020.

Anatomical characterization

In this study, our analyses focused on the nose, throat, trachea, lung, upper gastrointestinal tract, and the lower gastrointestinal tract (GI). We categorized all reported sample types into these six tissue categories, and we distinguished between invasive and non-invasive sampling methods (Table S2.3). We also grouped the six tissues into three broader categories as follows: (i) upper respiratory tract: nose and throat; (ii) lower respiratory tract: trachea and lung; and (iii) gastrointestinal tract: upper and lower GI. We refer to these broad tissue categories as 'organ groups.'

Key metrics for characterizing kinetics

To guide our analysis, we selected five key metrics to characterize within-host infection kinetics in any given tissue for any individual, namely: (i) the probability of ever testing positive, (ii) the time until becoming detectably infected, (iii) the time until reaching the peak titer, (iv) the quantitative peak titer, and (v) the time until the infection becomes undetectable (Figure 2.1c). From the five primary metrics, we also calculated the duration of detectable infection (the time elapsed between becoming detectable and undetectable) and the area under the infection curve (0.5 * the duration of detectable infection * the peak titer). We extracted all of these metrics for the following five primary tissues that can be sampled repeatedly by non-invasive methods: nose, throat, trachea, lung, and the lower gastrointestinal tract. For the upper gastrointestinal tract, which was only accessible by invasive methods, we only estimated the probability of testing positive and the time until becoming detectably infected.

Extracting metrics for all individuals

Given that sampling occurs at discrete times, our metrics cannot be observed exactly. To account for this, we extracted bounded intervals during which the events could have occurred for every individual that had data for any given tissue location and assay type. Brief descriptions of these extraction methods are outlined below for each metric, with example individuals illustrated in Figure 2.1D.

Probability of testing positive and time to detectability. For all individuals that tested positive in a given tissue location for a given assay, we bounded their time to detectability between the day of their first observed positive test and the day of their previous negative test. For individuals that never tested positive in that tissue for that assay, we considered two possibilities: either the individual would have never tested positive, or they would have tested positive if observed later post infection. In the latter case, we assumed that their time to detectability must be bounded between their last observed negative test and day forty-five post infection, reflecting that a month and a half (or more) delay for initial positivity is highly unlikely.

Peak time and peak titer. For all individuals with positive quantitative titers for at least two days post inoculation, we identified the day with their largest observed titer. We used the previous and subsequent sampling days as the lower and upper bounds, respectively, for that individual's time to peak titer. If the individual's highest titer was observed on the final sampling day, then we set the upper bound as day fifty post infection. We used the titer from the observed peak time for the peak titer model.

Time to undetectability. For all individuals with at least one negative sample after their final observed positive sample, we bounded their time to undetectability between the day of their last observed positive sample and their subsequent (negative) sample. If an individual tested

positive on their final sample day, then we set their upper bound as day fifty-five post infection, reflecting that prolonged infection beyond approximately two months post inoculation is highly unlikely in otherwise healthy animals.

Modeling framework

Survival analysis methods can estimate event times from bounded (or 'censored') observations (Bogaerts et al., 2017). We used these techniques as a basis to develop our Bayesian model, given that, during animal infection experiments, samples are collected at discrete times to study an on-going infection process. As described above, we characterized within-host kinetics for all considered tissues according to three event times: the time to viral detectability (TD), the time to peak viral titer (TP), and the time to viral undetectability (TU). We used an accelerated failure time model for all three, where we assumed that the time delay between any two sequential events (i.e., between inoculation and TD, between TD and TP, and between TP and TU) was distributed according to the Weibull distribution, which allows for flexible event time distributions. We fit our model to the median of each distribution, which is given by the equation $\lambda(\ln 2)^{1/k}$, where λ is the Weibull scale parameter and k is the Weibull shape parameter. We assumed that the medians were predicted by a linear combination of a set of j covariates (X_j; see next section), all with their own unique regression coefficients ($\beta_{TD,j}$, $\beta_{TP,j}$, $\beta_{TU,j}$). On top of those standard covariates, the time to peak titer had an additional term that captured any dependence on the time to detectability ($\beta_{TP,TD}$TD), and the time to undetectability had an additional term to capture any dependence on the peak titer ($\beta_{TU,PT}$PT). We also estimated Weibull shape parameters (k_{TD}, k_{TP}, k_{TU}) that were shared among cofactors but unique to each event time and organ group. For numerical stability, we required that these shape parameters be greater than or equal to one.

To capture that some individuals may never test positive (e.g., because of failed infection in a given tissue or low assay sensitivity), we adapted our time to detectability model into a mixture cure model (Amico & Keilegom, 2018) that also estimated whether an individual will ever test positive (P) in a given location. We assumed that P was Bernoulli distributed with probability p, which is predicted by a linear combination of the standard j covariates ($\beta_P X_P$) with a logit link function. Thus, the overall probability that an individual will test positive by a given time *t,* which we represent by the function S(*t*), depends both on p as well as the probability of testing positive by time *t* when conditioned on ever testing positive ($S_p(t)$). All other metrics are conditional on the individual ever testing positive.

We modeled peak titers differently, as they are not event times. We assumed that all true peak titer values (in log10 units; PT_{true}) are normally distributed, where the mean is a linear combination of our standard j covariates with their own regression coefficients ($\beta_{PT} X_{PT}$). We included an additional term to capture any dependence of the peak titer on the time to peak titer ($\beta_{PT,TP}$TP). We allowed this relationship to differ between exposed and not exposed tissues, because exposed tissues often peak within the first day, possibly due to resampling the inoculum. The standard deviation of these titers (σ_{PT}) is specific to the tissue group (URT, LRT, GI). Given that an individual's true peak titer likely differs from their observed largest titer (PT_{obs}), we treated PT_{obs} as normally distributed around the sum of PT_{true} and an article- and assay-specific offset ($\delta_{lab,assay}$).

To capture quantitative differences in all metrics due to methodological variation among articles, we included linear offset terms for article and assay effects (see *Covariates* for more details). We also allowed the standard deviations of the observed peak titers to differ across

articles, given that sampling schemes and other methodological choices may affect variability in observed titers.

Below is the general form of this model, where α are the intercept parameters and all other parameters are described above.

$$S(t) = (1 - p) + p\ S_p(t)$$

$$P \sim \textit{Bernoulli}\ (p)$$

$$p = \text{logit}^{-1}(\alpha_P + \sum_j \beta_{P,j} X_j)$$

$$TD \sim \textit{Weibull}\ (\lambda_{TD}, k_{TD})$$

$$\textit{Median}(TD) = \exp(\alpha_{TD} + \sum_j \beta_{TD,j} X_j)$$

$$TP \sim \textit{Weibull}\ (\lambda_{TP}, k_{TP})$$

$$\textit{Median}(TP) = \exp(\alpha_{TP} + \beta_{TP,TD}\ TD + \sum_j \beta_{TP,j} X_j)$$

$$TU \sim \textit{Weibull}\ (\lambda_{TU}, k_{TU})$$

$$\textit{Median}(TU) = \exp(\alpha_{TU} + \beta_{TU,TP}\ TP + \sum_j \beta_{TU,j} X_j)$$

$$PT_{true} \sim \textit{Normal}(\alpha_{PT} + \beta_{PT,TP}\ TP + \sum_j \beta_{PT,j} X_j, \sigma_{PT})$$

$$PT_{obs} \sim \textit{Normal}(PT_{true} + \delta_{lab,assay}, \exp(\sigma + \sigma_{lab,assay}))$$

As described above, we cannot exactly observe when an individual experiences their three true event times ($TD_{true,i}$, $TP_{true,i}$, $TU_{true,i}$). Instead, we treated them as bounded quantities, such that the true time for any individual *i* occurs within their lower and upper bound (e.g., [$LB_{TD,i}$, $UB_{TD,i}$] for TD_i). Each individual's true times must occur within these intervals, where the probabilities of any given event time within that interval are given (as above) by the Weibull distribution for their

unique combination of cofactors (e.g., $TD_{true,i} \sim Weibull(\lambda_{TD,i}, k_{TD})$ where the median is $exp(\alpha_{TD} + \sum_j \beta_{TD,j,i} X_{j,i})$).

Covariates

We allowed all of our metrics to vary across multiple covariates, which have been hypothesized to influence within-host kinetics. All categorical cofactors with more than two groups (exposure route, age, species, article, assay) were treated as unordered index variables. Binary predictors (sex, tissue location) were treated as indicator variables. When age, sex, assay, or tissue location (within an organ group) were unknown, we marginalized over all possibilities.

Biological cofactors

We included exposure route as a categorical cofactor with the following classifications: (i) upper respiratory exposure, (ii) lower respiratory exposure, (iii) combined upper and lower respiratory exposure via liquid administration, (iv) combined upper and lower respiratory exposure via aerosol inhalation, and (v) upper gastrointestinal exposure. We grouped all reported inoculation routes (e.g., ocular, intranasal) into these categories (Table S2.2). For all analyses, we generated predictions for the following representative route for each category: (i) intranasal, (ii) intratracheal, (iii) equal combination of intranasal and intratracheal, (iv) aerosol, and (v) intragastric.

We included exposure dose by stratifying the total inoculation dose (in log10 pfu) into location-specific categories. For every individual, we calculated the dose administered specifically to the nose, throat, trachea, lung, and stomach. We assumed that the total dose was split among locations for each inoculation route as follows: (i) ocular: 100% nose; (ii) intranasal: 50% nose, 50% throat; (iii) oral: 100% throat; (iv) intratracheal: 100% trachea; (v) intrabronchial: 100% lung; (vi) aerosol: 25% nose, 25% throat, 25% trachea, 25% lung; and (vii) intragastric: 100% stomach.

We assumed ocular inoculation resulted in nasal exposure, given that fluids administered to the eye rapidly drain into the nose via the nasolacrimal duct (Belser et al., 2013). A small number of studies included intravenous inoculation in addition to other routes (Table S2.2), but we did not include a parameter in our model for this route given small sample sizes. When studies reported inoculation dose as TCID50 values, we converted to pfu using a standard conversion factor (1 TCID50=0.69 pfu; Carter & Saunders, 2007).

We included age, sex, and non-human primate species as our demographic effects. For species, we distinguished between rhesus macaques, cynomolgus macaques, and African green monkeys. For age class, we distinguished between juvenile, adult, and geriatric individuals, where we assigned age classes as described in Snedden & Lloyd-Smith, 2024. Briefly, ages less than 5 years were considered juveniles for all three species. Adults included ages 5-19 years for both macaque species and 5-14 for African green monkeys. All older individuals were geriatrics.

Finally, we included a binary predictor for tissue location to account for differences between the two distinct tissues studied within an organ group (i.e., for nose and throat in the model of the upper respiratory tract, and for the trachea and lung in the model of the lower respiratory tract).

Methodological cofactors

We incorporated multiple cofactors to handle methodological variation among articles. Given that virus detection and virus quantification can vary across assays (e.g., PCR vs. virus culture), we included a cofactor for assay type with the following four categories based on our prior work (Snedden & Lloyd-Smith, 2024): (i) total RNA assays targeting the N gene, (ii) any genomic RNA assay or total RNA assays targeting less expressed genes, (iii) sgRNA assays, and

(iv) culture assays. When presenting results for a total RNA or culture assay, we use categories (i) and (iv), respectively. To account for differences in other methodological factors among articles (e.g., RNA extraction methods, viral strains), we included a linear term for each article and assay combination. For example, if an article included data from both a total RNA and a culture assay, then that article would have its own unique offset term for each assay.

Parameter sharing within organ groups

Each organ group (upper respiratory, lower respiratory, and gastrointestinal tracts) has their own set of equations, such that, for example, the nose and throat share most regression coefficients with each other, but they do not share any with the lower respiratory or gastrointestinal tissues. In particular, the following parameters are shared within organ groups: intercepts, demographic effects (age, sex, species), location effect, assay effects, lab effects, and the dependence on previous metrics (i.e., $\beta_{TP,TD}$, $\beta_{PT,TP,}$ $\beta_{TU,TP}$).

Cofactor combinations

When generating predictions from our model, it is necessary to choose a route, dose, age, sex, and species of interest. For most of our analyses and unless otherwise specified, we focus on total doses of 10^4 and 10^7 pfu. Given there are five exposure route categories, two focal dose values, three species, three ages, and two sexes, there are 180 possible combinations of cofactors to choose from. We refer to any one of these 180 options as an individual 'cofactor combination.' In many of our analyses, we report results that include predictions for all 180 possible cofactor combinations, or for more combinations when we consider additional doses (e.g., in Figure 2.2). In some cases, we report results for a 'standard cofactor combination,' which corresponds to the following: an adult, male rhesus macaque.

Prior probabilities

For all covariates in our model, we used weakly informative priors to exclude implausible relationships, but we made no *a priori* prediction on the direction of those individual effects (i.e., the priors for each cofactor were centered on zero). The only exception was for the relationship between dose and probability of positivity (see above). Prior predictive simulations confirmed variable but reasonable expectations for all metrics.

Model predictions and determining significance

Unless otherwise noted, we used at least 100 post-warmup parameter samples to generate predictions for each cofactor combination for all presented results. Each prediction is generated using grouped parameter samples (e.g., samples from the same chain and iteration) to preserve correlation structure. We also assume there is no article effect when generating predictions, unless otherwise stated (i.e., we set all article terms to zero). To determine whether any differences in predictions were significant, we analyzed 90% prediction intervals. If they did not include zero, then we considered the difference to be significant.

Ranking the importance of biological cofactors

To determine which biological cofactors had the largest impact on each metric for each tissue, we generated predictions for all cofactor combinations. From these predictions, we calculated the differences for all possible pairwise combinations of the categories within each cofactor (e.g., juvenile vs. adult, adult vs. geriatric, and juvenile vs. geriatric for age). Then, for each cofactor and metric, we computed the mean value of their differences. The cofactor with the largest such mean for a given metric thus had the largest average difference among its categories and thus exerted the greatest influence on that given metric. We assigned this cofactor an effect of

'1' for that metric. Finally, we calculated metric-specific relative effects for all other cofactors by scaling their mean differences by the largest mean difference.

Computational methods and software

All data preparation, analysis, and plotting were completed with R version 4.2.0. Posterior sampling of the Bayesian model was performed with No-U-Turn Sampling (NUTS) via the probabilistic programming language Stan using the interface CmdStanR version 0.5.2. All model fits were generated by running six replicate chains with 2000 iterations each, of which the first 1000 iterations were treated as the warmup period and the final 1000 iterations were used to generate parameter estimates. Model convergence was assessed by the sampling software using $\hat{R}$, effective sample sizes, and other diagnostic measures employed by CmdStan by default. No issues were detected.

Results

Data and model overview

During our comprehensive literature search, we identified 107 articles that reported viral RNA load or infectious virus for at least one biological specimen from an NHP challenged with ancestral SARS-CoV-2 strains (i.e., ones that circulated prior to the emergence of Alpha variants; Figure S2.1; Table S2.1). From these studies, we extracted 22,183 observations from 721 animals across the respiratory, gastrointestinal, and other systems (Figure 2.1a). This includes many different exposure routes, a range of exposure doses ($10^{1.2}$-$10^{7.4}$ pfu), three NHP species (rhesus macaque, cynomolgus macaque, African green monkey), both sexes, and three age classes (juvenile, adult, geriatric).

Our analyses focused on the nose, throat, trachea, lung, upper gastrointestinal tract, and lower gastrointestinal tract (Figure 2.1b; see Table S2.3 for the sample types available for each included tissue). In each location, we characterized infection by: (i) the probability of ever testing positive, (ii) the time to viral detectability, (iii) the time to peak viral titer, (iv) the peak titer itself, and (v) the time to undetectability (Figure 2.1c). From these metrics, we also calculated the duration of infection and the area under the infection curve (AUC). Due to sampling constraints, each event is not directly observable. However, for any given animal in our database, we bounded each metric within an interval based on their sampling dates, first observed positive, largest observed titer, and last observed positive (examples in Figure 2.1d; sample sizes in Figure 2.1e). This censoring approach allows us to explicitly account for differences in sampling times and frequency across tissues and studies. We used these observations to fit our Bayesian time-to-event model, which estimates the effects of exposure conditions (dose, route), demographic factors (age,

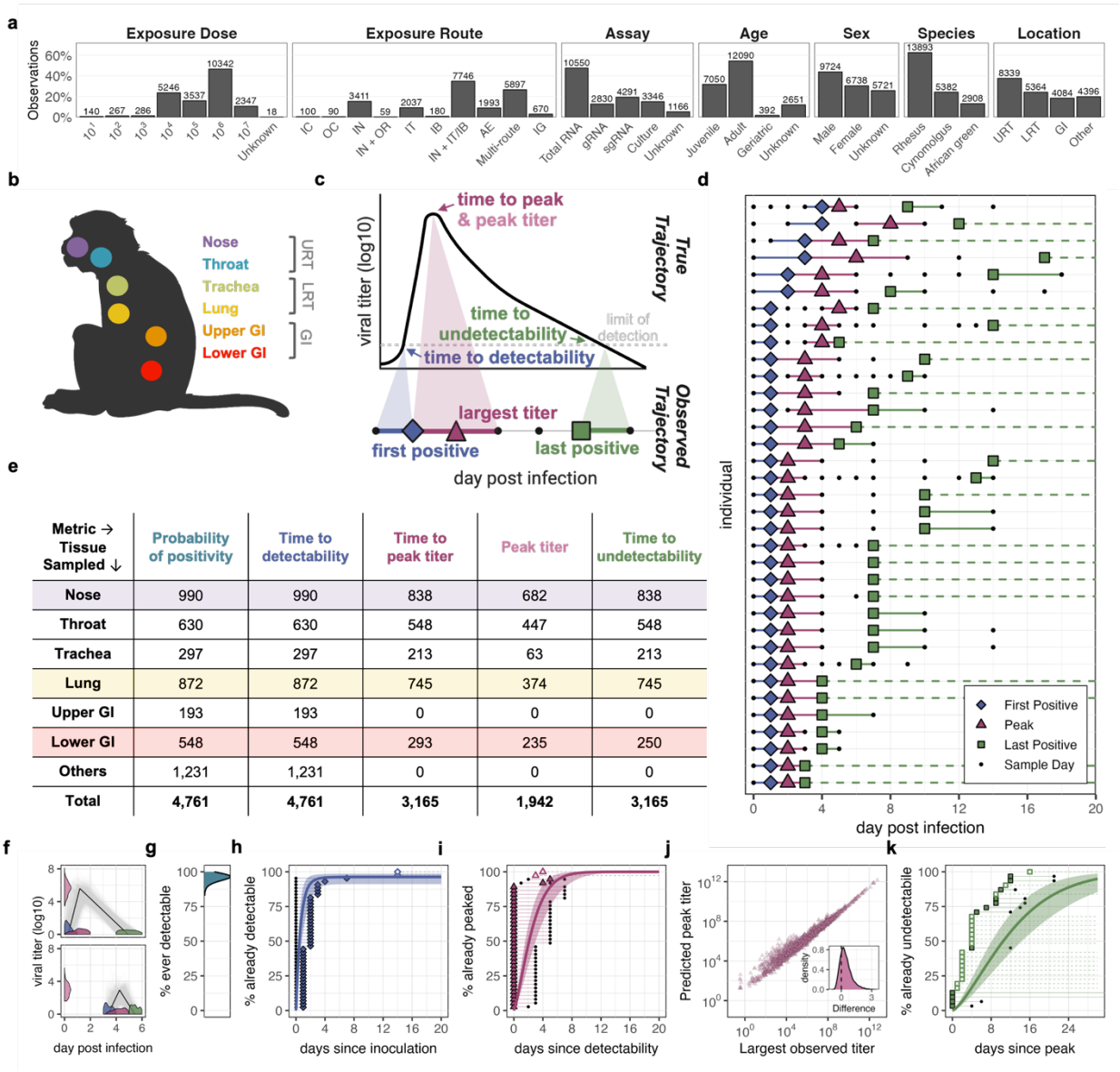

Metric → Tissue Sampled ↓	Probability of positivity	Time to detectability	Time to peak titer	Peak titer	Time to undetectability
Nose	990	990	838	682	838
Throat	630	630	548	447	548
Trachea	297	297	213	63	213
Lung	872	872	745	374	745
Upper GI	193	193	0	0	0
Lower GI	548	548	293	235	250
Others	1,231	1,231	0	0	0
Total	**4,761**	**4,761**	**3,165**	**1,942**	**3,165**

Figure 2.1 | Overview of data and modeling approach.
a, Data distribution across key cofactors in the full database. Bar heights give the percentage of all samples, and annotated numbers give the total number of observations. Exposure route acronyms are as follows: IC, intracranial; OC, ocular; IN, intranasal; OR, oral; IT, intratracheal; IB, intrabronchial; AE, aerosol; IG, intragastric. Multi-route includes all exposures via three or more distinct locations. **b**, Diagram of the six primary tissues, grouped into three categories: URT, upper respiratory tract, LRT, lower respiratory tract, GI, gastrointestinal tract. **c**, Diagram of the key metrics on a hypothetical time series (not pictured: probability of positivity). The true continuous trajectory (top) contains labels for the key metrics. The observed trajectory (bottom) includes the observed event times (first positive, diamond; largest titer, triangle; last positive, square) and all other sampling days (black days). Each event time is censored and must occur within the time range indicated by the bold colored lines, which are connected to the corresponding true times by

shaded regions. **d**, A small subset of the available time series from our database, classified by bounded event times and colored as in panel c. Each row is a unique individual. Solid lines correspond to interval-censored observations. Dashed lines indicate the individual was positive on their final sample day, so their event is right censored. **e**, Sample sizes across tissues and metrics. Tissues with shaded rows are the primary focus for the analyses in this study. **f**, Model predictions for two individuals' event times and peak titers. Densities give the estimated probabilities for a given time or titer (colored as in panel c). The black line gives the individual's median inferred trajectory, with 300 samples of the posteriors shown in gray. **g**, Model predictions for the percent of individuals that will ever test positive, corresponding with the observed event times in panel h. **h, i, k**, Median model fit (bold line) and 90% credible intervals (shaded regions) against individual bounded event times (points in rows) for (h) the times to detectability, (j) peak titer, and (k) undetectability. The y axis displays the percent of individuals predicted to have experienced the event by the given days since the previous event. Predictions in each panel were based on 100 posterior samples each for all possible combinations of age, sex, species, and doses ranging from 10^4-10^7 (in increments of 1 order of magnitude), specifically for IN-exposed individuals sampled by a total RNA assay targeting the N gene. The plotted data are also restricted to these cofactors (but allowing all PCR assays). Models are fit to the censored intervals and not to the symbols. Filled points are interval-censored observations, and open points with dashed lines are right-censored observations. See Figures S2.2-2.4 for the fits for all other routes and assays. **j**, Relationship between the largest observed titer and the mean true peak titer predicted by the model. Each point is an individual sampled in a given tissue by a given assay. The inset shows the distribution of differences between the true and observed titers.

sex, species), and methodological variation (assay, unique random effects for each article) on overall infection patterns while also inferring true event times and peak titers for each individual (see examples in Figure 2.1f). Formally, we fit each event as a delay from the previous event (e.g., days between detectability and peak titer; Figure 2.1g,h,j), but for interpretability we report results in calendar days since inoculation.

The model fits the data well for all metrics, generating predictions that are highly concordant with the observed number of positive individuals (Figure 2.1g;S2.2) and the bounded event times (Figure 2.1g,h,j;S2.2-S2.4). Predicted peak titers are highly correlated with the largest observed titers (r=0.98; Figure 2.1i), where estimated peak titers are, on average, 0.44 log10 titer units (TCID50 or pfu) larger than the largest measured titers (Figure 2.1i,inset). This reflects the reality that it is highly unlikely to sample exactly when an individual peaks, and so the largest

observed value reflects an individual's still-increasing or already-decreasing viral load. Notably, model predictions for all metrics differed more among assays than across all other sources of article-level variation combined (Figure S2.5). Subsequent analyses report results for a baseline study (i.e., controlling for article effects but not visualizing them).

Infection patterns are highly variable within tissues

Infection patterns varied substantially within each tissue (Figure 2.2) when considering model predictions for all 380 possible combinations of exposure conditions and demographic groups (termed 'cofactor combinations'; e.g., female adult rhesus macaques intranasally challenged with 10^4 pfu). The median probability of an animal ever testing culture positive in specimens from a given tissue exhibited up to a 6.5-fold change among all cofactor combinations (squares in the top row of Figure 2.2a), corresponding to a 72.5% difference in the probability (Figure 2.2b,c). Temporal metrics based on infectious virus measurements in specimens exhibited fold changes from 1.7 to 6.2, with raw differences ranging from 0.8 days to 13.3 days (Figure 2.2a,b). This variation resulted in highly heterogeneous median infection trajectories within each tissue, especially in the gastrointestinal (GI) and lower respiratory (LRT) tracts (Figure 2.2d). Individual-level trajectories (i.e., sampling from the full posterior distributions on event times instead of their central tendencies; Methods) are even more variable (Figure S2.6). Total viral RNA data exhibited similar fold changes to culture data for all metrics except the probability of positivity (circles in Figure 2.2a); for all tissues, RNA positivity is much more likely than culture positivity (Figure 2.2c).

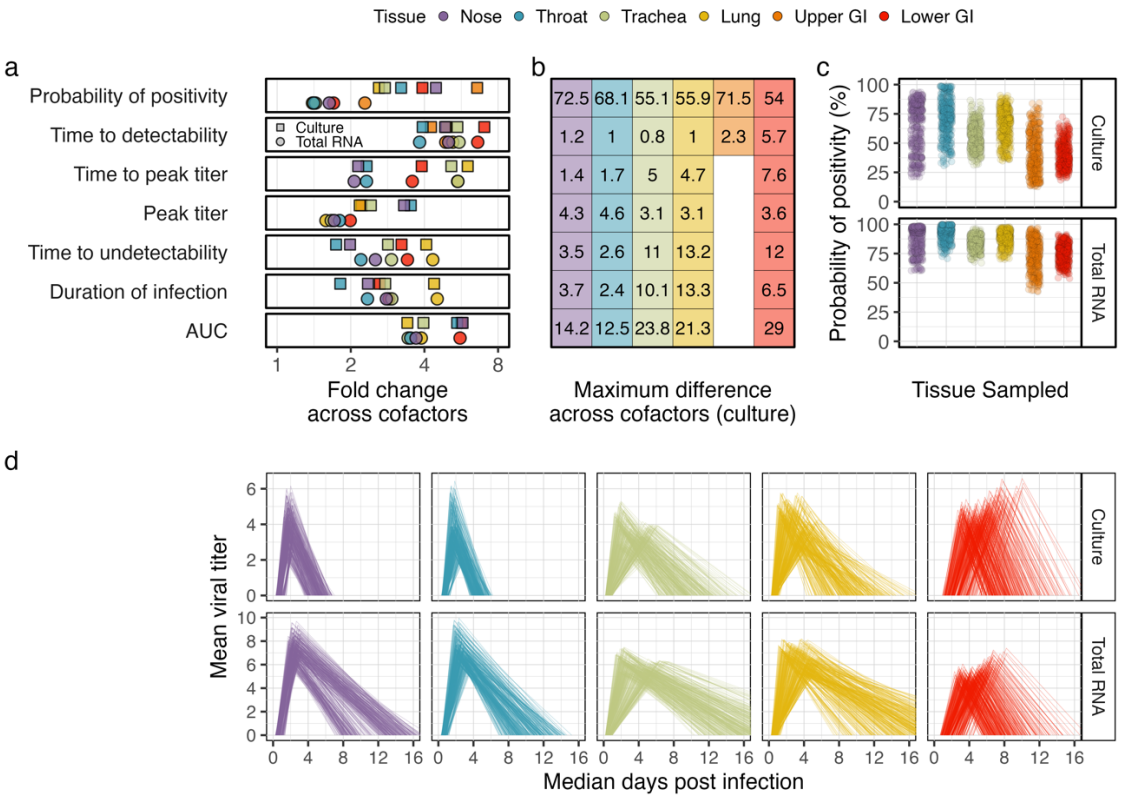

Figure 2.2 | Infection dynamics within tissues are highly heterogeneous.
Colors in all panels distinguish between sampled tissues, as indicated in the legend at the top. Model predictions were generated and compared for all possible combinations of age, sex, species, exposure route, and exposure dose (including 10^4, 10^5, 10^6, and 10^7 pfu). The Upper GI is only accessible by invasive sampling, so we could only estimate the probability of positivity and the time to detectability for this tissue. The Lower GI can be sampled non-invasively (e.g., via rectal swabs), so we were able to estimate all metrics (see Table S2.3 for all sample types available for each included tissue). **a**, Fold changes in predictions between the cofactor combinations with the smallest and largest median predictions for each metric (rows). Each point corresponds to one tissue. Squares and circles display results for culture and total RNA assays, respectively. Fold changes were similar though often smaller when restricting analyses only to the cofactor combinations with data that was available for fitting the model. **b**, Maximum observed differences in culture predictions across all possible cofactor combinations for each metric (rows). This panel shares the same row labels as panel a. Columns and colors distinguish between tissues. Units for each row correspond to the metric, so the probability of positivity displays the difference in percentage, temporal metrics display differences in days, peak titer displays differences in log10 culture units (pfu or TCID50), and AUC displays differences in AUC units. **c**, The median probability of positivity by culture (top) and total RNA (bottom) in each tissue. Each point is the median for one cofactor combination. **d**, The median trajectory as measured by culture (top) and total RNA (bottom) in each tissue. Each line gives the median value for one cofactor combination for the median time to detectability, median time to peak titer, mean peak titer, and median times to undetectability.

Exposure route has the largest effect on within-host infection patterns

Most of the variation in median infection patterns within each tissue was attributable to differences in exposure conditions (Figure 2.3). Strikingly, exposure route had the largest effect on 35 of the 37 total tissue-level metrics (indicated by a '1' in each row of Figure 2.3a; calculated based on mean differences among cofactors, see Methods; all other values are normalized to the largest effect). It also had the largest aggregate impact for each metric when summing across tissues (Figure 2.3b). Considering all metrics and tissues jointly, via either culture or PCR assay, route was most influential by a large measure (Figure 2.3c). There were limited exceptions to this finding: age was most important for the time to peak titer in the nose, while species ranked highest for lower GI positivity (Figure 2.3a). Although dose never ranked highest for any individual metric (Figure 2.3a,b), it ranked second in aggregate importance across metrics and tissues (Figure 2.3c). The finding that route and dose ranked highest overall was robust to choice of summary statistic and to additional dose comparisons (Figure S2.7).

Early infection dynamics differ among exposed and non-exposed tissues

We then analyzed infection patterns across the five major exposure routes: intranasal (IN), intratracheal (IT), combined intranasal and intratracheal (IN+IT), aerosol (AE), and intragastric (IG) inoculation. Within-host dissemination and early spatiotemporal infection patterns clearly varied among exposed and non-exposed tissues (Figure 2.4). Infection patterns in the throat and trachea largely mirrored the nose and lung, respectively (Figure S2.8), so subsequent analyses focus chiefly on the nose, lung, and lower GI. Both non-invasive and invasive samples were available for these three focal tissues (e.g., rectal swabs and necropsy samples of the colon for the lower GI; Table S2.3).

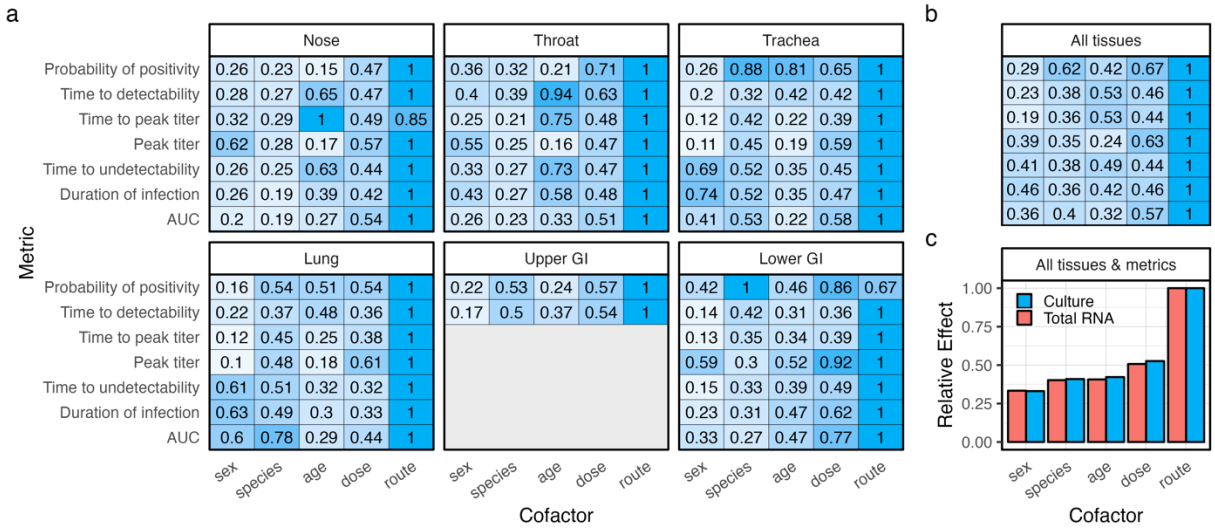

Figure 2.3 | Exposure route and dose are the top two determinants of within-host kinetics. Model predictions were generated for all possible combinations of age, sex, species, exposure route, and exposure dose (restricting to 10^4 and 10^7 pfu). Sensitivity analyses for these results are in Figure S2.7. **a**, Relative effects of each cofactor (columns) on the predictions for viral culture for each metric (rows) in the tissue indicated by panel labels. The cofactor with a '1' and the darkest blue had the largest mean effect. The intensity of the color for all other cofactors are scaled according to their relative effect (against the largest mean effect). Predictions for the upper GI were only available for the probability of positivity and the time to detectability, given the upper GI is only accessible using invasive sampling. See the Methods for further details on obtaining these values. **b**, The sum of the relative effects for each cofactor across all tissues in panel a, which were then scaled to relative effects within each row. These were calculated for each metric separately. Metrics (rows) are ordered as in panel a. **c**, The sum of the relative effects for each cofactor across all metrics and tissues in panel a, which were then scaled to relative effects. Results are stratified by assay type (culture, blue; total RNA, red).

Tissues exposed during inoculation (or adjacently exposed; i.e., lung for IT) had higher probabilities of culture positivity (darker colors in Figure 2.4a,e), and they became detectable earlier than non-exposed tissues (Figure 2.4b,f; most pairwise comparisons were significant, Figure S2.9). Notably, IT exposure was the only route that resulted in substantially higher probabilities of lung positivity than nasal positivity, with a clear pattern of infection spreading from the LRT to the URT and then the GI. This contrasts starkly with IN exposure, which resulted in the lowest probability of lung detection, and which was the only route where nasal positivity

preceded lung positivity. In the lower GI, the probabilities of culture positivity were small for all routes (Figure 2.4a,e; few pairwise differences were significant, Figure S2.9), and detectability always occurred after the respiratory tract but earliest for IG exposure (Figure 2.4e,f). Total RNA assays recapitulated these patterns, but with overall higher probabilities of positivity and slightly earlier times to detectability (Figure S2.5b,S2.10).

Patterns in the timing of culture detectability across all six tissues revealed a functional within-host connectivity structure that aligned with physical proximity. When considering IN, IT, and IG exposures, all tissues had the most similar times to detectability as an anatomically superior tissue (indicated by a column-wise rank '1' in Figure 2.4c), with the exception of the nose which had no such tissue and was most similar to its nearest inferior tissue. These findings are consistent with the connectivity structure displayed in Figure 2.4d, where the nose and throat are highly connected to both the lower respiratory and gastrointestinal tracts, with directionality consistent with the importance of the mucociliary escalator and swallowing as mechanisms of within-host dissemination.

Upper respiratory exposure results in different patterns in the peak and conclusion of infection

Across exposure routes, differences in the peak and conclusion of infection were largely driven by whether inoculation included nasal exposure (Figure 2.4g). Peak times for culture in the nose were remarkably consistent and occurred before peak titers in the lung (except for AE exposure; Figure 2.4g,h,j; Figure S2.9). However, the nose had larger peak titers (Figure 2.4g,i,k), later times to undetectability (Figure 2.4g,l,n), and overall longer infection durations (Figure 2.4g,m,p) when it was exposed (IN, IN+IT, AE) than when it was not exposed (IT, IG). Some of these effects were reversed in the lung, which often had earlier peak times (Figure 2.4g,h,j), larger

peak titers (Figure 2.4g,i,k), earlier times to undetectability (Figure 2.4g,l,n), and shorter infection durations (Figure 2.4g,m,o) when the nose was exposed. In the lower GI, URT inoculation resulted in later peak times (Figure 2.4g,h,j), similar (though slightly larger) peak titers (Figure 2.4g,i,k), later times to undetectability (Figure 2.4g,l,n), and longer infection durations (Figure 2.4g,m,o). Patterns were similar for total RNA (Figure S2.10). Interestingly, peak times rarely deviated by more than one day between total RNA and culture, but total RNA remained detectable much longer than viable virus in the respiratory tract, in contrast to the GI where undetectability occurred almost simultaneously (Figure S2.5b).

Aerosol exposure leads to different infection dynamics than other routes

When considering the full course of infection across tissues, AE exposure clearly resulted in different spatiotemporal patterns than all other routes, given it had the largest total number of significant differences with other routes across all metrics and tissues (Figure 2.4p). AE exposure was the only route where infection dynamics in the lung clearly tracked those in the nose, with almost simultaneous times to detectability, peak titer, and undetectability for viral culture (Figure 2.4q). AE exposure also resulted in significantly higher peak titers in the nose and lower GI, as well as delayed and prolonged GI positivity. These patterns ultimately resulted in shorter infection durations in the lung but longer durations in the nose and lower GI for AE exposure compared to all other routes. Crucially, despite IN+IT exposure being commonly used as a tractable model for AE exposure, the resulting infections differed significantly for many metrics (Figure 2.4p; Figure S2.9) and their dynamics were visibly distinct (Figure 2.4q). Ultimately, these discrepancies emphasize that no other exposure route approximates all features of infection patterns following AE inoculation.

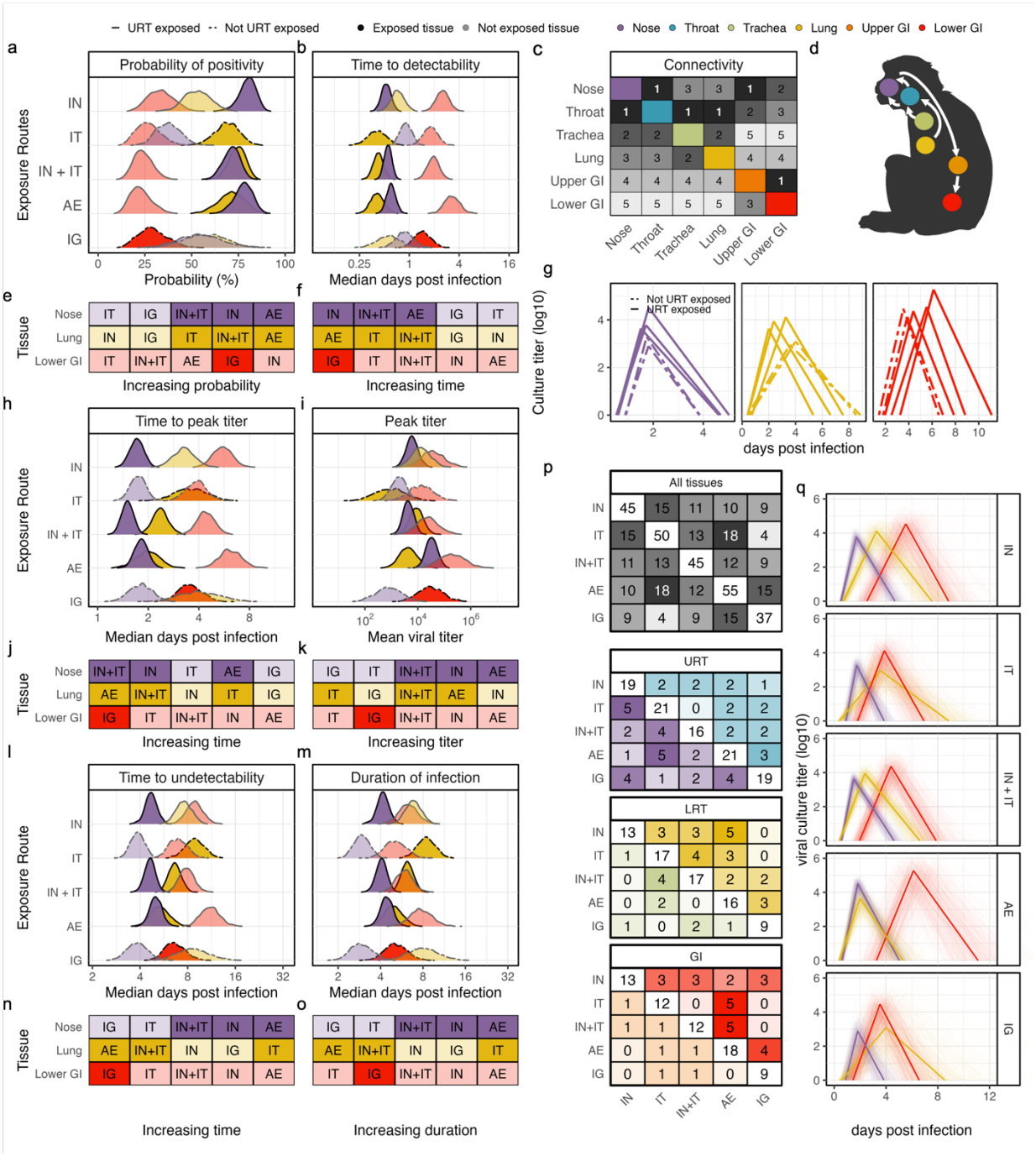

Figure 2.4 | Effects of exposure route on spatiotemporal spread of infectious virus.
All results in this figure are displayed for viral culture. See Figure S2.10 for results for total RNA. Results in panels a, b, h, i, l, m, and q were generated specifically for an adult male rhesus macaque exposed to 10^4 pfu by the indicated route, for visual clarity. All other panels integrate across all possible combinations of demographic cofactors and the following exposure doses: 10^4, 10^5, 10^6, and 10^7 pfu. Colors for all panels correspond with the sampled tissue, as indicated in the legend along the top (purple: nose; blue: throat; green: trachea; yellow: lung; orange: upper GI; red: lower

GI). Dashed lines in panels a, b, g, h, i, l, and m distinguish between routes that include upper respiratory exposure (solid lines; IN, IN+IT, AE) and those that do not (dashed lines; IT, IG). Exposure route acronyms are as follows: IN, intranasal; IT, intratracheal; IN+IT, combined intranasal and intratracheal; AE, aerosol; and IG, intragastric. Tissues that were exposed or adjacently-exposed during inoculation have more intense colors in panels a, b, e, f, and h-o. **a**, Model predictions for the probability of positivity across exposure routes. **b**, Model predictions for the median time to detectability. **c**, Similarities in the median time to detectability among tissues for IT, IN, and IG exposures. For each tissue indicated by the column label, their times are most similar to the tissue (on the row) with rank 1 and least similar to the tissue with rank 5. Annotated text gives the rankings in all cells, with white text for rank 1 for visual clarity. More similar tissues have darker shading. We did not include IN+IT and AE exposures in these calculations to reduce bias, given these routes inoculate many tissues, leading to highly similar dynamics in all exposed tissues. Calculations were based on the average of the absolute value for all pairwise differences across tissues. **d**, Connectivity structure based on all rank 1 similarities in panel c. For each tissue in the columns in panel c, we included an arrow between that tissue and its rank 1 tissue. The arrow points from the tissue that becomes detectable earlier on average towards the tissue that becomes detectable later on average. **e**, Rankings of the median probabilities of positivity for all exposure routes within each tissue (rows). Probabilities increase from left to right of this figure, with annotated text indicating the corresponding route. **f**, Rankings as in panel e for the median time to detectability. **g**, Median trajectories for all five routes separated into panels by tissues, where the inoculation routes were distinguished by whether they included nasal exposure (solid lines; IN, IN+IT, AE) or not (dashed; IT, IG). **h**, Model predictions for the median time to peak titer. **i**, Model predictions for the mean peak titer. **j**, Rankings as in panel e for the median time to peak titer. **k**, Rankings as in panel e for the mean peak titer. **l**, Model predictions for the median time to undetectability. **m**, Model predictions for the median duration of infection. **n**, Rankings as in panel e for the median time to undetectability. **o**, Rankings as in panel e for the median duration of infection. **p**, The number of significant differences among all tested infection metrics (e.g., probability of positivity) between any given pair of exposure routes, for all tissues (top panel, both diagonals, greyscale), upper respiratory tissues (URT; nose, bottom diagonal; throat, upper diagonal), lower respiratory tissues (LRT; trachea, bottom diagonal; lung, upper diagonal), and gastrointestinal tissues (GI; upper GI, lower diagonal; lower GI, upper diagonal). Intensity scales with the total number of significant differences. Diagonals sum across all significant differences for a given route in the panel. The total possible number of significances within each off-diagonal cell was 32 for all tissues, 6 for the nose, throat, trachea, lung, and lower GI, and 2 for the upper GI. **q**, Median trajectories for each route indicated in the panel label. Thick, opaque lines give the median across 1000 samples for each tissue, while thin transparent lines display 200 randomly sampled trajectories.

The effects of dose are route- and location-specific

Exposure dose affected infection patterns in many ways, although the direction, strength, and significance of these effects often varied across exposure routes and tissues (Figure 2.5). As expected, larger doses led to significantly higher probabilities of detectable infection across all tissues and routes (Figure 2.5e; dose-specific predictions for an AE-exposed individual and the standard cofactor set are displayed in Figure 2.5a,b,d,f-i,j and for all other routes in Figure S2.11,2.12). When considering all demographic groups jointly, median infectious dose values (ID50) based on the detection of infectious virus were much lower in exposed tissues than non-exposed tissues (Figure 2.5c). Estimates in the nose ranged from $10^{1.5}$ pfu for IN exposure up to $>10^{7.4}$ pfu for IT and IG exposure, with AE exposure falling at the lower end of this range ($10^{2.2}$ pfu). ID50 estimates in the lung were as low as $<10^{1}$ pfu for IT exposure and as high as $10^{5.3}$ pfu for IN exposure. The lower GI had consistently large ID50 estimates for culture positivity, ranging from $10^{6.4}$ to $>10^{7.4}$ pfu. ID50 values for the detection of total RNA is markedly lower than for infectious virus, with median estimates $<10^{1}$ pfu for nearly all routes and tissues.

Dose effects on all other metrics often differed between routes that did or did not include nasal exposure. For routes with nasal exposure (IN, IN+IT, AE; dark outline in Figure 2.5e), larger doses significantly: (i) decreased the time to detectability in the nose but had no effect in the lung or lower GI (Figure 2.5d,e), (ii) decreased the time to peak titer in the respiratory tract and increased them in the lower GI or had no effect (Figure 2.5e,f), (iii) increased peak titers in all tissues (Figure 2.5e,g), (iv) increased time to undetectability in the lower GI but not in the respiratory tract (Figure 2.5e,h), and (v) increased infection duration in the lower GI (Figure 2.5e,i). For AE exposure in particular, larger doses increased the peak but minimally affected the duration of infection in the nose, while causing a quicker and more intense infection in the lung

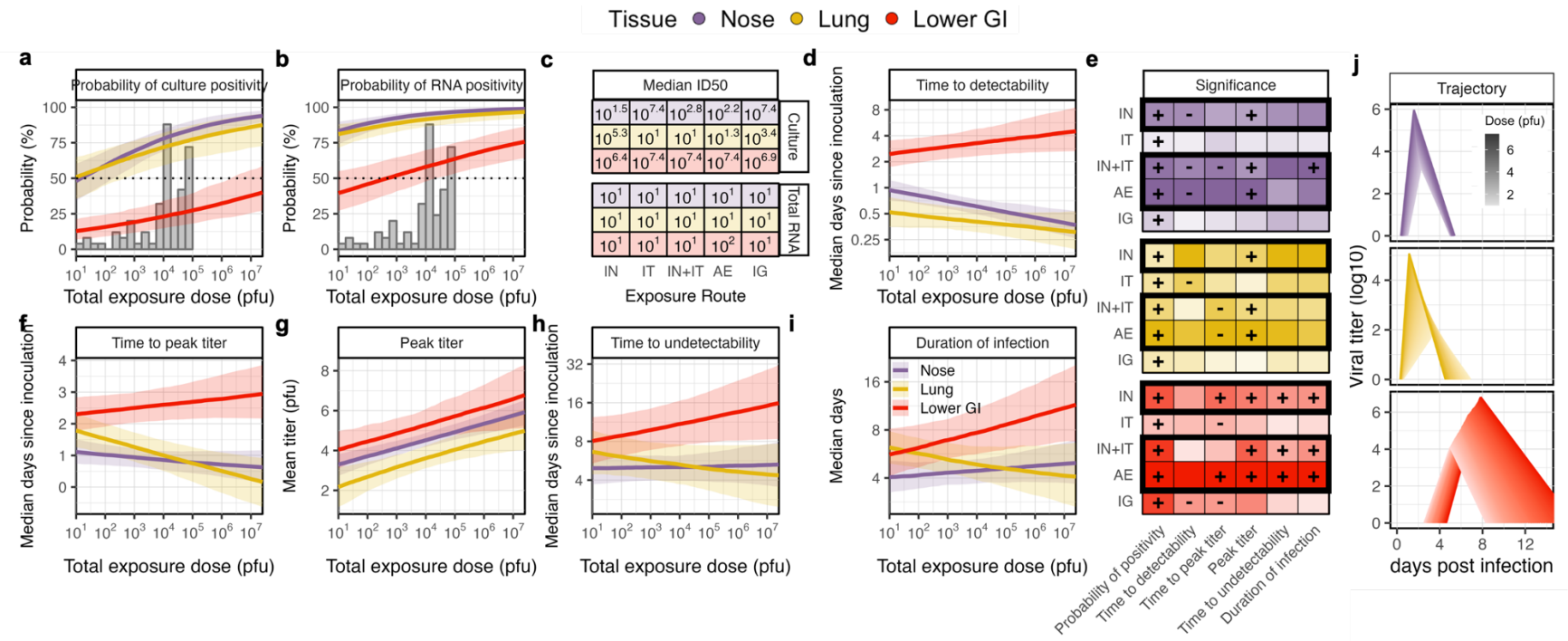

Figure 2.5 | Effects of exposure dose on spatiotemporal spread of infectious virus.
Results in panels a, b, d-i, and j are for a male, adult, AE-exposed rhesus macaque. For all other routes, see Figure S2.11. All other panels (c, e) were generated using predictions for all demographic groups and the indicated exposure route. Colors in all panels correspond with the sampled tissue, as in the legend at the top (purple: nose; yellow: lung; red: lower GI). **a**, The probability of culture positivity across a range of exposure doses. The thick lines are the median prediction at each dose, and the shaded regions correspond with the 90% prediction interval. The overlaid histograms give the distribution of doses available for model fitting from an aerosol-inoculated individual for all assays. **b**, As in panel a, but for the probability of total RNA positivity. **c**, The median estimate of the 50% infectious dose for each route and for both total RNA and culture. The rows correspond with different tissues, colored as in the legend. Tissues with an estimate of 10^1 or $10^{7.4}$ are upper and lower bounds, respectively (i.e., the ID50 estimate is $<10^1$ or $>10^{7.4}$). **d**, The median time to detectability. The thick line is the median prediction for the median time to detectability, and the shaded regions correspond with the 90% prediction interval on the median time to detectability. **e**, Significances of the effects for each combination of metric (columns), route (rows), and tissue (panels). These were generated by comparing the prediction between doses of 10^1 and 10^7 pfu. A "+" indicates

the metric significantly increases as dose increases, while "-" indicates the metric significantly decreases as dose increases. No label indicates there was no significant effect. Intensities of the colors are scaled against the relative effect (more intense colors indicate a larger effect). Dark boxes enclose the routes that included upper respiratory exposure. **f**, As in panel d, but for the time to peak titer. **g**, The mean peak viral titer. The thick line is the median prediction for the mean peak viral titer, and the shaded region gives the 90% prediction interval. **h**, As in panel d, but for the time to undetectability. **i**, As in panel d, but for the duration of infection. **j**, Trajectories in each location for variable doses, computed based on the median values for the median time to detectability, median time to peak titer, mean viral titer, and median time to undetectability. More intense colors correspond with larger doses.

(Figure 2.5j;see Figure S2.11,S2.12 for other routes). Both the duration of infection and the peak titer in the lower GI increased with dose. For routes without nasal exposure (IT, IG), there were few measurable dose effects. Larger doses decreased the time to detectability in adjacently-exposed tissues (e.g., lung for IT, lower GI for IG), and they decreased the time to peak titer in the lower GI, but they otherwise had no significant effects (Figures 2.5e,S2.9,S2.11,S2.12). All patterns were similar for total RNA (Figure S2.13). Overall, dose had the biggest impact on the kinetics of nasally-challenged individuals, perhaps due to the centrality of the nose in the tissue connectivity structure (Figure 2.4c,d).

Clinical profiles vary significantly across exposure conditions and demographics

Finally, we analyzed tissue-specific AUC values to assess the impacts of exposure conditions and demographic effects on nasal shedding (the best available proxy for infectiousness) and GI shedding. We used lung AUC as our best available metric for disease severity, given our database does not include symptom scores or immunological markers. Once again, AE exposure had a significantly different profile from all other routes, with the highest overall nasal and GI shedding but the lowest lung severity (Figure 2.6a,b,c). Crucially, IN+IT and AE exposures differed substantially, and IN+IT was more similar to IN exposure than to AE. Nasal and GI shedding were largest for routes including nasal exposure (AE, IN, IN+IT), while lung severity was largest following IN exposure. IT and IG exposures resulted in nearly identical profiles (Figure 2.6a,b,c), given they only differed significantly for four metrics across all tissues (Figure 2.5p). Shedding increased as dose increased for all routes, with the only exception being reduced nasal shedding following larger IG doses, although this effect was small.

Although demographic groups had similar probabilities of testing culture positive (Figure 2.7b), their clinical profiles often differed. Among species, African green monkeys (AGM) had significantly higher lung severity than rhesus and cynomolgus macaques (RM and CM; Figure 2.6d,e,f), which can be explained by their significantly larger peak titers and longer infection

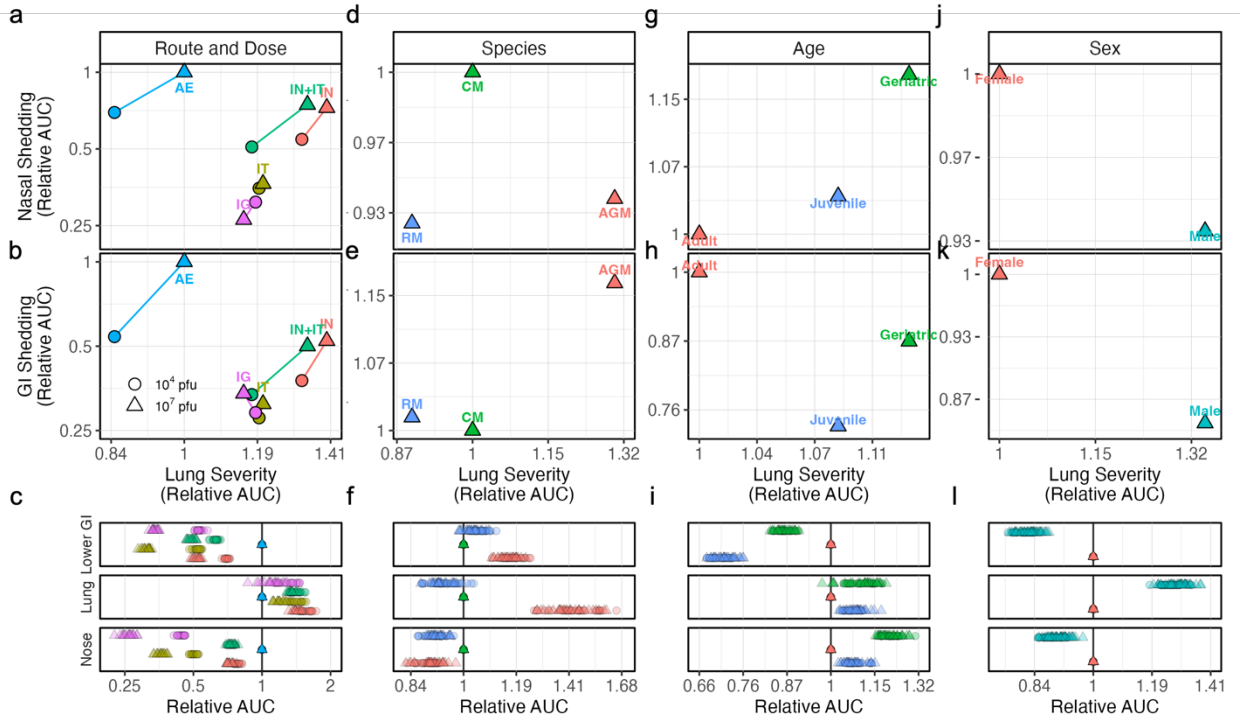

Figure 2.6 | Clinical profiles across exposure conditions and demographics.
a and b, Relationship between median lung severity and (a) nasal shedding or (b) GI shedding, all of which were calculated as culture AUC values. Colored shapes and labels distinguish between the exposure routes, with shapes indicating the total exposure dose. All values are expressed relative to the AUC value for aerosol exposure with 10^7 pfu. **c**, Median AUC predictions for all possible combinations of cofactors, relative to the corresponding prediction for an AE-exposed individual. Colors and shapes are the same as in panels a and b, distinguishing between the route and the dose. Panels separate the tissues (nose, bottom; lung, middle; lower GI, top). **d, e, and f**, As in panels a, b, and c, except comparing species with color (RM, rhesus macaque; CM, cynomolgus macaque; AGM, African green monkey). Values were calculated relative to cynomolgus macaques. **g, h, and i**, As in panels a, b, and c, except comparing age classes with color. Values were calculated relative to adults. **j, k, and l**, As in panels a, b, and c, except comparing sexes with color. Values were calculated relative to females.

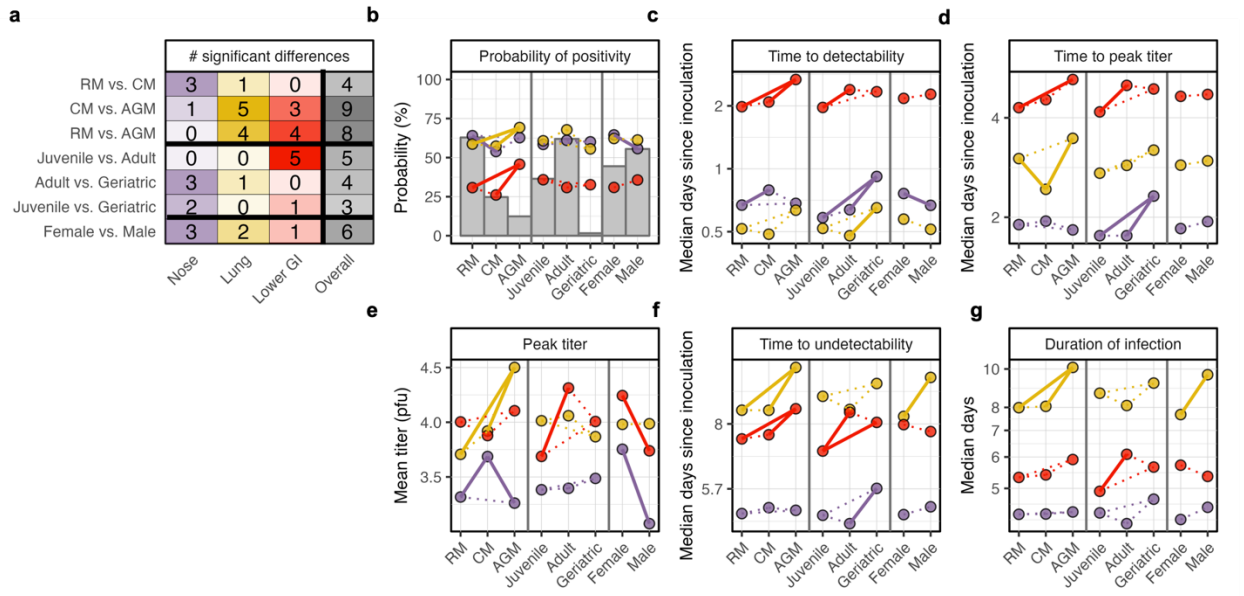

Figure 2.7 | Effects of demographic factors on spatiotemporal spread of infectious virus. Colors in all panels denote the tissue being sampled (purple: nose; yellow: lung; red: lower GI). All results were generated for viral culture. **a**, The number of significant differences among all infection metrics (e.g., probability of positivity) in each location (columns) between the demographic groups labeled on the rows. The overall column sums across the tissues to give the total number of significant differences for those demographic groups. There were 6 possible differences for each cell, except for the overall column where there were 18 possible differences. The intensity of the color scales with the percent of differences that were significant. Species acronyms are: RM, rhesus macaque; CM, cynomolgus macaque; AGM, African green monkey. **b**, The median probability of positivity for each demographic group indicated along the y axis. The histograms are the percent of the data used for model fitting for each demographic group (including all assays). All estimates were based on predictions generated for all routes, one dose (10^4 pfu), and all possible demographic factors except the one being varied (e.g., the RM estimates include predictions for all ages and sexes but not for CM or AGM). Colored lines connecting the dots in panels b-g indicate the corresponding difference was significant. Dotted lines correspond with an insignificant difference. **c-g**, As in panel b except for the median predictions of (c) the median time to detectability, (d) the median time to peak titer, (e) the mean peak titer, (f) the time to undetectability, and (g) the duration of infection.

durations (Figure 2.7e,g). CMs had the highest nasal shedding (Figure 2.6d) given their significantly larger peak titers (Figure 2.7e), while AGMs had the highest GI shedding (Figure 2.6e) given their slightly (but insignificantly) larger peak titers and longer durations (Figure 2.7e,g). Adults had significantly lower nasal shedding, higher GI shedding, and lower lung severity

than juveniles and geriatrics (Figure 2.6g-i). Geriatrics had the highest nasal shedding and lung severity (Figure 2.6g), although sample sizes were small so cautious interpretation is warranted (Figure 2.7b). Females had significantly higher nasal and GI shedding than males (Figure 2.6j.k), given they had similar durations but larger peak titers (Figure 2.7e,g). However, males had significantly higher lung severity (Figure 2.6j), which arose from longer infection durations with no difference in peak titer (Figure 2.7e).

Discussion

This study addresses long-standing, fundamental questions on the determinants of spatiotemporal infection patterns inside hosts by conducting the most comprehensive quantitative analysis of non-human primate (NHP) challenge experiments to date. We demonstrate that exposure route shapes the probability, onset, peak, and conclusion of SARS-CoV-2 infection across the respiratory and gastrointestinal tracts more than exposure dose or demographic factors do. Our results show that infection patterns following aerosol inhalation are clearly distinct from any other exposure route, including intranasal or combined intranasal/intratracheal inoculation. We also demonstrate that dose affects infection patterns in nuanced ways (e.g., primarily when administered to the nose), beyond standard discussions of infection probability. Altogether, our study identifies the determinants of infection patterns inside hosts for an important respiratory virus in an important animal model for human disease, offering a foundation and direction to uncover general principles that constrain the success of human respiratory pathogens.

All aspects of within-host infection varied significantly across exposure routes, including spatiotemporal patterns and shedding profiles. Tissues exposed during inoculation became detectably infected before non-exposed tissues, followed by physically proximate tissues. Exposure routes that included URT inoculation (e.g., intranasal [IN], aerosol [AE], combined intranasal and intratracheal [IN+IT]) resulted in longer infections with larger peak titers in the nose, shorter infections with earlier and larger peak titers in the lung, and delayed but prolonged infections in the lower GI. In accordance with work on influenza (Lai et al., 2024) but in contrast with a study on SARS-CoV-2 (with small sample sizes; Blair et al., 2021), AE exposure resulted in different dynamics than IN or IN+IT exposures, which are both used regularly as tractable

alternatives to aerosol inhalation in animal experiments. For example, AE exposure was the only route with synchronous temporal patterns in the nose and lung, and it had significantly higher nasal shedding. Intriguingly, AE exposure also resulted in the lowest lung severity because it had the shortest infection duration, which contrasts with a report for influenza A that aerosol inoculation resulted in more severe symptoms than intranasal inoculation (Lindsley et al., 2015). This discrepancy could stem from our choice of severity metric (culture AUC in the lung), which treats longer infections even at lower titers as more severe than quick, intense infections. The most accurate correlate of severity remains to be identified, especially given that positive, negative, and no relationships have been observed between infection duration and illness severity for SARS-CoV-2 (Cevik et al., 2021). However, this pattern could also be related to theories and some experimental evidence that smaller doses lead to gentler immune responses and lower severity (Marois et al., 2012; Van Damme et al., 2021): aerosol exposure distributes the same dose across more respiratory locations, including the lung, which could allow the infection to be controlled more easily than following a flood of liquid inoculum. Overall, given stark differences in infection dynamics across all routes, extreme caution is warranted when extrapolating insights from any other inoculation procedure to aerosol exposure, including in transmission experiments, where discrepancies between donor (typically IN exposed) and sentinel animals could be explained by differences in the route of exposure as opposed to, or in addition to, differences in dose.

Our model showed that the probability of successful infection in any given tissue was strongly dependent on exposure route, dose, and detection assay. Based on viral culture, exposed tissues were more likely to test positive and had smaller ID50 values. For example, our ID50 estimates in the nose were $10^{1.5}$, $10^{2.2}$, and $>10^{7.4}$ pfu for intranasal, aerosol, and intratracheal inoculations, respectively, which is consistent with previous human challenge experiments that

have estimated variable ID50 values for aerosol versus intranasal inoculation of respiratory viruses (Alford et al., 1966; Couch et al., 1966; Lindsley et al., 2015). Lung positivity varied less across routes, likely given the lower respiratory tropism of early SARS-CoV-2 strains (named variants were not included in our database), but differences were still substantial between aerosol ($10^{1.3}$ pfu) and intranasal exposures ($10^{5.3}$ pfu). In contrast, median ID50 estimates based on total RNA positivity did not exceed 10^2 pfu for any location or exposure route, emphasizing that within-host dissemination of viable virus from exposed tissues often fails to occur or fails to become detectable, despite widespread RNA positivity. This highlights the importance of discussing infection probability and infectiousness in the context of within-host spatial structure, and it warns that investigations of the source of exhaled, virus-laden aerosols must carefully consider which tissues were truly infected.

Exposure dose influenced many aspects of within-host dynamics besides the probability of infection, including shedding and severity. Larger doses have been hypothesized to decrease the incubation period, increase viral load, lead to faster infection progression, and increase disease severity for SARS-CoV-2 (Mølbak et al., 2024; Van Damme et al., 2021; Wang et al., 2021). While we could not measure incubation directly without symptom data, our model did predict that larger doses would significantly decrease the time to detectability in all exposed tissues but not in non-exposed tissues. We also found that larger aerosol doses resulted in shorter infections with larger peak titers in the lung, ultimately increasing severity (measured as culture lung AUC), thus lending support to those theories while corroborating the dose-severity relationship identified for other respiratory viruses (e.g., hCoV 229E in a human challenge trial, Bradburne et al., 1967; SARS-CoV-2 and influenza A in murine models, Imai et al., 2020; Marois et al., 2012). Intriguingly, larger doses increased nasal shedding and lung severity for all routes that included

upper respiratory exposure (AE, IN, IN+IT), however they did not substantially affect either metric for intratracheal or intragastric inoculation. These results emphasize that shedding and severity for early SARS-CoV-2 strains are particularly sensitive to dose administered to the nose and throat, and that studies employing other inoculation procedures would likely not identify a strong dose-severity or dose-shedding relationship.

Our study offers the unique opportunity to contrast the overall infection patterns observed in humans with those in NHPs, which are an important animal model for human disease (Estes et al., 2018). Based on PCR data, we estimated ID50 values at or below 10^1 pfu (or equivalently $10^{1.4}$ TCID50) for respiratory tissues regardless of exposure route. This is nearly identical to the dose that resulted in PCR-detectable upper respiratory infections for 53% of participants in the SARS-CoV-2 human challenge trial (10^1 TCID50; Killingley et al., 2022), and it is similar to ID50 estimates in humans for other respiratory viruses (e.g., human coronavirus 229E, Watanabe et al., 2010; influenza A H2N2, Alford et al., 1966; and rhinovirus NIH 1734, Couch et al., 1966). Two early SARS-CoV-2 studies, including one large meta-analysis, reported that 48% of COVID-19 patients were RNA positive in GI samples (Cheung et al., 2020; Lin et al., 2020), although this likely overestimates population-wide prevalence since many individuals were hospitalized. Based on our model predictions that the median ID50 values for RNA detection in the lower GI are $\leq 10^2$ pfu for all exposure routes, this suggests that the average natural exposure dose in humans could be less than 10^2 pfu.

Comparisons of temporal infection patterns between humans and NHPs were more difficult, given they are highly route- and dose-specific and given that most descriptions in humans are necessarily based on times since symptom onset rather than since exposure (Cevik et al., 2021; He et al., 2020; Weiss et al., 2020; Wölfel et al., 2020). However, our model predictions for low-

dose, aerosol-exposed rhesus macaques (10^1-10^2 pfu; aggregating across age and sex) were similar to estimates from a prospective sampling study (Kissler et al., 2021), namely for the proliferation phase (i.e., time between detectability and peak titer; 2.2 vs. 3.3 days), the clearance phase (i.e., time between peak titer and undetectability; 9.0 vs. 8.5 days), and the overall infection duration (11.3 vs. 11.7 days) when monitoring the nose via PCR. We also estimated, for the same exposure conditions as above, that culture titers in the nose would peak 1.5 days after becoming detectable, which is consistent with another estimate in humans that culture probability peaks in the nose 1.8 days after the onset of shedding (Jones et al., 2021). Notably, given we identified distinct infection profiles for all respiratory exposure routes and given infection trajectories were remarkably consistent among all participants in the human challenge experiment (Killingley et al., 2022), the observed heterogeneity in naturally-acquired infections in humans could stem from variable routes or doses of exposure.

Despite compiling the largest ever database of non-human primate challenge experiments, our study was still limited along some dimensions. Available doses and overall sample sizes were unevenly distributed across routes: combined intranasal/intratracheal inoculation comprised 62% of the full database, and aerosol inhalation was the only route with doses that may be more relevant to natural exposure (10^1-$10^{3.5}$ pfu). More comprehensive coverage across exposures would further improve ID50 estimates and comparisons of spatiotemporal kinetics. As with all analyses of animal challenge experiments, there is risk that some infections were not observed or that statistical noise obscured true patterns. These risks, however, should be lower for our study than individual experiments conducted with few animals, given that we integrated across articles to identify aggregate patterns across more than 700 individual NHPs and given that our model predicted minimal differences in our infection metrics across studies. Finally, all NHPs included in our

database were immunologically naive to SARS-CoV-2 and were inoculated with ancestral SARS-CoV-2 strains that circulated prior to the emergence of Alpha variants, so future work that characterizes infection across diverse immune profiles and viral genetic landscapes would be highly valuable.

Our study presents the most comprehensive and quantitative evidence to date that exposure conditions shape infection patterns inside hosts, in ways that affect an individual's disease risk and shedding potential. With our study, we demonstrate the ability of meta-analysis to answer fundamental questions that are inaccessible for individual experiments, ultimately enhancing the value of each constituent study and improving adherence to the 3R principles. Future studies can increase their statistical power by contrasting their results with our database of historical control individuals, including to compare patterns across SARS-CoV-2 variants, evaluate the efficacy of pharmaceutical interventions, or identify differences across disparate pathogens. Overall, quantitative tools like ours show immense promise to transform our understanding of pathogen-host biology and to launch us into a new era of microbiology and improved human health.

Data and Code Availability

The full database compiled during the literature search will be made available on GitHub alongside the published version of this manuscript. All data and code used to produce the results and figures in this manuscript will also be made available on the same GitHub.

Supplementary Figures

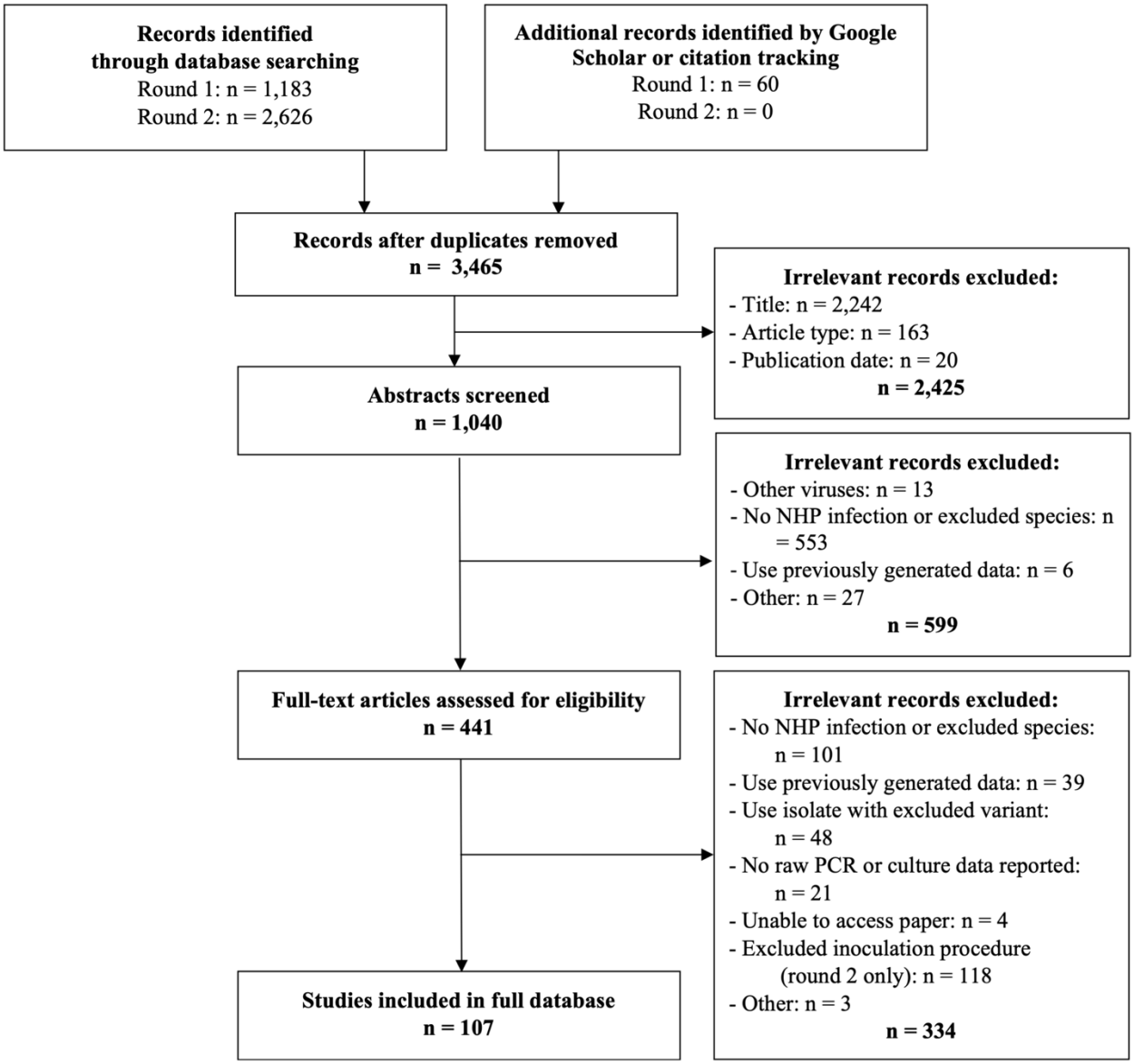

Figure S 2.1 | Screening and selection procedure for database compilation, including both literature searches.
We created this figure by adapting the template flowchart provided in Moher et al., 2009, which offers guidelines and resources for systematic reviews and meta-analyses. We incorporated all of their suggested steps for reporting the results of systematic literature searches, but all of the substantive content (e.g., numbers, exclusion reasons) is based entirely on our literature search. Additional detail on the screening procedure is provided in the Supplementary Methods.

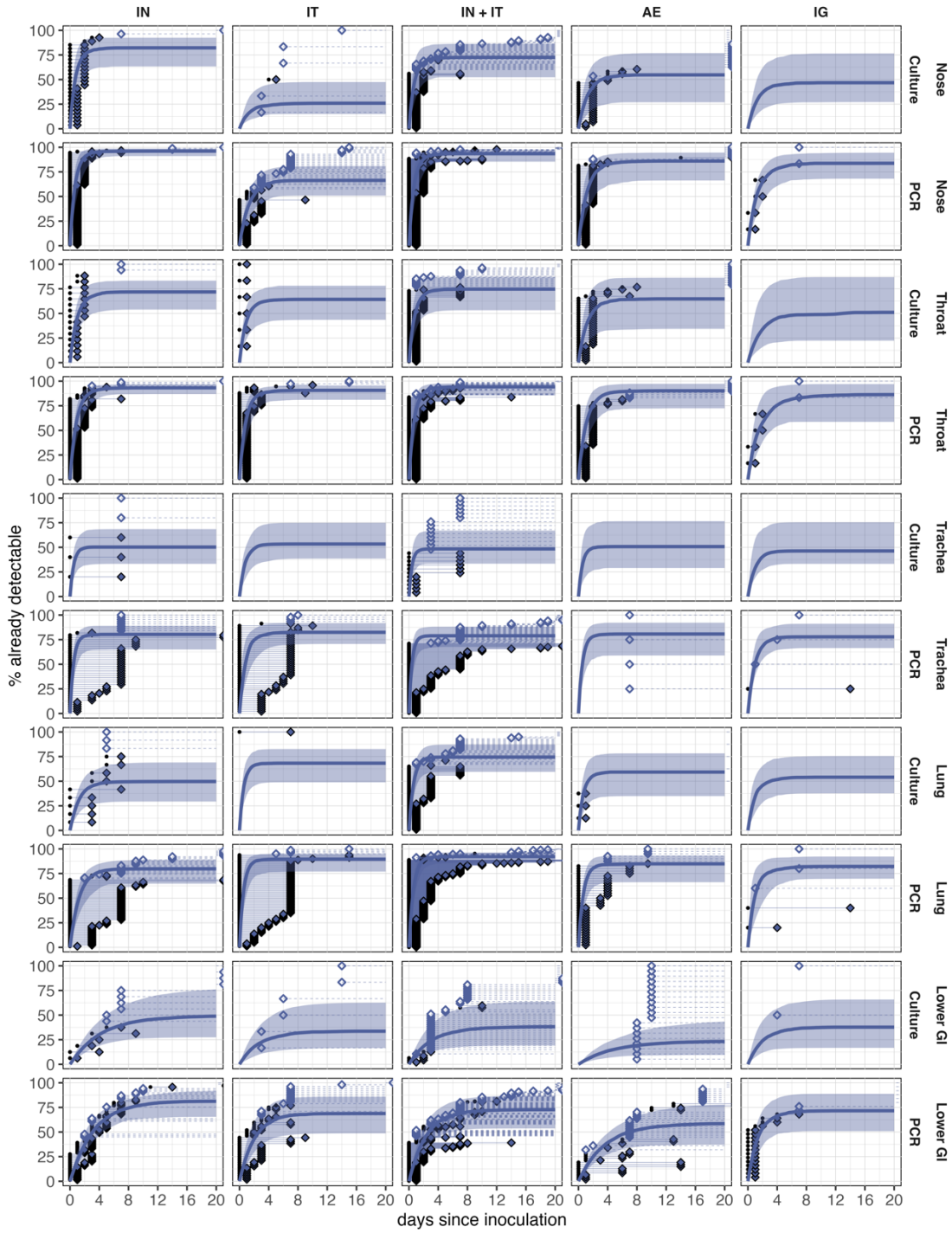

Figure S 2.2 | Model fits for the probability of positivity and time to detectability.
All panels are as presented in Figure 2.1h, except this figure includes PCR and culture assays, all tissue locations except the upper GI, and all exposure routes. Some observations occurred after day 20 post inoculation, resulting in points that are either not visible or partially visible along the far right side of each panel. We were still able to generate predictions for panels without data because of information sharing in our model.

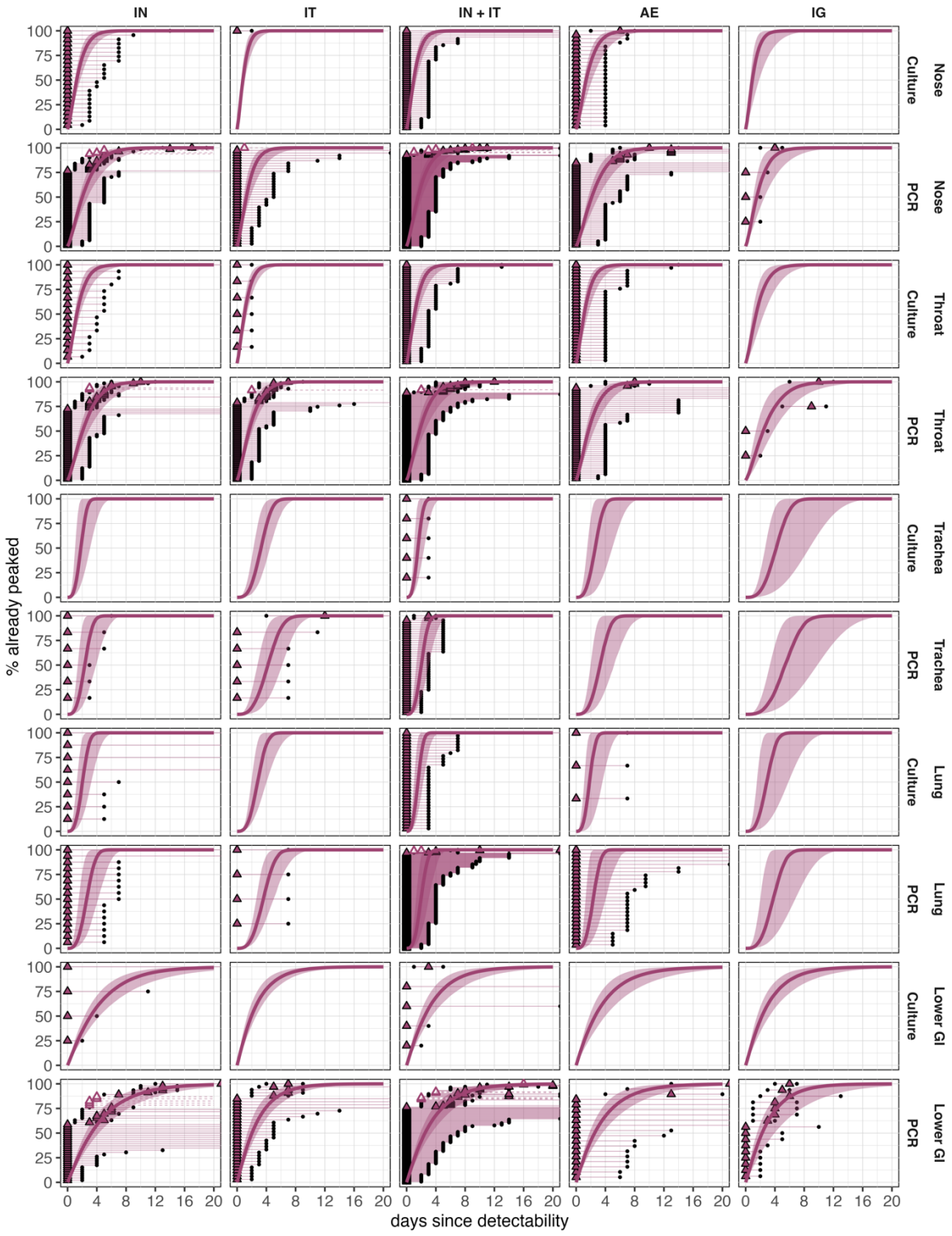

Figure S 2.3 | Model fits for the time to peak titer.
All panels are as presented in Figure 2.1i, except this figure includes both PCR and culture assays, all tissue locations except the upper GI, and all exposure routes. We were still able to generate predictions for panels without data because of information sharing in our model.

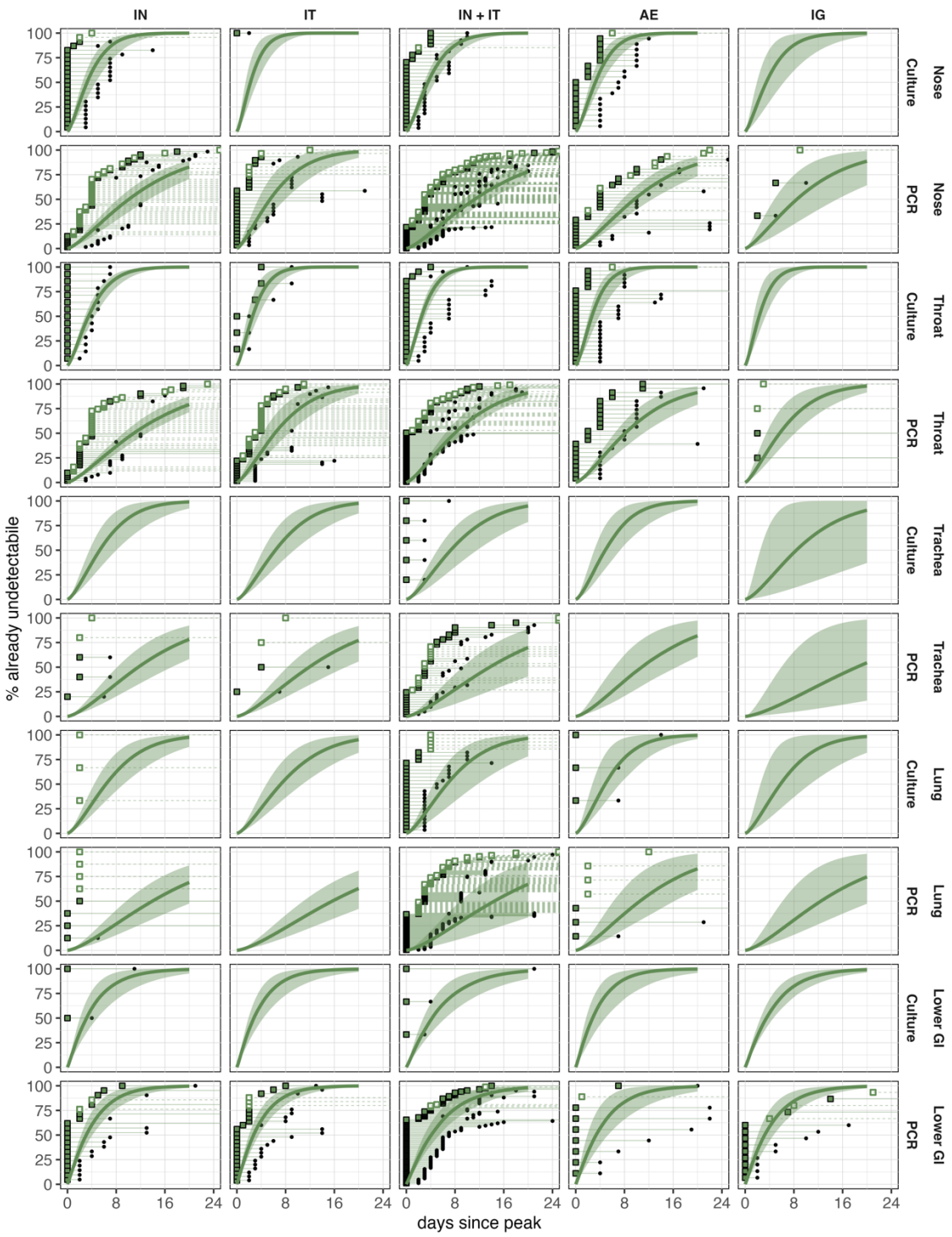

Figure S 2.4 | Model fits for the time to undetectability.
All panels are as presented in Figure 2.11, except this figure includes both PCR and culture assays, all tissue locations except the upper GI, and all exposure routes. We were still able to generate predictions for panels without data because of information sharing in our model. Predictions are also available but not shown for 20 or more days since the peak titer.

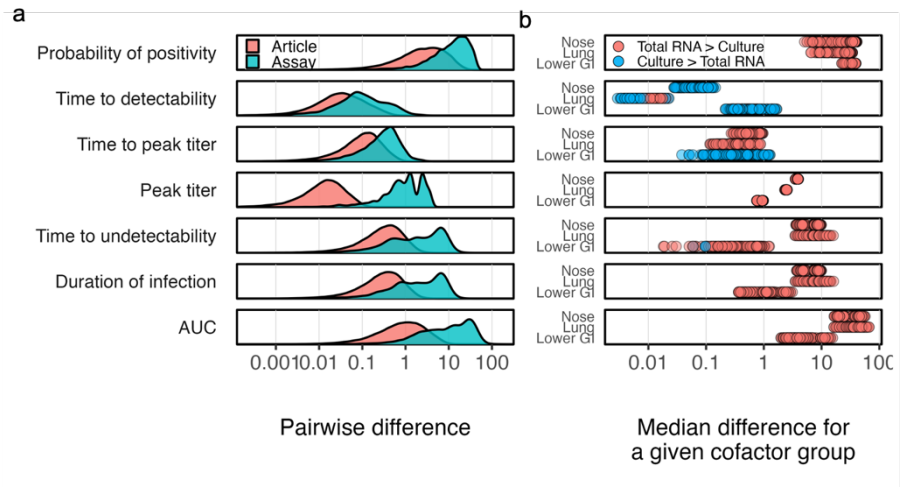

Figure S 2.5 | Differences in model predictions among assays and among articles.
Within both panels, results are grouped into rows by metric, which are labeled along the left-hand side with panel a. **a**, Pairwise differences in the predictions for each metric across all assays (assuming no article effect; blue) and across all articles (conditioned on using the same assay; red). These were generated for any possible combination of cofactors. **b**, Differences between total RNA and viral culture in the median predictions for all metrics. Each point presents the differences for a given combination of cofactors, where color denotes which assay has the larger metric (red: total RNA is larger than culture; blue: culture is larger than total RNA).

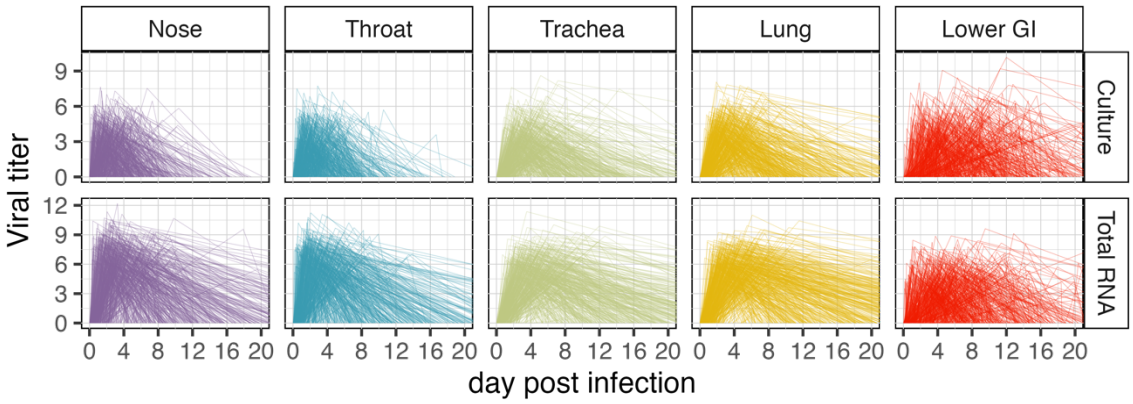

Figure S 2.6 | Variation in individual-level trajectories.
Each line is one example individual-level trajectory. Each panel includes all five routes, all ages, all sexes, all species, and one dose (10^4 pfu).

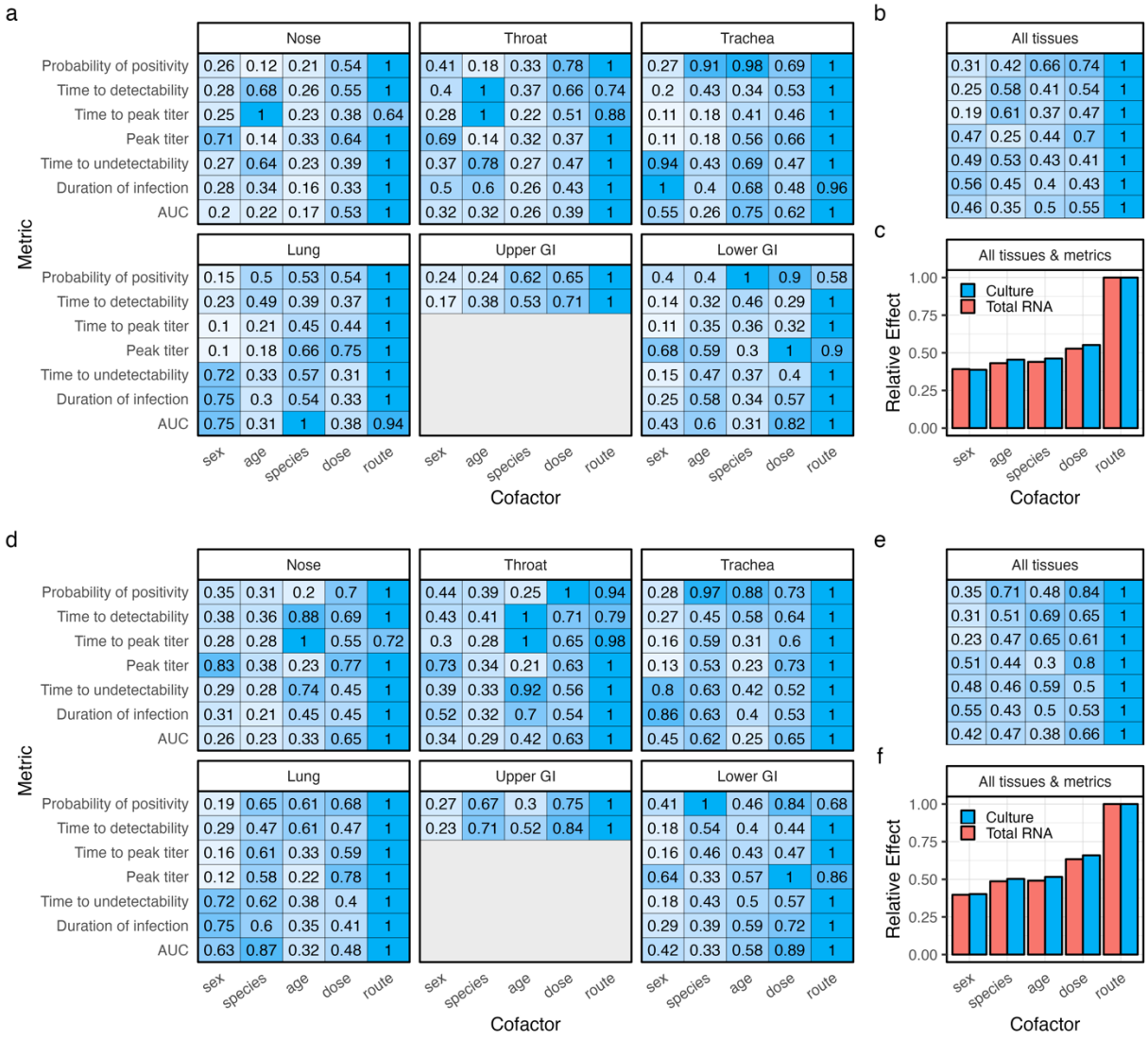

Figure S 2.7 | Sensitivity of rankings to summary statistic and dose comparisons.
a-c, Rankings of relative cofactor effects as in Figure 2.2, except calculated using the median differences. **d-f**, Rankings of relative cofactor effects as in Figure 2.2, except allowing dose comparisons between 10^1 and 10^4 pfu as well as 10^4 and 10^7 pfu.

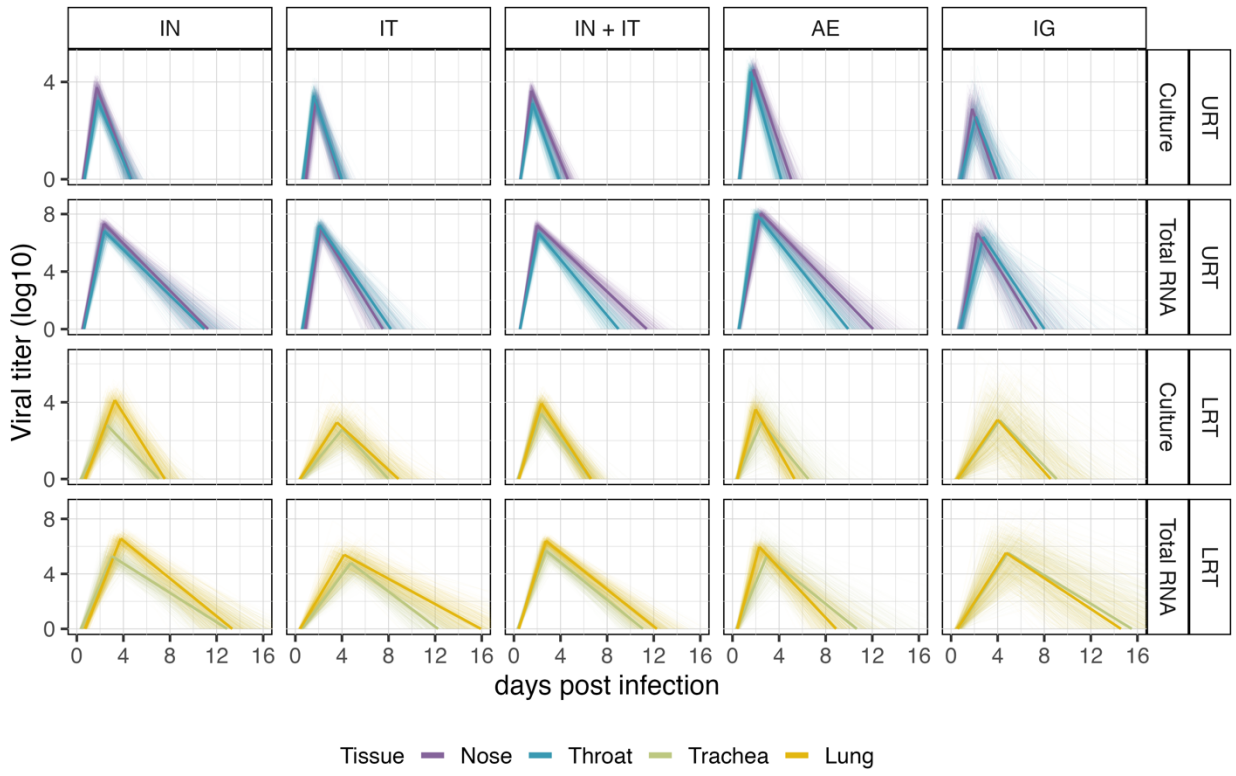

Figure S 2.8 | Trajectories within the upper and lower respiratory tract, for total RNA and culture.
Rows stratify results into organ groups and assays, while columns denote the exposure route. Colors distinguish between the tissues, as in the legend at the bottom (purple: nose; blue: throat; green: trachea; yellow: lung). Thick, opaque lines give the median trajectory, and thin, transparent lines give samples of the median trajectory.

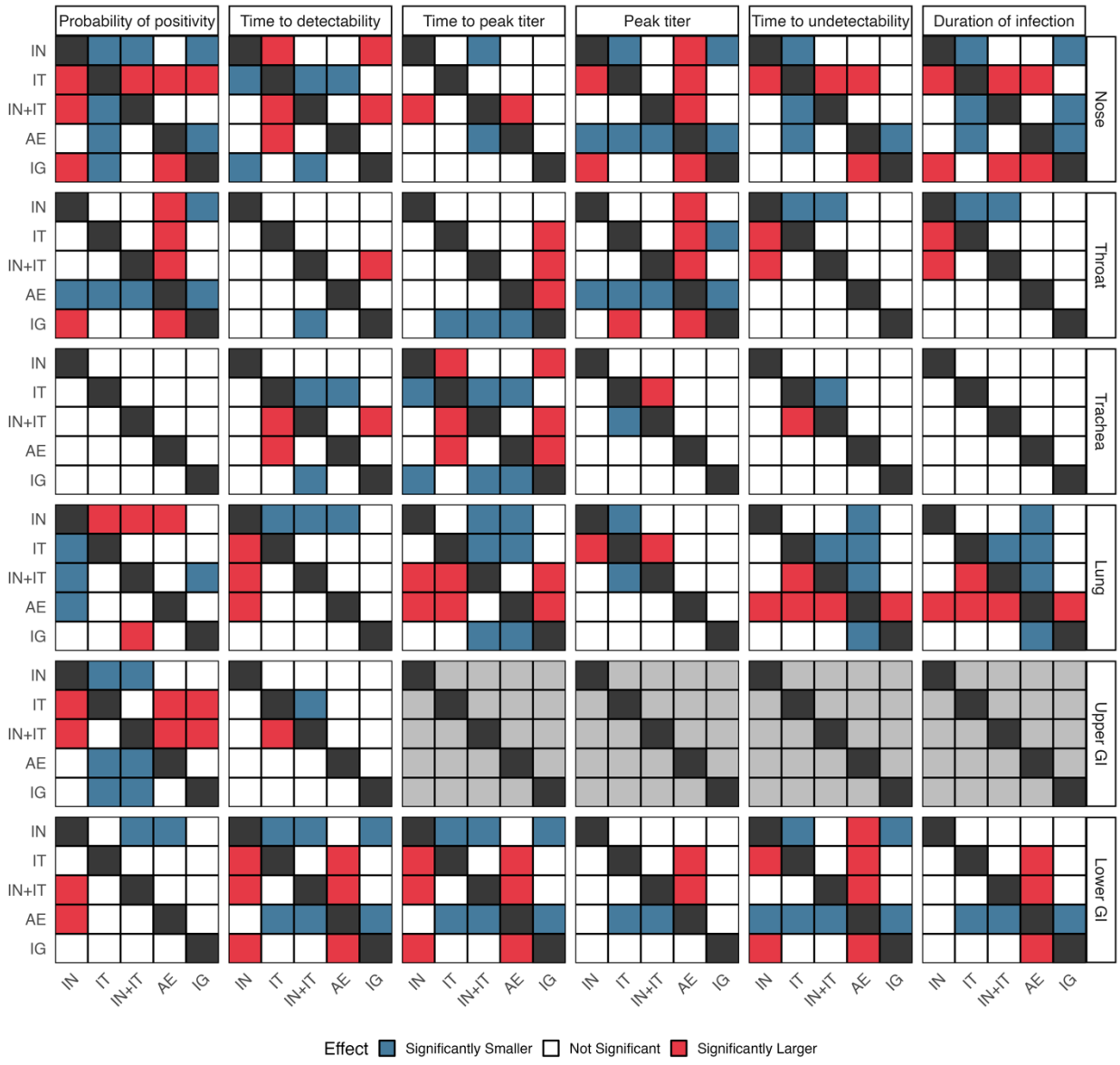

Figure S 2.9 | Significant differences for culture among all routes and all locations.
Effects are relative to the route indicated on the row, compared to the route on the column. For example, IN inoculation results in larger probabilities of positivity in the nose than IG (red cell), but IT exposure results in lower probabilities of positivity than all other routes (blue cell). Light gray cells indicate no comparison was possible. These were generated for predictions from the standard cofactor set.

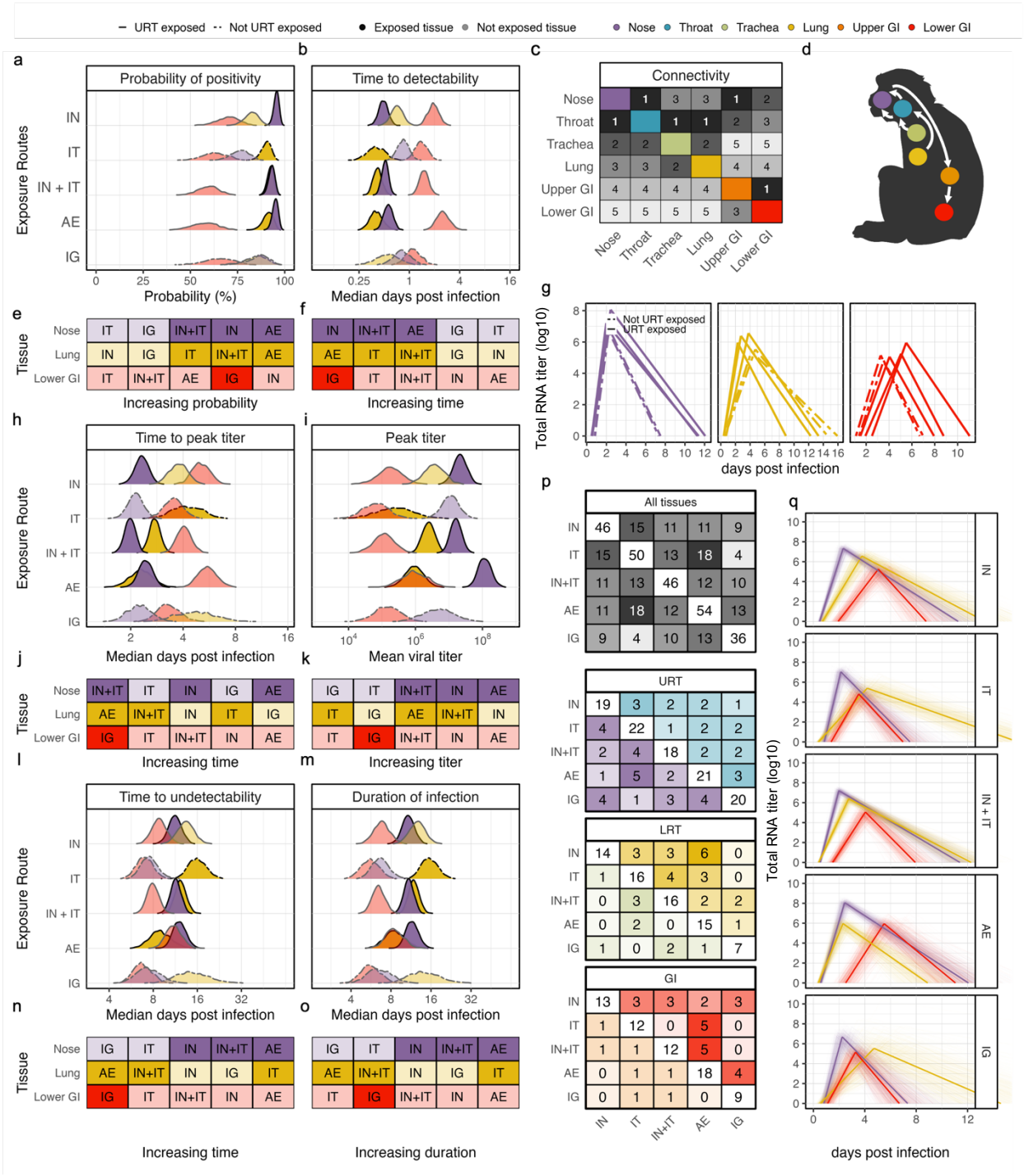

Figure S 2.10 | Route effects visualized for total RNA.
All panels are presented as in Figure 2.4, except that this figure displays results for total RNA assays.

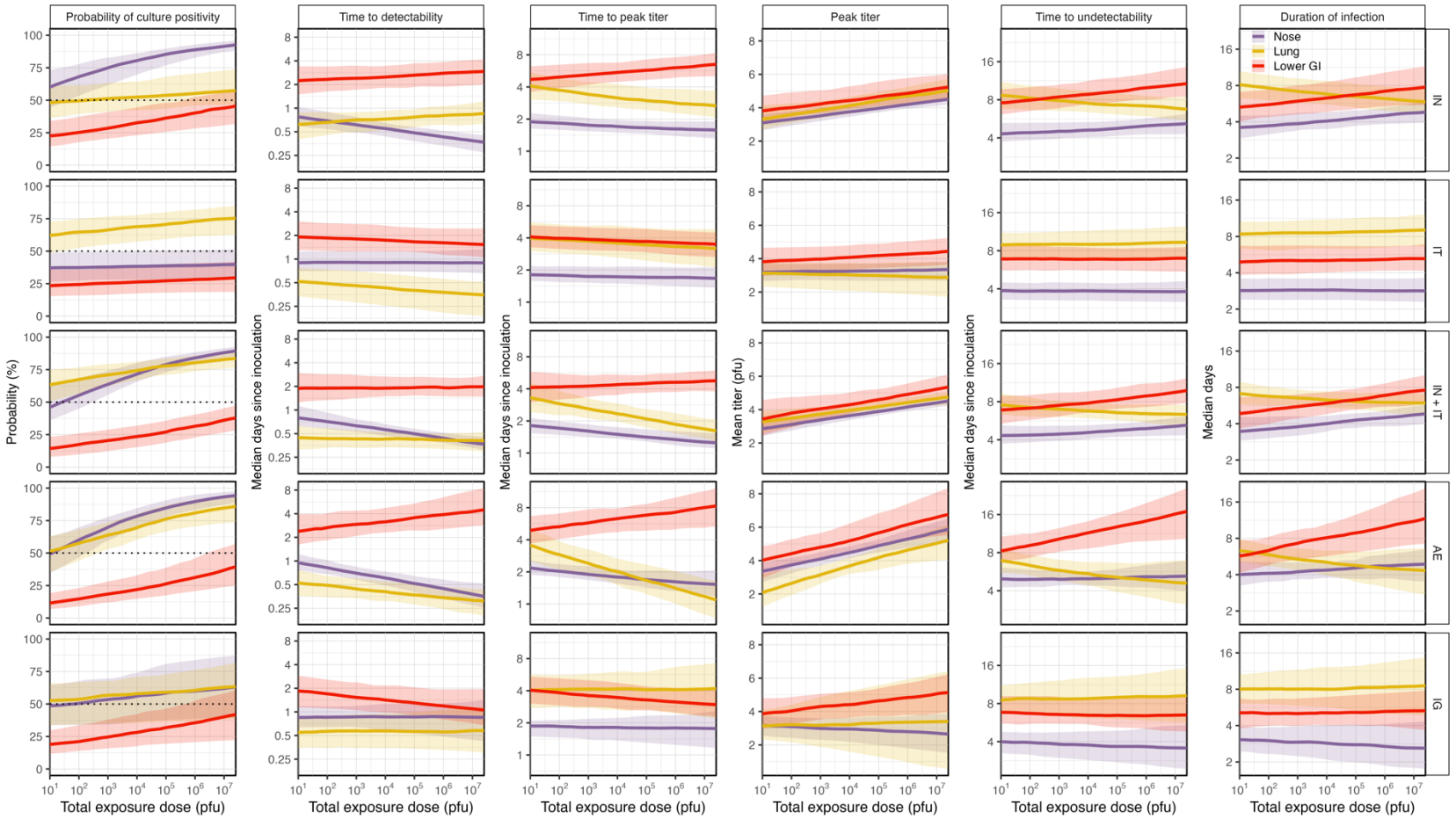
Probability of culture positivity
Time to detectability
Time to peak titer
Peak titer
Time to undetectability
Duration of infection
Nose
Lung
Lower GI
IN
IT
IN + IT
AE
IG
Probability (%)
Median days since inoculation
Mean titer (pfu)
Median days
Total exposure dose (pfu)

Figure S 2.11 | Dose effects on culture metrics for all exposure routes.
Visualization techniques are the same as for Figure 2.5, except this figure includes predictions for all exposure routes.

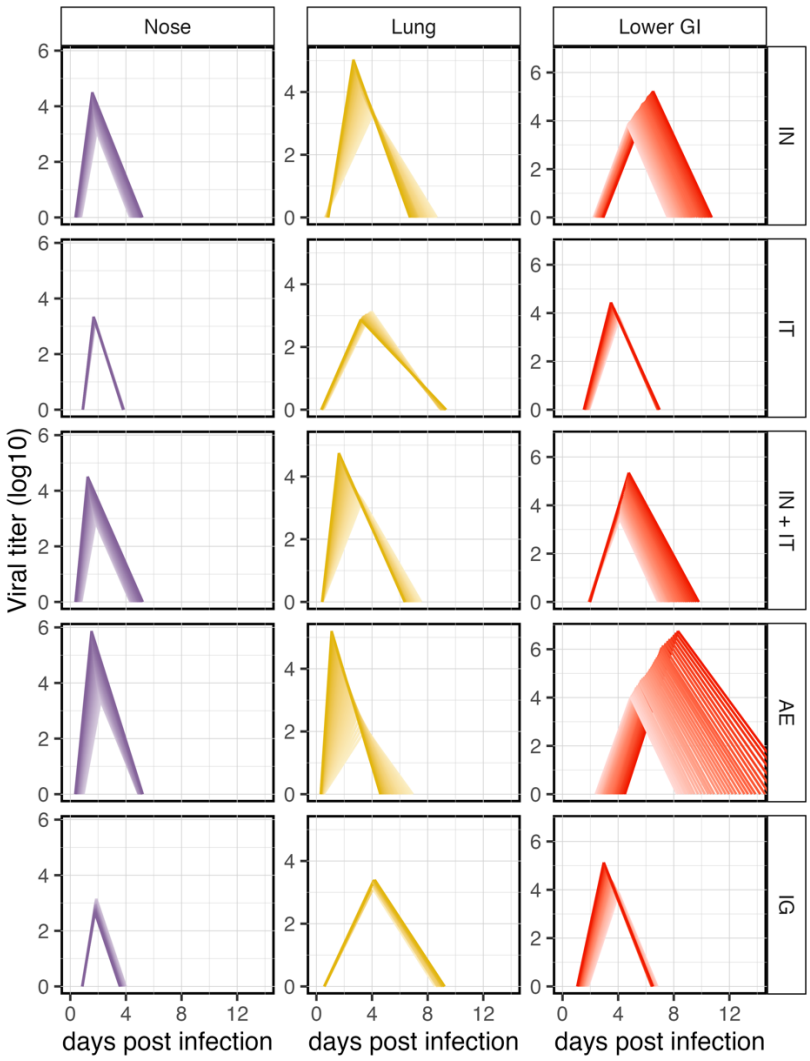

Figure S 2.12 | Dose effects on culture trajectories for all exposure routes.
Results are presented as in Figure 2.5j, with lighter colors corresponding to smaller exposure doses.

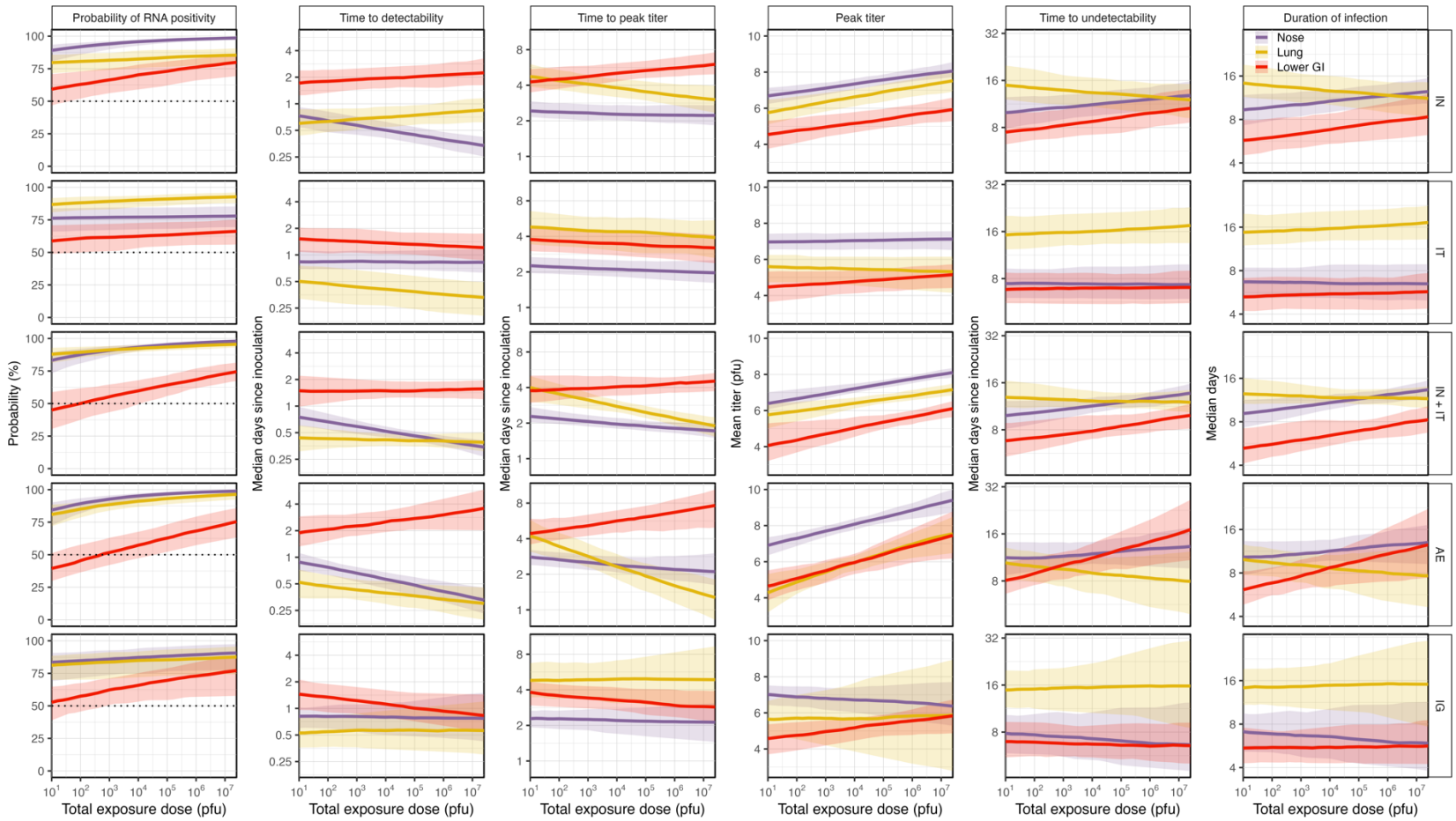
Probability of RNA positivity
Time to detectability
Time to peak titer
Peak titer
Time to undetectability
Duration of infection
Nose
Lung
Lower GI
IN
IT
IN + IT
AE
IG
Probability (%)
Median days since inoculation
Mean titer (pfu)
Median days
Total exposure dose (pfu)

Figure S 2.13 | Dose effects on total RNA metrics for all exposure routes.
Visualization techniques are the same as for Figure 2.5, except this figure includes predictions for all exposure routes and for total RNA.

Supplementary Tables

Article	# indivs.	# obs.	Route	Dose (log10 pfu)	Age Class	Sex	Species	PCR type	PCR gene	Culture assay	Cell line	Sample Type	Strain
An et al. 2021	3	42	IT	6.1*	J	U	RM	T	N			I	CHN/U (ID: 20SF107)
Arunachalam et al. 2020	4	32	IT, IN	6.5	J, A, U	M	RM	SG	N, E			NI	USA/WA1/2020
Baum et al. 2020	10	183	IT, IN	6, 5	A, U	M, F	RM	T, SG	N, E			NI	USA/WA1/2020
Berry et al. 2022	6	262	IN	4.5*	U	F	CM	T, SG	E, ORF7	U	VeroE6-SS2	NI, I	AUS/VIC01/2020
Bewley et al. 2020	6	43	IT, IN	6.7	J	U	RM	T	N			NI	AUS/VIC01/2020
Bixler et al. 2022	8	264	AE	4.8	A	U	RM, CM	T, SG	U, E	PFU	Vero 76	NI	USA/WA1/2020
Bixler et al. 2022	8	264	IT, IN	7.4	A	U	RM, CM	T, SG	U, E	PFU	Vero 76	NI	USA/WA1/2020
Blair et al. 2021	4	92	AE	4	A, G	M, F	RM, AGM	T	N			NI	USA/WA1/2020
Blair et al. 2021	4	89	IT, IN, OR, CJ	6.6	A, G	M, F	RM, AGM	T	N			NI	USA/WA1/2020
Böszörményi et al. 2020	8	1180	IT, IN	4.8*	J, A	M	RM, CM	G, SG	ORF1, E			NI, I	DEU/BavPat1/2020
Brouwer et al. 2021	4	124	IT, IN	6	A	F	CM	G, SG	ORF1, E			NI	FRA/1DF0372/2020
Chandrashekar et al. 2020	13	341	IT, IN	6, 5, 4	A	U	RM	T, SG	N, E	PFU	Vero E6	NI, I	USA/WA1/2020
Chen et al. 2021	8§	34	IN	5.1*	J	U	RM	U	U			I	CHN/KMS1/2020
Corbett et al. 2020	15	63	EB	4, 5	A	M, F	RM	U	U			NI	USA/WA1/2020
Corbett et al. 2020	23	167	IT, IN	5.9, 5, 4	J, A	M, F	RM	T, SG, U	N, E, U			NI	USA/WA1/2020
Cross et al. 2020	6	403	IN	6.4	A	F	AGM	T	N	PFU	Vero E6	NI, I	ITA/INMI1/2020
Cross et al. 2021	2	85	IT, IN	5.7	U	U	AGM	T	N	PFU	Vero E6	NI, I	ITA/INMI1/2020
Dabisch et al. 2021	16	448	AE	1.2-3.5*†	J, A	M, F	CM	G	ORF1	TCID50	Vero	NI	USA/WA1/2020
Dagotto et al. 2021	4	16	IT, IN	4	A	U	RM	T	N, E			NI	USA/WA1/2020
Deng et al. 2020A	7	207	IT	5.8*	J	U	RM	T	E			NI, I	CHN/WH-09/2020
Deng et al. 2020B	2	90	CJ	5.8*	J	M	RM	T	E	TCID50	Vero E6	NI, I	CHN/WH-09/2020
Deng et al. 2020B	2	83	IG	5.8*	J	M	RM	T	E			NI, I	CHN/WH-09/2020
Deng et al. 2020B	1	74	IT	5.8*	J	M	RM	T	E	TCID50	Vero E6	NI, I	CHN/WH-09/2020
Fears et al. 2022	8	544	AE	4*	A	M	RM, AGM	T, SG	N	TCID50	Vero E6	NI, I	USA/WA1/2020
Fears et al. 2022	8	543	IT, IN	6.1*	A	M	RM, AGM	T, SG	N	TCID50	Vero E6	NI, I	USA/WA1/2020
Feng et al. 2020	6	63	IT	4.2, 2.4*	A	M, F	RM	T	S			NI, I	CHN/WIV04/2019
Finch et al. 2020	3	117	IB	6.6	J	M, F	CM	T	N			NI	USA/WA1/2020
Fischer et al. 2024	4	68	AE	2.8-3.3*†	J	M	RM	G	ORF1			NI, I	USA/WA1/2020
Fischer et al. 2024	4	68	IN	5.7*	J	M	RM	G	ORF1			NI, I	USA/WA1/2020
Francica et al. 2021	7	42	IT, IN	6.5	U	U	RM	SG	E			NI	USA/WA1/2020
Furuyama et al. 2022	4	124	IT, IN, OR, OC	6.3*	U	F	RM	T, SG	E			NI, I	USA/WA1/2020
Gabitzsch et al. 2021	2	48	IT, IN	5.8*	J	M, F	RM	T, SG	N, E			NI	USA/WA1/2020

Gorman et al. 2021	4	64	IT, IN	6	A	U	RM	T, SG	N, E			NI, I	USA/WA1/2020
Gu et al. 2020	1	1	IT, IN	6.6	A	M	RM	T	E			I	KOR/U (ID: NCCP43326)
Gu et al. 2021	1	7	IT	4.8*	A	U	RM	T	S			NI	CHN/WIV04/2019
Guebre-Xabier et al. 2020	4	16	IT, IN	4	J, A	M, F	CM	SG	E			NI	USA/WA1/2020
Guo et al. 2021	3	45	IT	4.8*	A	U	RM	T	N			NI, I	CHN/WIV04/2019
Hassan et al. 2021	6	138	IN, IB	5.8*	A	U	RM	U, G	N, ORF1	TCID50	Vero E6	NI, I	USA/WA1/2020
He et al. 2021	10	20	IT, IN	4	A	U	RM	SG	E			NI	USA/WA1/2020
Hoang et al. 2021	4	164	IT, IN	6	A	M, F	RM	T	N			NI, I	USA/WA1/2020
Huang et al. 2021	8	104	AE	4*	A	M	RM, AGM	T	N			NI	USA/WA1/2020
Ishigaki et al. 2021	3	393	IT, IN, OR, CJ	6.2*	A	M, F	CM	T	N	TCID50	Vero E6	NI, I	JPN/WK-521/2020
Ishii et al. 2022	4	48	IN	4.8*	J	F	CM	T, SG	U	TCID50	Vero E6-SS2	NI, I	JPN/WK-521/2020
Jiao et al. 2021A	5	335	IG	7	U	M	RM	T	N	TCID50	Vero E6	NI, I	CHN/U
Jiao et al. 2021A	5	326	IN	7	U	M	RM	T	N	TCID50	Vero E6	NI, I	CHN/U
Jiao et al. 2021B	2	100	IC	5, 6	J	M	RM	T	N			NI, I	CHN/U
Jiao et al. 2021B	5	147	IN	7	J	M	RM	T	N			NI, I	CHN/U
Johnston et al. 2020	11	473	AE	4.5, 4.6, 4.7	J, A	M, F	RM, CM, AGM	T	N	PFU	Vero 76	NI	USA/WA1/2020
Jones et al. 2021	4	88	IT, IN	5	A	F	RM	T, SG	N, E			NI, I	USA/WA1/2020
Kim et al. 2021	3	90	IT, IN, OR, OC	6.3*	A	U	RM	T	S	TCID50	Vero E6	NI, I	KOR/U
Kobiyama et al. 2021	2	76	IT, IN, OR, CJ	7.3	A	F	CM	T	N	TCID50	VeroE6-SS2	NI, I	U
Koo et al. 2020	16	567	IT, IN, OR, CJ, IV	7.3*	U	U	RM, CM	G	ORF1	TCID50	Vero	NI, I	KOR/U (ID: NCCP43326)
Lakshmanappa et al. 2021	6	24	IT, IN, OC	6.4	J	M, F	RM	T	N			NI	USA/CA-CZB-59X002/2020
Lambe et al. 2021	6	26	IT, IN	6.7	J	U	RM	T	N			NI	AUS/VIC01/2020
Li (Dandan) et al. 2021	2	34	IN	4.8*	J	M	RM	T	N			NI, I	CHN/KMS1/2020
Li (Dapeng) et al. 2021	11	182	IT, IN	5	J, A	M, F	CM	T, SG	E, N			NI	USA/WA1/2020
Li (Mingxi) et al. 2021	2	24	IT	6	A	M	RM	U, SG	U, E			NI, I	CHN/Wuhan-Hu-1/2020
Li (Yuzhong) et al. 2021	5	15	IT	6.5*	J	U	RM	T	N			I	CHN/Kunming-BP16/2020
Liang et al. 2021	6	136	IT, IN	6.3*	U	M	RM	T	N			NI, I	CHN/U (ID: 107)
Liu (Xiaolei) et al. 2022	4	72	IN	4.8*	J	M, F	RM	T	E			NI, I	CHN/KMS1/2020
Liu (Jiang-Feng) et al. 2022	5	10	IN	5.7	A	U	RM	T	N			I	CHN/U (ID: GD108#)
Liu (Zezhong) et al. 2022	3	48	IT	5.8*	J	U	RM	T	N			NI, I	CHN/WH-09/2020
Lu et al. 2020A	20	760	IT, IN, CJ	6.7, 6.4	J, A	M, F, U	RM, CM	T	N			NI, I	CHN/Wuhan-Hu-1/2020
Lu et al. 2020B	3	27	IT, IN, CJ	6.7	J, A	F	RM	T	N			NI	CHN/Wuhan-Hu-1/2020
Ma et al. 2022	4	92	IT	4.8	J	M, F	RM	T	S			NI, I	CHN/WIV04/2019
Maisonnasse et al. 2020	8	214	IT, IN	6	J	M, F	CM	G	ORF1			NI	FRA/1DF0372/2020

Maisonnasse et al. 2021	5	100	IT, IN	6	U	F	CM	G, SG	ORF1, E			NI	FRA/1DF0372/2020
McMahan et al. 2020	5	56	IT, IN	4	J	M, F, U	RM	SG	E			NI	USA/WA1/2020
Mercado et al. 2020	20	204	IT, IN	4	A	U	RM	SG	E	PFU	Vero E6	NI	USA/WA1/2020
Munster et al. 2020	8	646	IT, IN, OR, OC	6.3*	J, A	M, F	RM	T, SG	E, ORF7	TCID50	Vero E6	NI, I	USA/WA1/2020
Nagata et al. 2021	6	495	IT, IN, CJ	7.4*	A	F	CM	T, SG	N	TCID50	VeroE6-SS2	NI, I	JPN/WK-521/2020
Nawaz et al. 2020	4	59	IN, OR	6.1*	U	U	RM	U	U			NI, I	PAK/Lahore-IV/2020
Nomura et al. 2022	6	295	IN	5.7, 4.7, 3.7*	J, A	M, F	CM	T, SG	U	TCID50	VeroE6-SS2	NI	JPN/WK-521/2020
Pan et al. 2022	4	68	IT	4.8*	A	U	RM	T	S			NI, I	CHN/WIV04/2019
Patel et al. 2021	5	130	IT, IN	4	J	M, F	RM	T, SG	N, E			NI	USA/WA1/2020
Philippens et al. 2021	8	224	IT, IN	4.8*	J, A	M	RM, CM	G, SG	ORF1, E			I	DEU/BavPat1/2020
Qin et al. 2020	2	38	IN	4.8*	J	F	RM	U	U			NI, I	CHN/KMS1/2020
Rauch et al. 2020	6	88	IT, IN	6.7	U	M, F, U	RM	U, SG	N, E			NI, I	AUS/VIC01/2020
Rockx et al. 2020	8	371	IT, IN	6.8*	A	F	CM	U	U	TCID50	Vero E6	NI, I	DEU/BavPat1/2020
Roozendaal et al. 2021	7	84	IT, IN	4.8*	J	M, F	RM	SG	E			NI	USA/WA1/2020
Rosenke et al. 2020	10	482	IT, IN, OR, OC	6.3*	J	M	RM	U	E	TCID50	Vero E6	NI, I	USA/WA1/2020
Rosenke et al. 2021	5	575	IN	6	A, U	M, F	AGM	SG, T	E, N	TCID50	Vero E6	NI, I	USA/RML-7/2020
Routhu et al. 2021	5	60	IT	4.7	J	M	RM	SG	E			NI	USA/WA1/2020
Salguero et al. 2021	12	437	IT, IN	6.7	J	M, F, U	RM, CM	T, SG	N, E	PFU	Vero E6	NI, I	AUS/VIC01/2020
Sanchez-Felipe et al. 2021	6	24	IT, IN	4*	J, A	M	CM	G	ORF1			NI	BEL/GHB-03021/2020
Saunders et al. 2021	5	46	IT, IN	5	J, A	M, F	CM	SG	E, N	PFU	Vero E6	NI	USA/WA1/2020
Seo et al. 2021	3	54	IT, IN, OR, CJ, IV	7.3*	U	U	CM	G	ORF1	TCID50	Vero	NI	KOR/U (ID: NCCP43326)
Shan et al. 2020	8	330	IT	6.7, 5.8*	A	M, F	RM	T	S	TCID50	Vero E6	NI, I	CHN/WIV04/2019
Shi et al. 2020	1§	1	IT	4.8*	A	U	RM	T	S			NI	CHN/IVDC-HB-envF13/2020
Singh et al. 2020	16	592	IT, IN, OC	6	J, G	M, F	RM	T, SG	N, E	PFU	Vero E6	NI, I	USA/WA1/2020
Sokol et al. 2021	4	83	IT, IN	7.3	J, A	F	RM, CM	G	ORF1			NI	FRA/1DF0372/2020
Song et al. 2020	8	280	IT	6.8*	A	M	RM	T	N			NI, I	CHN/U (ID: 107)
Song et al. 2021	3	48	IT	6.8*	A	M	RM	U	U			NI, I	CHN/U (ID: 107)
Song et al. 2021	3	48	IT, IN	6.8*	A	M	RM	U	U			NI, I	CHN/U (ID: 107)
Speranza et al. 2020	8	557	IT, IN, OR, OC	6.3*	A	M, F	AGM	T, SG	E	TCID50	Vero E6	NI, I	USA/WA1/2020
Sun (Shiyu) et al. 2021	6	180	IN	6.8*	J	M, F	RM	T	N			NI, I	CHN/U (ID: 107)
Sun (Shihui) et al. 2021	4	24	IT, IN, OC	6.3*	J	M, F	CM	T	S			I	CHN/IME-BJ01/2020
Sun et al. 2023	4	83	IN	5.7	A	U	RM	T	N			NI, I	CHN/U (ID: GD108#)
Tan (Shudan) et al. 2023	4	148	IT	4.8*	A	M, F	RM	T	S			NI, I	CHN/WIV04/2019
Tan (Janessa) et al. 2023	4	144	IT	6.3*	U	U	CM	T	N			NI	SG/WX-56/2020

van Doremalen et al. 2020	6	456	IT, IN, OR, OC	6.3*	J	U	RM	G, SG	ORF1, E	TCID50	Vero E6	NI, I	USA/WA1/2020
Vogel et al. 2021	9	130	IT, IN	6	J	M	RM	T	N			NI	USA/WA1/2020
Wang (Gan) et al. 2020	3	90	IT, IN	6.8*	A	M	RM	T	N			NI, I	CHN/U (ID: GD108#)
Wang (Shuang) et al. 2020	3	84	IT	4.8*	A	U	RM	T	S			NI, I	CHN/WIV04/2019
Wang (Hui) et al. 2020	2	26	IT	5.8*	J	U	RM	T	N			NI, I	CHN/WH-09/2020
Wang et al. 2022	6	180	IT	4.8*	A	M, F	RM	SG	S			NI, I	CHN/WIV04/2019
Williamson et al. 2020	6	441	IT, IN, OR, OC	6.3*	J	M, F	RM	T	E	TCID50	Vero E6	NI, I	USA/WA1/2020
Woolsey et al. 2020	6	470	IT, IN	5.7	A	M, F, U	AGM	T	N	PFU	Vero E6	NI, I	ITA/INMI1/2020
Yadav et al. 2021A	5	313	IT, IN	6.5*	A	U	RM	T, SG	E			NI, I	IND/UN-770/2020
Yadav et al. 2021B	4	262	IT, IN	6.5*	A	U	RM	T, SG	E	U	Vero CCL-81	NI, I	U
Yang et al. 2020	5	166	IN	5.7	A	U	RM	T, SG	N, E			NI, I	U
Yao et al. 2021	3	30	IT	5.8*	A	U	RM	T	S			NI, I	CHN/WIV04/2019
Yu (Jingyou) et al. 2020	10	209	IT, IN	4	A	U	RM	T, SG	N, E	PFU	Vero E6	NI	U
Yu (Pin) et al. 2020	5	21	IT	5.8*	J, A	U	RM	T	E			NI, I	CHN/IVDC-HB-01/2020
Yu et al. 2022	9	252	IG	5.8*	A	U	RM	T, SG	N, E			NI	USA/WA1/2020
Yu et al. 2022	12	240	IT, IN	4.8*	A	U	RM	SG	E			NI	USA/WA1/2020
Zheng et al. 2020	14	670	IN	5.1*	J	M	RM	G	ORF1	TCID50	Vero	NI, I	CHN/KMS1/2020
Zost et al. 2020	4	20	IT, IN	4	A	U	RM	SG	E			NI	USA/WA1/2020

Table S 2.1 | Database summary.

Each row is for a distinct exposure route, so articles with multiple routes have multiple rows. Acronyms are: IN, intranasal; IT, intratracheal; IC, intracranial; OR, oral; OC: ocular; CJ: conjunctival; IV, intravenous; AE, aerosol; IB, intrabronchial; EB: endobronchial; U, unknown; J, juvenile; A, adult; G, geriatric; M, male; F, female; RM, rhesus macaque; CM, cynomolgus macaque; AGM, African green monkey; T, total RNA; G, genomic RNA; SG, subgenomic RNA; VeroE6-SS2, VeroE6-TMPRS22. *: dose reported as TCID50 was converted to pfu. †: includes many doses in the indicated range. §: more than this number of animals were included in the indicated study, but we were only able to extract individual-level data for some of them. For articles where the first author has the same last name as another author, we also include the first name of the first author in parentheses.

Exposure category	URT	LRT	URT + LRT (Liquid)	URT + LRT (Aerosol)	GI
Reported Inoculation Routes	IN OC	IT IB EB	IT, IN IB, IN IT, IN, OC IT, IN, OR, OC IT, IN, OR, OC, IV	AE	IG

Table S 2.2 | Categorization of reported inoculation routes into exposure categories for model fitting.
Acronyms are as follows: IN: intranasal; OC: ocular; IT: intratracheal; IB: intrabronchial; EB: endobronchial; OR: oral; IV: intravenous; AE: aerosol; IG: intragastric. Underlines indicate the route used when generating predictions for each category.

Tissue Group	Non-invasive sample types	Invasive sample types	
Nose	Nasal swab / wash Nasopharyngeal swab / fluid	Nasal mucosa / tissue	
Throat	Throat swab Pharyngeal swab Oropharyngeal swab	Oropharynx Laryngeal mucosa	
Trachea	Tracheal swab / brush / fluid	Trachea Carina	
Lung	BAL Bronchial brush / swab	Bronchus Lung (any lobe)	
Upper GI		Esophagus Stomach Liver Small intestine	Duodenum Ileum Jejunum
Lower GI	Rectal swab / fluid Anal swab Feces / Fecal swab	Colon Cecum	

Table S 2.3 | Reported sample types grouped into tissue categories.

References

Alford, R. H., Kasel, J. A., Gerone, P. J., & Knight, V. (1966). Human influenza resulting from aerosol inhalation. *Proceedings of the Society for Experimental Biology and Medicine*. Society for Experimental Biology and Medicine (New York, N.Y.), 122(3), 800–804. https://doi.org/10.3181/00379727-122-31255

Althouse, B. M., Durbin, A. P., Hanley, K. A., Halstead, S. B., Weaver, S. C., & Cummings, D. A. T. (2014). Viral kinetics of primary dengue virus infection in non-human primates: A systematic review and individual pooled analysis. *Virology*, 452–453, 237–246. https://doi.org/10.1016/j.virol.2014.01.015

Amico, M., & Keilegom, I. V. (2018). Cure Models in Survival Analysis. *Annual Review of Statistics and Its Application*, 5(Volume 5, 2018), 311–342. https://doi.org/10.1146/annurev-statistics-031017-100101

An, Y., Li, S., Jin, X., Han, J., Xu, K., Xu, S., Han, Y., Liu, C., Zheng, T., Liu, M., Yang, M., Song, T.-Z., Huang, B., Zhao, L., Wang, W., A, R., Cheng, Y., Wu, C., Huang, E., … Gao, G. F. (2022). A tandem-repeat dimeric RBD protein-based covid-19 vaccine zf2001 protects mice and nonhuman primates. *Emerging Microbes & Infections*, 11(1), 1058–1071. https://doi.org/10.1080/22221751.2022.2056524

Anton, A., Geraldi, N. R., Lovelock, C. E., Apostolaki, E. T., Bennett, S., Cebrian, J., Krause-Jensen, D., Marbà, N., Martinetto, P., Pandolfi, J. M., Santana-Garcon, J., & Duarte, C. M. (2019). Global ecological impacts of marine exotic species. *Nature Ecology & Evolution*, 3(5), 787–800. https://doi.org/10.1038/s41559-019-0851-0

Arunachalam, P. S., Walls, A. C., Golden, N., Atyeo, C., Fischinger, S., Li, C., Aye, P., Navarro, M. J., Lai, L., Edara, V. V., Röltgen, K., Rogers, K., Shirreff, L., Ferrell, D. E., Wrenn, S., Pettie, D., Kraft, J. C., Miranda, M. C., Kepl, E., … Pulendran, B. (2021). Adjuvanting a subunit COVID-19 vaccine to induce protective immunity. *Nature*, 594(7862), 253–258. https://doi.org/10.1038/s41586-021-03530-2

Baum, A., Ajithdoss, D., Copin, R., Zhou, A., Lanza, K., Negron, N., Ni, M., Wei, Y., Mohammadi, K., Musser, B., Atwal, G. S., Oyejide, A., Goez-Gazi, Y., Dutton, J., Clemmons, E., Staples, H. M., Bartley, C., Klaffke, B., Alfson, K., … Kyratsous, C. A. (2020). REGN-COV2 antibodies prevent and treat SARS-CoV-2 infection in rhesus macaques and hamsters. *Science*, 370(6520), 1110–1115. https://doi.org/10.1126/science.abe2402

Belser, J. A., Rota, P. A., & Tumpey, T. M. (2013). Ocular Tropism of Respiratory Viruses. *Microbiology and Molecular Biology Reviews*, 77(1), 144–156. https://doi.org/10.1128/MMBR.00058-12

Berry, N., Ferguson, D., Kempster, S., Hall, J., Ham, C., Jenkins, A., Rannow, V., Giles, E., Leahy, R., Goulding, S., Fernandez, A., Adedeji, Y., Vessillier, S., Rajagopal, D., Prior, S., Le Duff, Y., Hurley, M., Gilbert, S., Fritzsche, M., … Almond, N. (2022). Intrinsic host susceptibility among multiple species to intranasal SARS-CoV-2 identifies diverse virological, biodistribution and pathological outcomes. *Scientific Reports*, 12(1), 18694. https://doi.org/10.1038/s41598-022-23339-x

Bewley, K. R., Gooch, K., Thomas, K. M., Longet, S., Wiblin, N., Hunter, L., Chan, K., Brown, P., Russell, R. A., Ho, C., Slack, G., Humphries, H. E., Alden, L., Allen, L., Aram, M., Baker, N., Brunt, E., Cobb, R., Fotheringham, S., … Carroll, M. (2021). Immunological and pathological outcomes of SARS-CoV-2 challenge following formalin-inactivated vaccine in ferrets and rhesus macaques. *Science Advances*, 7(37), eabg7996. https://doi.org/10.1126/sciadv.abg7996

Bixler, S. L., Stefan, C. P., Jay, A. N., Rossi, F. D., Ricks, K. M., Shoemaker, C. J., Moreau, A. M., Zeng, X., Hooper, J. W., Dyer, D. N., Frick, O. M., Koehler, J. W., Kearney, B. J., DiPinto, N., Liu, J., Tostenson, S. D., Clements, T. L., Smith, J. M., Johnson, J. A., … Pitt, M. L. M. (2022). Exposure Route Influences Disease Severity in the COVID-19 Cynomolgus Macaque Model. *Viruses*, 14(5), Article 5. https://doi.org/10.3390/v14051013

Blair, R. V., Vaccari, M., Doyle-Meyers, L. A., Roy, C. J., Russell-Lodrigue, K., Fahlberg, M., Monjure, C. J., Beddingfield, B., Plante, K. S., Plante, J. A., Weaver, S. C., Qin, X., Midkiff, C. C., Lehmicke, G., Golden, N., Threeton, B., Penney, T., Allers, C., Barnes, M. B., … Rappaport, J. (2021). Acute Respiratory Distress in Aged, SARS-CoV-2–Infected African Green Monkeys but Not Rhesus Macaques. *The American Journal of Pathology*, 191(2), 274–282. https://doi.org/10.1016/j.ajpath.2020.10.016

Bogaerts, K., Komárek, A., & Lesaffre, E. (2017). Survival Analysis with Interval-Censored Data: A Practical Approach with Examples in R, SAS, and BUGS. Chapman and Hall/CRC. https://doi.org/10.1201/9781315116945

Bonapersona, V., Hoijtink, H., Sarabdjitsingh, R. A., & Joëls, M. (2021). Increasing the statistical power of animal experiments with historical control data. *Nature Neuroscience*, 24(4), Article 4. https://doi.org/10.1038/s41593-020-00792-3

Böszörményi, K. P., Stammes, M. A., Fagrouch, Z. C., Kiemenyi-Kayere, G., Niphuis, H., Mortier, D., van Driel, N., Nieuwenhuis, I., Vervenne, R. A. W., Haaksma, T., Ouwerling, B., Adema, D., Acar, R. F., Zuiderwijk-Sick, E., Meijer, L., Mooij, P., Remarque, E. J., Oostermeijer, H., Koopman, G., … Verstrepen, B. E. (2021). The Post-Acute Phase of SARS-CoV-2 Infection in Two Macaque Species Is Associated with Signs of Ongoing Virus Replication and Pathology in Pulmonary and Extrapulmonary Tissues. *Viruses*, 13(8), Article 8. https://doi.org/10.3390/v13081673

Bradburne, A. F., Bynoe, M. L., & Tyrrell, D. A. (1967). Effects of a “new” human respiratory virus in volunteers. *British Medical Journal*, 3(5568), 767–769.

Brouwer, P. J. M., Brinkkemper, M., Maisonnasse, P., Dereuddre-Bosquet, N., Grobben, M., Claireaux, M., Gast, M. de, Marlin, R., Chesnais, V., Diry, S., Allen, J. D., Watanabe, Y., Giezen, J. M., Kerster, G., Turner, H. L., Straten, K. van der, Linden, C. A. van der, Aldon, Y., Naninck, T., … Sanders, R. W. (2021). Two-component spike nanoparticle vaccine protects macaques from SARS-CoV-2 infection. *Cell*, 184(5), 1188-1200.e19. https://doi.org/10.1016/j.cell.2021.01.035

Carter, J., & Saunders, V. A. (2007). Virology: Principles and Applications. John Wiley & Sons.

Cevik, M., Tate, M., Lloyd, O., Maraolo, A. E., Schafers, J., & Ho, A. (2021). SARS-CoV-2, SARS-CoV, and MERS-CoV viral load dynamics, duration of viral shedding, and infectiousness: A systematic review and meta-analysis. *The Lancet Microbe*, 2(1), e13–e22. https://doi.org/10.1016/S2666-5247(20)30172-5

Chandrashekar, A., Liu, J., Martinot, A. J., McMahan, K., Mercado, N. B., Peter, L., Tostanoski, L. H., Yu, J., Maliga, Z., Nekorchuk, M., Busman-Sahay, K., Terry, M., Wrijil, L. M., Ducat, S., Martinez, D. R., Atyeo, C., Fischinger, S., Burke, J. S., Slein, M. D., … Barouch, D. H. (2020). SARS-CoV-2 infection protects against rechallenge in rhesus macaques. *Science*, eabc4776–eabc4776. https://doi.org/10.1126/science.abc4776

Chen, H., Xie, Z., Long, R., Fan, S., Li, H., He, Z., Xu, K., Liao, Y., Wang, L., Zhang, Y., Li, X., Dong, X., Mou, T., Zhou, X., Yang, Y., Guo, L., Yang, J., Zheng, H., Xu, X., … Li, Q. (2021). Immunological evaluation of an inactivated SARS-CoV-2 vaccine in rhesus macaques. *Molecular Therapy Methods & Clinical Development*, 23, 108–118. https://doi.org/10.1016/j.omtm.2021.08.005

Cheung, K. S., Hung, I. F. N., Chan, P. P. Y., Lung, K. C., Tso, E., Liu, R., Ng, Y. Y., Chu, M. Y., Chung, T. W. H., Tam, A. R., Yip, C. C. Y., Leung, K.-H., Fung, A. Y.-F., Zhang, R. R., Lin, Y., Cheng, H. M., Zhang, A. J. X., To, K. K. W., Chan, K.-H., … Leung, W. K. (2020). Gastrointestinal Manifestations of SARS-CoV-2 Infection and Virus Load in Fecal Samples From a Hong Kong Cohort: Systematic Review and Meta-analysis. *Gastroenterology*, 159(1), 81–95. https://doi.org/10.1053/j.gastro.2020.03.065

Corbett, K. S., Flynn, B., Foulds, K. E., Francica, J. R., Boyoglu-Barnum, S., Werner, A. P., Flach, B., O'Connell, S., Bock, K. W., Minai, M., Nagata, B. M., Andersen, H., Martinez, D. R., Noe, A. T., Douek, N., Donaldson, M. M., Nji, N. N., Alvarado, G. S., Edwards, D. K., … Graham, B. S. (2020). Evaluation of the mRNA-1273 Vaccine against SARS-CoV-2 in Nonhuman Primates. *The New England Journal of Medicine*, NEJMoa2024671–NEJMoa2024671. https://doi.org/10.1056/NEJMoa2024671

Couch, R. B., Cate, T. R., Douglas, R. G., Gerone, P. J., & Knight, V. (1966). Effect of route of inoculation on experimental respiratory viral disease in volunteers and evidence for airborne transmission. *Bacteriological Reviews*, 30(3), 517–529.

Cross, R. W., Agans, K. N., Prasad, A. N., Borisevich, V., Woolsey, C., Deer, D. J., Dobias, N. S., Geisbert, J. B., Fenton, K. A., & Geisbert, T. W. (2020). Intranasal exposure of African green monkeys to SARS-CoV-2 results in acute phase pneumonia with shedding and lung injury still present in the early convalescence phase. *Virology Journal*, 17(1), 125–125. https://doi.org/10.1186/s12985-020-01396-w

Cross, R. W., Prasad, A. N., Borisevich, V., Woolsey, C., Agans, K. N., Deer, D. J., Dobias, N. S., Geisbert, J. B., Fenton, K. A., & Geisbert, T. W. (2021). Use of convalescent serum reduces severity of COVID-19 in nonhuman primates. *Cell Reports*, 34(10), 108837. https://doi.org/10.1016/j.celrep.2021.108837

Dabisch, P. A., Biryukov, J., Beck, K., Boydston, J. A., Sanjak, J. S., Herzog, A., Green, B., Williams, G., Yeager, J., Bohannon, J. K., Holland, B., Miller, D., Reese, A. L., Freeburger, D., Miller, S., Jenkins, T., Rippeon, S., Miller, J., Clarke, D., … Hevey, M. (2021). Seroconversion and fever are dose-dependent in a nonhuman primate model of inhalational COVID-19. *PLOS Pathogens*, 17(8), e1009865. https://doi.org/10.1371/journal.ppat.1009865

Dagotto, G., Mercado, N. B., Martinez, D. R., Hou, Y. J., Nkolola, J. P., Carnahan, R. H., Crowe, J. E., Baric, R. S., & Barouch, D. H. (2021). Comparison of Subgenomic and Total RNA in SARS-CoV-2-Challenged Rhesus Macaques. *Journal of Virology*, 95(8). https://doi.org/10.1128/JVI.02370-20

de Wit, E., Bushmaker, T., Scott, D., Feldmann, H., & Munster, V. J. (2011). Nipah Virus Transmission in a Hamster Model. *PLoS Neglected Tropical Diseases*, 5(12), e1432–e1432. https://doi.org/10.1371/journal.pntd.0001432

Deng, W., Bao, L., Gao, H., Xiang, Z., Qu, Y., Song, Z., Gong, S., Liu, J., Liu, J., Yu, P., Qi, F., Xu, Y., Li, F., Xiao, C., Lv, Q., Xue, J., Wei, Q., Liu, M., Wang, G., … Qin, C. (2020). Ocular conjunctival inoculation of SARS-CoV-2 can cause mild COVID-19 in rhesus macaques. *Nature Communications*, 11(1), Article 1. https://doi.org/10.1038/s41467-020-18149-6

Deng, W., Bao, L., Liu, J., Xiao, C., Liu, J., Xue, J., Lv, Q., Qi, F., Gao, H., Yu, P., Xu, Y., Qu, Y., Li, F., Xiang, Z., Yu, H., Gong, S., Liu, M., Wang, G., Wang, S., … Qin, C. (2020). Primary exposure to SARS-CoV-2 protects against reinfection in rhesus macaques. *Science*, eabc5343–eabc5343. https://doi.org/10.1126/science.abc5343

Dudley, D. M., Newman, C. M., Lalli, J., Stewart, L. M., Koenig, M. R., Weiler, A. M., Semler, M. R., Barry, G. L., Zarbock, K. R., Mohns, M. S., Breitbach, M. E., Schultz-Darken, N., Peterson, E., Newton, W., Mohr, E. L., Capuano III, S., Osorio, J. E., O'Connor, S. L., O'Connor, D. H., … Aliota, M. T. (2017). Infection via mosquito bite alters Zika virus tissue tropism and replication kinetics in rhesus macaques. *Nature Communications*, 8(1), Article 1. https://doi.org/10.1038/s41467-017-02222-8

Estes, J. D., Wong, S. W., & Brenchley, J. M. (2018). Nonhuman primate models of human viral infections. *Nature Reviews Immunology*, 18(6), Article 6. https://doi.org/10.1038/s41577-018-0005-7

Fahlberg, M. D., Blair, R. V., Doyle-Meyers, L. A., Midkiff, C. C., Zenere, G., Russell-Lodrigue, K. E., Monjure, C. J., Haupt, E. H., Penney, T. P., Lehmicke, G., Threeton, B. M., Golden, N., Datta, P. K., Roy, C. J., Bohm, R. P., Maness, N. J., Fischer, T., Rappaport, J., & Vaccari, M. (2020). Cellular events of acute, resolving or progressive COVID-19 in SARS-CoV-2 infected non-human primates. *bioRxiv*, 21, 2020.07.21.213777-2020.07.21.213777. https://doi.org/10.1101/2020.07.21.213777

Fears, A. C., Beddingfield, B. J., Chirichella, N. R., Slisarenko, N., Killeen, S. Z., Redmann, R. K., Goff, K., Spencer, S., Picou, B., Golden, N., Midkiff, C. C., Bush, D. J., Branco, L. M., Boisen, M. L., Gao, H., Montefiori, D. C., Blair, R. V., Doyle-Meyers, L. A., Russell-Lodrigue, K., … Roy, C. J. (2022). Exposure modality influences viral kinetics but not respiratory outcome of COVID-19 in multiple nonhuman primate species. *PLOS Pathogens*, 18(7), e1010618. https://doi.org/10.1371/journal.ppat.1010618

Feng, L., Wang, Q., Shan, C., Yang, C., Feng, Y., Wu, J., Liu, X., Zhou, Y., Jiang, R., Hu, P., Liu, X., Zhang, F., Li, P., Niu, X., Liu, Y., Zheng, X., Luo, J., Sun, J., Gu, Y., … Chen, L. (2020). An adenovirus-vectored COVID-19 vaccine confers protection from SARS-COV-2 challenge in rhesus macaques. *Nature Communications*, 11(1), 4207–4207. https://doi.org/10.1038/s41467-020-18077-5

Finch, C. L., Crozier, I., Lee, J. H., Byrum, R., Cooper, T. K., Liang, J., Sharer, K., Solomon, J., Sayre, P. J., Kocher, G., Bartos, C., Aiosa, N. M., Castro, M., Larson, P. A., Adams, R., Beitzel, B., Paola, N. D., Kugelman, J. R., Kurtz, J. R., … Kuhn, J. H. (2020). Characteristic and quantifiable COVID-19-like abnormalities in CT- and PET/CT-imaged lungs of SARS-CoV-2-infected crab-eating macaques (Macaca fascicularis) (p. 2020.05.14.096727). *bioRxiv*. https://doi.org/10.1101/2020.05.14.096727

Fischer, R. J., Bushmaker, T., Williamson, B. N., Pérez-Pérez, L., Feldmann, F., Lovaglio, J., Scott, D., Saturday, G., Feldmann, H., Munster, V. J., de Wit, E., & van Doremalen, N. (2024). Compartmentalized SARS-CoV-2 Replication in the Upper vs Lower Respiratory Tract After Intranasal Inoculation or Aerosol Exposure. *The Journal of Infectious Diseases*, 230(3), 657–661. https://doi.org/10.1093/infdis/jiae018

Francica, J. R., Flynn, B. J., Foulds, K. E., Noe, A. T., Werner, A. P., Moore, I. N., Gagne, M., Johnston, T. S., Tucker, C., Davis, R. L., Flach, B., O'Connell, S., Andrew, S. F., Lamb, E., Flebbe, D. R., Nurmukhambetova, S. T., Donaldson, M. M., Todd, J.-P. M., Zhu, A. L., … Seder, R. A. (2021). Protective antibodies elicited by SARS-CoV-2 spike protein vaccination are boosted in the lung after challenge in nonhuman primates. *Science Translational Medicine*. https://www.science.org/doi/abs/10.1126/scitranslmed.abi4547

Furuyama, W., Shifflett, K., Pinski, A. N., Griffin, A. J., Feldmann, F., Okumura, A., Gourdine, T., Jankeel, A., Lovaglio, J., Hanley, P. W., Thomas, T., Clancy, C. S., Messaoudi, I., O'Donnell, K. L., & Marzi, A. (2022). Rapid Protection from COVID-19 in Nonhuman Primates Vaccinated Intramuscularly but Not Intranasally with a Single Dose of a Vesicular Stomatitis Virus-Based Vaccine. *mBio*, 13(1), e03379-21. https://doi.org/10.1128/mbio.03379-21

Gabitzsch, E., Safrit, J. T., Verma, M., Rice, A., Sieling, P., Zakin, L., Shin, A., Morimoto, B., Adisetiyo, H., Wong, R., Bezawada, A., Dinkins, K., Balint, J., Peykov, V., Garban, H., Liu, P., Bacon, A., Bone, P., Drew, J., … Soon-Shiong, P. (2021). Dual-Antigen COVID-19 Vaccine Subcutaneous Prime Delivery With Oral Boosts Protects NHP Against SARS-CoV-2 Challenge. *Frontiers in Immunology*, 12. https://www.frontiersin.org/articles/10.3389/fimmu.2021.729837

Gandhi, M., & Rutherford, G. W. (2020). Facial Masking for Covid-19—Potential for "Variolation" as We Await a Vaccine. *New England Journal of Medicine*, 383(18), e101. https://doi.org/10.1056/NEJMp2026913

Gao, Q., Bao, L., Mao, H., Wang, L., Xu, K., Yang, M., Li, Y., Zhu, L., Wang, N., Lv, Z., Gao, H., Ge, X., Kan, B., Hu, Y., Liu, J., Cai, F., Jiang, D., Yin, Y., Qin, C., … Qin, C. (2020). Development of an inactivated vaccine candidate for SARS-CoV-2. *Science*, 369(6499), eabc1932–eabc1932. https://doi.org/10.1126/science.abc1932

Gorman, M. J., Patel, N., Guebre-Xabier, M., Zhu, A. L., Atyeo, C., Pullen, K. M., Loos, C., Goez-Gazi, Y., Carrion, R., Tian, J.-H., Yuan, D., Bowman, K. A., Zhou, B., Maciejewski, S., McGrath, M. E., Logue, J., Frieman, M. B., Montefiori, D., Mann, C., … Alter, G. (2021). Fab and Fc contribute to maximal protection against SARS-CoV-2 following NVX-CoV2373 subunit vaccine with Matrix-M vaccination. *Cell Reports Medicine*, 2(9), 100405. https://doi.org/10.1016/j.xcrm.2021.100405

Gu, C., Cao, X., Wang, Z., Hu, X., Yao, Y., Zhou, Y., Liu, P., Liu, X., Gao, G., Hu, X., Zhang, Y., Chen, Z., Gao, L., Peng, Y., Jia, F., Shan, C., Yu, L., Liu, K., Li, N., … Deng, S.-J. (2021). A human antibody of potent efficacy against SARS-CoV-2 in rhesus macaques showed strong blocking activity to B.1.351. *mAbs,* 13(1), 1930636. https://doi.org/10.1080/19420862.2021.1930636

Gu, S. H., Ho Yu, C., Song, Y., Young Kim, N., Sim, E., Young Choi, J., Hyun Song, D., Haeng Hur, G., Kee Shin, Y., & Tae Jeong, S. (2020). A Small interfering RNA lead targeting RNA-dependent RNA-polymerase effectively inhibit the SARS-CoV-2 infection in Golden Syrian hamster and Rhesus macaque. *bioRxiv*, 2020.07.07.190967-2020.07.07.190967. https://doi.org/10.1101/2020.07.07.190967

Guebre-Xabier, M., Patel, N., Tian, J.-H., Zhou, B., Maciejewski, S., Lam, K., Portnoff, A. D., Massare, M. J., Frieman, M. B., Piedra, P. A., Ellingsworth, L., Glenn, G., & Smith, G. (2020). NVX-CoV2373 vaccine protects cynomolgus macaque upper and lower airways against SARS-CoV-2 challenge. *Vaccine*, 38(50), 7892–7896. https://doi.org/10.1016/j.vaccine.2020.10.064

Guo, Q., Zhao, Y., Li, J., Liu, J., Yang, X., Guo, X., Kuang, M., Xia, H., Zhang, Z., Cao, L., Luo, Y., Bao, L., Wang, X., Wei, X., Deng, W., Wang, N., Chen, L., Chen, J., Zhu, H., … You, F. (2021). Induction of alarmin S100A8/A9 mediates activation of aberrant neutrophils in the pathogenesis of COVID-19. *Cell Host & Microbe*, 29(2), 222-235.e4. https://doi.org/10.1016/j.chom.2020.12.016

Guo, Y., Huang, L., Zhang, G., Yao, Y., Zhou, H., Shen, S., Shen, B., Li, B., Li, X., Zhang, Q., Chen, M., Chen, D., Wu, J., Fu, D., Zeng, X., Feng, M., Pi, C., Wang, Y., Zhou, X., … Rao, Z. (2021). A SARS-CoV-2 neutralizing antibody with extensive Spike binding coverage and modified for optimal therapeutic outcomes. *Nature Communications*, 12(1), 2623. https://doi.org/10.1038/s41467-021-22926-2

Hassan, A. O., Feldmann, F., Zhao, H., Curiel, D. T., Okumura, A., Tang-Huau, T.-L., Case, J. B., Meade-White, K., Callison, J., Chen, R. E., Lovaglio, J., Hanley, P. W., Scott, D. P., Fremont, D. H., Feldmann, H., & Diamond, M. S. (2021). A single intranasal dose of chimpanzee adenovirus-vectored vaccine protects against SARS-CoV-2 infection in rhesus macaques. *Cell Reports. Medicine*, 2(4), 100230. https://doi.org/10.1016/j.xcrm.2021.100230

He, X., Chandrashekar, A., Zahn, R., Wegmann, F., Yu, J., Mercado, N. B., McMahan, K., Martinot, A. J., Piedra-Mora, C., Beecy, S., Ducat, S., Chamanza, R., Huber, S. R., van Heerden, M., van der Fits, L., Borducchi, E. N., Lifton, M., Liu, J., Nampanya, F., … Barouch, D. H. (2021). Low-dose Ad26.COV2.S protection against SARS-CoV-2 challenge in rhesus macaques. *Cell*, 184(13), 3467-3473.e11. https://doi.org/10.1016/j.cell.2021.05.040

He, X., Lau, E. H. Y., Wu, P., Deng, X., Wang, J., Hao, X., Lau, Y. C., Wong, J. Y., Guan, Y., Tan, X., Mo, X., Chen, Y., Liao, B., Chen, W., Hu, F., Zhang, Q., Zhong, M., Wu, Y., Zhao, L., … Leung, G. M. (2020). Temporal dynamics in viral shedding and transmissibility of COVID-19. *Nature Medicine*, 26(5), 672–675. https://doi.org/10.1038/s41591-020-0869-5

Hoang, T. N., Pino, M., Boddapati, A. K., Viox, E. G., Starke, C. E., Upadhyay, A. A., Gumber, S., Nekorchuk, M., Busman-Sahay, K., Strongin, Z., Harper, J. L., Tharp, G. K., Pellegrini, K. L., Kirejczyk, S., Zandi, K., Tao, S., Horton, T. R., Beagle, E. N., Mahar, E. A., … Paiardini, M. (2021). Baricitinib treatment resolves lower-airway macrophage inflammation and neutrophil recruitment in SARS-CoV-2-infected rhesus macaques. *Cell*, 184(2), 460-475.e21. https://doi.org/10.1016/j.cell.2020.11.007

Huang, Z., Ning, B., Yang, H. S., Youngquist, B. M., Niu, A., Lyon, C. J., Beddingfield, B. J., Fears, A. C., Monk, C. H., Murrell, A. E., Bilton, S. J., Linhuber, J. P., Norton, E. B., Dietrich, M. L., Yee, J., Lai, W., Scott, J. W., Yin, X.-M., Rappaport, J., … Hu, T. Y. (2021). Sensitive tracking of circulating viral RNA through all stages of SARS-CoV-2 infection. *The Journal of Clinical Investigation*, 131(7). https://doi.org/10.1172/JCI146031

Imai, M., Iwatsuki-Horimoto, K., Hatta, M., Loeber, S., Halfmann, P. J., Nakajima, N., Watanabe, T., Ujie, M., Takahashi, K., Ito, M., Yamada, S., Fan, S., Chiba, S., Kuroda, M., Guan, L., Takada, K., Armbrust, T., Balogh, A., Furusawa, Y., … Kawaoka, Y. (2020). Syrian hamsters as a small animal model for SARS-CoV-2 infection and countermeasure development. *Proceedings of the National Academy of Sciences of the United States of America*, 117(28), 16587–16595. https://doi.org/10.1073/pnas.2009799117

Ishigaki, H., Nakayama, M., Kitagawa, Y., Nguyen, C. T., Hayashi, K., Shiohara, M., Gotoh, B., & Itoh, Y. (2021). Neutralizing antibody-dependent and -independent immune responses against SARS-CoV-2 in cynomolgus macaques. *Virology*, 554, 97–105. https://doi.org/10.1016/j.virol.2020.12.013

Ishii, H., Nomura, T., Yamamoto, H., Nishizawa, M., Thu Hau, T. T., Harada, S., Seki, S., Nakamura-Hoshi, M., Okazaki, M., Daigen, S., Kawana-Tachikawa, A., Nagata, N., Iwata-Yoshikawa, N., Shiwa, N., Suzuki, T., Park, E.-S., Ken, M., Onodera, T., Takahashi, Y., … Matano, T. (2022). Neutralizing-antibody-independent SARS-CoV-2 control correlated with intranasal-vaccine-induced CD8+ T cell responses. *Cell Reports. Medicine*, 3(2), 100520. https://doi.org/10.1016/j.xcrm.2022.100520

Jiao, L., Li, H., Xu, J., Yang, M., Ma, C., Li, J., Zhao, S., Wang, H., Yang, Y., Yu, W., Wang, J., Yang, J., Long, H., Gao, J., Ding, K., Wu, D., Kuang, D., Zhao, Y., Liu, J., … Peng, X. (2021). The Gastrointestinal Tract Is an Alternative Route for SARS-CoV-2 Infection in a Nonhuman Primate Model. *Gastroenterology*, 160(5), 1647–1661. https://doi.org/10.1053/j.gastro.2020.12.001

Jiao, L., Yang, Y., Yu, W., Zhao, Y., Long, H., Gao, J., Ding, K., Ma, C., Li, J., Zhao, S., Wang, H., Li, H., Yang, M., Xu, J., Wang, J., Yang, J., Kuang, D., Luo, F., Qian, X., … Peng, X. (2021). The olfactory route is a potential way for SARS-CoV-2 to invade the central nervous system of rhesus monkeys. *Signal Transduction and Targeted Therapy*, 6(1), Article 1. https://doi.org/10.1038/s41392-021-00591-7

Johnston, S. C., Ricks, K. M., Jay, A., Raymond, J. L., Rossi, F., Zeng, X., Scruggs, J., Dyer, D., Frick, O., Koehler, J. W., Kuehnert, P. A., Clements, T. L., Shoemaker, C. J., Coyne, S. R., Delp, K. L., Moore, J., Berrier, K., Esham, H., Shamblin, J., … Nalca, A. (2021). Development of a coronavirus disease 2019 nonhuman primate model using airborne exposure. *PLOS ONE*, 16(2), e0246366. https://doi.org/10.1371/journal.pone.0246366

Jones, B. E., Brown-Augsburger, P. L., Corbett, K. S., Westendorf, K., Davies, J., Cujec, T. P., Wiethoff, C. M., Blackbourne, J. L., Heinz, B. A., Foster, D., Higgs, R. E., Balasubramaniam, D., Wang, L., Zhang, Y., Yang, E. S., Bidshahri, R., Kraft, L., Hwang, Y., Žentelis, S., … Falconer, E. (2021). The neutralizing antibody, LY-CoV555, protects against SARS-CoV-2 infection in nonhuman primates. *Science Translational Medicine*, 13(593), eabf1906. https://doi.org/10.1126/scitranslmed.abf1906

Jones, T. C., Biele, G., Mühlemann, B., Veith, T., Schneider, J., Beheim-Schwarzbach, J., Bleicker, T., Tesch, J., Schmidt, M. L., Sander, L. E., Kurth, F., Menzel, P., Schwarzer, R., Zuchowski, M., Hofmann, J., Krumbholz, A., Stein, A., Edelmann, A., Corman, V. M., & Drosten, C. (2021). Estimating infectiousness throughout SARS-CoV-2 infection course. *Science*, 373(6551), eabi5273. https://doi.org/10.1126/science.abi5273

Kieran, T. J., Maines, T. R., & Belser, J. A. (2024). Data alchemy, from lab to insight: Transforming in vivo experiments into data science gold. *PLOS Pathogens*, 20(8), e1012460. https://doi.org/10.1371/journal.ppat.1012460

Killingley, B., Mann, A. J., Kalinova, M., Boyers, A., Goonawardane, N., Zhou, J., Lindsell, K., Hare, S. S., Brown, J., Frise, R., Smith, E., Hopkins, C., Noulin, N., Löndt, B., Wilkinson, T., Harden, S., McShane, H., Baillet, M., Gilbert, A., … Chiu, C. (2022). Safety, tolerability and viral kinetics during SARS-CoV-2 human challenge in young adults. *Nature Medicine*, 1–11. https://doi.org/10.1038/s41591-022-01780-9

Kim, C., Ryu, D.-K., Lee, J., Kim, Y.-I., Seo, J.-M., Kim, Y.-G., Jeong, J.-H., Kim, M., Kim, J.-I., Kim, P., Bae, J. S., Shim, E. Y., Lee, M. S., Kim, M. S., Noh, H., Park, G.-S., Park, J. S., Son, D., An, Y., … Lee, S.-Y. (2021). A therapeutic neutralizing antibody targeting receptor binding domain of SARS-CoV-2 spike protein. *Nature Communications*, 12(1), 288. https://doi.org/10.1038/s41467-020-20602-5

Kissler, S. M., Fauver, J. R., Mack, C., Olesen, S. W., Tai, C., Shiue, K. Y., Kalinich, C. C., Jednak, S., Ott, I. M., Vogels, C. B. F., Wohlgemuth, J., Weisberger, J., DiFiori, J., Anderson, D. J., Mancell, J., Ho, D. D., Grubaugh, N. D., & Grad, Y. H. (2021). Viral dynamics of acute SARS-CoV-2 infection and applications to diagnostic and public health strategies. *PLOS Biology*, 19(7), e3001333. https://doi.org/10.1371/journal.pbio.3001333

Kobiyama, K., Imai, M., Jounai, N., Nakayama, M., Hioki, K., Iwatsuki-Horimoto, K., Yamayoshi, S., Tsuchida, J., Niwa, T., Suzuki, T., Ito, M., Yamada, S., Watanabe, T., Kiso, M., Negishi, H., Temizoz, B., Ishigaki, H., Kitagawa, Y., Nguyen, C. T., … Ishii, K. J. (2021). Optimization of an LNP-mRNA vaccine candidate targeting SARS-CoV-2 receptor-binding domain (p. 2021.03.04.433852). *bioRxiv*. https://doi.org/10.1101/2021.03.04.433852

Koo, B.-S., Oh, H., Kim, G., Hwang, E.-H., Jung, H., Lee, Y., Kang, P., Park, J.-H., Ryu, C.-M., & Hong, J. J. (2020). Transient lymphopenia and interstitial pneumonia with endotheliitis in SARS-CoV-2-infected macaques. *The Journal of Infectious Diseases*. https://doi.org/10.1093/infdis/jiaa486

Lai, J., Mesquita, P. J. B. de, Hong, F., Ma, T., Cowling, B. J., & Milton, D. K. (2024). Influenza A (H3) viral aerosol shedding in nasally inoculated and naturally infected cases (p. 2024.09.09.24313370). *medRxiv*. https://doi.org/10.1101/2024.09.09.24313370

Lakshmanappa, Y. S., Elizaldi, S. R., Roh, J. W., Schmidt, B. A., Carroll, T. D., Weaver, K. D., Smith, J. C., Verma, A., Deere, J. D., Dutra, J., Stone, M., Franz, S., Sammak, R. L., Olstad, K. J., Rachel Reader, J., Ma, Z.-M., Nguyen, N. K., Watanabe, J., Usachenko, J., … Iyer, S. S. (2021). SARS-CoV-2 induces robust germinal center CD4 T follicular helper cell responses in rhesus macaques. *Nature Communications*, 12(1), 541. https://doi.org/10.1038/s41467-020-20642-x

Lambe, T., Spencer, A. J., Thomas, K. M., Gooch, K. E., Thomas, S., White, A. D., Humphries, H. E., Wright, D., Belij-Rammerstorfer, S., Thakur, N., Conceicao, C., Watson, R., Alden, L., Allen, L., Aram, M., Bewley, K. R., Brunt, E., Brown, P., Cavell, B. E., … Gilbert, S. C. (2021). ChAdOx1 nCoV-19 protection against SARS-CoV-2 in rhesus macaque and ferret challenge models. *Communications Biology*, 4(1), 1–12. https://doi.org/10.1038/s42003-021-02443-0

Li, D., Edwards, R. J., Manne, K., Martinez, D. R., Schäfer, A., Alam, S. M., Wiehe, K., Lu, X., Parks, R., Sutherland, L. L., Oguin, T. H., McDanal, C., Perez, L. G., Mansouri, K., Gobeil, S. M. C., Janowska, K., Stalls, V., Kopp, M., Cai, F., … Saunders, K. O. (2021). In vitro and in vivo functions of SARS-CoV-2 infection-enhancing and neutralizing antibodies. *Cell*, 184(16), 4203-4219.e32. https://doi.org/10.1016/j.cell.2021.06.021

Li, D., Luan, N., Li, J., Zhao, H., Zhang, Y., Long, R., Jiang, G., Fan, S., Xu, X., Cao, H., Wang, Y., Liao, Y., Wang, L., Liu, L., Liu, C., & Li, Q. (2021). Waning antibodies from inactivated SARS-CoV-2 vaccination offer protection against infection without antibody-enhanced immunopathology in rhesus macaque pneumonia models. *Emerging Microbes & Infections*, 10(1), 2194–2198. https://doi.org/10.1080/22221751.2021.2002670

Li, M., Guo, J., Lu, S., Zhou, R., Shi, H., Shi, X., Cheng, L., Liang, Q., Liu, H., Wang, P., Wang, N., Wang, Y., Fu, L., Xing, M., Wang, R., Ju, B., Liu, L., Lau, S.-Y., Jia, W., … Zhang, L. (2021). Single-Dose Immunization With a Chimpanzee Adenovirus-Based Vaccine Induces Sustained and Protective Immunity Against SARS-CoV-2 Infection. *Frontiers in Immunology*, 12. https://doi.org/10.3389/fimmu.2021.697074

Li, Y., Bi, Y., Xiao, H., Yao, Y., Liu, X., Hu, Z., Duan, J., Yang, Y., Li, Z., Li, Y., Zhang, H., Ding, C., Yang, J., Li, H., He, Z., Liu, L., Hu, G., Liu, S., Che, Y., … Cun, W. (2021). A novel DNA and protein combination COVID-19 vaccine formulation provides full protection against SARS-CoV-2 in rhesus macaques. *Emerging Microbes & Infections*, 10(1), 342–355. https://doi.org/10.1080/22221751.2021.1887767

Liang, J. G., Su, D., Song, T.-Z., Zeng, Y., Huang, W., Wu, J., Xu, R., Luo, P., Yang, X., Zhang, X., Luo, S., Liang, Y., Li, X., Huang, J., Wang, Q., Huang, X., Xu, Q., Luo, M., Huang, A., … Liang, P. (2021). S-Trimer, a COVID-19 subunit vaccine candidate, induces protective immunity in nonhuman primates. *Nature Communications*, 12(1), 1346. https://doi.org/10.1038/s41467-021-21634-1

Lin, L., Jiang, X., Zhang, Z., Huang, S., Zhang, Z., Fang, Z., Gu, Z., Gao, L., Shi, H., Mai, L., Liu, Y., Lin, X., Lai, R., Yan, Z., Li, X., & Shan, H. (2020). Gastrointestinal symptoms of 95 cases with SARS-CoV-2 infection. *Gut*, 69(6), 997–1001. https://doi.org/10.1136/gutjnl-2020-321013

Lindsley, W. G., Noti, J. D., Blachere, F. M., Thewlis, R. E., Martin, S. B., Othumpangat, S., Noorbakhsh, B., Goldsmith, W. T., Vishnu, A., Palmer, J. E., Clark, K. E., & Beezhold, D. H. (2015). Viable Influenza A Virus in Airborne Particles from Human Coughs. *Journal of Occupational and Environmental Hygiene*, 12(2), 107–113. https://doi.org/10.1080/15459624.2014.973113

Liu, J.-F., Zhou, Y.-N., Lu, S.-Y., Yang, Y.-H., Wu, S.-F., Liu, D.-P., Peng, X.-Z., & Yang, J.-T. (2022). Proteomic and phosphoproteomic profiling of COVID-19-associated lung and liver injury: A report based on rhesus macaques. *Signal Transduction and Targeted Therapy*, 7(1), 1–4. https://doi.org/10.1038/s41392-022-00882-7

Liu, X., Liu, Y., Jin, X., He, Z., Huang, Z., Sun, S., Gao, Y., Li, J., Ning, Q., Xie, Z., Jin, N., & Liu, M. (2022). Rapidly developable therapeutic-grade equine immunoglobulin against the SARS-CoV-2 infection in rhesus macaques. *Signal Transduction and Targeted Therapy*, 7(1), 1–3. https://doi.org/10.1038/s41392-022-01095-8

Liu, Z., Zhou, J., Xu, W., Deng, W., Wang, Y., Wang, M., Wang, Q., Hsieh, M., Dong, J., Wang, X., Huang, W., Xing, L., He, M., Tao, C., Xie, Y., Zhang, Y., Wang, Y., Zhao, J., Yuan, Z., … Lu, L. (2022). A novel STING agonist-adjuvanted pan-sarbecovirus vaccine elicits potent and durable neutralizing antibody and T cell responses in mice, rabbits and NHPs. *Cell Research*, 32(3), 269–287. https://doi.org/10.1038/s41422-022-00612-2

Lockwood, J. L., Cassey, P., & Blackburn, T. (2005). The role of propagule pressure in explaining species invasions. *Trends in Ecology & Evolution*, 20(5), 223–228. https://doi.org/10.1016/j.tree.2005.02.004

Lu, S., Zhao, J., Dong, J., Liu, H., Zhu, Y., Li, H., Liu, L., Yang, Y., Sun, S., Song, Y., Zhao, Y., She, R., Luo, T., Deng, H., & Peng, X. (2021). Effective treatment of SARS-CoV-2-infected rhesus macaques by attenuating inflammation. *Cell Research*, 31(2), 229–232. https://doi.org/10.1038/s41422-020-00414-4

Lu, S., Zhao, Y., Yu, W., Yang, Y., Gao, J., Wang, J., Kuang, D., Yang, M., Yang, J., Ma, C., Xu, J., Qian, X., Li, H., Zhao, S., Li, J., Wang, H., Long, H., Zhou, J., Luo, F., … Peng, X. (2020). Comparison of nonhuman primates identified the suitable model for COVID-19. *Signal Transduction and Targeted Therapy*, 5(1), Article 1. https://doi.org/10.1038/s41392-020-00269-6

Ma, Q., Li, R., Guo, J., Li, M., Ma, L., Dai, J., Shi, Y., Dai, J., Huang, Y., Dai, C., Pan, W., Zhong, H., Zhang, H., Wen, J., Zhao, H., Wu, L., Yang, W., Zhang, B., & Yang, Z. (2022). Immunization with a Prefusion SARS-CoV-2 Spike Protein Vaccine (RBMRNA-176) Protects against Viral Challenge in Mice and Nonhuman Primates. *Vaccines*, 10(10), Article 10. https://doi.org/10.3390/vaccines10101698

Mack, C. D., DiFiori, J., Tai, C. G., Shiue, K. Y., Grad, Y. H., Anderson, D. J., Ho, D. D., Sims, L., LeMay, C., Mancell, J., & Maragakis, L. L. (2021). SARS-CoV-2 Transmission Risk Among National Basketball Association Players, Staff, and Vendors Exposed to Individuals With Positive Test Results After COVID-19 Recovery During the 2020 Regular and Postseason. *JAMA Internal Medicine*, 181(7), 960–966. https://doi.org/10.1001/jamainternmed.2021.2114

Maisonnasse, P., Aldon, Y., Marc, A., Marlin, R., Dereuddre-Bosquet, N., Kuzmina, N. A., Freyn, A. W., Snitselaar, J. L., Gonçalves, A., Caniels, T. G., Burger, J. A., Poniman, M., Bontjer, I., Chesnais, V., Diry, S., Iershov, A., Ronk, A. J., Jangra, S., Rathnasinghe, R., … Le Grand, R. (2021). COVA1-18 neutralizing antibody protects against SARS-CoV-2 in three preclinical models. *Nature Communications*, 12(1), 6097. https://doi.org/10.1038/s41467-021-26354-0

Maisonnasse, P., Guedj, J., Contreras, V., Behillil, S., Solas, C., Marlin, R., Naninck, T., Pizzorno, A., Lemaitre, J., Gonçalves, A., Kahlaoui, N., Terrier, O., Fang, R. H. T., Enouf, V., Dereuddre-Bosquet, N., Brisebarre, A., Touret, F., Chapon, C., Hoen, B., … Le Grand, R. (2020). Hydroxychloroquine use against SARS-CoV-2 infection in non-human primates. *Nature*, 585(7826), 584–587. https://doi.org/10.1038/s41586-020-2558-4

Marois, I., Cloutier, A., Garneau, É., & Richter, M. V. (2012). Initial infectious dose dictates the innate, adaptive, and memory responses to influenza in the respiratory tract. *Journal of Leukocyte Biology*, 92(1), 107–121. https://doi.org/10.1189/jlb.1011490

McCall, L.-I. (2021). Quo vadis? Central Rules of Pathogen and Disease Tropism. *Frontiers in Cellular and Infection Microbiology*, 11, 56. https://doi.org/10.3389/fcimb.2021.640987

McMahan, K., Yu, J., Mercado, N. B., Loos, C., Tostanoski, L. H., Chandrashekar, A., Liu, J., Peter, L., Atyeo, C., Zhu, A., Bondzie, E. A., Dagotto, G., Gebre, M. S., Jacob-Dolan, C., Li, Z., Nampanya, F., Patel, S., Pessaint, L., Van Ry, A., … Barouch, D. H. (2021). Correlates of protection against SARS-CoV-2 in rhesus macaques. *Nature*, 590(7847), 630–634. https://doi.org/10.1038/s41586-020-03041-6

Memoli, M. J., Czajkowski, L., Reed, S., Athota, R., Bristol, T., Proudfoot, K., Fargis, S., Stein, M., Dunfee, R. L., Shaw, P. A., Davey, R. T., & Taubenberger, J. K. (2015). Validation of the Wild-type Influenza A Human Challenge Model H1N1pdMIST: An A(H1N1)pdm09 Dose-Finding Investigational New Drug Study. *Clinical Infectious Diseases*, 60(5), 693–702. https://doi.org/10.1093/cid/ciu924

Mercado, N. B., Zahn, R., Wegmann, F., Loos, C., Chandrashekar, A., Yu, J., Liu, J., Peter, L., McMahan, K., Tostanoski, L. H., He, X., Martinez, D. R., Rutten, L., Bos, R., van Manen, D., Vellinga, J., Custers, J., Langedijk, J. P., Kwaks, T., … Barouch, D. H. (2020). Single-shot Ad26 vaccine protects against SARS-CoV-2 in rhesus macaques. *Nature*, 1–11. https://doi.org/10.1038/s41586-020-2607-z

Mitchell, J., Dean, K., & Haas, C. (2020). Ebola Virus Dose Response Model for Aerosolized Exposures: Insights from Primate Data. *Risk Analysis*, 40(11), 2390–2398. https://doi.org/10.1111/risa.13551

Moher, D., Liberati, A., Tetzlaff, J., & Altman, D. G. (2009). Preferred Reporting Items for Systematic Reviews and Meta-Analyses: The PRISMA Statement. *Annals of Internal Medicine*, 151(4), 264–269. https://doi.org/10.7326/0003-4819-151-4-200908180-00135

Mølbak, K., Sørensen, T. I. A., Bhatt, S., Lyngse, F. P., Simonsen, L., & Aaby, P. (2024). Severity of respiratory tract infections depends on the infectious dose. Perspectives for the next pandemic. *Frontiers in Public Health*, 12. https://doi.org/10.3389/fpubh.2024.1391719

Munster, V. J., Feldmann, F., Williamson, B. N., van Doremalen, N., Pérez-Pérez, L., Schulz, J., Meade-White, K., Okumura, A., Callison, J., Brumbaugh, B., Avanzato, V. A., Rosenke, R., Hanley, P. W., Saturday, G., Scott, D., Fischer, E. R., & de Wit, E. (2020). Respiratory disease in rhesus macaques inoculated with SARS-CoV-2. *Nature*, 585(7824), Article 7824. https://doi.org/10.1038/s41586-020-2324-7

Nagata, N., Iwata-Yoshikawa, N., Sano, K., Ainai, A., Shiwa, N., Shirakura, M., Kishida, N., Arita, T., Suzuki, Y., Harada, T., Kawai, Y., Ami, Y., Iida, S., Katano, H., Fujisaki, S., Sekizuka, T., Shimizu, H., Suzuki, T., & Hasegawa, H. (2021). The peripheral T cell population is associated with pneumonia severity in cynomolgus monkeys experimentally infected with severe acute respiratory syndrome coronavirus 2 (p. 2021.01.07.425698). *bioRxiv*. https://doi.org/10.1101/2021.01.07.425698

Nawaz, M., Ali, M. A., Ashraf, M. A., Shabbir, M. Z., Shabbir, M. A. B., Altaf, I., Raza, S., Rafique, S., Hassan, S., Sardar, N., Mehmood, A., Aziz, M. W., Fazal, S., Khan, M. T., Attique, M. M., Asif, A., Ullah, Z., Iqbal, M., Imtiaz, T., … Yaqub, T. (2020). An assessment of efficacy of Iodine complex (Renessans) against SARS-CoV-2 in non-human primates (Rhesus macaque) (p. 2020.11.17.377432). *bioRxiv*. https://doi.org/10.1101/2020.11.17.377432

Nomura, T., Yamamoto, H., Nishizawa, M., Hau, T. T. T., Harada, S., Ishii, H., Seki, S., Nakamura-Hoshi, M., Okazaki, M., Daigen, S., Kawana-Tachikawa, A., Nagata, N., Iwata-Yoshikawa, N., Shiwa, N., Iida, S., Katano, H., Suzuki, T., Park, E.-S., Maeda, K., … Matano, T. (2021). Subacute SARS-CoV-2 replication can be controlled in the absence of CD8+ T cells in cynomolgus macaques. *PLOS Pathogens*, 17(7), e1009668. https://doi.org/10.1371/journal.ppat.1009668

Pan, X., Shi, J., Hu, X., Wu, Y., Zeng, L., Yao, Y., Shang, W., Liu, K., Gao, G., Guo, W., Peng, Y., Chen, S., Gao, X., Peng, C., Rao, J., Zhao, J., Gong, C., Zhou, H., Lu, Y., … Xiao, G. (2021). RBD-homodimer, a COVID-19 subunit vaccine candidate, elicits immunogenicity and protection in rodents and nonhuman primates. *Cell Discovery*, 7(1), 1–15. https://doi.org/10.1038/s41421-021-00320-y

Patel, A., Walters, J. N., Reuschel, E. L., Schultheis, K., Parzych, E., Gary, E. N., Maricic, I., Purwar, M., Eblimit, Z., Walker, S. N., Guimet, D., Bhojnagarwala, P., Adeniji, O. S., Doan, A., Xu, Z., Elwood, D., Reeder, S. M., Pessaint, L., Kim, K. Y., … Broderick, K. E. (2021). Intradermal-delivered DNA vaccine induces durable immunity mediating a reduction in viral load in a rhesus macaque SARS-CoV-2 challenge model. *Cell Reports. Medicine*, 2(10), 100420. https://doi.org/10.1016/j.xcrm.2021.100420

Pechous, R. D., Sivaraman, V., Stasulli, N. M., & Goldman, W. E. (2016). Pneumonic Plague: The Darker Side of Yersinia pestis. *Trends in Microbiology*, 24(3), 190–197. https://doi.org/10.1016/j.tim.2015.11.008

Philippens, I. H. C. H. M., Böszörményi, K. P., Wubben, J. A. M., Fagrouch, Z. C., van Driel, N., Mayenburg, A. Q., Lozovagia, D., Roos, E., Schurink, B., Bugiani, M., Bontrop, R. E., Middeldorp, J., Bogers, W. M., de Geus-Oei, L.-F., Langermans, J. A. M., Verschoor, E. J., Stammes, M. A., & Verstrepen, B. E. (2022). Brain Inflammation and Intracellular α-Synuclein Aggregates in Macaques after SARS-CoV-2 Infection. *Viruses*, 14(4), Article 4. https://doi.org/10.3390/v14040776

Poisot, T. (2011). The digitize package: Extracting numerical data from scatterplots [Computer software]. http://rjournal.github.io/archive/2011-1/RJournal_2011-1.pdf#page=25

Port, J. R., Yinda, C. K., Owusu, I. O., Holbrook, M., Fischer, R., Bushmaker, T., Avanzato, V. A., Schulz, J. E., Martens, C., van Doremalen, N., Clancy, C. S., & Munster, V. J. (2021). SARS-CoV-2 disease severity and transmission efficiency is increased for airborne compared to fomite exposure in Syrian hamsters. *Nature Communications*, 12(1), Article 1. https://doi.org/10.1038/s41467-021-25156-8

Qin, M., Cao, Z., Wen, J., Yu, Q., Liu, C., Wang, F., Zhang, J., Yang, F., Li, Y., Fishbein, G., Yan, S., Xu, B., Hou, Y., Ning, Z., Nie, K., Jiang, N., Liu, Z., Wu, J., Yu, Y., … Lu, Y. (2020). An Antioxidant Enzyme Therapeutic for COVID-19. *Advanced Materials*, 32(43), 2004901. https://doi.org/10.1002/adma.202004901

R Core Team. (2022). R: A Language and Environment for Statistical Computing [Computer software]. R Foundation for Statistical Computing. https://www.R-project.org/

Rauch, S., Gooch, K., Hall, Y., Salguero, F. J., Dennis, M. J., Gleeson, F. V., Harris, D., Ho, C., Humphries, H. E., Longet, S., Ngabo, D., Paterson, J., Rayner, E. L., Ryan, K. A., Sharpe, S., Watson, R. J., Mueller, S. O., Petsch, B., & Carroll, M. W. (2020). mRNA vaccine CVnCoV protects non-human primates from SARS-CoV-2 challenge infection (p. 2020.12.23.424138). *bioRxiv*. https://doi.org/10.1101/2020.12.23.424138

Riedel, S. (2005). Edward Jenner and the History of Smallpox and Vaccination. Baylor University Medical Center Proceedings, 18(1), 21–25. https://doi.org/10.1080/08998280.2005.11928028

Rockx, B., Kuiken, T., Herfst, S., Bestebroer, T., Lamers, M. M., Munnink, B. B. O., Meulder, D. de, Amerongen, G. van, Brand, J. van den, Okba, N. M. A., Schipper, D., Run, P. van, Leijten, L., Sikkema, R., Verschoor, E., Verstrepen, B., Bogers, W., Langermans, J., Drosten, C., … Haagmans, B. L. (2020). Comparative pathogenesis of COVID-19, MERS, and SARS in a nonhuman primate model. *Science*, 368(6494), 1012–1015. https://doi.org/10.1126/science.abb7314

Roozendaal, R., Solforosi, L., Stieh, D. J., Serroyen, J., Straetemans, R., Dari, A., Boulton, M., Wegmann, F., Rosendahl Huber, S. K., van der Lubbe, J. E. M., Hendriks, J., Le Gars, M., Dekking, L., Czapska-Casey, D. N., Guimera, N., Janssen, S., Tete, S., Chandrashekar, A., Mercado, N. B., … Zahn, R. (2021). SARS-CoV-2 binding and neutralizing antibody levels after Ad26.COV2.S vaccination predict durable protection in rhesus macaques. *Nature Communications*, 12(1), 5877. https://doi.org/10.1038/s41467-021-26117-x

Rosenke, K., Feldmann, F., Okumura, A., Hansen, F., Tang-Huau, T.-L., Meade-White, K., Kaza, B., Callison, J., Lewis, M. C., Smith, B. J., Hanley, P. W., Lovaglio, J., Jarvis, M. A., Shaia, C., & Feldmann, H. (2021). UK B.1.1.7 (Alpha) variant exhibits increased respiratory replication and shedding in nonhuman primates. *Emerging Microbes & Infections*, 10(1), 2173–2182. https://doi.org/10.1080/22221751.2021.1997074

Rosenke, K., Jarvis, M. A., Feldmann, F., Schwarz, B., Okumura, A., Lovaglio, J., Saturday, G., Hanley, P. W., Meade-White, K., Williamson, B. N., Hansen, F., Perez-Perez, L., Leventhal, S., Tang-Huau, T.-L., Callison, J., Haddock, E., Stromberg, K. A., Scott, D., Sewell, G., … Feldmann, H. (2020). Hydroxychloroquine prophylaxis and treatment is ineffective in macaque and hamster SARS-CoV-2 disease models. *JCI Insight*, 5(23). https://doi.org/10.1172/jci.insight.143174

Routhu, N. K., Cheedarla, N., Gangadhara, S., Bollimpelli, V. S., Boddapati, A. K., Shiferaw, A., Rahman, S. A., Sahoo, A., Edara, V. V., Lai, L., Floyd, K., Wang, S., Fischinger, S., Atyeo, C., Shin, S. A., Gumber, S., Kirejczyk, S., Cohen, J., Jean, S. M., … Amara, R. R. (2021). A modified vaccinia Ankara vector-based vaccine protects macaques from SARS-CoV-2 infection, immune pathology, and dysfunction in the lungs. *Immunity*, 54(3), 542-556.e9. https://doi.org/10.1016/j.immuni.2021.02.001

Salguero, F. J., White, A. D., Slack, G. S., Fotheringham, S. A., Bewley, K. R., Gooch, K. E., Longet, S., Humphries, H. E., Watson, R. J., Hunter, L., Ryan, K. A., Hall, Y., Sibley, L., Sarfas, C., Allen, L., Aram, M., Brunt, E., Brown, P., Buttigieg, K. R., … Carroll, M. W. (2021). Comparison of rhesus and cynomolgus macaques as an infection model for COVID-19. *Nature Communications*, 12(1), Article 1. https://doi.org/10.1038/s41467-021-21389-9

Sanchez-Felipe, L., Vercruysse, T., Sharma, S., Ma, J., Lemmens, V., Van Looveren, D., Arkalagud Javarappa, M. P., Boudewijns, R., Malengier-Devlies, B., Liesenborghs, L., Kaptein, S. J. F., De Keyzer, C., Bervoets, L., Debaveye, S., Rasulova, M., Seldeslachts, L., Li, L.-H., Jansen, S., Yakass, M. B., … Dallmeier, K. (2021). A single-dose live-attenuated YF17D-vectored SARS-CoV-2 vaccine candidate. *Nature*, 590(7845), 320–325. https://doi.org/10.1038/s41586-020-3035-9

Saunders, K. O., Lee, E., Parks, R., Martinez, D. R., Li, D., Chen, H., Edwards, R. J., Gobeil, S., Barr, M., Mansouri, K., Alam, S. M., Sutherland, L. L., Cai, F., Sanzone, A. M., Berry, M., Manne, K., Bock, K. W., Minai, M., Nagata, B. M., … Haynes, B. F. (2021). Neutralizing antibody vaccine for pandemic and pre-emergent coronaviruses. *Nature*, 594(7864), 553–559. https://doi.org/10.1038/s41586-021-03594-0

Schreiber, S. J., & Lloyd-Smith, J. O. (2009). Invasion Dynamics in Spatially Heterogeneous Environments. *The American Naturalist*, 174(4), 490–505. https://doi.org/10.1086/605405

Seo, Y. B., Suh, Y. S., Ryu, J. I., Jang, H., Oh, H., Koo, B.-S., Seo, S.-H., Hong, J. J., Song, M., Kim, S.-J., & Sung, Y. C. (2021). Soluble Spike DNA Vaccine Provides Long-Term Protective Immunity against SARS-CoV-2 in Mice and Nonhuman Primates. *Vaccines*, 9(4), Article 4. https://doi.org/10.3390/vaccines9040307

Shan, C., Yao, Y.-F., Yang, X.-L., Zhou, Y.-W., Gao, G., Peng, Y., Yang, L., Hu, X., Xiong, J., Jiang, R.-D., Zhang, H.-J., Gao, X.-X., Peng, C., Min, J., Chen, Y., Si, H.-R., Wu, J., Zhou, P., Wang, Y.-Y., … Yuan, Z.-M. (2020). Infection with novel coronavirus (SARS-CoV-2) causes pneumonia in Rhesus macaques. *Cell Research*, 1–8. https://doi.org/10.1038/s41422-020-0364-z

Shi, R., Shan, C., Duan, X., Chen, Z., Liu, P., Song, J., Song, T., Bi, X., Han, C., Wu, L., Gao, G., Hu, X., Zhang, Y., Tong, Z., Huang, W., Liu, W. J., Wu, G., Zhang, B., Wang, L., … Yan, J. (2020). A human neutralizing antibody targets the receptor binding site of SARS-CoV-2. *Nature*, 1–5. https://doi.org/10.1038/s41586-020-2381-y

Singh, D. K., Singh, B., Ganatra, S. R., Gazi, M., Cole, J., Thippeshappa, R., Alfson, K. J., Clemmons, E., Gonzalez, O., Escobedo, R., Lee, T.-H., Chatterjee, A., Goez-Gazi, Y., Sharan, R., Gough, M., Alvarez, C., Blakley, A., Ferdin, J., Bartley, C., … Kaushal, D. (2021). Responses to acute infection with SARS-CoV-2 in the lungs of rhesus macaques, baboons and marmosets. *Nature Microbiology*, 6(1), Article 1. https://doi.org/10.1038/s41564-020-00841-4

Snedden, C. E., & Lloyd-Smith, J. O. (2024). Predicting the presence of infectious virus from PCR data: A meta-analysis of SARS-CoV-2 in non-human primates. *PLOS Pathogens*, 20(4), e1012171. https://doi.org/10.1371/journal.ppat.1012171

Snedden, C. E., Makanani, S. K., Schwartz, S. T., Gamble, A., Blakey, R. V., Borremans, B., Helman, S. K., Espericueta, L., Valencia, A., Endo, A., Alfaro, M. E., & Lloyd-Smith, J. O. (2021). SARS-CoV-2: Cross-scale Insights from Ecology and Evolution. *Trends in Microbiology*. https://doi.org/10.1016/j.tim.2021.03.013

Sokol, H., Contreras, V., Maisonnasse, P., Desmons, A., Delache, B., Sencio, V., Machelart, A., Brisebarre, A., Humbert, L., Deryuter, L., Gauliard, E., Heumel, S., Rainteau, D., Dereuddre-Bosquet, N., Menu, E., Ho Tsong Fang, R., Lamaziere, A., Brot, L., Wahl, C., … Trottein, F. (2021). SARS-CoV-2 infection in nonhuman primates alters the composition and functional activity of the gut microbiota. *Gut Microbes*, 13(1), 1–19. https://doi.org/10.1080/19490976.2021.1893113

Song, T.-Z., Han, J.-B., Yang, X., Li, M.-H., & Zheng, Y.-T. (2021). Tissue distribution of SARS-CoV-2 in non-human primates after combined intratracheal and intranasal inoculation. *Science China Life Sciences*, 64(10), 1792–1794. https://doi.org/10.1007/s11427-020-1877-4

Song, T.-Z., Zheng, H.-Y., Han, J.-B., Jin, L., Yang, X., Liu, F.-L., Luo, R.-H., Tian, R.-R., Cai, H.-R., Feng, X.-L., Liu, C., Li, M.-H., & Zheng, Y.-T. (2020). Delayed severe cytokine storm and immune cell infiltration in SARS-CoV-2-infected aged Chinese rhesus macaques. *Zoological Research*, 41(0), 1–10. https://doi.org/10.24272/j.issn.2095-8137.2020.202

Speranza, E., Williamson, B. N., Feldmann, F., Sturdevant, G. L., Pérez, L. P.-, Meade-White, K., Smith, B. J., Lovaglio, J., Martens, C., Munster, V. J., Okumura, A., Shaia, C., Feldmann, H., Best, S. M., & Wit, E. de. (2021). Single-cell RNA sequencing reveals SARS-CoV-2 infection dynamics in lungs of African green monkeys. *Science Translational Medicine*, 13(578). https://doi.org/10.1126/scitranslmed.abe8146

Sun, C., Kong, D., Guo, E., Zhao, J., Jia, J., Wang, R., Ma, J., Chen, M., Lu, J., Yu, C., Li, K., & Xie, L. (2023). A Polysaccharide-RBD-Fc-Conjugated COVID-19 Vaccine, SCTV01A, Showed High Immunogenicity and Low Toxicity in Animal Models. *Vaccines*, 11(3), Article 3. https://doi.org/10.3390/vaccines11030526

Sun, S., Cai, Y., Song, T.-Z., Pu, Y., Cheng, L., Xu, H., Sun, J., Meng, C., Lin, Y., Huang, H., Zhao, F., Zhang, S., Gao, Y., Han, J.-B., Feng, X.-L., Yu, D.-D., Zhu, Y., Gao, P., Tang, H., … Peng, H. (2021). Interferon-armed RBD dimer enhances the immunogenicity of RBD for sterilizing immunity against SARS-CoV-2. *Cell Research*, 31(9), 1011–1023. https://doi.org/10.1038/s41422-021-00531-8

Sun, S., He, L., Zhao, Z., Gu, H., Fang, X., Wang, T., Yang, X., Chen, S., Deng, Y., Li, J., Zhao, J., Li, L., Li, X., He, P., Li, G., Li, H., Zhao, Y., Gao, C., Lang, X., … Sun, Y. (2021). Recombinant vaccine containing an RBD-Fc fusion induced protection against SARS-CoV-2 in nonhuman primates and mice. *Cellular & Molecular Immunology*, 18(4), 1070–1073. https://doi.org/10.1038/s41423-021-00658-z

Tan, J. Y. J., Anderson, D. E., Rathore, A. P. S., O'Neill, A., Mantri, C. K., Saron, W. A. A., Lee, C. Q. E., Cui, C. W., Kang, A. E. Z., Foo, R., Kalimuddin, S., Low, J. G., Ho, L., Tambyah, P., Burke, T. W., Woods, C. W., Chan, K. R., Karhausen, J., & John, A. L. S. (2023). Mast cell activation in lungs during SARS-CoV-2 infection associated with lung pathology and severe COVID-19. *The Journal of Clinical Investigation*, 133(19). https://doi.org/10.1172/JCI149834

Tan, S., Zhao, J., Hu, X., Li, Y., Wu, Z., Lu, G., Yu, Z., Du, B., Liu, Y., Li, L., Chen, Y., Li, Y., Yao, Y., Zhang, X., Rao, J., Gao, G., Peng, Y., Liu, H., Yuan, Z., … Lin, J. (2023). Preclinical evaluation of RQ3013, a broad-spectrum mRNA vaccine against SARS-CoV-2 variants. *Science Bulletin*, 68(24), 3192–3206. https://doi.org/10.1016/j.scib.2023.11.024

Tao, X., Garron, T., Agrawal, A. S., Algaissi, A., Peng, B.-H., Wakamiya, M., Chan, T.-S., Lu, L., Du, L., Jiang, S., Couch, R. B., & Tseng, C.-T. K. (2015). Characterization and Demonstration of the Value of a Lethal Mouse Model of Middle East Respiratory Syndrome Coronavirus Infection and Disease. *Journal of Virology*, 90(1), 57–67. https://doi.org/10.1128/JVI.02009-15

Tellier, R. (2006). Review of Aerosol Transmission of Influenza A Virus. *Emerging Infectious Diseases*, 12(11), 1657–1662. https://doi.org/10.3201/eid1211.060426

Van Damme, W., Dahake, R., van de Pas, R., Vanham, G., & Assefa, Y. (2021). COVID-19: Does the infectious inoculum dose-response relationship contribute to understanding heterogeneity in disease severity and transmission dynamics? *Medical Hypotheses*, 146, 110431. https://doi.org/10.1016/j.mehy.2020.110431

van Doremalen, N., Lambe, T., Spencer, A., Belij-Rammerstorfer, S., Purushotham, J. N., Port, J. R., Avanzato, V. A., Bushmaker, T., Flaxman, A., Ulaszewska, M., Feldmann, F., Allen, E. R., Sharpe, H., Schulz, J., Holbrook, M., Okumura, A., Meade-White, K., Pérez-Pérez, L., Edwards, N. J., … Munster, V. J. (2020). ChAdOx1 nCoV-19 vaccine prevents SARS-CoV-2 pneumonia in rhesus macaques. *Nature*, 1–8. https://doi.org/10.1038/s41586-020-2608-y

Vogel, A. B., Kanevsky, I., Che, Y., Swanson, K. A., Muik, A., Vormehr, M., Kranz, L. M., Walzer, K. C., Hein, S., Güler, A., Loschko, J., Maddur, M. S., Ota-Setlik, A., Tompkins, K., Cole, J., Lui, B. G., Ziegenhals, T., Plaschke, A., Eisel, D., … Sahin, U. (2021). BNT162b vaccines protect rhesus macaques from SARS-CoV-2. *Nature*, 592(7853), 283–289. https://doi.org/10.1038/s41586-021-03275-y

Wang, C. C., Prather, K. A., Sznitman, J., Jimenez, J. L., Lakdawala, S. S., Tufekci, Z., & Marr, L. C. (2021). Airborne transmission of respiratory viruses. *Science*, 373(6558), eabd9149. https://doi.org/10.1126/science.abd9149

Wang, G., Yang, M.-L., Duan, Z.-L., Liu, F.-L., Jin, L., Long, C.-B., Zhang, M., Tang, X.-P., Xu, L., Li, Y.-C., Kamau, P. M., Yang, L., Liu, H.-Q., Xu, J.-W., Chen, J.-K., Zheng, Y.-T., Peng, X.-Z., & Lai, R. (2021). Dalbavancin binds ACE2 to block its interaction with SARS-CoV-2 spike protein and is effective in inhibiting SARS-CoV-2 infection in animal models. *Cell Research*, 31(1), 17–24. https://doi.org/10.1038/s41422-020-00450-0

Wang, H., Zhang, Y., Huang, B., Deng, W., Quan, Y., Wang, W., Xu, W., Zhao, Y., Li, N., Zhang, J., Liang, H., Bao, L., Xu, Y., Ding, L., Zhou, W., Gao, H., Liu, J., Niu, P., Zhao, L., … Yang, X. (2020). Development of an Inactivated Vaccine Candidate, BBIBP-CorV, with Potent Protection against SARS-CoV-2. *Cell.* https://doi.org/10.1016/j.cell.2020.06.008

Wang, S., Peng, Y., Wang, R., Jiao, S., Wang, M., Huang, W., Shan, C., Jiang, W., Li, Z., Gu, C., Chen, B., Hu, X., Yao, Y., Min, J., Zhang, H., Chen, Y., Gao, G., Tang, P., Li, G., … Liu, D. (2020). Characterization of neutralizing antibody with prophylactic and therapeutic efficacy against SARS-CoV-2 in rhesus monkeys. *Nature Communications,* 11(1), 5752. https://doi.org/10.1038/s41467-020-19568-1

Wang, Z., An, J., Liu, K., Yu, P., Fang, X., Li, J., Zhu, H., Zhu, Q., Huang, C., Zhang, C., Zhao, B., Bao, L., Song, Y., Cao, X., Hu, D., Jiang, Y., Shi, L., Zhou, L., Fan, J., … Liu, G. (2022). A potent, broadly protective vaccine against SARS-CoV-2 variants of concern. *Npj Vaccines*, 7(1), 1–13. https://doi.org/10.1038/s41541-022-00571-0

Watanabe, T., Bartrand, T. A., Weir, M. H., Omura, T., & Haas, C. N. (2010). Development of a Dose-Response Model for SARS Coronavirus. *Risk Analysis*, 30(7), 1129–1138. https://doi.org/10.1111/j.1539-6924.2010.01427.x

Weiss, A., Jellingsø, M., & Sommer, M. O. A. (2020). Spatial and temporal dynamics of SARS-CoV-2 in COVID-19 patients: A systematic review and meta-analysis. *eBioMedicine*, 58. https://doi.org/10.1016/j.ebiom.2020.102916

Williamson, B. N., Feldmann, F., Schwarz, B., Meade-White, K., Porter, D. P., Schulz, J., van Doremalen, N., Leighton, I., Yinda, C. K., Pérez-Pérez, L., Okumura, A., Lovaglio, J., Hanley, P. W., Saturday, G., Bosio, C. M., Anzick, S., Barbian, K., Cihlar, T., Martens, C., … de Wit, E. (2020). Clinical benefit of remdesivir in rhesus macaques infected with SARS-CoV-2. *Nature*, 1–7. https://doi.org/10.1038/s41586-020-2423-5

Wölfel, R., Corman, V. M., Guggemos, W., Seilmaier, M., Zange, S., Müller, M. A., Niemeyer, D., Jones, T. C., Vollmar, P., Rothe, C., Hoelscher, M., Bleicker, T., Brünink, S., Schneider, J., Ehmann, R., Zwirglmaier, K., Drosten, C., & Wendtner, C. (2020). Virological assessment of hospitalized patients with COVID-2019. *Nature*, 581(7809), Article 7809. https://doi.org/10.1038/s41586-020-2196-x

Woolsey, C., Borisevich, V., Prasad, A. N., Agans, K. N., Deer, D. J., Dobias, N. S., Heymann, J. C., Foster, S. L., Levine, C. B., Medina, L., Melody, K., Geisbert, J. B., Fenton, K. A., Geisbert, T. W., & Cross, R. W. (2021). Establishment of an African green monkey model for COVID-19 and protection against re-infection. *Nature Immunology*, 22(1), Article 1. https://doi.org/10.1038/s41590-020-00835-8

Yadav, P. D., Ella, R., Kumar, S., Patil, D. R., Mohandas, S., Shete, A. M., Vadrevu, K. M., Bhati, G., Sapkal, G., Kaushal, H., Patil, S., Jain, R., Deshpande, G., Gupta, N., Agarwal, K., Gokhale, M., Mathapati, B., Metkari, S., Mote, C., … Bhargava, B. (2021). Immunogenicity and protective efficacy of inactivated SARS-CoV-2 vaccine candidate, BBV152 in rhesus macaques. *Nature Communications*, 12(1), 1386. https://doi.org/10.1038/s41467-021-21639-w

Yadav, P. D., Kumar, S., Agarwal, K., Jain, M., Patil, D. R., Maithal, K., Mathapati, B., Giri, S., Mohandas, S., Shete, A., Sapkal, G., Patil, D. Y., Dey, A., Chandra, H., Deshpande, G., Gupta, N., Nyayanit, D., Kaushal, H., Sahay, R., … Abraham, P. (2021). Assessment of immunogenicity and protective efficacy of ZyCoV-D DNA vaccine candidates in Rhesus macaques against SARS-CoV-2 infection (p. 2021.02.02.429480). *bioRxiv*. https://doi.org/10.1101/2021.02.02.429480

Yang, J., Wang, W., Chen, Z., Lu, S., Yang, F., Bi, Z., Bao, L., Mo, F., Li, X., Huang, Y., Hong, W., Yang, Y., Zhao, Y., Ye, F., Lin, S., Deng, W., Chen, H., Lei, H., Zhang, Z., … Wei, X. (2020). A vaccine targeting the RBD of the S protein of SARS-CoV-2 induces protective immunity. *Nature*, 586(7830), 572–577. https://doi.org/10.1038/s41586-020-2599-8

Yao, Y.-F., Wang, Z.-J., Jiang, R.-D., Hu, X., Zhang, H.-J., Zhou, Y.-W., Gao, G., Chen, Y., Peng, Y., Liu, M.-Q., Zhang, Y.-N., Min, J., Lu, J., Gao, X.-X., Guo, J., Peng, C., Shen, X.-R., Li, Q., Zhao, K., … Shi, Z.-L. (2021). Protective Efficacy of Inactivated Vaccine against SARS-CoV-2 Infection in Mice and Non-Human Primates. *Virologica Sinica*, 36(5), 879–889. https://doi.org/10.1007/s12250-021-00376-w

Yu, J., Collins, N. D., Mercado, N. B., McMahan, K., Chandrashekar, A., Liu, J., Anioke, T., Chang, A., Giffin, V. M., Hope, D. L., Sellers, D., Nampanya, F., Gardner, S., Barrett, J., Wan, H., Velasco, J., Teow, E., Cook, A., Van Ry, A., … Barouch, D. H. (2022). Protective Efficacy of Gastrointestinal SARS-CoV-2 Delivery against Intranasal and Intratracheal SARS-CoV-2 Challenge in Rhesus Macaques. *Journal of Virology*, 96(2), e01599-21. https://doi.org/10.1128/JVI.01599-21

Yu, J., Tostanoski, L. H., Peter, L., Mercado, N. B., McMahan, K., Mahrokhian, S. H., Nkolola, J. P., Liu, J., Li, Z., Chandrashekar, A., Martinez, D. R., Loos, C., Atyeo, C., Fischinger, S., Burke, J. S., Slein, M. D., Chen, Y., Zuiani, A., Lelis, F. J. N., … Barouch, D. H. (2020). DNA vaccine protection against SARS-CoV-2 in rhesus macaques. *Science*, 369(6505), 806–811. https://doi.org/10.1126/science.abc6284

Yu, P., Qi, F., Xu, Y., Li, F., Liu, P., Liu, J., Bao, L., Deng, W., Gao, H., Xiang, Z., Xiao, C., Lv, Q., Gong, S., Liu, J., Song, Z., Qu, Y., Xue, J., Wei, Q., Liu, M., … Qin, C. (2020). Age-related rhesus macaque models of COVID-19. *Animal Models and Experimental Medicine*, 3(1), 93–97. https://doi.org/10.1002/ame2.12108

Zheng, H., Li, H., Guo, L., Liang, Y., Li, J., Wang, X., Hu, Y., Wang, L., Liao, Y., Yang, F., Li, Y., Fan, S., Li, D., Cui, P., Wang, Q., Shi, H., Chen, Y., Yang, Z., Yang, J., … Liu, L. (2020). Virulence and pathogenesis of SARS-CoV-2 infection in rhesus macaques: A nonhuman primate model of COVID-19 progression. *PLOS Pathogens*, 16(11), e1008949. https://doi.org/10.1371/journal.ppat.1008949

Zost, S. J., Gilchuk, P., Case, J. B., Binshtein, E., Chen, R. E., Nkolola, J. P., Schäfer, A., Reidy, J. X., Trivette, A., Nargi, R. S., Sutton, R. E., Suryadevara, N., Martinez, D. R., Williamson, L. E., Chen, E. C., Jones, T., Day, S., Myers, L., Hassan, A. O., … Crowe, J. E. (2020). Potently neutralizing and protective human antibodies against SARS-CoV-2. *Nature*, 584(7821), 443–443. https://doi.org/10.1038/s41586-020-2548-6

Chapter 3. Spatial models reveal principles that govern SARS-CoV-2 infection patterns inside hosts

Abstract

Viral infection dynamics inside hosts depend on pathogen fitness and dissemination across the internal landscape of host tissues, but the relative effects of these two governing processes on realized spatiotemporal patterns are difficult to disentangle from observational data. In this study, we developed a mechanistic model of SARS-CoV-2 infection that captures the inherent spatial structure and connectivity of tissues across the respiratory and gastrointestinal tracts. We fit this model to data from nine articles that experimentally challenged rhesus macaques with SARS-CoV-2, which allowed us to identify consistent patterns across disparate exposure conditions and sampling methodologies. Our model estimated high rates of viral dissemination across tissues, especially into the throat. We found that tissue-specific temperature often had larger estimated effects on infection rates than local receptor or protease expression. Our results also indicated that most infections resulted in fewer than 10% of all available target cells in a given tissue becoming infected and, relatedly, that most infections were subcritical. Upper respiratory tissues more frequently experienced supercritical infection, and they almost always produced more infectious virus than the lung or lower GI over the full course of infection. Our mechanistic modeling framework is the first to formally investigate how tissue traits and connectivity structure interact to determine spatiotemporal infection patterns inside hosts, and it lays the foundation for within-host mechanistic models to help answer long-standing questions in virology about the determinants of tissue tropism.

Introduction

Spatiotemporal patterns of viral infection inside hosts can vary widely depending on the pathogen-host system, ranging from systemic infections to those that are highly localized in key tissues or cell types (McCall, 2021). In humans, for example, rotaviruses primarily infect gastrointestinal tissues, whereas Nipah virus disseminates broadly via the circulatory system (Crawford et al., 2017; de Wit & Munster, 2015). These spatial infection patterns are often referred to as 'tissue tropism,' and they can vary across host species, as observed for MERS-CoV, which preferentially infects the lower respiratory tract of humans but the upper respiratory tract of dromedary camels (Van Doremalen & Munster, 2015). Tropism is typically determined by observing symptoms, swabbing orifices, collecting invasive tissue samples post mortem, and occasionally by fluorescent imaging of labeled viruses during experimental infection of small animal models (Karlsson et al., 2015). However, the generative processes that give rise to observed tropism are largely unobservable *in vivo*, and the viral and host factors that ultimately determine tropism remain incompletely understood. Both epidemiology and public health would benefit immensely from better characterizing these factors, as transmissibility and pathogenicity are inextricably linked to how well a virus infects and spreads within its host.

Current discourse largely attributes tropism patterns to the availability of cellular receptors and proteases, both of which mediate virus-cell membrane fusion (Baggen et al., 2021; Bourgonje et al., 2020). Yet observed tropism does not always map neatly onto receptor or protease expression, likely due to other tissue-specific factors that constrain viral infectivity, proliferation, and persistence, given that observed tropism requires sufficient local infection as well as local replication. These factors fall into several categories. Physical barriers can prevent access to

permissive cells (e.g., via the mucus coating respiratory epithelial cells; Zanin et al., 2016), interferon-signaling can trigger antiviral cellular states (Samuel, 2001), and immune cells can directly clear infectious viral particles or induce cell-mediated apoptosis (Mercer & Greber, 2013; Zhou et al., 2017). *In vitro* experiments have shown that viral expression and replication patterns can differ across the variable temperatures observed throughout the human respiratory tract (e.g., influenza A, Laporte et al., 2019; influenza C, Sreenivasan et al., 2019) or at different tissue-relevant pH values (e.g., influenza, Russell et al., 2018; SARS-CoV-1, Laporte et al., 2021). In fact, abiotic sensitivities are well-established barriers for the adaptation of avian influenza to mammals (Lipsitch et al., 2016; Russell et al., 2018). Within-host dissemination mechanisms likely also limit observed tropism, given that viruses must be able to access permissive tissues, either by spreading locally to physically proximate locations (e.g., cell-free or cell-to-cell transmission; Cifuentes-Muñoz et al., 2018) or by long-range movements throughout the host body (e.g., via the lymph or blood; Fenner et al., 1987), though this is typically not observable *in vivo* and difficult to approximate in *in vitro* settings. Ultimately, although cellular receptors, proteases, and abiotic conditions clearly impact viral infectivity and replication *in vitro*, no systematic study has yet disentangled the relative effects of these host tissue factors, along with connectivity among tissues, on determining *in vivo* spatiotemporal infection patterns.

Given the wealth of experimental and clinical data generated during the COVID-19 pandemic, SARS-CoV-2 provides a unique opportunity to investigate the drivers of tropism for an important pandemic-turned-endemic virus. SARS-CoV-2 primarily causes respiratory infection in humans, but it is known to also cause extrapulmonary complications (Gupta et al., 2020) and viral RNA has been detected in many different organ systems of deceased patients (Puelles et al., 2020; Stein et al., 2022; Yao et al., 2021). This broad tropism could be explained by the relatively

widespread expression of ACE2 (Salamanna et al., 2020; Sungnak et al., 2020), which is the primary cellular receptor for SARS-CoV-2 (Hoffman et al. 2020). However, ACE2 is moderately expressed in some tissues where infection is rare (e.g., cornea) but has seemingly lower expression in some tissues with high rates of infection (e.g., lung; Sungnak et al., 2020), and one study found that roughly half of all deceased COVID-19 patients showed signs of extrapulmonary infection, but half did not (Yao et al., 2021). Together, this emphasizes that receptor availability cannot fully explain tropism and that other mechanisms likely constrain the spatial distribution of SARS-CoV-2, either by preventing access to seemingly permissive tissues or by limiting infection once it reaches them.

The seeming discordance between observed ACE2 and SARS-CoV-2 distributions could be explained by other host factors, including the usage of alternate cellular receptors. Some have been proposed for SARS-CoV-2 (e.g., CD147), but their relevance for cellular entry *in vivo* remains unclear (Baggen et al., 2021; Jackson et al., 2022; Lim et al., 2022; Shilts et al., 2021). Meanwhile, many proteases have demonstrated the ability to cleave the SARS-CoV-2 spike protein at the cellular surface (e.g., TMPRSS2, TMPRSS4, TMRPSS11a, HAT), in endosomes (e.g., cathepsin B, cathepsin L), or even before exocytosis (e.g., furin; Beumer et al., 2021; Hoffmann et al., 2020, 2020; Kishimoto et al., 2021; Laporte et al., 2021; Shang et al., 2020; Zang et al., 2020). However, TMPRSS2 expression results in higher levels of cleavage, cellular entry, and replication *in vitro* relative to the other functional proteases, and it is generally considered the primary protease, suggesting SARS-CoV-2 tropism could be constrained by its availability across tissues. Other experiments have also demonstrated that SARS-CoV-2 infected more cells and replicated to higher titers when cultured at the ambient temperature of the human upper respiratory tract (33°C) compared to the core body temperature of the lower respiratory tract (37°C; Laporte

et al., 2021; V'kovski et al., 2021). These factors may all impact *in vivo* SARS-CoV-2 dynamics, but their relative effects on tropism are difficult to disentangle with direct observation or statistics on patient derived data, because they are inherently confounded by the processes that generated the observable patterns.

The processes governing viral tropism are directly parallel to those determining habitat selection and species distribution in ecology, since within-host infection can be viewed as a virus invading the tissue landscape of its host (Snedden et al., 2021). Similar to how resource availability and environmental conditions determine wildlife fitness in habitat patches, the cellular properties and abiotic conditions of individual tissues also determine local viral fitness. Seminal work in spatial ecology has demonstrated that landscape-wide population dynamics are highly sensitive to spatial heterogeneity in fitness and to connectivity patterns in multi-patch systems (Becker et al., 2018; Pulliam, 1988; Schreiber & Lloyd-Smith, 2009). For example, dispersal patterns can substantially impact species distributions and can result in misleading signals about habitat suitability: regions with positive growth rates can maintain populations in those with negative growth rates given sufficient dispersal (i.e., source-sink dynamics), and suitable habitat can remain unoccupied unless individuals are introduced (i.e., dispersal limitation; Pulliam, 1988, 2000). Huge untapped potential exists in bringing these ecological theories and their methods to bear on modern problems in virology, especially in harnessing mechanistic models to identify the underlying processes that give rise to observed infection patterns.

Mathematical models of within-host infection can be designed to capture any mechanisms hypothesized to underlie tropism patterns, and these hypotheses can then be tested by fitting the model to data, ideally from both *in vivo* and *in vitro* sources. The traditional model of virus infection within a host individual can track the growth and decline of target cells and viruses in a

given tissue for any virus-host system of interest (e.g., HIV in the blood in humans; Perelson, 2002). This model framework can be extended to consider multiple host tissues simultaneously (e.g., upper vs. lower respiratory tract; Gonçalves et al., 2021; Rodriguez & Dobrovolny, 2021), though such analyses are much less common than single-tissue analyses and, when available, rarely involve more than two tissues. Some modeling work for SARS-CoV-2 included viral movement between multiple respiratory compartments in their preliminary models but not their main analyses, given insufficient data to fully estimate movement rates between tissues (Alexandre et al., 2022; Gonçalves et al., 2021). In contrast, a single study modeled viral dynamics among eight distinct tissues, and they were able to estimate nonzero movement rates among them, although these movement estimates relied on data from hamsters and not humans (Dogra et al., 2021). Given the many mechanisms by which viruses could disseminate between tissues (e.g., aspiration, mucociliary escalator, local transport, blood; Fenner et al., 1987) and given the clear lesson from ecology that connectivity can be a crucial driver of population distribution, more modeling research is needed to characterize the effects of virus dissemination on observed infection patterns. In fact, multi-tissue models may be the best currently available method that can integrate connectivity structure with heterogeneous fitness landscapes to identify the determinants of spatiotemporal infection patterns across the host body.

In this study, we developed a model of SARS-CoV-2 infection that captures the inherent spatial structure and connectivity of tissues across the respiratory and gastrointestinal (GI) tracts. We fit this model to data from 9 articles that experimentally challenged rhesus macaques with SARS-CoV-2, which increased our sample sizes relative to individual studies and which allowed us to identify consistent patterns across disparate exposure conditions and sampling methodologies. We investigated the determinants of SARS-CoV-2 tissue tropism by estimating

the dependence of tissue-specific infection rates on local ACE2 expression, TMPRSS2 availability, ACE2-TMPRSS2 coexpression levels, and temperature. We also estimated tissue-specific reproductive numbers, and we characterized local viral production as well as dispersal rates among the nose, throat, lung, and lower GI. With our modeling framework, we quantitatively tested the influence of multiple putative drivers of tropism, all while accounting for connectivity among tissues and the mechanisms underlying within-host viral replication, which, to our knowledge, has not been attempted before.

Methods

Data compilation

For this study, to ensure adequate temporal resolution, we included all articles from our larger database (see Chapter 2) that obtained repeated non-invasive samples from rhesus macaques (*Macaca mulatta*) in the nose, throat, lung, and lower GI. Nine articles included sufficient data for analysis, resulting in a dataset composed of males, females, juveniles, and adults (Table 3.1**;** Bixler et al., 2022; Blair et al., 2021; Fears et al., 2022; Hoang et al., 2021; Munster et al., 2020; Rosenke et al., 2020; Salguero et al., 2021; Vogel et al., 2021; Williamson et al., 2020). It includes animals exposed by aerosol inhalation, combined intranasal and intratracheal inoculation, and combined intranasal, intratracheal, ocular/conjunctival, and oral (i.e., 'multi-route') inoculation. Total exposure doses ranged from 10^4 to $10^{7.4}$ plaque forming units. Quantitative titers were available for total RNA PCR, sgRNA PCR, and culture assays. All studies used either the USA/WA1/2020 or the AUS/VIC01/2020 isolate of SARS-CoV-2.

Determining tissue-level expression patterns and temperature

We sought to classify ACE2 expression, TMPRSS2 expression, cell-specific ACE2-TMPRSS2 co-expression, and ambient temperature across tissues in rhesus macaques. Recognizing the limitations in available data, we classified these factors qualitatively as high, medium, low, or absent. When available, we prioritized data from rhesus macaques, followed in order by data from cynomolgus macaques, other non-human primates, or humans.

To determine tissue-level receptor and protease expression, we used cell-type specific ACE2 expression, TMPRSS2 expression, and ACE2-TMPRSS2 co-expression values from data published in Han et al., 2022. This included single-cell transcriptomics data from the lower

respiratory tract (trachea, bronchus, lung) and the gastrointestinal tract (stomach, duodenum, colon) of cynomolgus macaques (*Macaca fascicularis*), among other tissues. Given that the non-invasive lower respiratory samples included in our dataset (i.e., bronchoalveolar lavage, bronchial brush) could reasonably contain viruses produced in the trachea, lung, or bronchus, we considered all three tissues to classify overall expression for our lung tissue compartment. Similarly, given that the gastrointestinal tissue(s) where SARS-CoV-2 replication may occur is unknown, plus the inherently directional flow through the gastrointestinal tract, we considered all three GI tissues when classifying lower GI expression. For all six tissues separately (trachea, bronchus, lung, stomach, duodenum, colon), we identified the cell type with the highest mean expression values for ACE2, TMPRSS2, and co-expression. For both the lower respiratory and GI compartments, we averaged the corresponding maximum ACE2, TMPRSS2, and co-expression values for the constituent tissues to generate overall expression profiles (Table S3.1). Semi-quantitative rankings of these expression profiles (i.e., low, medium, high) were unchanged when using the maximum of the maximum expression values instead of when averaging over the maximum expression values. The resulting quantities were consistent with other reports suggesting that ACE2 is more expressed in some gastrointestinal tissues than in the lung of macaques (Gao et al., 2022; Ziegler et al., 2020).

Comparable expression values were not available for upper respiratory tissues in macaques, but other studies have noted that ACE2 is highly expressed in the nose of rhesus macaques (Liu et al., 2011) and that ACE2 expression decreases down the respiratory tract in humans (Hou et al., 2020). Based on these findings, we set ACE2 expression in the nose and throat as the average of the expression values in the lung and lower GI, which preserves the key qualitative patterns in available data, namely: (i) the expression gradient down the respiratory tract,

and (ii) the high levels of expression in the macaque GI. TMPRSS2 expression has been shown to be relatively consistent across the respiratory tract of humans (Hou et al., 2020), so we set TMPRSS2 expression values in the nose and throat as equal to those in the lung. One study observed co-expression of ACE2 and TMPRSS2 in the nasal epithelium and bronchioles of humans but found negligible co-expression in the alveoli (Carossino et al., 2024). Another study found higher cell-specific percentages of co-expression in the human nasal cavity than in the bronchial tissues or the lung parenchyma (Sungnak et al., 2020). Based on these reports, we assumed that the difference in co-expression values between the upper respiratory tissues and the lungs was equal to the difference between the lungs and the lower GI. This captures the expectation of higher co-expression in the nose and throat than in the lung.

Temperatures vary along the respiratory tract from approximately 30-32°C in the human nasal cavity to 37°C in human lungs (Lindemann et al., 2002; McFadden et al., 1985). We assumed rhesus macaques have a similar temperature gradient, with lower temperatures in the nose and throat than the core body temperature found in the lung and lower GI. Relative quantities for the expression patterns and temperature conditions of each tissue are displayed in Figure 1C.

Modeling viral dynamics within each tissue

We model the infection dynamics within each considered tissue (nose, throat, lung, lower GI) with a system of ordinary differential equations, as in the traditional model of within-host infection (Perelson, 2002), although we make various adjustments to better align with our data and context. We track the growth and decline of target cells (T), eclipse phase cells (E), infected cells (I), infectious virus particles (V), full-length genomic RNA (G; not packaged inside a virion), and subgenomic RNA (sgRNA; S) over time (Figure 3.1A). All rates are expressed in their occurrence

per day. As is typical for modeling acute infections, we assume that cells are not proliferating and that only infected cells die during our time period of interest. Infectious viral particles successfully infect target cells with rate β, at which point the cells enter the eclipse phase. Eclipse phase cells do not generate infectious virus by definition, but they do produce genomic RNA and subgenomic RNA at rates σ_E and η_E, respectively. Eclipse phase cells become infected cells with rate γ, which we fix at 4 per day as in other studies for SARS-CoV-2 (Ke et al., 2021; Marc et al., 2023). Infected cells produce virus at rate p, genomic RNA at rate σ_I, and subgenomic RNA at rate η_I. Infected cell death occurs at rate δ. To capture that the average infected cell lifespan should not exceed one day, we set 1 as the lower bound for δ. Both RNA types are degraded or cleared by the immune system at rate c_R, for which we set a lower bound of 0.2 to reflect that we do not expect the average RNA lifespan to exceed 5 days. Without this lower bound, the fits from our model occasionally predicted durations of RNA positivity that were much longer than typically observed in immunocompetent animals (as in our dataset). Infectious virus is cleared, degraded, or otherwise rendered non-infectious at rate c_V, which we enforced must be larger than c_R. All rates are tissue-specific (e.g., viral production rates are allowed to vary between all four tissues). Model equations are given after the next section, which outlines the spatial coupling between tissues.

Modeling connectivity between tissues

Our model tracks infection dynamics in the nose, throat, lung, and lower GI separately, but we allow viral particles, gRNA, and sgRNA to move between these tissue compartments based on hypothesized within-host dissemination mechanisms (Figure 3.1B). We refer to these tissues in our parameters using the following numbers: 1, nose; 2, throat; 3, lung; 4, lower GI. The movement rates of infectious viral particles from tissue i to tissue j are unique (m_{Vij}), but movement rates are

shared between gRNA and sgRNA (m_{Rij}). Particles may move down the respiratory tract one tissue at a time via local transport or inhalation (i.e., nose to throat [m_{V12}, m_{R12}], throat to lung [m_{V23}, m_{R23}]). They may also move up the respiratory tract sequentially via local transport, exhalation, coughing, or the mucociliary escalator (i.e., lung to throat [m_{V32}, m_{R32}], throat to nose [m_{V21}, m_{R21}]). Swallowing can transport virus or RNA into the lower GI from the nose (m_{V14}, m_{R14}) or throat (m_{V24}, m_{R24}). The lung and lower GI can exchange virus or RNA via systemic spread, at direction- and assay-specific rates (m_{V34}, $m_{R34,}$ m_{V43}, m_{R43}). We also include movement from the lower GI to the throat to capture fecal-oral self-transmission or systemic spread (m_{V42}, m_{R42}). To constrain the model to reasonable parameter space and aid identifiability, we do not allow the sum of all movement rates out of a given tissue to exceed 0.5 (for virus and RNA separately), given we do not expect more than half of all available virus or RNA to be transported out of a tissue within a single day on average.

Compartmental model equations

Model equations for a given tissue *i* are indicated below, where J is the set of all tissues that flow into tissue *i* and K is the set of all tissues that tissue *i* flows out to (see above section). All other parameters are explained two sections above.

$$\frac{dT_i}{dt} = -\beta_i T_i V_i$$

$$\frac{dE_i}{dt} = \beta_i T_i V_i - \gamma_i E_i$$

$$\frac{dI_i}{dt} = \gamma_i E_i - \delta_i I_i$$

$$\frac{dV_i}{dt} = p_i I_i + \sum_{j \in J} m_{Vji} V_j - \sum_{k \in K} m_{Vik} V_i - c_{Vi} V_i$$

$$\frac{dG_i}{dt} = \sigma_E E_i + \sigma_I I_i + \sum_{j \in J} m_{Rji} G_j - \sum_{k \in K} m_{Rik} G_i - c_{Ri} G_i$$

$$\frac{dS_i}{dt} = \eta_E E_i + \eta_I I_i + \sum_{j \in J} m_{Rji} S_j - \sum_{k \in K} m_{Rik} S_i - c_{Ri} S_i$$

Setting and estimating initial conditions

Simulating a system of ordinary differential equations requires fixing or estimating initial conditions for all state variables (in our case: target cells, eclipse cells, infected cells, virus, gRNA, and sgRNA). When we fit our model with wide priors on the initial number of target cells, there were clear correlations between the number of target cells and other parameters. Thus, we followed convention and fixed the number of target cells in each tissue compartment, since only the product of the number of target cells and the viral production rates are identifiable (Zitzmann et al., 2024). We set the number of target cells in the nose and throat to each be $10^{4.5}$, based on a recent measurement in the nose of a cynomolgus macaque ($10^{4.3}$; Gonçalves et al., 2021). Similar to previous studies, we set the number of target cells in the lung to be 10-fold higher than the nose ($10^{5.5}$; Ciupe & Tuncer, 2022) and the number in the GI to be the same as the nose ($10^{4.5}$; Dogra et al., 2021). We assumed that time starts immediately after the inoculum has been deposited in the target tissues such that no cells are infected yet, and so we set the initial number of eclipse and infected cells at zero.

Approximate exposure doses of infectious viral particles are reported for each route in each study, and we used these values as our initial conditions for the virus state variables. The amount

of free (i.e., not virion-associated) gRNA or sgRNA contained in the inoculum is not typically measured or reported in animal challenge experiments, so we first considered models that estimated their initial quantities for each tissue based on reported exposure doses, alongside all other viral dynamic parameters. For example, we estimated the initial $\log_{10}$ gRNA quantity in the nose ($\log_{10}(G_1(t=0))$) as a scalar multiple ($\alpha_{G,1}$) of the reported $\log_{10}$ dose administered to the nose ($\log_{10}(D_1)$), resulting in the following relationship: $\log_{10}(G_1(t=0))=\alpha_{G,1}\log_{10}(D_1)$. These models often fit poorly with frequent divergent transitions, likely due to issues with parameter identifiability. The models also struggled to fit when we fixed the initial gRNA quantity at zero, but the fits performed well when we instead fixed the initial gRNA quantity at the local dose. This reflects that the inoculum likely also contains detectable free RNA or RNA associated with non-infectious viral particles, and it is consistent with many studies detecting large quantities of RNA one day post infection. One article with particularly large RNA quantities resulted in poor fits under this relationship (Bixler et al., 2022; aerosol exposure only), so we allowed this model only to estimate initial virus and gRNA quantities without restraint, which substantially improved model performance. We fixed initial sgRNA quantities at zero for all studies and tissue locations. No article included in this study inoculated animals intragastrically, so we set all initial virus and RNA quantities in the lower GI to zero, such that any flow of the inoculum into the gastrointestinal system must happen after the inoculation procedure via the included movement parameters.

We determined location-specific doses (i.e., D_1, D_2, D_3) similarly to our previous work (Chapter 2). Given sample sizes were too small to include a trachea compartment in this analysis, we instead allowed intratracheal inoculation to increase the dose in the lung. We assumed that the reported route-specific doses were distributed across respiratory tissues as follows: (i) intranasal: 50% nose, 50% throat; (ii) oral: 100% throat; (iii) intratracheal: 100% lung; (iv) ocular or

conjunctival, 100% nose; and (v) aerosol: 25% nose, 25% throat, 50% lung. As in our previous work, we assumed ocular or conjunctival inoculation ultimately resulted in nasal exposure, given that we do not include a compartment for the eyes and given that fluids administered ocularly rapidly drain into the nose via the nasolacrimal duct (Belser et al., 2013).

Incorporating dependence of the infection rate on tissue conditions

In our model, the infection rate for a given tissue *i* (β_i) can be influenced by local ACE2 expression ($ACE2_i$), TMPRSS2 expression ($TMPRSS2_i$), ACE2-TMPRSS2 coexpression in cells ($COEXP_i$), and temperature ($TEMP_i$). For simplicity, we express the log infection rate as a linear combination of these cofactors, each with their own unique regression coefficients (λ_{ACE2}, $\lambda_{TMPRSS2}$, λ_{COEXP}, λ_{TEMP}, respectively) and with an intercept shared across all tissues (ψ). Unlike most other parameters in our model, these trait parameters (λ_{ACE2}, $\lambda_{TMPRSS2}$, λ_{COEXP}, λ_{TEMP}) are not tissue-specific and are instead shared by all tissues. This allows us to capitalize on trait variation across tissues to determine their relative effects on the infection rate. Given the nose and throat have the same tissue conditions for the considered factors (Figure 3.1C), we include an additional term that allows their infection rates to differ from each other according to any unmodeled factors (λ_{URT}). The full equation for the infection rate is as follows:

$$\log_{10}(\beta_i) = \psi + \lambda_{ACE2}ACE2_i + \lambda_{TMPRSS2}TMRPSS2_i +$$
$$\lambda_{COEXP}COEXP_i + \lambda_{TEMP}TEMP_i + \lambda_{URT}URT_i$$

Tissue specific conditions are displayed in Figure 3.1C. For $ACE2_i$ and $COEXP_i$, we encode low expression as the value -0.5, medium expression as the value 0, and high expression

as the value 0.5. For $TMRPSS2_i$ and $TEMP_i$, we encode low values as 0 and high values as 1. URT_i is encoded as 1 for the throat and 0 for all other tissues. Given that ACE2 and TMPRSS2 are known to facilitate viral entry *in vitro,* we constrain λ_{ACE2}, $\lambda_{TMPRSS2}$, λ_{COEXP} to be greater than or equal to zero, reflecting that higher expression should not reduce local infectivity. Similarly, given SARS-CoV-2 infected more cells and replicated to higher titers when cultured at the lower temperatures of the human upper respiratory tract than at the core body temperature, we constrain λ_{TEMP} to be less than or equal to 0. We do not set any constraints on λ_{URT}. The shared intercept parameter (ψ) is allowed to be any negative value, given that prior estimates of the SARS-CoV-2 infection rate have not exceeded 1.

Fitting the model to data

To estimate all parameter values, we fit the compartmental model to each article in our dataset separately. For studies that included multiple exposure routes (Bixler et al., 2022; Blair et al., 2021; Fears et al., 2022), we also fit each route separately, resulting in twelve total fits. Our data includes quantitative measurements of total RNA, subgenomic RNA, and infectious virus titers, which we fit to different state variables on the $\log_{10}$ scale. Given total RNA PCR could amplify full-length genomic RNA, subgenomic RNA, and virion-associated RNA, we assumed that total RNA quantities (TR) were normally distributed around the sum of the model predictions for the state variables G, S, and V, with some estimated standard deviation (σ_{TR}). Similarly, we assumed sgRNA quantities (SG) were normally distributed around the predictions of S and that culture titers (C) were normally distributed around the predictions for V, each with their own standard deviations (σ_{SG}, σ_C). These relationships are expressed statistically as follows:

$$\log_{10}(\mathrm{TR}) \sim \mathit{Normal}\left(\log_{10}(\mathrm{G}+\mathrm{S}+\mathrm{V}),\ \sigma_{\mathrm{TR}}\right)$$

$$\log_{10}(\mathrm{SG}) \sim \mathit{Normal}\left(\log_{10}(\mathrm{S}),\ \sigma_{\mathrm{SG}}\right)$$

$$\log_{10}(\mathrm{C}) \sim \mathit{Normal}\left(\log_{10}(\mathrm{V}),\ \sigma_{\mathrm{C}}\right)$$

We treat all samples reported as falling below the limit of detection as censored data, with the limit of detection as the upper bound of the true value. In practice, this is done by incrementing the log probability by the log cumulative normal probability at the reported limit of detection. When detection limits were not reported, we used the smallest value reported for the given assay in that article as our best available proxy. For one article, the limit of detection for culture was not available and there were no reported positives, so we set the limit at a conservative value of 1.7 $\log_{10}$.

We model all virus production rates (p) on the natural log scale, such that the model fits values for $p_{log}=\log_e(p)$. We used this transformation because it led to better model fits than when fitting to untransformed p or $\log_{10}(p)$. RNA production rates (σ_E, η_E, σ_I, η_I) are expressed as scalar multiples of the log virus production rates (p_{log}). For example, $\sigma_E=\exp(\theta_E\, p_{log})$ and $\eta_E=\exp(\tau_E\, p_{log})$. All other rates are expressed similarly, and the scalar multiples are unique to each tissue. To aid with parameter identifiability and given clear evidence of substantially higher detectable RNA quantities than infectious virus titers, we constrain these scalar multiples (θ_E, θ_I, τ_E, τ_I) to be greater than or equal to 0.5.

Prior distributions

We used weakly informative priors for all estimated parameters to reflect patterns expected based on prior *in vitro* experiments or other modeling work. All parameters are described in the

previous methods sections. The priors for the regression model on the infection rates are shown below. Note that we truncated these distributions to constrain the model to reasonable parameter space. In particular, we force λ_{ACE2}, $\lambda_{TMPRSS2}$, and λ_{COEXP} to be greater than 0, but λ_{TEMP} and Ψ to be less than 0.

$$\Psi \sim Normal(-7, 1.5); \text{ truncated such that } \Psi \leq 0$$

$$\lambda_{ACE2} \sim Normal(0.5, 2); \text{ truncated such that } \lambda_{ACE2} \geq 0$$

$$\lambda_{TMPRSS2} \sim Normal(0.5, 2); \text{ truncated such that } \lambda_{TMPRSS2} \geq 0$$

$$\lambda_{COEXP} \sim Normal(0.5, 2); \text{ truncated such that } \lambda_{COEXP} \geq 0$$

$$\lambda_{TEMP} \sim Normal(-0.5, 2); \text{ truncated such that } \lambda_{TEMP} \leq 0$$

$$\lambda_{URT} \sim Normal(0, 0.25); \text{ not truncated}$$

The priors for the viral dynamic model were equal across tissues. As with the infection rates, the priors are truncated at certain values, as indicated below and justified in the above methods sections.

$$\delta \sim Normal\ (1.7, 1); \text{ truncated such that } \delta \geq 1$$

$$c_V \sim Normal\ (15, 5); \text{ truncated such that } c_V \geq c_R$$

$$c_R \sim Normal\ (2, 1); \text{ truncated such that } c_R \geq 0.2$$

$$\log_e(p) \sim Normal\ (\log_e(50), 1); \text{ not truncated}$$

$$\theta_E \sim Normal\ (1, 1); \text{ truncated such that } \theta_E \geq 0.5$$

$$\theta_I \sim Normal\ (1, 1); \text{ truncated such that } \theta_I \geq 0.5$$

$$\tau_E \sim Normal\ (1, 1); \text{ truncated such that } \tau_E \geq 0.5$$

$$\tau_I \sim Normal\ (1, 1);\ \text{truncated such that } \tau_I \geq 0.5$$

For one study with particularly large RNA quantities (Bixler et al. 2022; aerosol exposure), we increased the prior on $\log_e(p)$ to instead be centered at $\log_e(100)$ with a standard deviation of two. We also altered the priors on θ_E, θ_I, τ_E, and τ_I to be Normal (2, 2), with the same truncation at 0.5 as for all other models. This improved this model's ability to fit. The priors on the observation model for all articles were:

$$\sigma_{TR} \sim Exponential(1)$$

$$\sigma_{SG} \sim Exponential(1)$$

$$\sigma_{C} \sim Exponential(1)$$

We did not set priors on specific movement rates, though they all had 0 as their lower bound. We did set priors on the sum of all movement rates out of each tissue (for virus and RNA separately). They all had the same priors: *Normal* (0.2, 0.2) truncated above 0.

Computational methods and software

All data preparation, analysis, and plotting were completed with R version 4.2.0. Posterior sampling of the Bayesian model was performed with No-U-Turn Sampling (NUTS) via the probabilistic programming language Stan using the interface CmdStanR version 0.5.2. We used the Stan ODE solver designed for stiff systems (ode_bdf) with larger relative and absolute tolerances than the default (10^{-4} vs. 10^{-6}) to speed up computation. Due to computational constraints, we generated all model fits by running two replicate chains with 1000 iterations each,

of which the first 500 samples of each chain were treated as the warm-up period and the final 500 iterations were used to generate parameter estimates. Some model fits included a small number of divergent transitions, but they still fit the data well.

Generating predictions

We estimated median parameter values and their 90% credible intervals using all available post-warmup samples. When calculating other derived quantities (e.g., the number of infected cells), we used at least 100 post-warmup parameter samples to generate predictions from simulated trajectories. Each prediction was generated using grouped parameter samples (e.g., samples from the same chain and iteration) to preserve correlation structure. When we calculated posterior probabilities, we computed the fraction of all predictions that resulted in the particular outcome of interest versus all other possible outcomes.

Results

Data and model overview

We analyzed the data from 9 articles that challenged rhesus macaques with ancestral SARS-CoV-2 strains (USA/WA1/2020 or AUS/VIC01/2020) and that reported viral RNA or infectious virus measurements from the nose, throat, lung, and lower GI (Table 3.1). This dataset includes 1,600 total observations from 62 individuals, spanning three different exposure routes (aerosol; combined intranasal and intratracheal; combined intranasal, intratracheal, ocular/conjunctival, and oral) and total exposure doses ranging from 10^4-$10^{7.4}$ plaque forming units (pfu). Given different exposure routes can result in clearly distinct dynamics (Chapter 2), we analyzed routes from the same article separately. All included individuals were either juveniles or adults, and the dataset included both sexes.

Article	Route	Dose (log10)	Assays	Species	Age	Sex	# of Indivs	# of observations				
								Total	Nose	Throat	Lung	Lower GI
Bixler et al. 2022	AE	4.8	T, SG, C	RM	A	U	4	124	52	32	8	32
Bixler et al. 2022	IT+IN	7.4	T, SG, C	RM	A	U	4	124	52	32	8	32
Blair et al. 2021	AE	4	T	RM	A	M	2	39	10	11	6	12
Blair et al. 2021	IT+IN+OR+CJ	6.6	T	RM	A	M, F	2	27	8	5	7	7
Fears et al. 2022	AE	4	T, SG, C	RM	A	M	4	176	48	48	48	32
Fears et al. 2022	IT+IN	6.1	T, SG, C	RM	A	M	4	176	48	48	48	32
Hoang et al. 2021	IT+IN	6	T	RM	A	M, F	4	112	32	32	16	32
Munster et al. 2020	IT+IN+OR+OC	6.3	T, C	RM	A, J	M, F	8	156	44	44	24	44
Rosenke et al. 2020	IT+IN+OR+OC	6.3	U	RM	J	M	9	210	56	56	42	56
Salguero et al. 2021	IT+IN	6.7	T, SG, C	RM	J	M, F	6	116	50	39	11	16
Vogel et al. 2021	IT+IN	6	T	RM	J	M	9	97	27	27	17	26
Williamson et al. 2020	IT+IN+OR+OC	6.3	T, C	RM	J	M, F	6	243	81	75	30	57

Table 3.1 | Sample sizes across tissue locations for each article.
Acronyms in the route column are: AE, aerosol; IT, intratracheal; IN, intranasal; OR, oral; CJ, conjunctival; OC, ocular. Dose is presented in log10 plaque forming units. Assay acronyms are: T, total RNA; SG, subgenomic RNA; C, culture. Age acronyms are: A, adult; J, juvenile. Sex acronyms are: M, male; F, female; U, unknown.

We fit the data from each article to our model, which tracks infection dynamics using a system of ordinary differential equations (Figure 3.1A). In each tissue, we model changes over time in the available target cells (T), eclipse phase cells that are infected but not yet producing infectious viral particles (E), infected cells that do produce virus (I), and infectious viral particles themselves (V). Our dataset includes measurements of total RNA and sgRNA, so we include two additional state variables for full-length genomic RNA (G; not virion-associated) and subgenomic RNA (sgRNA; S), such that total RNA assays measure the sum of virion-associated RNA, all full-length genomic RNA, and all subgenomic RNA (i.e., V+G+S). We allow RNA and virus to move between tissues at differing rates, according to the topology in Figure 3.1B. Briefly, we include connections that account for physical proximity, the mucociliary escalator, swallowing, systemic spread, or fecal-oral self-transmission (see Methods for details). We also classified tissue-specific ACE2 expression, TMPRSS2 expression, ACE2-TMPRSS2 coexpression, and temperature as shown in Figure 3.1C (see Methods for details). This model broadly fits the data well (see example fit in Figure 3.1D).

Parameter estimates across articles

Given we fit each article to our model separately, we first investigated variability in the parameter estimates across tissues and articles (sorted by value in Figure 3.2; see Figure S3.1 for estimates sorted by article). Based on the median parameter values, the average infected cell lifespan was between 8 and 21 hours (Figure 3.2A). We fixed the average eclipse phase duration at 6 hours (based on prior work; Ke et al. 2021), and so the average total time between a virus entering a cell and that cell dying was predicted to range from 14 to 27 hours. Detectable virus

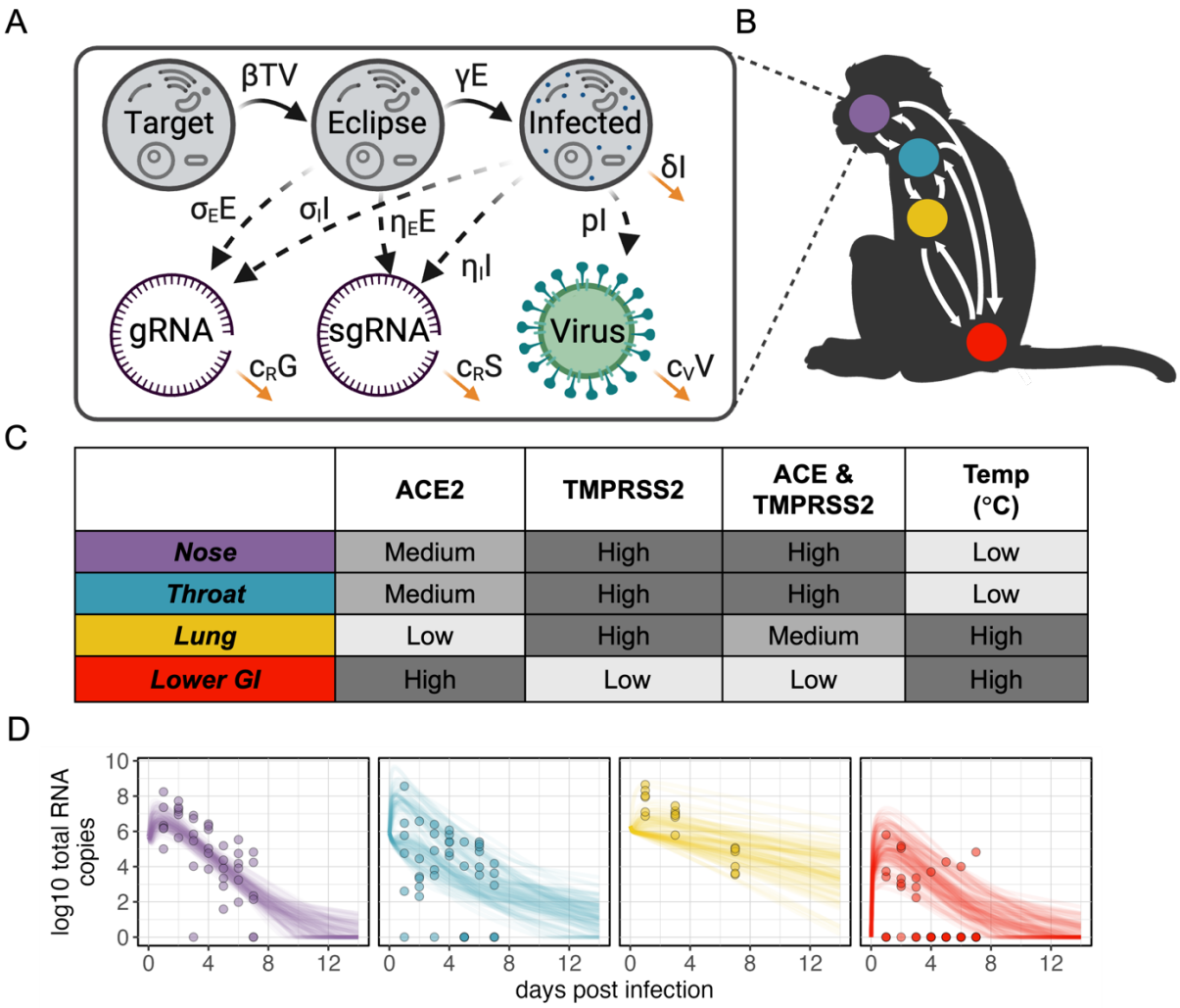

	ACE2	TMPRSS2	ACE & TMPRSS2	Temp (°C)
Nose	Medium	High	High	Low
Throat	Medium	High	High	Low
Lung	Low	High	Medium	High
Lower GI	High	Low	Low	High

Figure 3.1 | Model schematic and example fit.
A, Schematic of cellular and viral dynamics within each tissue. Transitions between state variables and removal from the system are denoted with solid black or orange arrows, respectively. Production of RNA and virus are denoted with dashed arrows. Parameters correspond with those outlined in the methods. **B,** Connectivity between tissues. Each circle is a tissue, which is colored as in the first column of panel C (purple, nose; blue, throat; yellow, lung; red, lower GI). White arrows indicate directional connections between two tissues that are included in the model. **C**, Tissue-specific expression patterns and temperature (Temp). Color intensity scales with the indicated expression level or temperature (e.g., light gray for low). **D**, Example model fit on total RNA data from Williamson et al. 2020, which includes data from 6 animals. Each point is an observation, and each semi-transparent line is a predicted trajectory sampled from all posterior parameters. Each panel distinguishes between tissues, which are colored as in panel B and C. Panels A and B were made with BioRender.com.

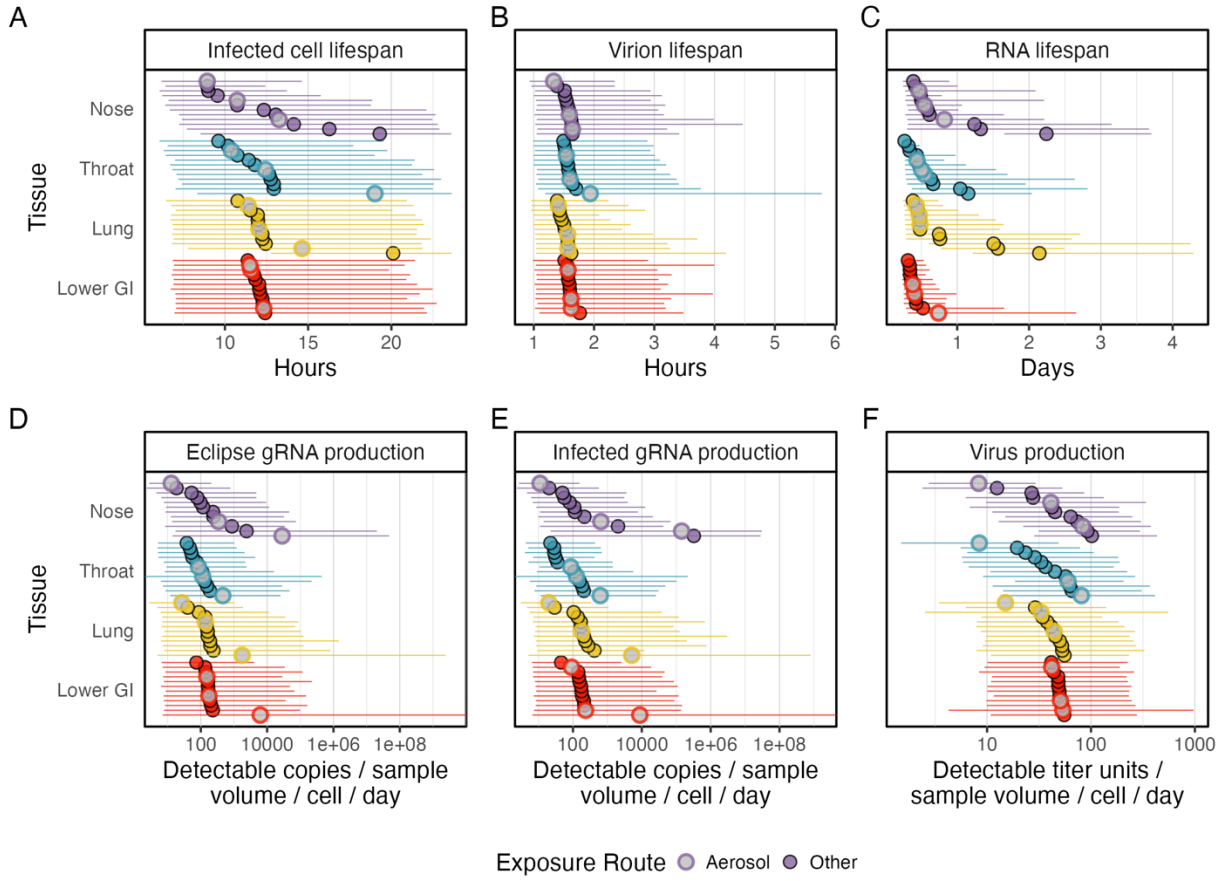

Figure 3.2 | Parameter estimates.
In all panels, we plot the median parameter values for each article-route combination as circles, and their corresponding 90% credible intervals as horizontal lines. Each color corresponds with the tissue indicated along the y axis (and as presented in Figure 3.1C). Circles filled with gray and outlined in color correspond with studies that used aerosol inoculation. All other routes are circles filled with color and outlined in black. The figure legend displays this with the color scheme for the nose as an example. For each tissue within each panel, we sorted the estimates for all article-route combinations by increasing median value. The presented parameter values are: **A**, the average time an infected cell lives ($1/\delta$, rescaled to hours), **B**, the average time until a detectable viral titer (i.e., pfu or TCID50 per sample volume) becomes undetectable ($1/c_V$, rescaled to hours), **C,** the average time until a detectable RNA copy number per sample volume becomes undetectable ($1/c_R$), **D,** the average production rate of detectable genomic RNA copies per sample volume per day for an eclipse cell (σ_E), **E,** the average production rate of detectable genomic RNA copies per sample volume per day for an infected cell (σ_E), and **F,** the average production rate of a detectable viral titer per sample volume per day for an infected cell (p).

(i.e., a pfu or TCID50 per sample volume) was predicted to become undetectable within 2 hours on average for all tissues and articles, though the 90% credible intervals extended up to 6 hours (Figure 3.2B). Detectable RNA (i.e., copy numbers per sample volume) persisted for much longer than infectious virus, namely from approximately 6 hours to 2.5 days on average (Figure 3.2C). RNA clearance was often faster in the GI than in the respiratory tract. The estimated production rates of (non-virion associated) genomic RNA were highly similar between eclipse and infected cells and among tissues (Figure 3.2D,E), with most producing on average around 100 detectable copy numbers per sample volume per cell per day (henceforth we do not mention sample volume). For a few articles, the median production of infected cells was especially high at values near or exceeding 10,000 detectable copies per day. sgRNA production rates were estimated as broadly similar to those for gRNA. Virus production rates were typically smaller than for RNA, with median values ranging from around 10 to 100 detectable pfu or TCID50 per infected cell per day (henceforth titer units per day; Figure 3.2F). Overall, these parameter estimates were remarkably similar across articles, with the median values for a given article falling within the 90% credible interval of most other studies.

Tissue-specific infection rates and their relationship with tissue conditions

We then investigated tissue-specific infection rates, and their dependence on local ACE2 expression, TMPRSS2 expression, ACE2-TMPRSS2 coexpression, and temperature (Figure 3.1C). Overall, median infection rates varied across tissues and articles from $10^{-10.9}$ to $10^{-2.6}$ cells per detectable titer units per day (Figure 3.3A). For all articles, median infection rates were nearly identical in the nose and throat (ordered by increasing value across tissues for each article in Figure

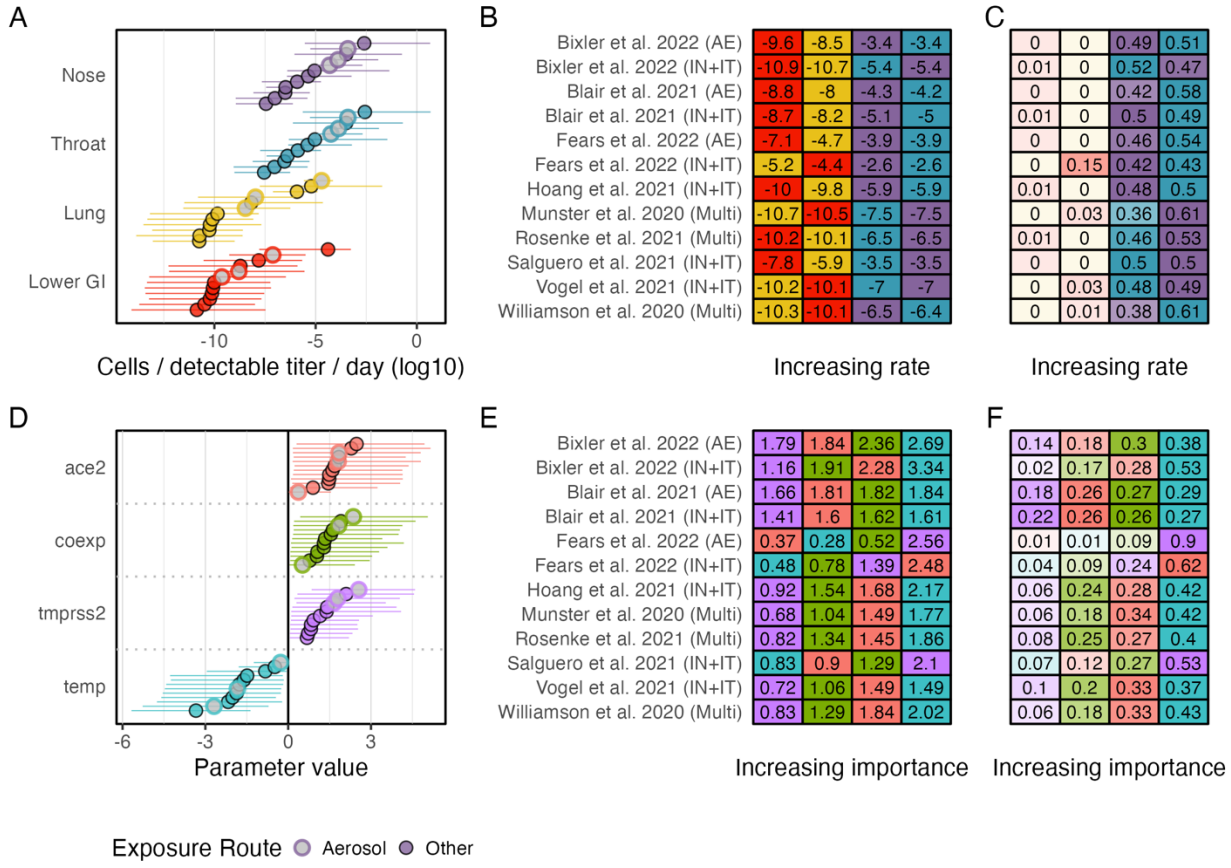

Figure 3.3 | Tissue-specific infection rates and their relationship with tissue conditions. **A,** Median parameter values (points) and the 90% credible intervals (horizontal lines) for tissue-specific infection rates. Each color corresponds with the tissue, as indicated along the y axis and as presented in Figure 1C. Circles filled with gray correspond with studies that used aerosol inoculation. The figure legend below panel D displays this with the color scheme for the nose as an example. For each tissue, we sorted the estimates for all article-route combinations by decreasing median value. **B,** Median infection rates for the article indicated along the y axis. Each cell is colored according to the corresponding tissue as in panel A, and they are ordered by increasing median infection rate (from left to right). Articles are ordered alphabetically on the y axis. **C,** The posterior probability of each tissue having the largest infection rate for each article. All orders and colors are consistent with panel B. The intensity of the color in each cell scales with the displayed probability (more intense colors indicate higher probability). **D,** Median parameter values (points) and the 90% credible intervals (horizontal lines) for the parameters that determine infection rates (ace2: ACE2 expression; coexp: ACE2-TMPRSS2 coexpression; tmprss2, TMPRSS2 expression; temp, Temperature). Colors correspond with the parameter indicated along the y axis. For each cofactor, we sorted the estimates for all article-route combinations by decreasing median value. **E,** Median values for the tropism parameters in panel B. Each cell is colored according to the corresponding cofactor in panel D. They are ordered from left to right by increasing posterior probability of each cofactor having the largest effect, which is shown in panel

F. Articles are ordered alphabetically on the y axis. **F,** Posterior probability of each tropism cofactor having the largest effect on the infection rate. All orders and colors are consistent with panel E. The intensity of the color in each cell scales with how likely that cofactor is to have the highest value relative to all other probabilities for that study (more intense colors indicate higher relative probability).

3.3B), and they had similarly large posterior probabilities of having the largest infection rate (Figure 3.3C). The lung and lower GI clearly had the lowest infection rates (Figure 3.3B), with no or nearly no posterior probabilities of having the largest value (Figure 3.3C). The lung had similar or larger median infection rates than the lower GI (Figure 3.3B), but both were very small in some cases ($<10^{-10}$; Figure 3.3A, B). Interestingly, studies that used aerosol inhalation had some of the highest infection rates, especially in the upper respiratory tract (gray circles in Figure 3.3A).

We then characterized and compared the effects of tissue conditions on predicted infection rates. In our model, we allowed receptor expression, protease availability, and receptor-protease coexpression to increase or have no effect on the infection rate, while higher temperatures were allowed to decrease or have no effect on the rate (given evidence of this trend *in vitro*; Laporte et al., 2021; V'kovski et al., 2021). The values in Figures 3.3D and 3.3E are standardized to reflect the raw increase or decrease in the $\log_{10}$ infection rate between low and high values for all cofactors (e.g., between low and high levels of ACE2 expression), which allowed us to compare them directly. The range of effect sizes was similar for all four cofactor types (Figure 3.3D). For each article, to determine which cofactors were predicted to have the largest impact on estimated infection rates, we computed the posterior probability of each cofactor having the largest effect (Figure 3.3F), which we then used to rank them by increasing importance. Some articles demonstrated clear support for one cofactor having a larger effect, while others estimated similar probabilities and effect sizes for multiple cofactors (Figure 3.3E,F).

For all studies, infection rates were predicted to change by at least a median value of 1 $\log_{10}$ units for at least one of the tested cofactors (Figure 3.3E), and for each article the cofactor with the largest median effect was predicted to increase beta anywhere from 1.5 to 3.3 $\log_{10}$ units (Figure 3.3F). Based on posterior probabilities for each article, there was always greater than a 93% or 71% chance that at least one of the traits would increase beta by at least 1 or 2 $\log_{10}$ units, respectively. Interestingly, temperature had the largest effect for more than half of the studies (n=9/12). TMPRSS2 had the largest effect for 2 of the 3 remaining articles, but it clearly ranked as least important for almost all others (Figure 3.3E,F). When taking the average of the probabilities across studies, temperature had the most posterior support for having the largest effect (0.30 probability), followed by ACE2 (0.27), TMPRSS2 (0.22), and coexpression (0.21).

Within-host reproductive number and the number of infected cells

To determine whether local infections were productive, we calculated within-host reproductive numbers assuming no virus movement (R_0; using the formula in Zitzmann et al. 2024) and the percent of cells that became infected (Figure 3.4). Strikingly, most infections were subcritical (i.e., median $R_0<1$), with aerosol inoculations being the most likely to result in supercritical infections (i.e., median $R_0\geq1$) in respiratory tissues (bars in Figure 3.4A, corresponding to the bottom axis). Median R_0 estimates exceeded 1 in the upper respiratory tract for a few other studies, but, for many of them, the 90% credible interval also included support for subcritical infections (horizontal lines in Figure 3.4A). Only two studies resulted in supercritical median R_0 values in the lung, which also included substantial posterior support for subcritical infections. All articles had clearly subcritical infections in the lower GI (i.e., median and 90%

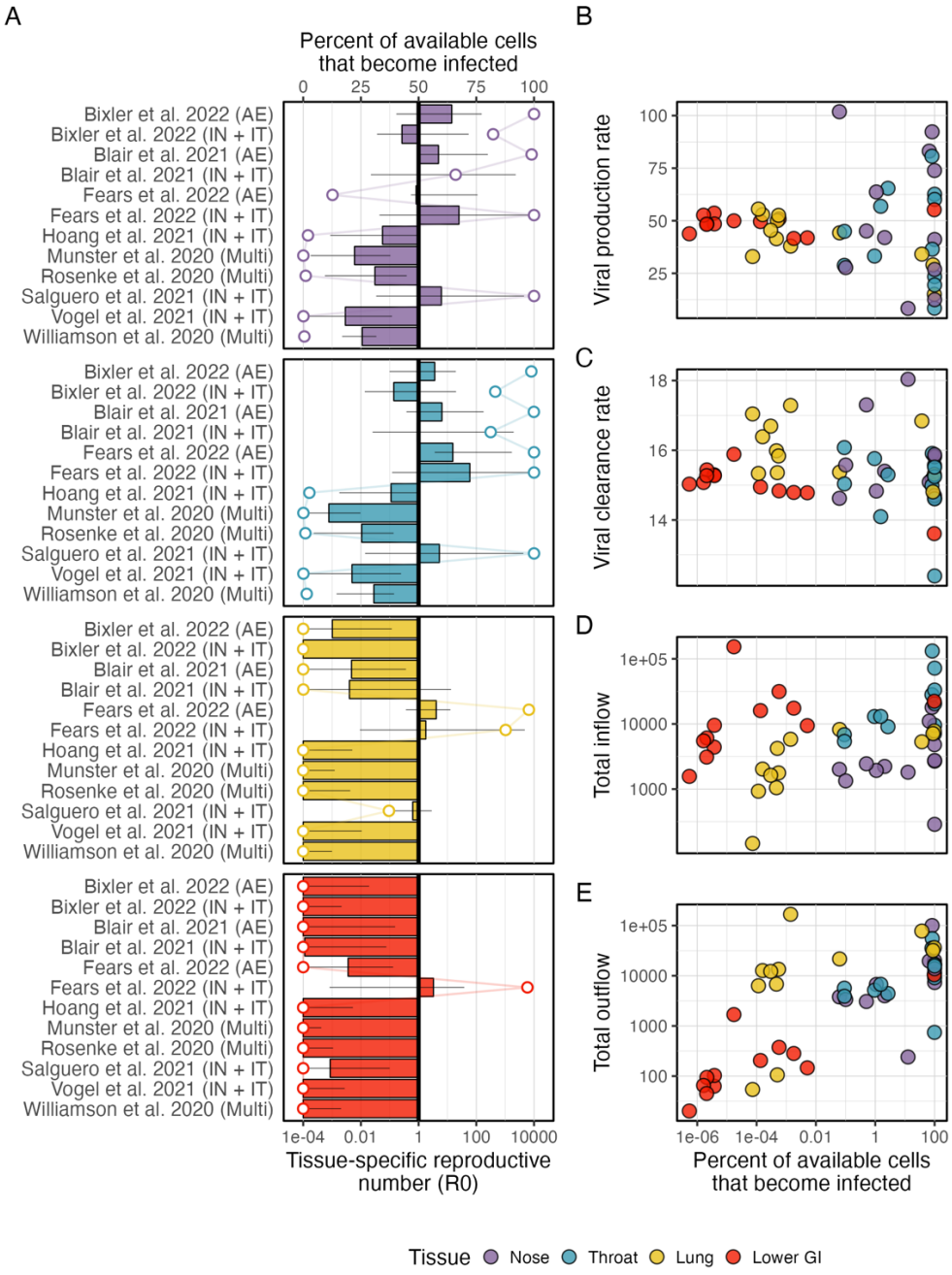

Figure 3.4 | Within-host reproductive number and the number of infected cells.
A, the median tissue-specific reproductive numbers (bars, bottom axis) and the median percent of available cells that became infected by day 40 post infection (points, top axis). Each row corresponds with the article indicated on the y axis. The black horizontal lines provide the article-specific 90% credible intervals for the tissue-specific reproductive numbers. Panels are separated by tissue, according to the colors in Figure 3.1C (purple: nose; blue: throat; yellow: lung; red:

lower GI). **B-E**, The relationship between the median percent of cells that become infected and (B) the median viral production rate, (C) the median viral clearance rate, (D) the median total inflow by day 40 post infection, and (E) the median total outflow by day 40 post infection. Each point corresponds with one tissue from one article, where tissues are distinguished by color as in panel A.

credible intervals below 1), with only one exception that had a median R_0 value above 1 but also substantial support for subcritical values.

The percent of all available target cells that became infected followed similar trends as the R_0 values, as expected (points in Figure 3.4A, corresponding with the top axis). Most infections resulted in fewer than 10% of cells becoming infected, especially in the lower GI (based on the median number per tissue by day 40 post inoculation). Tissues with larger R_0 values tended to have higher median percentages of infected cells (Figure S3.2). Many, though not all, infections with supercritical median R_0 values resulted in median predictions of all cells becoming infected, suggesting other unmodeled factors limit infection. When considering all articles jointly, the percent of infected cells was not strongly correlated with local viral production rates (Figure 3.4B) or clearance rates (Figure 3.4C). However, there was some evidence that, for a given tissue, the percent of infected cells increased with the total inflow into the tissue (Figure 3.4D) and with the total outflow from that tissue (Figure 3.4E). Ultimately, given that there was substantial variation in our predictions of R_0 and the percent of all infected cells, it is possible that unmodeled stochastic effects (e.g., dispersal limitation) may drive the apparent pattern of largely subcritical infections.

Tissue-specific virus production

We then determined which tissues produced the most infectious virus in each article. Although infections were largely subcritical with small percentages of infected cells (Figure 3.4), most still resulted in the median production of at least 10^3 titer units in the upper respiratory tract

(bars in Figure 3.5, corresponding with the bottom axis). For all but three studies, the nose or throat produced the most virus (darker bars in Figure 3.5) with high probabilities (points in Figure 3.5, top axis). The lung produced the most virus with relatively high probabilities for all three exceptions (Figure 3.5), which notably were the same studies that had supercritical or nearly supercritical median R_0 values in the lung (Figure 3.4A). However, infections in the lung for most other articles resulted in the median production of less than 10^3 detectable titer units, though this quantity had large amounts of uncertainty for some articles (i.e., large 90% credible intervals; indicated by black horizontal lines in Figure 3.5). Substantial production in the GI was rare, with only one article resulting in median values exceeding 10^3 titer units and with many resulting in less than one titer unit. As with the lung, however, there were large amounts of uncertainty on GI production for many articles. Aerosol exposures resulted in either the nose or lung having the

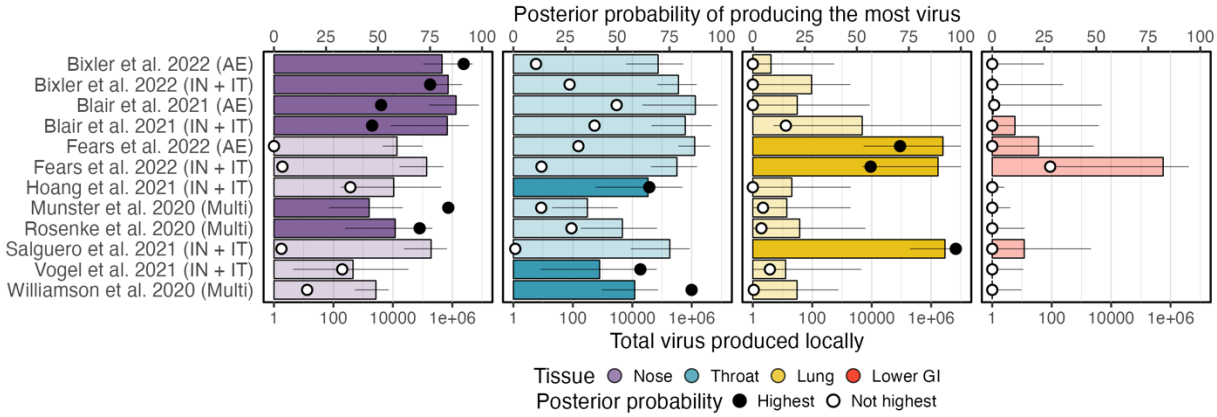

Figure 3.5 | Tissue-specific virus production.
Bars indicate the median amount of virus produced by each tissue by day 40 post infection (bottom axis), while the points display the posterior probability of that tissue producing the most virus (points, top axis). Each row corresponds with the article indicated on the y axis. Darker bars indicate that tissue had the highest median amount of virus produced for that article. Filled black points indicate that tissue had the highest posterior probability of producing the most virus for that article. All other points are white. The black horizontal lines provide the article-specific 90% credible intervals for the amount of virus produced. Panels are separated by tissue, according to the colors in Figure 1 (purple: nose; blue: throat; yellow: lung; red: lower GI).

largest median virus production (dark bars in Figure 3.5). This could be related to differences in the particle sizes used for each study which are known to affect deposition sites along the respiratory tract, but the information provided in the articles did not allow us to directly compare particle sizes. All of these patterns were qualitatively similar for genomic RNA but with larger quantities produced.

Connectivity and movement rates among tissues

To characterize viral dissemination across tissues, we compared estimated movement rates among the nose, throat, lung, and lower GI (Figure 3.6). For all articles, virus flowed out of the nose into the throat at a higher rate than into the lower GI (purple points in Figure 3.6A**;** larger circles indicate higher rates for a given article) with high posterior probability (Figure 3.6B). Viruses also moved from the throat into the nose at higher median rates than into the lung for nearly all articles, and median movement rates from the throat to the lower GI were always smallest (Figure 3.6A). However, these outflows from the throat often had similar, intermediate probabilities of having the largest flow rate (Figure 3.6B), suggesting outflow from the throat may be broadly comparable across tissue destinations. Movement rates from the lung to the throat were typically larger than from the lung to the lower GI (Figure 3.6A), and often with high probability (Figure 3.6B). In some instances, though, these movement rates had similar posterior probabilities of having the largest flow rate, which could be explained by infections that managed to spread systemically. The movement rates from the lower GI to the throat and to the lung were very similar (Figure 3.6A) and both had approximately equal posterior probability of having the largest outflow rate (Figure 3.6B). This suggests that lower GI-respiratory dissemination may be primarily driven by systemic spread rather than by fecal-oral self-transmission.

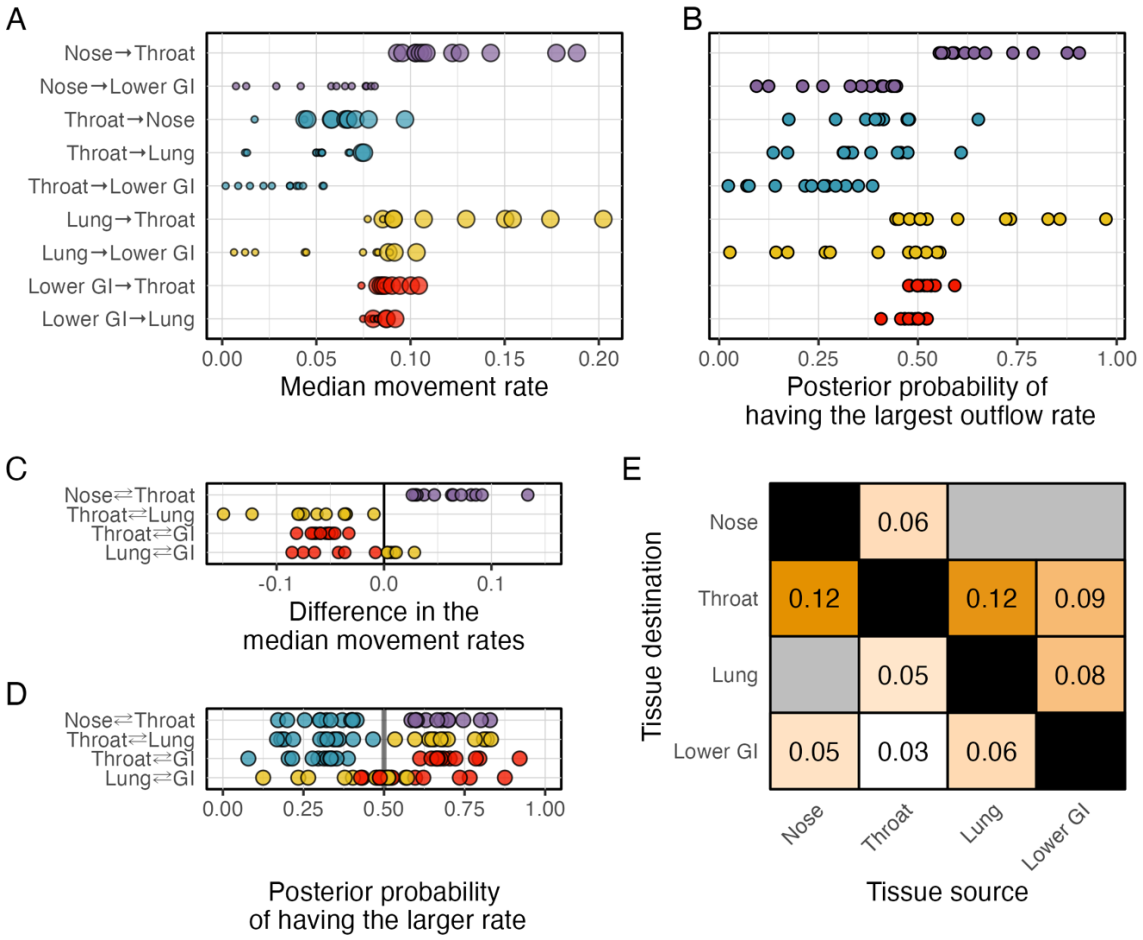

Figure 3.6 | Connectivity and movement rates among tissues.
A, Median movement rates of infectious virus for all connections included in the model. The y-axis labels have the form X→Y, which indicates the flow of virus from tissue X to tissue Y. Each point gives the median parameter value from one article. The points are colored by the source of the virus (i.e., tissue X) according to the color scheme displayed in Figure 3.1B. The size of the point indicates whether that movement rate is the largest of all movement rates out of the same tissue source (i.e., within the points with the same color) for each article. The large sizes correspond with the largest median rate. **B,** The posterior probability that the movement rate indicated on the y axis is the largest of all movement rates out of the same tissue source (i.e., for points with the same color). **C,** Difference in the median movement rates between tissues connected in both directions. Each point corresponds to one article. Points are colored based on the tissue source with the largest directional flow. For example, the purple points in the first row indicate the flow from the Nose→Throat is bigger than the Throat→Nose because purple corresponds with the nose. **D**, The posterior probability of the movement being larger for the tissues connected in both directions. Points are colored based on the tissue source (e.g., purple points in the top row correspond with the flow from the Nose→Throat while blue points correspond with the flow from the Throat→Nose). **E,** Mean value across articles for the movement

rates from the tissue along the x axis to the tissue on the y axis. Gray cells are connections not included in the model. Black cells are within-tissue flow rates, which we do not calculate.

Some tissue pairs were connected via bidirectional movement between them, which we compared to identify the directions with higher predicted flow rates (Figure 3.6C,D). The median movement rates were higher from the nose to the throat than from the throat to the nose for all articles (purple points in the first row of Figure 3.6C), with fairly high posterior probability (Figure 3.6D). Rates were greater from the lung to the throat than from the throat to the lung (yellow points in the second row of Figure 3.6C), which is consistent with the mucociliary escalator transporting material from the lower to the upper respiratory tract. Unexpectedly, predicted movement rates from the lower GI to respiratory tissues were almost always larger than those from the respiratory tissues to the lower GI (red points in the bottom two rows of Figure 3.6C), often with high posterior probability (Figure 3.6D). This would be consistent with virions frequently failing to maintain infectivity as they disseminate from the upper respiratory tract to the lower GI tract via the highly acidic upper GI. Median estimates for RNA movement rates were typically similar, though often smaller, than virus movement rates (Figure S3.2). When taking the mean of all virus movement rates across articles, the flow rate into the throat from other respiratory tissues was larger than all others (Figure 3.6E), highlighting the high rates of virus sharing among respiratory tissues.

Total viral inflow and outflow from each tissue

We then characterized the total amount of virus that flowed into and out of each tissue over the full infection course (Figure 3.7), which depends on both the movement rates and the local viral titers. The nose experienced more outflow than inflow for all but one article (i.e., flow ratios

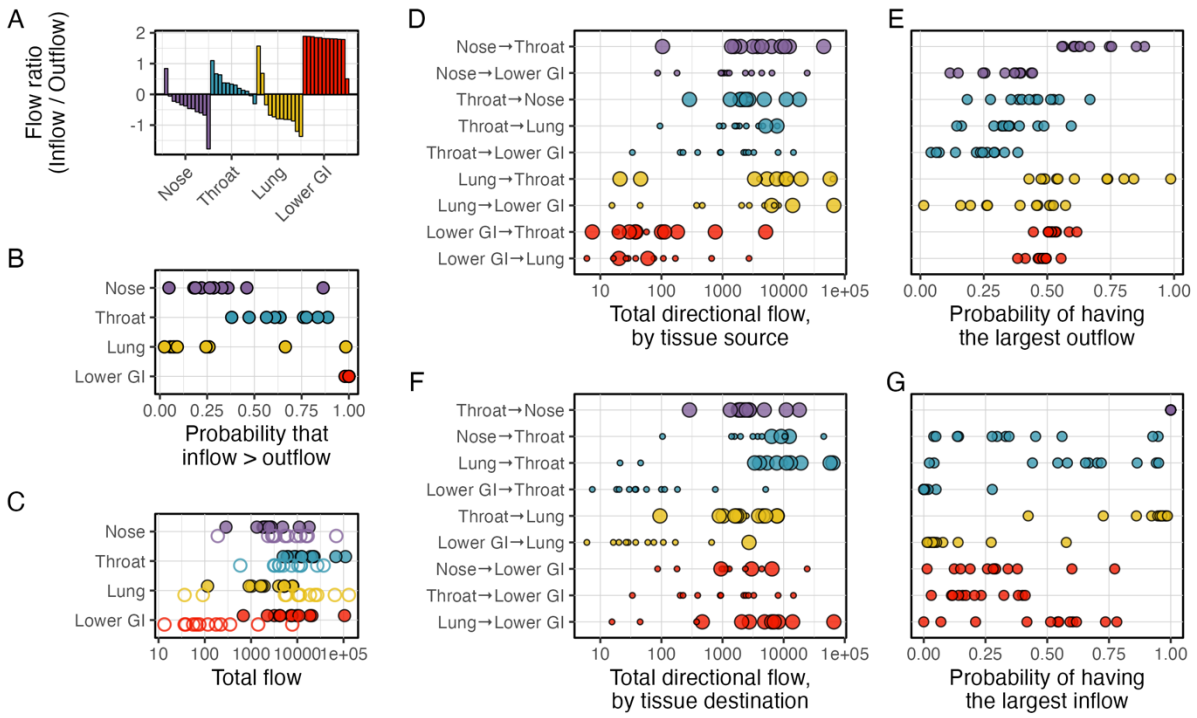

Figure 3.7 | Total viral inflow and outflow from each tissue.
A, the ratio of the median total inflow and median total outflow in each tissue along the x axis by day 40 post infection. Each bar corresponds with one article, and they are sorted by decreasing ratio within each tissue. The color corresponds with the tissue, as indicated on the y axis. **B**, the posterior probability that the total inflow is larger than the total outflow for each tissue on the y axis. Each point corresponds with one article. Points are colored based on the tissue, as in panel A. **C,** the total amount of virus that flows into (points with colored fill and black outlines) or out of (points with colored outline and white fill) the tissue indicated on the y axis. Colors correspond with the tissue as in panel A. **D,** the total virus that flowed between tissues for all connections included in the model. The y-axis labels have the form X→Y, which indicates the flow of virus from tissue X to tissue Y. Each point gives the median parameter value from one article. The points are colored by the source of the virus (i.e., tissue X) as in panel A. The size of the point indicates whether that virus outflow is the largest of all outflows from the same tissue source (i.e., within the points with the same color) for each article. The large sizes correspond with the largest flow. **E,** the posterior probability of that outflow being the largest of all outflows from the same tissue source (i.e., within the points with the same color). Points are colored as in panel E, by the tissue source. **F,** as in panel D but the points are colored by the destination of the virus (i.e., tissue Y) and the y axis is sorted to group connections based on the tissue destination. The size of the point indicates whether that virus inflow is the largest of all inflows into the same tissue destination (i.e., within the points with the same color) for each article. The large sizes correspond with the largest flow. **G,** The posterior probability of that inflow being the largest of all inflows into the same tissue destination (i.e., within the points with the same color). Points are colored as in panel F, by the tissue destination.

< 1 in Figure 3.7A), which had a very high posterior probability of experiencing more inflow (0.93; Figure 3.7B). Median total inflows and outflows from the nose both ranged from approximately $10^{2.5}$ to 10^5 titer units (points with colored fill versus points with colored outlines in Figure 3.7C). All inflow to the nose came from the throat by design (see Methods). For all articles, outflow from the nose primarily went into the throat (determined as the tissue with the largest median inflow quantities; large circles indicate the highest outflow for each tissue per article; Figure 3.7D), with posterior probabilities of this occurring always exceeding 0.5 (Figure 3.7E). Inflows exceeded outflows for the throat (Figure 3.7A) with relatively high probabilities for most studies (Figure 3.7B). The inflows into the throat most frequently stemmed from either the nose or lung (blue points in Figure 3.7F) often with high probability (Figure 3.7G). Outflows from the throat most frequently went to the nose though occasionally also to the lung (Figure 3.7D). The lower GI was not the primary inflow source or outflow destination for the throat for any article. Similar to the nose, the lung experienced primarily outflows (Figure 3.7A) with high posterior probabilities (Figure 3.7B). Both the inflows into and outflows from the lung were associated primarily with the throat (Figure 3.7D,F), where the inflow had remarkably high posterior probabilities (Figure 3.7G). The lower GI experienced primarily inflows (Figure 3.7A) with near certainty for most articles (Figure 3.7B) and with much higher total quantities (Figure 3.7C). The largest inflow of infectious virus into the lower GI typically originated from the lung (Figure 3.7F), possibly because this route does not involve exposure to the highly acidic upper GI. The outflow from the lower GI primarily went to the throat (Figure 3.7D), but posterior probabilities were often very similar for the throat and lung (Figure 3.7E). Given the apparent differences in the movement rates and overall virus flow among tissues, connectivity clearly impacts within-host dynamics and emphasizes the importance of modeling tissues jointly whenever possible.

Discussion

In this study, we developed a mechanistic model to analyze SARS-CoV-2 infection patterns in the upper respiratory, lower respiratory, and gastrointestinal tracts of experimentally challenged rhesus macaques. By jointly modeling infection dynamics across multiple tissues, we were able to estimate the connectivity structure among the nose, throat, lung, and lower GI based on inferred virus movement rates between them, which revealed particularly high rates of movement into the throat from other respiratory tissues. We also allowed tissue-specific infection rates to vary based on local receptor expression, protease availability, and temperature. Our analyses revealed that infections were overall more successful and productive in the nose and throat than in the lung and lower GI, which was consistent with an estimated increase in the local infection rates at lower temperatures. Because we fit this model to the data from nine studies separately, we were able to identify within-host infection patterns that were robust to exposure conditions and experimental designs and, conversely, we were able to characterize the variability in parameter estimates and predicted outcomes across studies. To our knowledge, no other modeling framework has formally investigated how tissue traits and connectivity structure interact to determine spatiotemporal infection patterns inside hosts, nor has any within-host modeling study of SARS-CoV-2 included as many datasets in a single analysis. Overall, our study demonstrates that spatial patterns of SARS-CoV-2 infection inside hosts are strongly influenced by the heterogeneous tissue landscape and virus dispersal patterns across tissues. Population invasions in ecology exhibit similar dependencies, emphasizing that ecological theories and analytical approaches are a valuable but currently underutilized toolkit to better understand within-host infection dynamics.

Viral kinetic parameters estimated by our model were remarkably consistent across the nine studies included in our analysis, and they were broadly comparable to those estimated in other modeling studies of SARS-CoV-2. We found that, in all articles, the median infectivity parameters governing cell infection rates were higher in upper respiratory than lower respiratory tissues, corroborating prior work that modeled SARS-CoV-2 dynamics in humans (Ciupe & Tuncer, 2022; Wang et al., 2020). The range of our estimated infection rates also aligns with estimates reported for similar tissues in other studies modeling data from humans and non-human primates (Alexandre et al., 2022; Ciupe & Tuncer, 2022; Gonçalves et al., 2021; Wang et al., 2020). Our estimates of virion lifespans were highly similar across studies and tissues, as were the estimates of RNA lifespan, though a few studies predicted prolonged RNA detection. Some parameters exhibited greater variability across studies and host tissues. These include the median infected cell death rate, but notably the range of our estimates is similar to those previously reported (Alexandre et al., 2022; Ciupe & Tuncer, 2022; Gonçalves et al., 2021; Ke et al., 2021). Prior modeling work has estimated higher virus or RNA production rates in the upper respiratory tract compared to the lower respiratory tract (Alexandre et al., 2022; Gonçalves et al., 2021; Wang et al., 2020) and higher clearance rates in the lower respiratory tract than the upper respiratory tract (Ciupe & Tuncer, 2022). This was true for some but not all articles in our analyses, suggesting these parameters may be particularly sensitive to individual heterogeneity. Altogether, the similarities in many parameter estimates across the studies we included were particularly striking. This highlights the value of analyzing many different datasets using the same model structure, as it can help identify parameters that could be fixed in future analyses with minimal risk of biasing other model outputs.

With our modeling framework, we quantitatively tested the influence of receptor expression, protease availability, receptor-protease co-expression, and temperature on tissue-specific infectivity rates, which, to our knowledge, has not been attempted before. Our models estimated that receptor and protease expression influence infection dynamics, but, interestingly, our results do not align with the common narrative that these traits are the primary determinants of spatial SARS-CoV-2 infection patterns inside hosts. Based on the data that was available for various tissue traits, we found that temperature often had a higher relative effect on tissue-specific infection rates than ACE2 expression, TMPRSS2 expression, or ACE2-TMPRSS2 co-expression in cells. Our models predicted that the lower temperatures of the upper respiratory tract are correlated with higher infection rates than at the core body temperature of the lung and lower GI, which is consistent with previous *in vitro* experiments conducted on SARS-CoV-2 (Laporte et al., 2021; V'kovski et al., 2021). Temperature is known to drive the tropism patterns of other viruses, including avian influenza (Lipsitch et al., 2016; Russell et al., 2018). While these results and concordances suggest that temperature likely does affect *in vivo* SARS-CoV-2 infection patterns, our analyses were limited by the available data and so they should be interpreted cautiously.

In particular, several factors hindered our ability to definitively determine the relative effects of receptor expression, protease availability, and abiotic conditions on SARS-CoV-2 tropism. All of the tissues we considered (nose, throat, lung, lower GI) are generally accepted as sites of SARS-CoV-2 infection, so it is possible that they all express sufficient levels of ACE2 and TMPRSS2 to support virus replication, leading to underestimates of the relative importance of these factors on local infection rates. The inclusion of tissues with lower or no expression would likely increase their predicted importance. Furthermore, while we assigned tissue conditions based on certain traits, it is possible that other underlying differences across tissues could have affected

our measured outcomes. Temperature, for example, may appear so important because it distinguishes between upper respiratory tissues and all others, which could also be explained by differences in an unmodeled cofactor (e.g., local pH or the expression of an alternate receptor). Also, although we classified tissue-specific expression patterns to the best of our ability, we were limited by the available trait data. Due to these data limitations, we had to use transcriptomic measurements, which can be poorly correlated with actual protein abundance (Haider & Pal, 2013), and it was necessary for us to combine trait data obtained from humans and non-human primates, which can have different expression profiles (Han et al., 2022). Because we integrated information from multiple sources and species, our analyses necessarily relied on semi-quantitative trait descriptions (e.g., low, medium, high) rather than truly quantitative comparisons, which likely also reduced our model's ability to estimate relative cofactor effects. Despite these data limitations, our modeling framework lays the foundation for within-host mathematical models to answer long-standing questions in virology about the determinants of tropism, and a simulation study conducted with our model would offer guidance on the data types and data resolution necessary to confidently attain these estimates. While our study advances a valuable hierarchical model to assess how tissue traits affect observed tropism, more definitive answers will require broader datasets that include tissues with higher trait variability and that can draw upon species-specific, quantitative expression patterns.

Because we jointly modeled infection dynamics in the nose, throat, lung, and lower GI, we were able to characterize virus movement across these tissues and its influence on overall infection patterns. Our models inferred high rates of viral dissemination among respiratory tissues, with the nose and lung experiencing larger quantities of viral outflow while the throat experienced larger quantities of viral inflow. The connections from the nose to the throat and from the lung to the

throat had the largest overall movement rates of any connections included in our model, emphasizing the centrality of the throat and the highly connected nature of the respiratory tract. These findings are not surprising, given the known importance of viral dissemination across the respiratory tract (e.g., mucociliary escalator, inhalation, exhalation), and since experiments with targeted routes of exposure have shown that infections can spread from the upper to the lower respiratory tract or vice versa (Chapter 2). Our findings are also concordant with prior within-host models of SARS-CoV-2 infection that estimated nonzero movement rates among respiratory tissues in humans (Ciupe & Tuncer, 2022; Dogra et al., 2021), but they contrast with others that estimated nonsignificant movement rates among upper and lower respiratory tissues in macaques (Alexandre et al., 2022; Gonçalves et al., 2021). However, the latter studies partially attributed their negative findings to insufficient data. The discrepancies between our results could also reflect differences in the underlying model assumptions and structure. Goncalves et al., for example, fixed the movement rate to be equal in both directions, while we included unique rates in all directions. Alexandre et al. may have found worse model performance when including tissue connectivity because these analyses involved fixing all other parameters to those estimated without movement, and these fixed parameters likely already accounted for movement effects in other ways (e.g., via higher local clearance rates). Future work that applies our modeling framework to their data could investigate whether these structural and analytical differences explain our disparate conclusions.

Our models also inferred significant virus movement among respiratory and gastrointestinal tissues. The lower GI clearly experienced higher rates of viral inflow than outflow, confirming its intuitive role as a ‘sink’ for SARS-CoV-2. Of the respiratory tissues, we found that the lung was the strongest source of infection to the lower GI, with the highest movement rate and often the largest overall flow of viruses. This surprising finding could be explained by successful

systemic spread from the lung, as suggested previously (Zhang et al., 2021), combined with large losses of infectivity when viruses swallowed from the upper respiratory tract pass through the highly acidic upper gastrointestinal tract (Evans et al., 1988; Fallingborg, 1999), as has been demonstrated in low pH *in vitro* systems (A. C.-Y. Lee et al., 2020). Our model fits were also consistent with possible systemic spread from the lower GI, given highly similar, nonzero movement rates from the lower GI to the throat and to the lung. This could be related to the accessibility of lymphatic tissue in the GI tract (e.g., Peyer's patches), which can facilitate access to the bloodstream (Fenner et al., 1987). However, virus production was minimal in the GI and outflow quantities were small, suggesting that respiratory dynamics are likely not strongly influenced by gastrointestinal infections following upper and lower respiratory inoculation (as in our dataset). Overall, our results demonstrate that observed infection dynamics inside hosts are the product of both local replication and high rates of viral movement among tissues, especially within the respiratory tract, emphasizing the importance of accounting for connectivity when studying spatiotemporal infection patterns.

In each tissue, we characterized the percent of all available target cells that became infected, and, relatedly, we determined whether local infections were productive and self-sustaining in the absence of viral movement. Our models estimated that most infections resulted in fewer than 10% of all available target cells becoming infected, especially in the lung and lower GI. This finding was concordant with our estimates that these tissues were typically subcritical with a median within-host reproductive number (R_0) less than one, which indicates that the infection did not spread significantly in the given tissue because, on average, each infected cell resulted in fewer than one additional cell becoming infected. However, many of these tissues also had substantial posterior support for being productive and supercritical, as the credible intervals

for R_0 often included values greater than one. Most of the supercritical infections in our analyses occurred in the nose and throat, with only two instances of supercritical infections in the lung and one instance in the lower GI. While initially surprising, these results are consistent with rhesus macaques broadly being considered good animal models for mild but not severe SARS-CoV-2 infection, especially in young animals like those in our dataset (C.-Y. Lee & Lowen, 2021). Other modeling work has also estimated supercritical R_0 values in the upper respiratory tissues of macaques (Alexandre et al., 2022; Gonçalves et al., 2021; Marc et al., 2023) and humans (Ke et al., 2021). However, in contrast with our results, studies have estimated supercritical R_0 values also in the lower respiratory tract of macaques (Alexandre et al., 2022; Gonçalves et al., 2021). This discrepancy could be explained by many factors, including that our models were fit to bronchoalveolar lavage or bronchial brush samples in rhesus macaques instead of tracheal swabs in cynomolgus macaques. Our model structure also differed substantially from these studies, especially with Alexandre et al., which (i) modeled the dynamics and clearance of the inoculum separately from virus produced during infection, (ii) expressed the production of and the relationships between RNA products and infectious viruses differently, and (iii) did not include viral movement between tissues, among other differences. The implications of these choices on our respective results are difficult to predict without theoretical exploration and simulation, and such work is needed to identify the best multi-tissue modeling approaches for high-dose exposures in animal challenge experiments.

Within individual tissues and also across studies, we observed high variability in our R_0 estimates, which could reflect unmodeled stochastic processes. Our prior work (Chapter 2) on a similar but larger dataset has shown that not all macaques become detectably infected in the nose, throat, trachea, lung, and GI following inoculation–viral invasion can succeed in some tissues yet

fail in others, even in those that could theoretically support productive infection. These failures likely correspond to observations of within-host bottlenecks, wherein small numbers of viral particles moving from one tissue to another are subject to chance events that can lead to success or failure (i.e., stochastic variation) and, consequently, variable infection outcomes and invasion speed (Snyder, 2003). Ordinary differential equations, which are the foundation of our models and all traditional within-host models of virus dynamics (Perelson, 2002), are deterministic and cannot capture stochastic effects. That means that any virus introduced into a tissue location will always trigger productive infection if R_0 is supercritical. Parameter estimates from fitting deterministic models will reflect the average of the successful and failed infections in any given tissue, likely resulting in smaller population-level estimates of the infection rates in successful infections, and consequently, smaller estimates of R_0 and the number of infected cells. Multi-tissue models are especially vulnerable to this effect given that there is substantial individual-level heterogeneity in spatiotemporal infection patterns, especially when compared to single-tissue models that are typically only applied to clearly infected tissues in clearly infected individuals. However, ecological theory cautions that, by disregarding viral movement, single-tissue models risk estimating supercritical R_0 values in truly subcritical tissues, because dispersal from populations with positive growth rates can make neighboring locations with negative growth rates appear suitable (Pulliam, 1988, 2000). Our model results suggest these source-sink dynamics may occur between the respiratory tract and the lower GI. Median R_0 values in the lower GI were almost always subcritical, minimal amounts of virus were produced in the GI, and yet GI infection was often detectable, likely due to high quantities of viral inflow from the respiratory tract. This emphasizes the need for new analytical methods, or techniques borrowed from other fields like ecology and systems biology, to overcome the challenges with modeling multi-tissue systems.

Once developed, these models could better characterize the unobservable processes that govern the spatial distributions of viruses inside their hosts.

We fit the data from nine different studies to our model, which allowed us to identify patterns that were or were not consistent across different exposure routes, doses, sampling schemes, and labs. Many findings were remarkably similar, including parameters describing within-tissue dynamics (e.g., cell death rates), the estimated connectivity structure across tissues, and the small R_0 values in the lung and lower GI. However, others differed substantially, even among articles that used the same exposure route, including which respiratory tissue produced the most virus and what the estimated R_0 values were in the upper respiratory tract. These discrepancies could be related to each lab's specific inoculation procedure, or individual heterogeneity and stochastic effects, especially given that there can be as few as two animals per study protocol. These differences caution against drawing strong conclusions after analyzing an individual dataset, as they may not reflect expected trends for other exposure conditions or for the broader population. A meta-analytic approach of fitting all datasets jointly in a single model would offer the best chance at accounting for statistical noise and identifying generalizable trends. While this was computationally impractical for our study, the similarities in many of our parameter estimates suggest that this approach would be feasible. To capitalize on contrasts and investigate generalizability across exposure conditions, such analyses would ideally include more variable exposure doses and routes than were available for this study. Despite our broader database containing more than 100 articles that experimentally challenged non-human primates with SARS-CoV-2 (Chapter 2), only nine articles fit our criteria for this study, and all of them simultaneously exposed the upper and lower respiratory tract, which can lead to different infection dynamics than exposure via a single location (Chapter 2). More consistent sampling coverage across tissues for

more variable experimental designs would be invaluable for post-hoc quantitative analyses of animal challenge experiments, with the added ethical benefits of enhancing the insights obtained per study animal (Prescott, 2010).

Our mechanistic models have demonstrated the importance of considering tissue heterogeneity and connectivity patterns to study viral infections inside hosts. Our analyses highlighted the potential rewards but also the challenges in modeling multi-tissue infection dynamics, which can be highly sensitive to stochasticity and individual-level heterogeneity. More theory and new techniques are clearly needed to model these complex systems, which should include simulation studies conducted with our model. Crucially, our mechanistic modeling framework is the first to formally investigate how tissue traits and connectivity structure interact to determine spatiotemporal infection patterns inside hosts, but more comprehensive profiles of receptor expression, protease availability, and abiotic factors in non-human primates are sorely needed to enable more accurate estimates. As these data become more available, we believe our analytical approach will help answer long-standing questions in virology about the determinants of tissue tropism.

Supplementary Figures

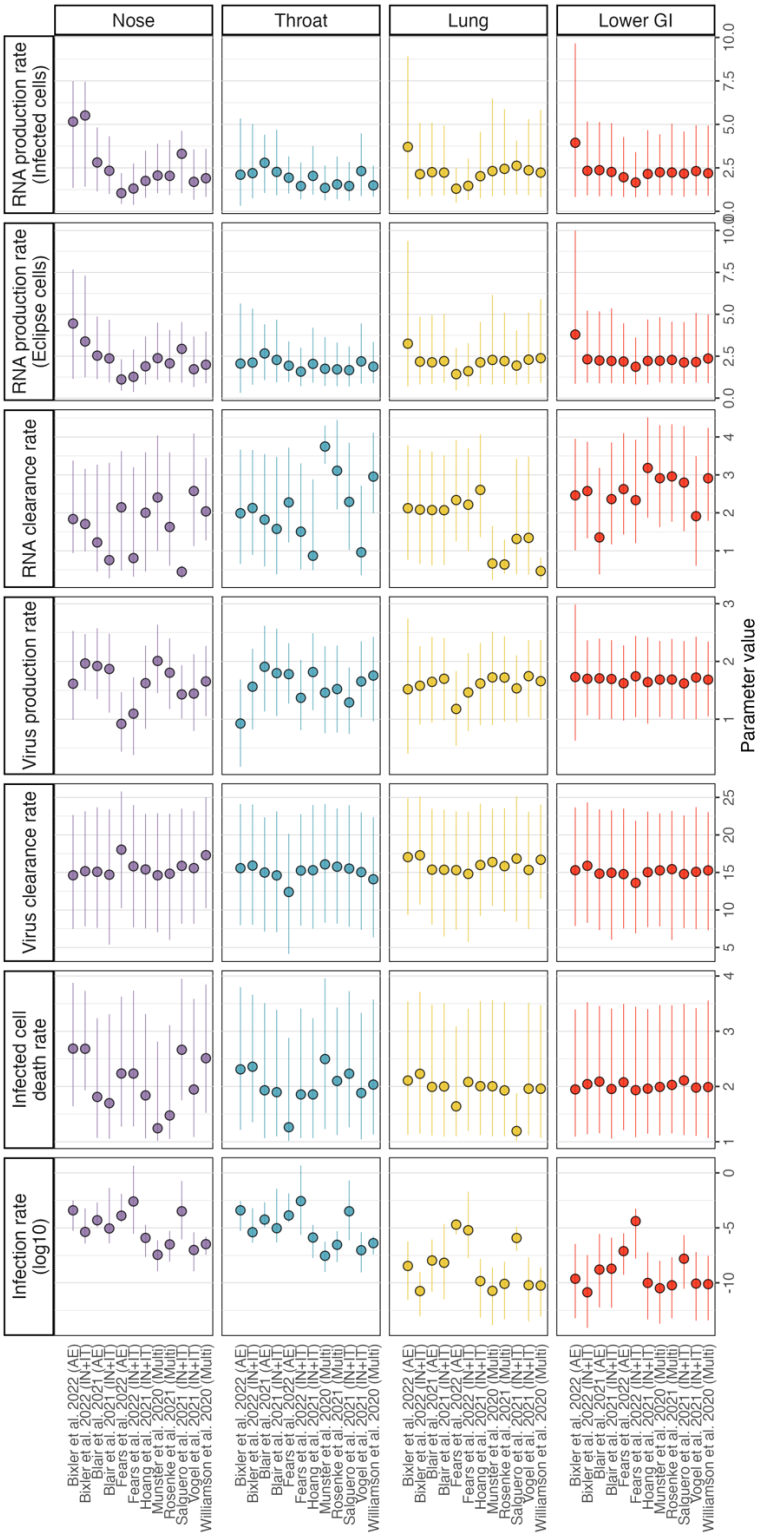

Figure S 3.1 | Article-specific parameter values.
Parameters are distinguished by the column header, and the tissue is indicated in the row labels. The article is indicated by the label on the y axis, which are sorted alphabetically. Each point gives the median prediction, colored by the corresponding tissue. The horizontal line gives the 90% credible interval of the parameter. Virus and RNA production rates are shown as the $\log_{10}$ parameter value. All parameters are displayed in their raw units (e.g., quantities per day).

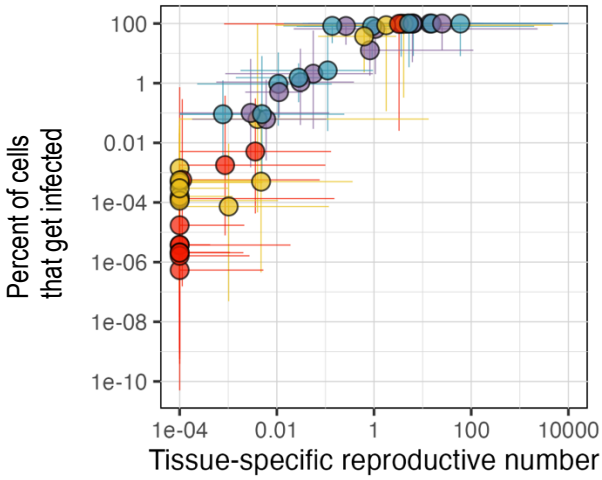

Figure S 3.2 | Relationship between R_0 and the percent of cells that become infected.
Each point is the median prediction for a given tissue in a given article. The horizontal and vertical lines give the 90% credible intervals for both displayed quantities for each point. Colors distinguish between tissues (purple: nose; blue: throat; yellow: lung; red: lower GI).

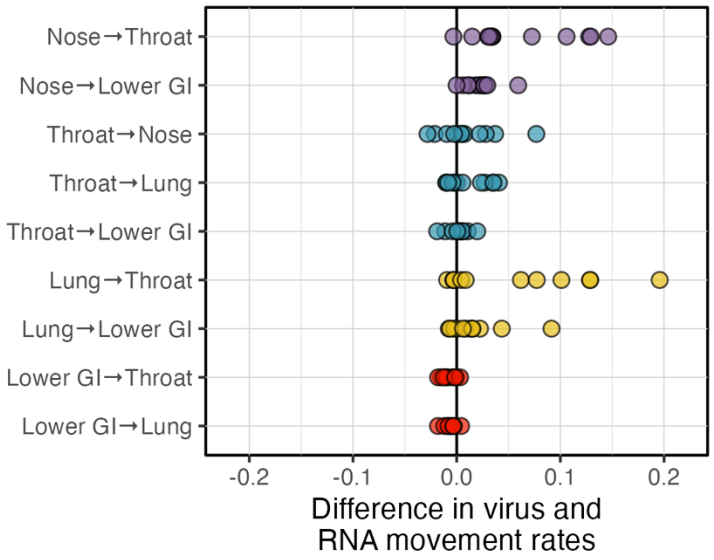

Figure S 3.3 | Difference in the median movement rates of infectious virus particles and RNA. All connections included in the model are displayed and indicated on the y axis. These have the form X→Y, which indicates the flow of virus from tissue X to tissue Y. Each point gives the median parameter value from one article. The points are colored by the source of the virus (i.e., tissue X) according to the color scheme displayed in Figure 3.1B (purple: nose; throat: blue; yellow: lung; red: lower GI). Points to the right of zero correspond with a higher movement rate of virus than of RNA.

Supplementary Tables

	Tissue	ACE2	TMPRSS2	ACE2-TMPRSS2
LRT	Trachea	0.431 *Goblet*	8.081 *Goblet*	5.228 *Goblet*
	Bronchus	0.534 *Goblet*	2.995 *Goblet*	2.662 *Goblet*
	Lung	0.59 *Alveolar type 2*	2.876 *Club*	2.759 *Ciliated*
	Average	0.518 (***Low***)	4.6504 (***High***)	3.5494 (***Medium***)
GI	Stomach	0.234 *Smooth muscle*	0.949 *Pit*	0.217 *Pit*
	Duodenum	1.718 *Enterocyte*	0.280 *Enterocyte*	3.963 *Enterocyte*
	Colon	0.012 *Smooth muscle*	0.905 *Enterocyte*	0 *All types*
	Average	0.655 (***High***)	0.712 (***Low***)	1.394 (***Low***)

Table S 3.1 | Tissue-specific expression patterns.
Each row gives the maximum expression value for each expression type and its associated cell-type in the indicated tissue. These values were calculated based on data presented in Han et al. 2022 (see Methods for details). The average rows give the mean of the expression values for that group of tissues, followed in parentheses by the assigned classification used in this study.

References

Alexandre, M., Marlin, R., Prague, M., Coleon, S., Kahlaoui, N., Cardinaud, S., Naninck, T., Delache, B., Surenaud, M., Galhaut, M., Dereuddre-Bosquet, N., Cavarelli, M., Maisonnasse, P., Centlivre, M., Lacabaratz, C., Wiedemann, A., Zurawski, S., Zurawski, G., Schwartz, O., … Thiébaut, R. (2022). Modelling the response to vaccine in non-human primates to define SARS-CoV-2 mechanistic correlates of protection. *eLife*, 11, e75427. https://doi.org/10.7554/eLife.75427

Baggen, J., Vanstreels, E., Jansen, S., & Daelemans, D. (2021). Cellular host factors for SARS-CoV-2 infection. *Nature Microbiology*, 6(10), Article 10. https://doi.org/10.1038/s41564-021-00958-0

Becker, D. J., Snedden, C. E., Altizer, S., & Hall, R. J. (2018). Host Dispersal Responses to Resource Supplementation Determine Pathogen Spread in Wildlife Metapopulations. *The American Naturalist*, 192(4), 503–517. https://doi.org/10.1086/699477

Beumer, J., Geurts, M. H., Lamers, M. M., Puschhof, J., Zhang, J., van der Vaart, J., Mykytyn, A. Z., Breugem, T. I., Riesebosch, S., Schipper, D., van den Doel, P. B., de Lau, W., Pleguezuelos-Manzano, C., Busslinger, G., Haagmans, B. L., & Clevers, H. (2021). A CRISPR/Cas9 genetically engineered organoid biobank reveals essential host factors for coronaviruses. *Nature Communications*, 12(1), Article 1. https://doi.org/10.1038/s41467-021-25729-7

Bixler, S. L., Stefan, C. P., Jay, A. N., Rossi, F. D., Ricks, K. M., Shoemaker, C. J., Moreau, A. M., Zeng, X., Hooper, J. W., Dyer, D. N., Frick, O. M., Koehler, J. W., Kearney, B. J., DiPinto, N., Liu, J., Tostenson, S. D., Clements, T. L., Smith, J. M., Johnson, J. A., … Pitt, M. L. M. (2022). Exposure Route Influences Disease Severity in the COVID-19 Cynomolgus Macaque Model. *Viruses*, 14(5), Article 5. https://doi.org/10.3390/v14051013

Blair, R. V., Vaccari, M., Doyle-Meyers, L. A., Roy, C. J., Russell-Lodrigue, K., Fahlberg, M., Monjure, C. J., Beddingfield, B., Plante, K. S., Plante, J. A., Weaver, S. C., Qin, X., Midkiff, C. C., Lehmicke, G., Golden, N., Threeton, B., Penney, T., Allers, C., Barnes, M. B., … Rappaport, J. (2021). Acute Respiratory Distress in Aged, SARS-CoV-2–Infected African Green Monkeys but Not Rhesus Macaques. *The American Journal of Pathology*, 191(2), 274–282. https://doi.org/10.1016/j.ajpath.2020.10.016

Bourgonje, A. R., Abdulle, A. E., Timens, W., Hillebrands, J.-L., Navis, G. J., Gordijn, S. J., Bolling, M. C., Dijkstra, G., Voors, A. A., Osterhaus, A. D., van der Voort, P. H., Mulder, D. J., & van Goor, H. (2020). Angiotensin-converting enzyme 2 (ACE2), SARS-CoV-2 and the pathophysiology of coronavirus disease 2019 (COVID-19). *The Journal of Pathology*, 251(3), 228–248. https://doi.org/10.1002/path.5471

Carossino, M., Izadmehr, S., Trujillo, J. D., Gaudreault, N. N., Dittmar, W., Morozov, I., Balasuriya, U. B. R., Cordon-Cardo, C., García-Sastre, A., & Richt, J. A. (2024). ACE2 and TMPRSS2 distribution in the respiratory tract of different animal species and its correlation with SARS-CoV-2 tissue tropism. *Microbiology Spectrum*, 12(2), e03270-23. https://doi.org/10.1128/spectrum.03270-23

Cifuentes-Muñoz, N., Dutch, R. E., & Cattaneo, R. (2018). Direct cell-to-cell transmission of respiratory viruses: The fast lanes. *PLOS Pathogens*, 14(6), 1–7. https://doi.org/10.1371/journal.ppat.1007015

Ciupe, S. M., & Tuncer, N. (2022). Identifiability of parameters in mathematical models of SARS-CoV-2 infections in humans. *Scientific Reports*, 12(1), 14637. https://doi.org/10.1038/s41598-022-18683-x

Crawford, S. E., Ramani, S., Tate, J. E., Parashar, U. D., Svensson, L., Hagbom, M., Franco, M. A., Greenberg, H. B., O'Ryan, M., Kang, G., Desselberger, U., & Estes, M. K. (2017). Rotavirus infection. *Nature Reviews Disease Primers*, 3(1), 1–16. https://doi.org/10.1038/nrdp.2017.83

de Wit, E., & Munster, V. J. (2015). Animal models of disease shed light on Nipah virus pathogenesis and transmission. *The Journal of Pathology*, 235(2), 196–205. https://doi.org/10.1002/path.4444

Dogra, P., Ruiz-Ramírez, J., Sinha, K., Butner, J. D., Peláez, M. J., Rawat, M., Yellepeddi, V. K., Pasqualini, R., Arap, W., Sostman, H. D., Cristini, V., & Wang, Z. (2021). Innate Immunity Plays a Key Role in Controlling Viral Load in COVID-19: Mechanistic Insights from a Whole-Body Infection Dynamics Model. *ACS Pharmacology & Translational Science*, 4(1), 248–265. https://doi.org/10.1021/acsptsci.0c00183

Evans, D. F., Pye, G., Bramley, R., Clark, A. G., Dyson, T. J., & Hardcastle, J. D. (1988). Measurement of gastrointestinal pH profiles in normal ambulant human subjects. *Gut*, 29(8), 1035–1041. https://doi.org/10.1136/gut.29.8.1035

Fallingborg, J. (1999). Intraluminal pH of the human gastrointestinal tract. *Danish Medical Bulletin*, 46(3), 183–196.

Fears, A. C., Beddingfield, B. J., Chirichella, N. R., Slisarenko, N., Killeen, S. Z., Redmann, R. K., Goff, K., Spencer, S., Picou, B., Golden, N., Midkiff, C. C., Bush, D. J., Branco, L. M., Boisen, M. L., Gao, H., Montefiori, D. C., Blair, R. V., Doyle-Meyers, L. A., Russell-Lodrigue, K., … Roy, C. J. (2022). Exposure modality influences viral kinetics but not respiratory outcome of COVID-19 in multiple nonhuman primate species. *PLOS Pathogens*, 18(7), e1010618. https://doi.org/10.1371/journal.ppat.1010618

Fenner, F., Bachmann, P. A., Gibbs, P. J., Murphy, F. A., Studdert, M. J., & White, D. O. (1987). Pathogenesis: Infection and the Spread of Viruses in the Body. In Veterinary Virology (pp. 133–152). Academic Press. https://doi.org/10.1016/B978-0-12-253055-5.50011-6

Gao, C.-C., Li, M., Deng, W., Ma, C.-H., Chen, Y.-S., Sun, Y.-Q., Du, T., Liu, Q.-L., Li, W.-J., Zhang, B., Sun, L., Liu, S.-M., Li, F., Qi, F., Qu, Y., Ge, X., Liu, J., Wang, P., Niu, Y., … Yang, Y.-G. (2022). Differential transcriptomic landscapes of multiple organs from SARS-CoV-2 early infected rhesus macaques. *Protein & Cell*, 13(12), 920–939. https://doi.org/10.1007/s13238-022-00915-5

Gonçalves, A., Maisonnasse, P., Donati, F., Albert, M., Behillil, S., Contreras, V., Naninck, T., Marlin, R., Solas, C., Pizzorno, A., Lemaitre, J., Kahlaoui, N., Terrier, O., Fang, R. H. T., Enouf, V., Dereuddre-Bosquet, N., Brisebarre, A., Touret, F., Chapon, C., … Guedj, J. (2021). SARS-CoV-2 viral dynamics in non-human primates. *PLOS Computational Biology*, 17(3), e1008785. https://doi.org/10.1371/journal.pcbi.1008785

Gupta, A., Madhavan, M. V., Sehgal, K., Nair, N., Mahajan, S., Sehrawat, T. S., Bikdeli, B., Ahluwalia, N., Ausiello, J. C., Wan, E. Y., Freedberg, D. E., Kirtane, A. J., Parikh, S. A., Maurer, M. S., Nordvig, A. S., Accili, D., Bathon, J. M., Mohan, S., Bauer, K. A., … Landry, D. W. (2020). Extrapulmonary manifestations of COVID-19. *Nature Medicine*, 26(7), Article 7. https://doi.org/10.1038/s41591-020-0968-3

Haider, S., & Pal, R. (2013). Integrated Analysis of Transcriptomic and Proteomic Data. *Current Genomics*, 14(2), 91–110. https://doi.org/10.2174/1389202911314020003

Han, L., Wei, X., Liu, C., Volpe, G., Zhuang, Z., Zou, X., Wang, Z., Pan, T., Yuan, Y., Zhang, X., Fan, P., Guo, P., Lai, Y., Lei, Y., Liu, X., Yu, F., Shangguan, S., Lai, G., Deng, Q., … Liu, L. (2022). Cell transcriptomic atlas of the non-human primate Macaca fascicularis. *Nature*, 604(7907), Article 7907. https://doi.org/10.1038/s41586-022-04587-3

Hoang, T. N., Pino, M., Boddapati, A. K., Viox, E. G., Starke, C. E., Upadhyay, A. A., Gumber, S., Nekorchuk, M., Busman-Sahay, K., Strongin, Z., Harper, J. L., Tharp, G. K., Pellegrini, K. L., Kirejczyk, S., Zandi, K., Tao, S., Horton, T. R., Beagle, E. N., Mahar, E. A., … Paiardini, M. (2021). Baricitinib treatment resolves lower-airway macrophage inflammation and neutrophil recruitment in SARS-CoV-2-infected rhesus macaques. *Cell*, 184(2), 460-475.e21. https://doi.org/10.1016/j.cell.2020.11.007

Hoffmann, M., Kleine-Weber, H., Schroeder, S., Krüger, N., Herrler, T., Erichsen, S., Schiergens, T. S., Herrler, G., Wu, N. H., Nitsche, A., Müller, M. A., Drosten, C., & Pöhlmann, S. (2020). SARS-CoV-2 Cell Entry Depends on ACE2 and TMPRSS2 and Is Blocked by a Clinically Proven Protease Inhibitor. *Cell*, 181(2), 271–280. https://doi.org/10.1016/j.cell.2020.02.052

Hou, Y. J., Okuda, K., Edwards, C. E., Martinez, D. R., Asakura, T., Dinnon, K. H., Kato, T., Lee, R. E., Yount, B. L., Mascenik, T. M., Chen, G., Olivier, K. N., Ghio, A., Tse, L. V., Leist, S. R., Gralinski, L. E., Schäfer, A., Dang, H., Gilmore, R., … Baric, R. S. (2020). SARS-CoV-2 Reverse Genetics Reveals a Variable Infection Gradient in the Respiratory Tract. *Cell*, 182(2), 429-446.e14. https://doi.org/10.1016/j.cell.2020.05.042

Jackson, C. B., Farzan, M., Chen, B., & Choe, H. (2022). Mechanisms of SARS-CoV-2 entry into cells. *Nature Reviews Molecular Cell Biology*, 23(1), Article 1. https://doi.org/10.1038/s41580-021-00418-x

Karlsson, E. A., Meliopoulos, V. A., Savage, C., Livingston, B., Mehle, A., & Schultz-Cherry, S. (2015). Visualizing real-time influenza virus infection, transmission and protection in ferrets. *Nature Communications*, 6(1), 6378–6378. https://doi.org/10.1038/ncomms7378

Ke, R., Zitzmann, C., Ho, D. D., Ribeiro, R. M., & Perelson, A. S. (2021). In vivo kinetics of SARS-CoV-2 infection and its relationship with a person's infectiousness. *Proceedings of the National Academy of Sciences*, 118(49), e2111477118. https://doi.org/10.1073/pnas.2111477118

Kishimoto, M., Uemura, K., Sanaki, T., Sato, A., Hall, W. W., Kariwa, H., Orba, Y., Sawa, H., & Sasaki, M. (2021). TMPRSS11D and TMPRSS13 Activate the SARS-CoV-2 Spike Protein. *Viruses*, 13(3), Article 3. https://doi.org/10.3390/v13030384

Laporte, M., Raeymaekers, V., Berwaer, R. V., Vandeput, J., Marchand-Casas, I., Thibaut, H.-J., Looveren, D. V., Martens, K., Hoffmann, M., Maes, P., Pöhlmann, S., Naesens, L., & Stevaert, A. (2021). The SARS-CoV-2 and other human coronavirus spike proteins are fine-tuned towards temperature and proteases of the human airways. *PLOS Pathogens*, 17(4), e1009500. https://doi.org/10.1371/journal.ppat.1009500

Laporte, M., Stevaert, A., Raeymaekers, V., Boogaerts, T., Nehlmeier, I., Chiu, W., Benkheil, M., Vanaudenaerde, B., Pöhlmann, S., & Naesens, L. (2019). Hemagglutinin Cleavability, Acid Stability, and Temperature Dependence Optimize Influenza B Virus for Replication in Human Airways. *Journal of Virology*. https://doi.org/10.1128/JVI.01430-19

Lee, A. C.-Y., Zhang, A. J., Chan, J. F.-W., Li, C., Fan, Z., Liu, F., Chen, Y., Liang, R., Sridhar, S., Cai, J.-P., Poon, V. K.-M., Chan, C. C.-S., To, K. K.-W., Yuan, S., Zhou, J., Chu, H., & Yuen, K.-Y. (2020). Oral SARS-CoV-2 Inoculation Establishes Subclinical Respiratory Infection with Virus Shedding in Golden Syrian Hamsters. *Cell Reports Medicine*, 1(7), 100121. https://doi.org/10.1016/j.xcrm.2020.100121

Lee, C.-Y., & Lowen, A. C. (2021). Animal models for SARS-CoV-2. *Current Opinion in Virology*, 48, 73–81. https://doi.org/10.1016/j.coviro.2021.03.009

Lim, S., Zhang, M., & Chang, T. L. (2022). ACE2-Independent Alternative Receptors for SARS-CoV-2. *Viruses*, 14(11), Article 11. https://doi.org/10.3390/v14112535

Lindemann, J., Leiacker, R., Rettinger, G., & Keck, T. (2002). Nasal mucosal temperature during respiration. *Clinical Otolaryngology & Allied Sciences*, 27(3), 135–139. https://doi.org/10.1046/j.1365-2273.2002.00544.x

Lipsitch, M., Barclay, W., Raman, R., Russell, C. J., Belser, J. A., Cobey, S., Kasson, P. M., Lloyd-Smith, J. O., Maurer-Stroh, S., Riley, S., Beauchemin, C. A., Bedford, T., Friedrich, T. C., Handel, A., Herfst, S., Murcia, P. R., Roche, B., Wilke, C. O., & Russell, C. A. (2016). Viral factors in influenza pandemic risk assessment. *eLife*, 5, e18491. https://doi.org/10.7554/eLife.18491

Liu, L., Wei, Q., Alvarez, X., Wang, H., Du, Y., Zhu, H., Jiang, H., Zhou, J., Lam, P., Zhang, L., Lackner, A., Qin, C., & Chen, Z. (2011). Epithelial Cells Lining Salivary Gland Ducts Are Early Target Cells of Severe Acute Respiratory Syndrome Coronavirus Infection in the Upper Respiratory Tracts of Rhesus Macaques. *Journal of Virology*, 85(8), 4025–4030. https://doi.org/10.1128/jvi.02292-10

Marc, A., Marlin, R., Donati, F., Prague, M., Kerioui, M., Hérate, C., Alexandre, M., Dereuddre-bosquet, N., Bertrand, J., Contreras, V., Behillil, S., Maisonnasse, P., Werf, S. V. D., Grand, R. L., & Guedj, J. (2023). Impact of variants of concern on SARS-CoV-2 viral dynamics in non-human primates. *PLOS Computational Biology*, 19(8), e1010721. https://doi.org/10.1371/journal.pcbi.1010721

McCall, L.-I. (2021). Quo vadis? Central Rules of Pathogen and Disease Tropism. *Frontiers in Cellular and Infection Microbiology*, 11, 56. https://doi.org/10.3389/fcimb.2021.640987

McFadden, E. R., Pichurko, B. M., Bowman, H. F., Ingenito, E., Burns, S., Dowling, N., & Solway, J. (1985). Thermal mapping of the airways in humans. *Journal of Applied Physiology* (Bethesda, Md.: 1985), 58(2), 564–570. https://doi.org/10.1152/jappl.1985.58.2.564

Mercer, J., & Greber, U. F. (2013). Virus interactions with endocytic pathways in macrophages and dendritic cells. *Trends in Microbiology*, 21(8), 380–388. https://doi.org/10.1016/j.tim.2013.06.001

Munster, V. J., Feldmann, F., Williamson, B. N., van Doremalen, N., Pérez-Pérez, L., Schulz, J., Meade-White, K., Okumura, A., Callison, J., Brumbaugh, B., Avanzato, V. A., Rosenke, R., Hanley, P. W., Saturday, G., Scott, D., Fischer, E. R., & de Wit, E. (2020). Respiratory disease in rhesus macaques inoculated with SARS-CoV-2. *Nature*, 585(7824), Article 7824. https://doi.org/10.1038/s41586-020-2324-7

Perelson, A. S. (2002). Modelling viral and immune system dynamics. *Nature Reviews Immunology*, 2(1), 28–36. https://doi.org/10.1038/nri700

Prescott, M. J. (2010). Ethics of primate use. *Advances in Science and Research*, 5(1), 11–22. https://doi.org/10.5194/asr-5-11-2010

Puelles, V. G., Lütgehetmann, M., Lindenmeyer, M. T., Sperhake, J. P., Wong, M. N., Allweiss, L., Chilla, S., Heinemann, A., Wanner, N., Liu, S., Braun, F., Lu, S., Pfefferle, S., Schröder, A. S., Edler, C., Gross, O., Glatzel, M., Wichmann, D., Wiech, T., … Huber, T. B. (2020). Multiorgan and Renal Tropism of SARS-CoV-2. *New England Journal of Medicine*. https://doi.org/10.1056/NEJMc2011400

Pulliam, H. R. (1988). Sources, Sinks, and Population Regulation. *The American Naturalist*, 132(5), 652–661.

Pulliam, H. R. (2000). On the relationship between niche and distribution. *Ecology Letters*, 3(4), 349–361. https://doi.org/10.1046/j.1461-0248.2000.00143.x

Rodriguez, T., & Dobrovolny, H. M. (2021). Estimation of viral kinetics model parameters in young and aged SARS-CoV-2 infected macaques. *Royal Society Open Science*, 8(11), 202345. https://doi.org/10.1098/rsos.202345

Rosenke, K., Jarvis, M. A., Feldmann, F., Schwarz, B., Okumura, A., Lovaglio, J., Saturday, G., Hanley, P. W., Meade-White, K., Williamson, B. N., Hansen, F., Perez-Perez, L., Leventhal, S., Tang-Huau, T.-L., Callison, J., Haddock, E., Stromberg, K. A., Scott, D., Sewell, G., … Feldmann, H. (2020). Hydroxychloroquine prophylaxis and treatment is ineffective in macaque and hamster SARS-CoV-2 disease models. *JCI Insight*, 5(23). https://doi.org/10.1172/jci.insight.143174

Russell, C. J., Hu, M., & Okda, F. A. (2018). Influenza Hemagglutinin Protein Stability, Activation, and Pandemic Risk. *Trends in Microbiology*, 26(10), 841–853. https://doi.org/10.1016/j.tim.2018.03.005

Salamanna, F., Maglio, M., Landini, M. P., & Fini, M. (2020). Body Localization of ACE-2: On the Trail of the Keyhole of SARS-CoV-2. *Frontiers in Medicine*, 7. https://www.frontiersin.org/article/10.3389/fmed.2020.594495

Salguero, F. J., White, A. D., Slack, G. S., Fotheringham, S. A., Bewley, K. R., Gooch, K. E., Longet, S., Humphries, H. E., Watson, R. J., Hunter, L., Ryan, K. A., Hall, Y., Sibley, L., Sarfas, C., Allen, L., Aram, M., Brunt, E., Brown, P., Buttigieg, K. R., … Carroll, M. W. (2021). Comparison of rhesus and cynomolgus macaques as an infection model for COVID-19. *Nature Communications*, 12(1), Article 1. https://doi.org/10.1038/s41467-021-21389-9

Samuel, C. E. (2001). Antiviral Actions of Interferons. *Clinical Microbiology Reviews*, 14(4), 778–809. https://doi.org/10.1128/cmr.14.4.778-809.2001

Schreiber, S. J., & Lloyd-Smith, J. O. (2009). Invasion Dynamics in Spatially Heterogeneous Environments. *The American Naturalist*, 174(4), 490–505. https://doi.org/10.1086/605405

Shang, J., Wan, Y., Luo, C., Ye, G., Geng, Q., Auerbach, A., & Li, F. (2020). Cell entry mechanisms of SARS-CoV-2. *Proceedings of the National Academy of Sciences*, 117(21), 11727–11734. https://doi.org/10.1073/pnas.2003138117

Shilts, J., Crozier, T. W. M., Greenwood, E. J. D., Lehner, P. J., & Wright, G. J. (2021). No evidence for basigin/CD147 as a direct SARS-CoV-2 spike binding receptor. *Scientific Reports*, 11(1), Article 1. https://doi.org/10.1038/s41598-020-80464-1

Snedden, C. E., Makanani, S. K., Schwartz, S. T., Gamble, A., Blakey, R. V., Borremans, B., Helman, S. K., Espericueta, L., Valencia, A., Endo, A., Alfaro, M. E., & Lloyd-Smith, J. O. (2021). SARS-CoV-2: Cross-scale Insights from Ecology and Evolution. *Trends in Microbiology*. https://doi.org/10.1016/j.tim.2021.03.013

Snyder, R. E. (2003). How Demographic Stochasticity Can Slow Biological Invasions. *Ecology*, 84(5), 1333–1339. https://doi.org/10.1890/0012-9658(2003)084[1333:HDSCSB]2.0.CO;2

Sreenivasan, C. C., Thomas, M., Antony, L., Wormstadt, T., Hildreth, M. B., Wang, D., Hause, B., Francis, D. H., Li, F., & Kaushik, R. S. (2019). Development and characterization of swine primary respiratory epithelial cells and their susceptibility to infection by four influenza virus types. *Virology*, 528, 152–163. https://doi.org/10.1016/j.virol.2018.12.016

Stein, S. R., Ramelli, S. C., Grazioli, A., Chung, J.-Y., Singh, M., Yinda, C. K., Winkler, C. W., Sun, J., Dickey, J. M., Ylaya, K., Ko, S. H., Platt, A. P., Burbelo, P. D., Quezado, M., Pittaluga, S., Purcell, M., Munster, V. J., Belinky, F., Ramos-Benitez, M. J., … Chertow, D. S. (2022). SARS-CoV-2 infection and persistence in the human body and brain at autopsy. *Nature*, 612(7941), 758–763. https://doi.org/10.1038/s41586-022-05542-y

Sungnak, W., Huang, N., Bécavin, C., Berg, M., Queen, R., Litvinukova, M., Talavera-López, C., Maatz, H., Reichart, D., Sampaziotis, F., Worlock, K. B., Yoshida, M., & Barnes, J. L. (2020). SARS-CoV-2 entry factors are highly expressed in nasal epithelial cells together with innate immune genes. *Nature Medicine*, 26(5), Article 5. https://doi.org/10.1038/s41591-020-0868-6

Van Doremalen, N., & Munster, V. J. (2015). Animal models of Middle East respiratory syndrome coronavirus infection. *Antiviral Research*, 122, 28–38. https://doi.org/10.1016/j.antiviral.2015.07.005

V'kovski, P., Gultom, M., Kelly, J. N., Steiner, S., Russeil, J., Mangeat, B., Cora, E., Pezoldt, J., Holwerda, M., Kratzel, A., Laloli, L., Wider, M., Portmann, J., Tran, T., Ebert, N., Stalder, H., Hartmann, R., Gardeux, V., Alpern, D., … Dijkman, R. (2021). Disparate temperature-dependent virus–host dynamics for SARS-CoV-2 and SARS-CoV in the human respiratory epithelium. *PLOS Biology*, 19(3), e3001158. https://doi.org/10.1371/journal.pbio.3001158

Vogel, A. B., Kanevsky, I., Che, Y., Swanson, K. A., Muik, A., Vormehr, M., Kranz, L. M., Walzer, K. C., Hein, S., Güler, A., Loschko, J., Maddur, M. S., Ota-Setlik, A., Tompkins, K., Cole, J., Lui, B. G., Ziegenhals, T., Plaschke, A., Eisel, D., … Sahin, U. (2021). BNT162b vaccines protect rhesus macaques from SARS-CoV-2. *Nature*, 592(7853), 283–289. https://doi.org/10.1038/s41586-021-03275-y

Wang, S., Pan, Y., Wang, Q., Miao, H., Brown, A. N., & Rong, L. (2020). Modeling the viral dynamics of SARS-CoV-2 infection. *Mathematical Biosciences*, 328, 108438. https://doi.org/10.1016/j.mbs.2020.108438

Williamson, B. N., Feldmann, F., Schwarz, B., Meade-White, K., Porter, D. P., Schulz, J., van Doremalen, N., Leighton, I., Yinda, C. K., Pérez-Pérez, L., Okumura, A., Lovaglio, J., Hanley, P. W., Saturday, G., Bosio, C. M., Anzick, S., Barbian, K., Cihlar, T., Martens, C., … de Wit, E. (2020). Clinical benefit of remdesivir in rhesus macaques infected with SARS-CoV-2. *Nature*, 1–7. https://doi.org/10.1038/s41586-020-2423-5

Yao, X.-H., Luo, T., Shi, Y., He, Z.-C., Tang, R., Zhang, P.-P., Cai, J., Zhou, X.-D., Jiang, D.-P., Fei, X.-C., Huang, X.-Q., Zhao, L., Zhang, H., Wu, H.-B., Ren, Y., Liu, Z.-H., Zhang, H.-R., Chen, C., Fu, W.-J., … Bian, X.-W. (2021). A cohort autopsy study defines COVID-19 systemic pathogenesis. *Cell Research*, 31(8), 836–846. https://doi.org/10.1038/s41422-021-00523-8

Zang, R., Castro, M. F. G., McCune, B. T., Zeng, Q., Rothlauf, P. W., Sonnek, N. M., Liu, Z., Brulois, K. F., Wang, X., Greenberg, H. B., Diamond, M. S., Ciorba, M. A., Whelan, S. P. J., & Ding, S. (2020). TMPRSS2 and TMPRSS4 promote SARS-CoV-2 infection of human small intestinal enterocytes. *Science Immunology*, 5(47), eabc3582. https://doi.org/10.1126/sciimmunol.abc3582

Zanin, M., Baviskar, P., Webster, R., & Webby, R. (2016). The Interaction between Respiratory Pathogens and Mucus. *Cell Host & Microbe*, 19(2), 159–168. https://doi.org/10.1016/j.chom.2016.01.001

Zhang, H., Shao, B., Dang, Q., Chen, Z., Zhou, Q., Luo, H., Yuan, W., & Sun, Z. (2021). Pathogenesis and Mechanism of Gastrointestinal Infection With COVID-19. *Frontiers in Immunology*, 12. https://doi.org/10.3389/fimmu.2021.674074

Zhou, X., Jiang, W., Liu, Z., Liu, S., & Liang, X. (2017). Virus Infection and Death Receptor-Mediated Apoptosis. *Viruses*, 9(11), Article 11. https://doi.org/10.3390/v9110316

Ziegler, C. G. K., Allon, S. J., Nyquist, S. K., Mbano, I. M., Miao, V. N., Tzouanas, C. N., Cao, Y., Yousif, A. S., Bals, J., Hauser, B. M., Feldman, J., Muus, C., Wadsworth, M. H., Kazer, S. W., Hughes, T. K., Doran, B., Gatter, G. J., Vukovic, M., Taliaferro, F., … Zhang, K. (2020). SARS-CoV-2 Receptor ACE2 Is an Interferon-Stimulated Gene in Human Airway Epithelial Cells and Is Detected in Specific Cell Subsets across Tissues. *Cell*, 181(5), 1016-1035.e19. https://doi.org/10.1016/j.cell.2020.04.035

Zitzmann, C., Ke, R., Ribeiro, R. M., & Perelson, A. S. (2024). How robust are estimates of key parameters in standard viral dynamic models? *PLOS Computational Biology*, 20(4), e1011437. https://doi.org/10.1371/journal.pcbi.1011437